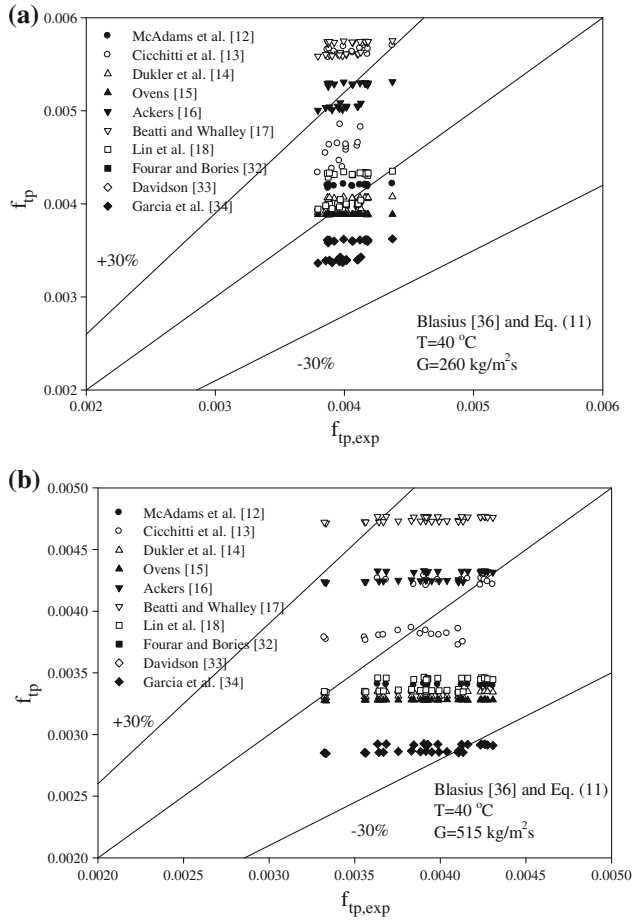

Fig. 3 Comparison of two-phase friction factors obtained from Blasius [36] equation and Eq. 11

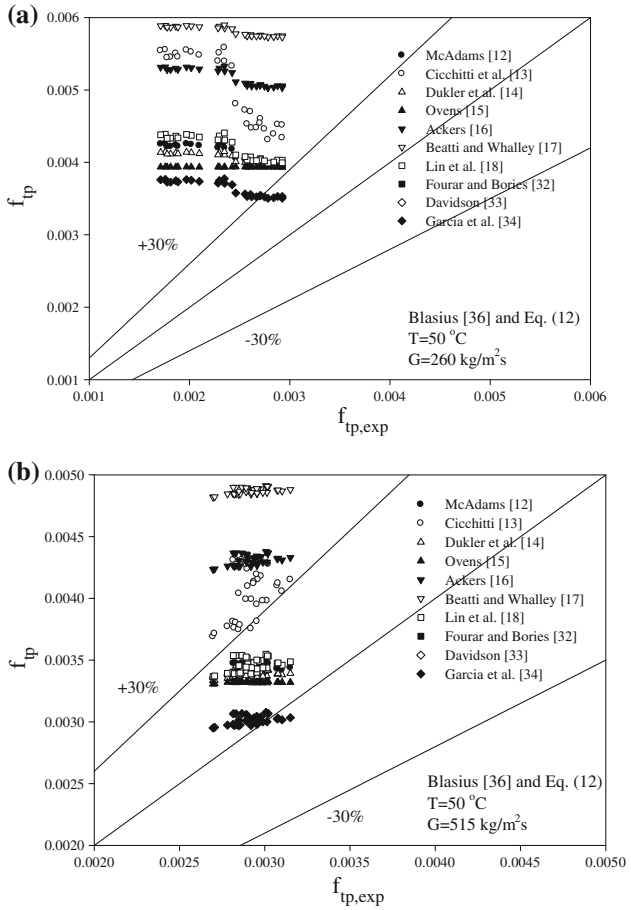

Fig. 4 Comparison of two-phase friction factors obtained from Blasius [36] equation and Eq. 12

where the homogeneous velocity is calculated from Dutkowski [11]:

$$u_{hom} = \frac{m_{total}}{\rho_{tp} A} \tag{16}$$

where the total mass flow is

$$m_{total} = GA \tag{17}$$

and the area of the flow is

$$A = \frac{\pi d^2}{4}. \tag{18}$$

The homogeneous dynamic viscosity correlations (μ_{tp}) in the literature are summarized in Table 2. They were the variable parameters in the related equations in the study and also numerical solution of the study.

The Fanning friction factor can be calculated using the Hagen-Poiseuille flow [35] in Eq. 19 for laminar–laminar flow and the Blasius equation [36] in Eq. 20 for turbulent–turbulent flow respectively as follows:

$$Re_{hom} < 2,300 \quad f_{tp} = \frac{16}{Re_{hom}} \tag{19}$$

$$Re_{hom} > 2,300 \quad f_{tp} = \frac{0.079}{Re_{hom}^{0.25}} \tag{20}$$

where the homogeneous Reynolds number can be determined as:

$$Re_{hom} = \frac{Gd}{\mu_{tp}} \tag{21}$$

3.4.2 *Separated flow model*

The two-phase pressure gradient is the sum of three contributions: the gravitational pressure gradient, the momentum pressure gradient, and the frictional pressure gradient:

$$\frac{dP}{dz} = \left(\frac{dP}{dz}\right)_G + \left(\frac{dP}{dz}\right)_M + \left(\frac{dP}{dz}\right)_F \tag{22}$$

Pressure drop due to gravity can be determined as in [37]:

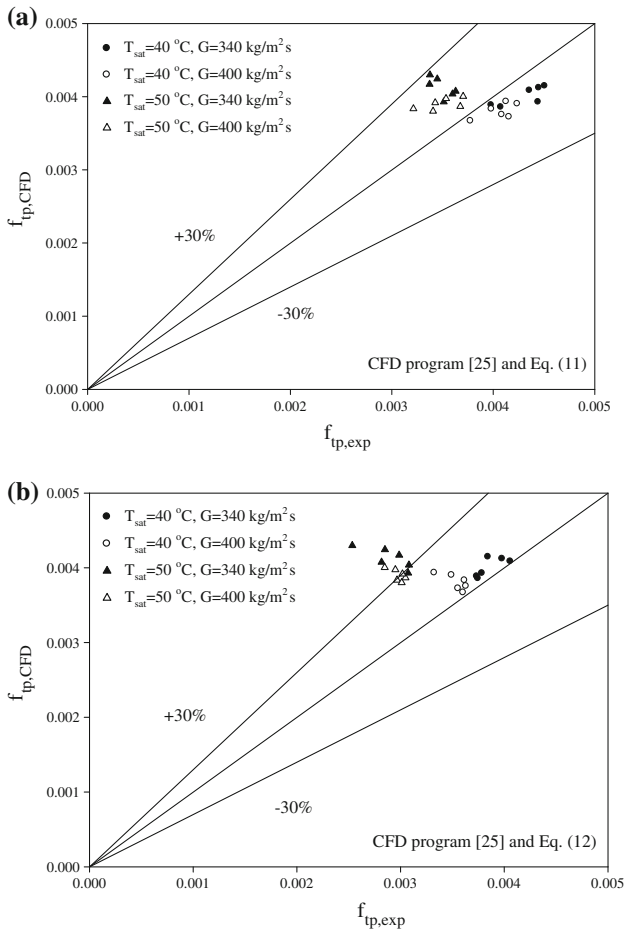

Fig. 5 Comparison of two-phase friction factors obtained from Eq. 11 (**a**) and (**b**) Eq. 12 and CFD program [25]

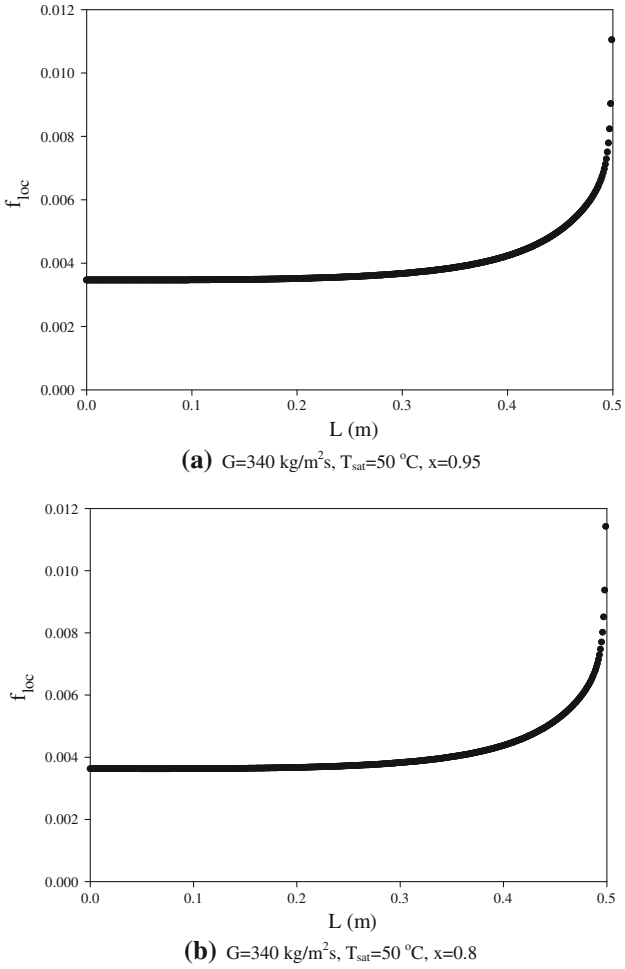

Fig. 6 Local alterations of two-phase friction factors obtained from CFD program [25] for various experimental conditions

$$(\Delta P)_G = g(\alpha\rho_g + (1-\alpha)\rho_l)L \tag{23}$$

where the void fraction, α, can be determined from the Chisholm [38] correlation shown in Table 3.

Generally, the characterization of two-phase flows depends on the void fraction which is an important value for the calculation of various parameters regarding the heat transfer and pressure drop. Accordingly, researchers have performed intensive studies to develop void fraction correlations for two-phase flows. In consequence of their efforts in the literature, Woldesemayat and Ghajar [43] stated that void fraction models and correlations can be specified as local, chordal, cross-sectional, and volumetric for different flow regimes. It should be noted that the determination of the proper void fraction models and correlations belonging to the authors' experimental database was performed in the authors' previous publications and these void fraction models and correlations are summarized in Table 3.

The momentum transfer term contributes to the overall pressure drop during condensation due to the mass transfer that occurs at the phase's interface. It was reported by Honda et al. [44] and Sami et al. [45] that the momentum pressure gradient can be neglected for the condensation, on the other hand, the momentum pressure gradient can be written according to the results of the one-dimensional two-phase separated-flow analysis which can be defined as follows [37]:

$$\left(\frac{dP}{dz}\right)_M = -G^2\frac{d}{dz}\left[\frac{x^2}{\rho_g\alpha} + \frac{(1-x)^2}{\rho_l(1-\alpha)}\right] \tag{24}$$

Equation 24 can be rearranged as follows:

$$\Delta P_M = G^2\left[\left\{\frac{(1-x)^2}{\rho_l(1-\alpha)} + \frac{x^2}{\rho_g\alpha}\right\}_o - \left\{\frac{(1-x)^2}{\rho_l(1-\alpha)} + \frac{x^2}{\rho_g\alpha}\right\}_i\right] \tag{25}$$

Akers et al. [46] developed a two-phase multiplier with the assumption that two-phase flows were similar to a single-phase flow. He predicted the frictional two-phase pressure drop by means of a multiplying factor, using the

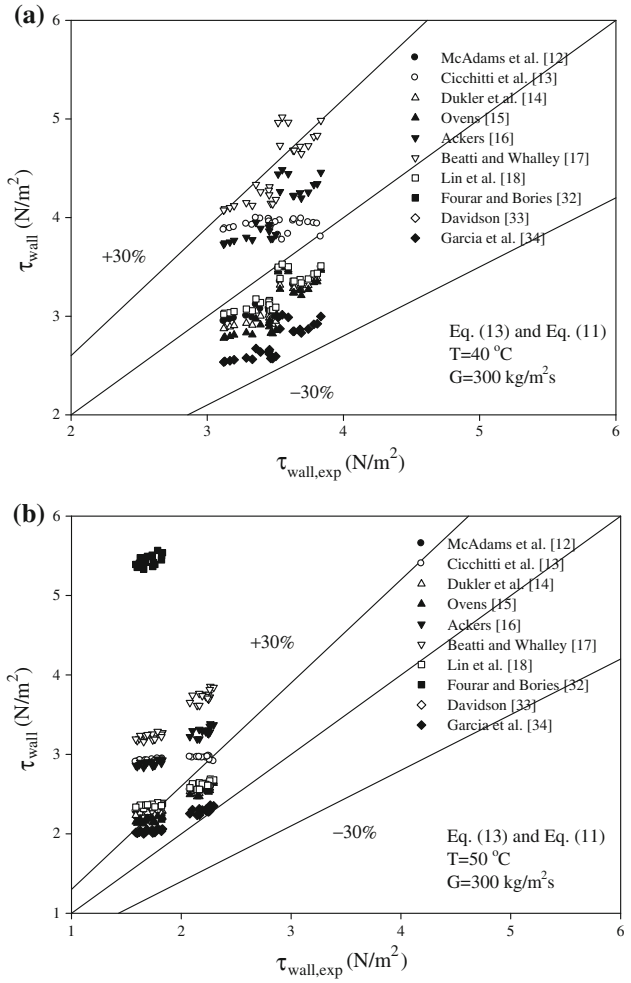

Fig. 7 Comparison of wall shear stresses obtained from Eqs. 13 and 11

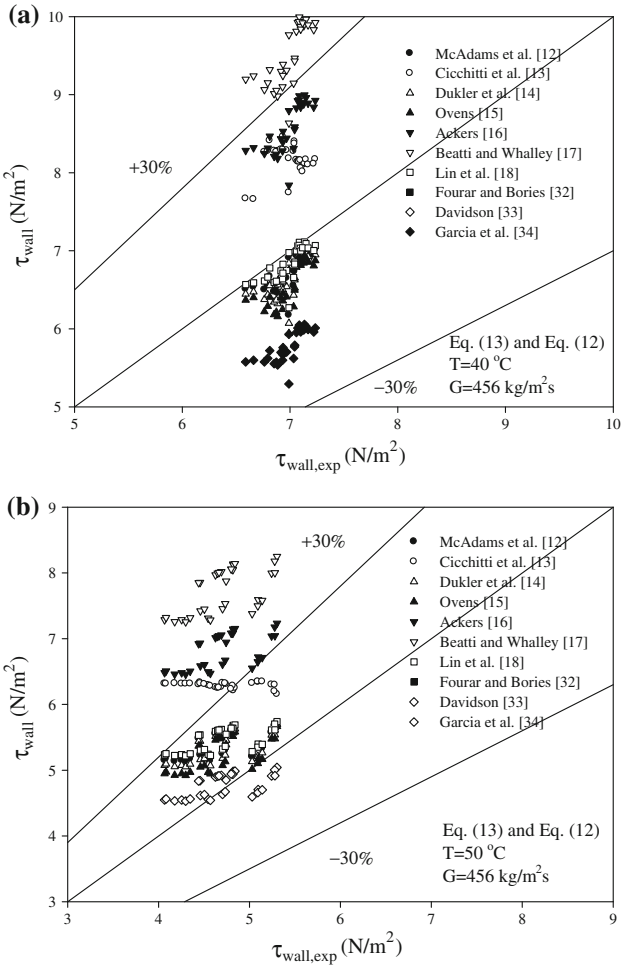

Fig. 8 Comparison of wall shear stresses obtained from Eqs. 13 and 12

same rationale as that behind the Lockhart Martinelli multiplier [7]. His model is known as the "equivalent Reynolds number model". It can be used for an annular flow regime which could be replaced by an equivalent all liquid flow that produces the same wall shear stress as that of the two-phase flow according to this model. Later, several researchers used this model, for example Moser et al. [24] and Ma et al. [47]. The two-phase frictional pressure drop is calculated from two-phase friction factor by the following equation based on all liquid *Re* number [46]:

$$f_{tp} = \frac{(\Delta P)_F}{G_{eq}^2/2\rho_l}\frac{d}{4L} = \frac{(\Delta P)_F 2\rho_l d^3}{Re_{eq}^2 \mu_l^2 4L} \tag{26}$$

where the all liquid equivalent *Re* number is

$$Re_{eq} = \frac{G_{eq} d}{\mu_l} \tag{27}$$

and equivalent liquid mass flux is

$$G_{eq} = G\left((1-x) + x\left(\frac{\rho_l}{\rho_g}\right)^{0,5}\right) \tag{28}$$

and two-phase friction factors are calculated by means of the correlations in Table 4.

Fukano and Furukawa [48] investigated the effects of liquid viscosity on the mean liquid film thickness, wave heights, and gas–liquid interfacial stresses in the vertical upward co-current annular flow in a 26 mm inner diameter tube using water and glycerol solutions as working fluids. Moeck [49] performed experiments on the diameter of entrained liquid droplets for air–water annular flow. Fore et al. [50] has obtained the film thickness and pressure gradient data for co-current upward flow of nitrogen and water under high pressure in a rectangular duct. Carey [37] developed Blasius's [36] friction factor and reported that the vapour flow in the tube can be treated as a single phase flow. Because the film is thin, the mean velocity of the

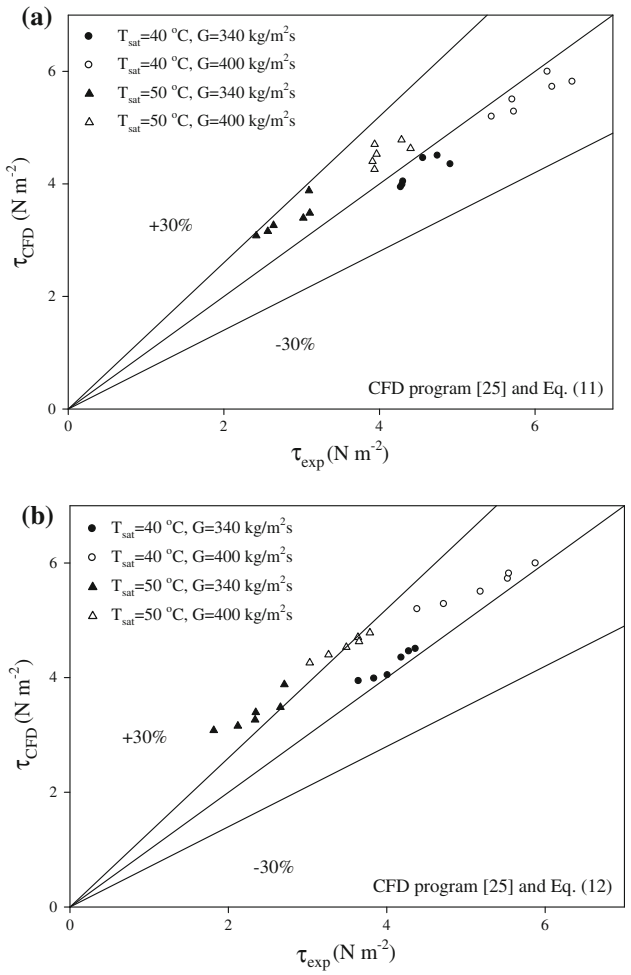

Fig. 9 Comparison of wall shear stresses obtained from Eq. 11 (**a**) and (**b**) Eq. 12 and CFD program [25]

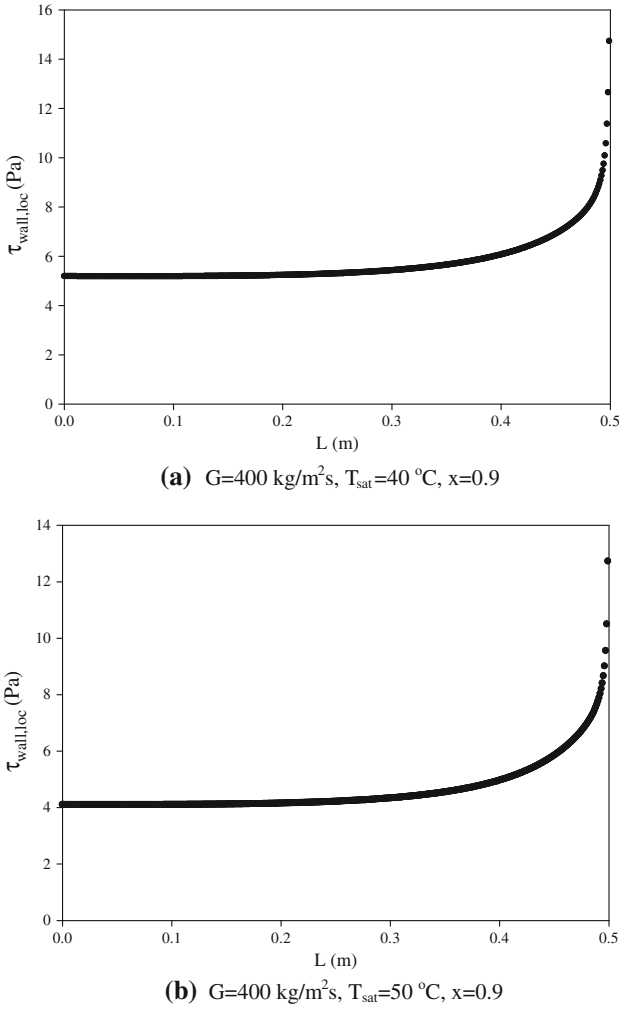

Fig. 10 Local alterations of wall shear stresses obtained from CFD program [25] for various experimental conditions

vapour is much larger than the liquid velocity at the interface due to the high viscosity of the liquid phase compared to the vapour phase. Moreover, the vapour velocity is assumed to be zero between the phases. The interfacial shear can be computed using the conventional single phase correlation by using these assumptions. The interfacial shear stress in annular two-phase flow is one of the main parameters governing transport phenomena and is required for modeling the flow. It has been intensively studied, especially for the flow assuming that all liquid travels in the liquid film. Some of the earliest works were performed by Cousins et al. [51], Wallis [52], Webb [53], Whalley [54, 55], Hewitt and Hall-Taylor [56], Asali et al. [57], Azzopardi and Teixeira [58], Fukano and Furukawa [48], Moeck [49], and Fore et al. [50].

3.4.3 Numerical model

This problem was solved by means of the processes in the Fluent CFD program [25]. Fluent is a commonly used software in CFD analysis in the literature and a detailed description of the mathematical model can be found in the Fluent User's Guide. This program uses a technique based on control volume theory to convert the governing equations to algebraic equations so they can be solved numerically. The control volume technique works by performing the integration of the governing equations about each control volume, and then generates discrimination of the equations which conserve each quantity based on control volume. Details of the selections in CFD program is given in Table 5. The necessary input values for the CFD program to run are obtained from the homogeneous flow model's correlations such as dynamic viscosity from Lin et al. [18].

The skin friction coefficient is defined by

$$C_f = \frac{\tau_{wall}}{\frac{1}{2}\rho U_\infty^2} \tag{29}$$

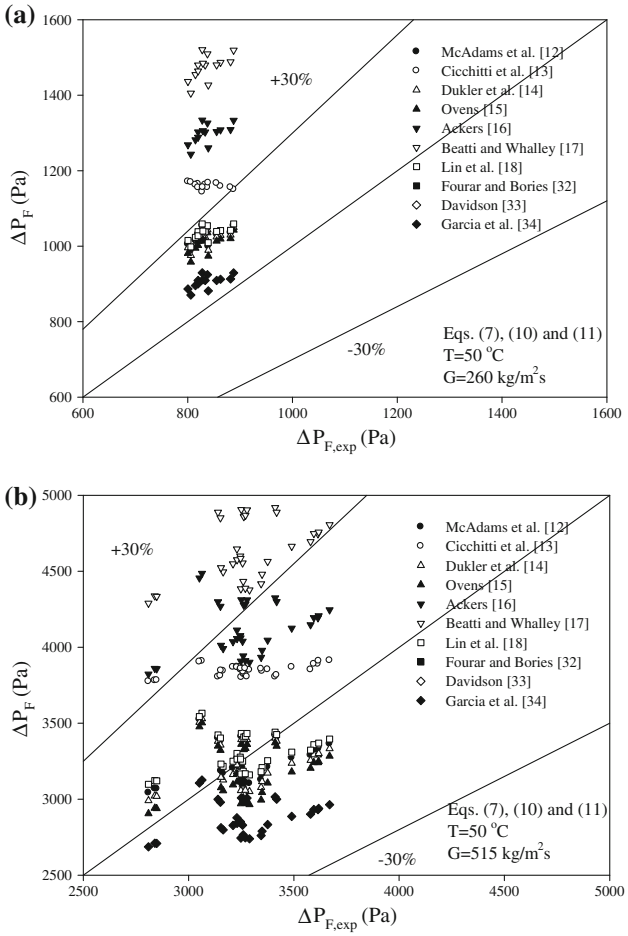

Fig. 11 Comparison of frictional pressure drops obtained from Eqs. 7, 10 and 11

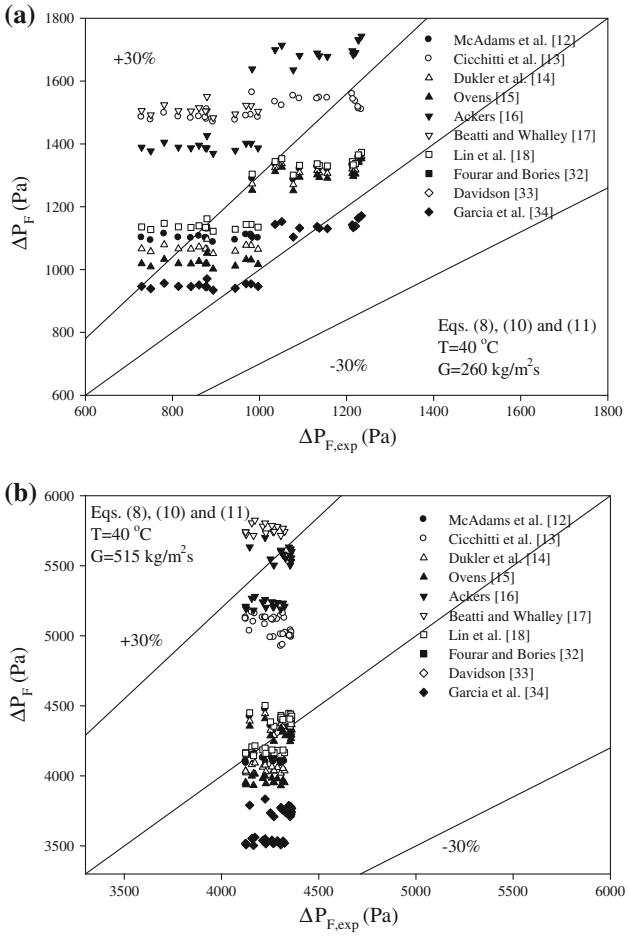

Fig. 12 Comparison of frictional pressure drops obtained from Eqs. 8, 10 and 11

where τ_{wall} is the local wall shear stress, ρ is the fluid density and U_{∞} is the free-stream velocity (usually taken outside of the boundary layer or at the inlet).

The wall shear stress, τ_{wall}, is given by

$$\tau_{wall} = \mu\left(\frac{\partial u}{\partial y}\right)_{y=0} \tag{30}$$

where μ is the dynamic viscosity, u is the flow velocity parallel to the wall, and y is the distance to the wall.

4 Results and discussion

The indirectly determined void fraction, wall shear stress, friction factor, frictional pressure drop, and total pressure drop were presented in the following paragraphs using a large number of measured data during the downward laminar condensation of R134a at a high mass flux in a vertical smooth tube over a range of experimental conditions shown in authors' previous publications. It should be noted that detailed explanations and some additional figures and tables with different experimental parameters related to this study on the void fraction models and correlations, film thickness models, friction factor and frictional pressure drop models, and heat transfer and pressure drop characteristics of data belonging to the experimental apparati can be seen in the authors' previous publications.

The experiments were performed to investigate the effect of empirical correlations such as dynamic viscosity correlations and friction factor correlations on the pressure drop characteristics using well-known flow models for the downward two-phase flow of R134a in a vertical round tube with an inner diameter of 8.1 mm. Pure HFC-134a was used in the experiments. The heat fluxes are between 10.16 and 66.61 kW/m^2 while the mass fluxes are between 260 and 515 kg/m^{2}s.

The data shown in all tables and figures for the study of R134a condensation in a vertical tube were found in the annular flow section according to the authors' investigation of flow identification studies using various flow pattern

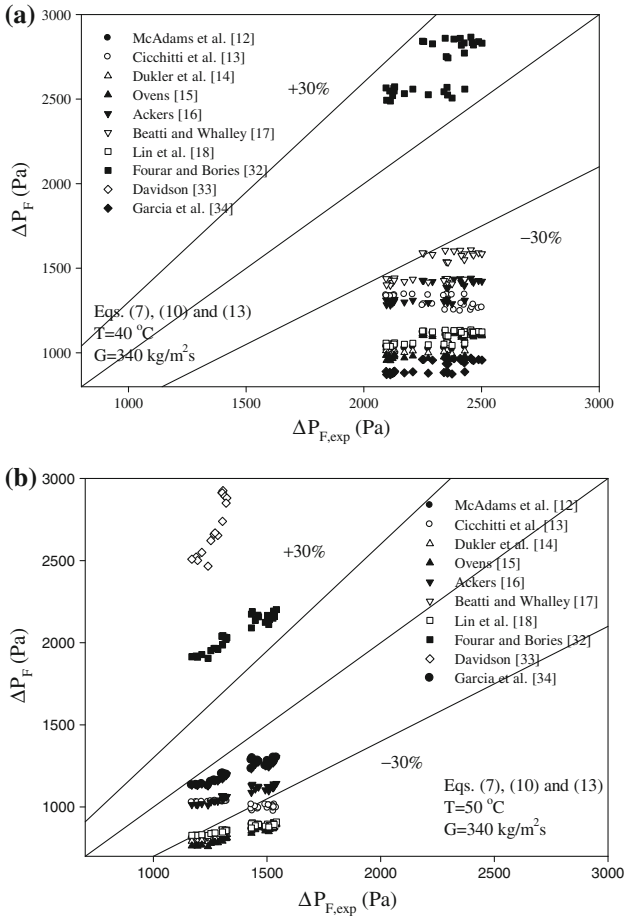

Fig. 13 Comparison of frictional pressure drops obtained from Eqs. 7, 10 and 13

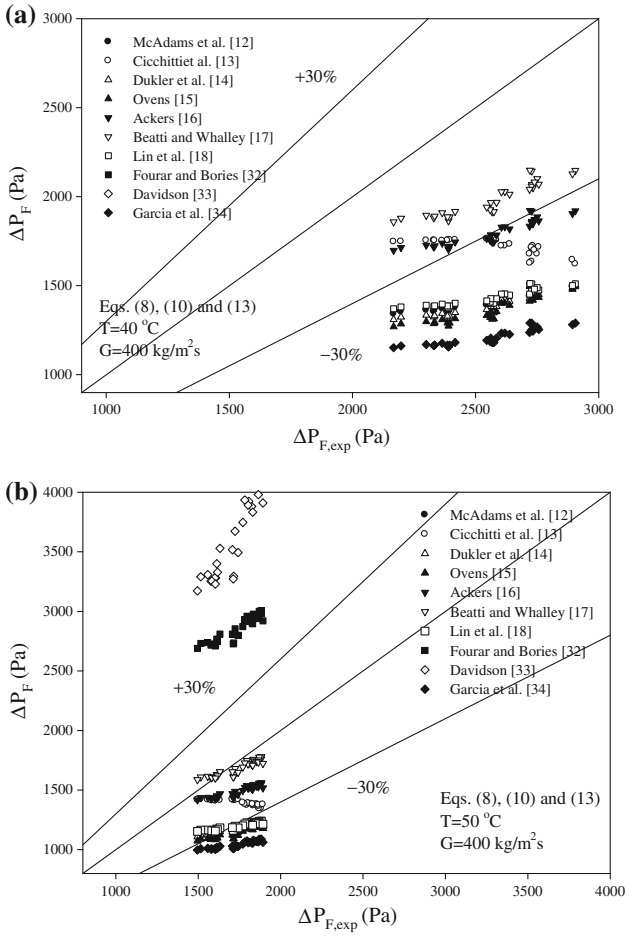

Fig. 14 Comparison of frictional pressure drops obtained from Eqs. 8, 10 and 13

maps and correlations and also checked by sight glass at the inlet and outlet of the test section.

The pressure drop is obtained by dividing the measured pressure drop by the length between pressure taps. In the vertical test section, the length between pressure taps is 0.7 m while the length of the heat exchanger is 0.5 m.

Table 3 shows the void fraction models and correlations that agree with the experimental database according to the authors' investigation of void fraction studies. As a result of the analysis, these void faction models and correlations give quite similar values such as gravitational and momentum pressure drops. For that reason, the Chisholm correlation [38] is used as a constant void faction correlation in the analysis.

Plots of the results belong to the homogeneous flow model are given from Figs. 3, 4, 5, 6, 7, 8, 9, 10, 11, 12, 13, and 14. The variations in these figures to calculate the two-phase friction factor, wall shear stress, frictional pressure drop and total pressure drop are generated by means of the two-phase homogeneous dynamic viscosity correlations such as Mc Adams et al. [12], Cicchitti et al. [13], Dukler et al. [14], Ovens [15], Ackers [16], Beattie and Whalley [17], Lin et al. [18], Fourar and Bories [32], Davidson [33], and Garcia et al. [34]. Alternative correlations from the literature are gathered for the determination of momentum pressure drop in Eqs. 7 and 8, and frictional pressure drop in Eqs. 11 and 12. The effects of these equations on the determined values are investigated in the paper. It should be noted that the two-phase homogeneous dynamic viscosity correlations of Fourar and Bories [31], and Davidson [32] have considerably large deviations from the experimental data due to their incompatible operating conditions; therefore, they are not presented in most of the figures.

Figures 3 and 4 show the comparison of two-phase friction factors calculated based on the Blasius [36] equation according to the dynamic viscosity correlations in Table 2 and different frictional pressure drop correlations in Eqs. 11 and 12. As a result of these plots, the two-phase friction factor obtained from Eq. 11 is found to be more predictive than those obtained by Eq. 12 according to the two-phase homogeneous dynamic viscosity correlations of

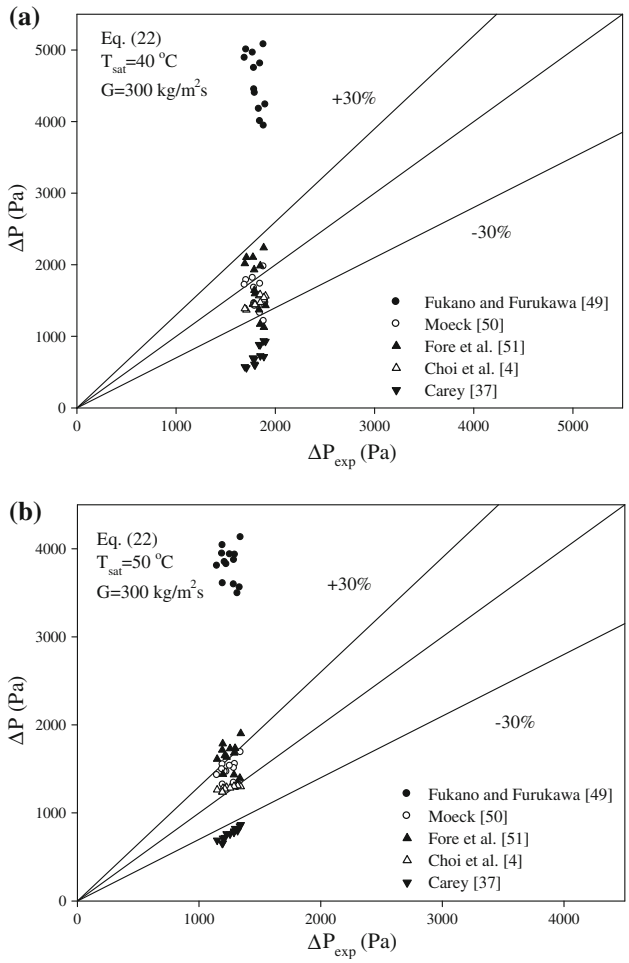

Fig. 15 Comparison of total pressure drop values between measured and calculated ones obtained from Eq. 22 during laminar flow of R134a

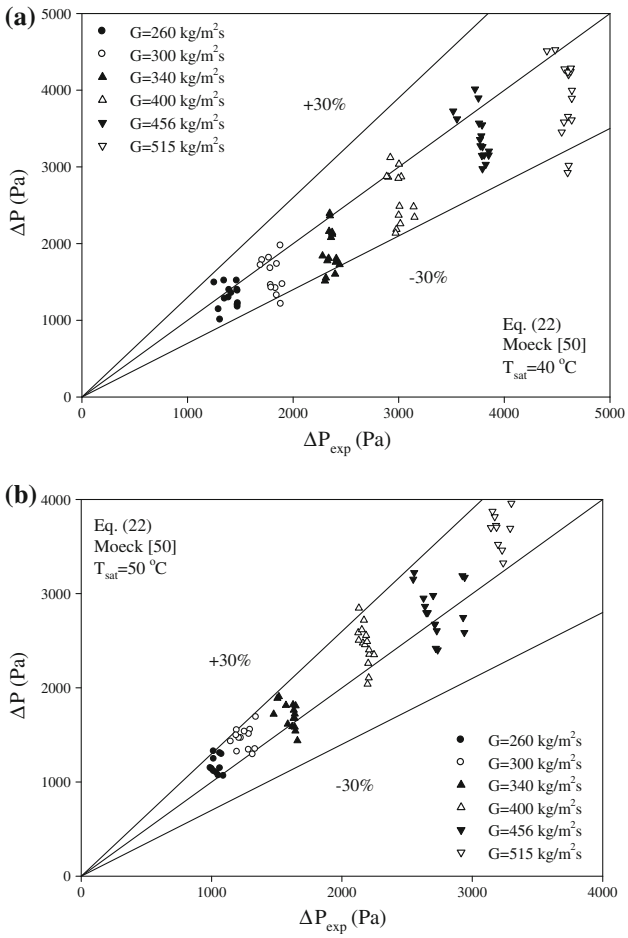

Fig. 16 Comparison of total pressure drop values between measured and calculated ones obtained from Eq. 22 and Moeck [49]'s two-phase friction factor during laminar flow of R134a

Mc Adams et al. [12], Dukler et al. [14], Ovens [15], Lin et al. [18] and Garcia et al. [34].

For the same purpose, in Figs. 3 and 4, the two-phase homogeneous friction factors are determined by means of the CFD program [25] in Fig. 5 according to the dynamic viscosity correlation of Lin et al. [18]. The numerical results are found to be in good agreement with those obtained from Eq. 11 and the same with the theoretical results. Figure 6 shows local variation of the two-phase homogeneous friction factors obtained from the numerical study. Their local values increase gradually along the tube length as expected.

In a similar way to the last figures, Figs. 7 and 8 show the comparison between the calculated wall shear stresses obtained from Eq. 13 and experimental ones. Figure 9 shows the numerical results for the determination of the wall shear stress. Consequently, similar results to the previous one, where the majority of the data belong to agreed correlations fall within the ±30% deviation band, are also obtained from these figures. Figure 10 illustrates the local wall shear stress values obtained from the CFD program [25]. The characteristics of the trend lines in the figure are in good agreement with those in the literature.

It can be clearly seen from Figs. 11 and 12 that the closest agreement comes from the two-phase homogeneous dynamic viscosity of Mc Adams et al. [12], Dukler et al. [14], Ovens [15], Lin et al. [18] and Garcia et al. [34] as explained before. The effect of the use of the different momentum pressure drop correlations in Eqs. 7 and 8 are also shown in these figures. A similar prediction performance is seen for the momentum pressure drop equations. The frictional pressure drop correlation in Eq. 11 is used in this figures.

Another frictional pressure drop correlation in Eq. 13 is used for the calculations in Figs. 13 and 14. The same variables with the previous figure are also used in these figures to investigate their effects. Although the dynamic viscosity correlations of Cicchitti et al. [13], Ackers [16], and Beattie and Whalley [17] have better prediction performance than others, none of them has satisfactory results for all experimental conditions in these figures.

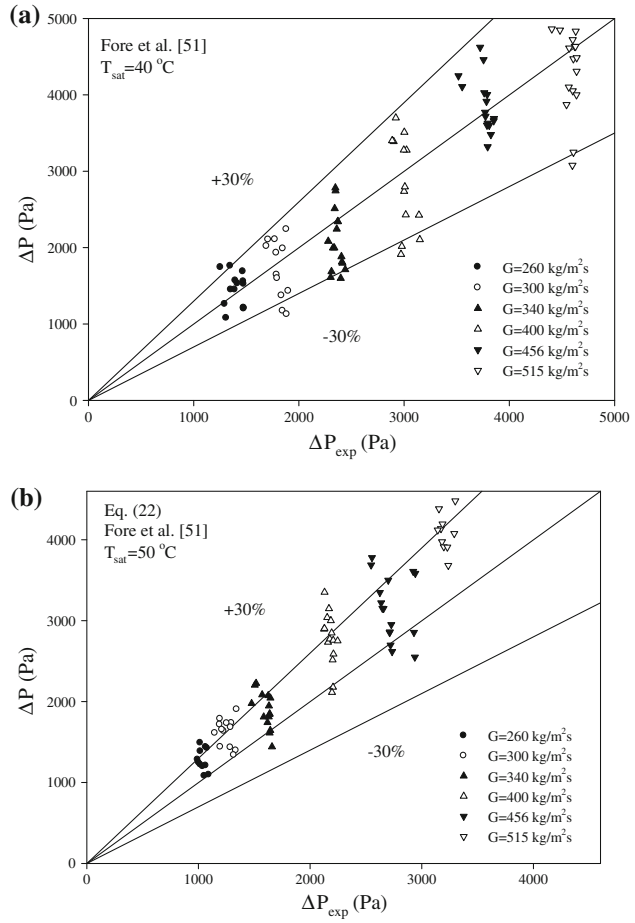

Fig. 17 Comparison of total pressure drop values between measured and calculated ones obtained from Eq. 22 and Fore et al. [50]'s two-phase friction factor during laminar flow of R134a

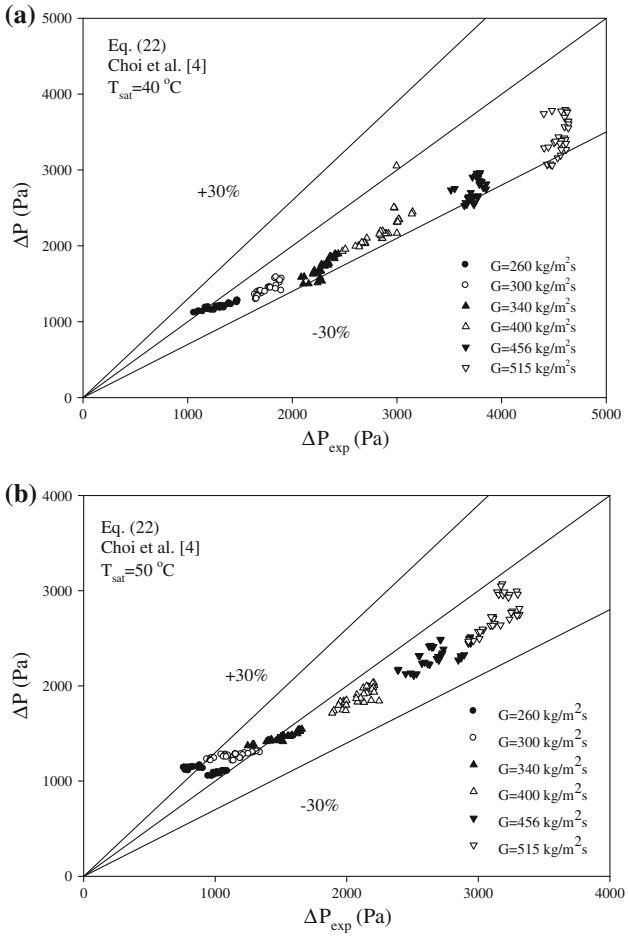

Fig. 18 Comparison of total pressure drop values between measured and calculated ones obtained from Eq. 22 and Choi et al. [6]'s two-phase friction factor during laminar and turbulent flows of R134a

Plots of the results from the separated flow model are given in Figs. 15, 16, and 17. The variations in these figures to calculate the two-phase total pressure drop are generated by means of the two-phase friction factor correlations such as Fukano and Furukawa [48], Moeck [49], Fore et al. [50], Choi et al. [6], and Carey [37]. An elimination process was performed in Fig. 15 to determine the best predictive friction factors. As a result, the friction factors of Moeck [49], Fore et al. [50] and Choi et al. [6] are found to be better than the others. It can be clearly seen from Figs. 16 and 17 that the distribution of the data between the error bands of ±30% seems quite balanced. It should be noted that the data in these figures belong to the laminar flow and none of these friction factors apart from Choi et al. [6] in Fig. 18 could predict well the total pressure drop during turbulent flow due to their large deviations from the experimental values. The prediction success of Choi et al. [6]'s correlation can be seen from Fig. 18 for laminar and turbulent flow data within ±30%. The total pressure drop increases with increasing mass fluxes in all figures as expected.

5 Conclusion

Experiments have been performed to predict the pressure drop characteristics using homogeneous and separated flow models by means of the proper two-phase dynamic viscosity correlations, some alternative correlations of momentum and pressure drop, and various two-phase friction factors and void fraction models and correlations. There is little research on the parameters and content used in this study in the current literature. The content of this study is expected to fill this gap in the literature. Accurate experiments were done for annular flow heat transfer data in a vertical tube for the condensation of R134a at high mass flux. The importance of the use of a large number of data with different experimental conditions is shown during the validation process of the results.

The calculated homogeneous two-phase friction factors, wall shear stresses, frictional pressure drops and total pressure drops by means of the two-phase homogeneous dynamic viscosity correlations of Mc Adams et al., Dukler

et al., Ovens, Lin et al. and Garcia et al. are found to be in good agreement with the experimental data: within ±30%.

Moreover, the correlations of the two-phase friction factors of Moeck and Fore et al. for the laminar flow and Choi et al. for the laminar and turbulent flows are the best predictive models, within ±30%, for the investigation of the separated flow model's total pressure drop correlation and could reflect the effect of mass flux on the total pressure drop.

Acknowledgments The authors would like to thank King Mongkut's University of Technology Thonburi (KMUTT), the Thailand Research Fund, and the National Research University Project for the financial support. Especially, the first author wishes to thank KMUTT for providing him with a Post-doctoral fellowship.

References

1. Nusselt W (1916) Die Oberflachen Kondenastion des Wasserdamfes. Zeitschrift des Vereines Deutscher Ingenieure 60:541–546 (569–575)
2. Wasden FK, Dukler AE (1989) Insights into the hydrodynamics of free falling wavy films. AIChE J 35:187–195
3. Kritsadathikarn P, Songnetichaovalit T, Lokathada N, Wongwises S (2002) Pressure distribution of refrigerant flow in an adiabatic capillary tube. Sci Asia 28:71–76
4. Choi JY, Kedzierski MA, Domanski PA (1999) A generalized pressure drop correlation for evaporation and condensation of alternative refrigerants in smooth and micro-fin tubes. NISTIR 6333:1–50
5. Pierre B (1964) Flow resistance with boiling refrigerants-part 1. ASHRAE J 6:58–65
6. Choi K, Pamitran AS, Oh CY, Oh JT (2008) Two-phase pressure drop of R-410A in horizontal smooth minichannels. Int J Refrig 31:119–129
7. Lockhart RW, Martnelli RC (1949) Proposed correlation of data for isothermal two-phase, two-component flow in pipes. Chem Eng Prog 45:39–48
8. Baudouy B (2002) Pressure drop in two-phase He I natural circulation loop at low vapor quality. In: Gistau Baguer PSG (ed) International cryogenic engineering proceedings, vol 19, France, pp 817–820
9. Friedel L (1979) Improved friction pressure drop correlations for horizontal and vertical two phase pipe flow. Eur Two-phase Flow Group Meet 18:485–491
10. Huq RH, Loth JL (1992) Analytical two-phase flow void prediction method. J Thermophys 6:139–144
11. Dutkowski K (2010) Air-water two-phase frictional pressure drop in minichannels. Heat Transf Eng 31:321–330
12. McAdams WH, Woods WK, Heroman LC (1942) Vaporization inside horizontal tubes II-benzene-oil mixtures. Trans ASME 64:193–200
13. Cicchitti A, Lombaradi C, Silversti M, Soldaini G, Zavattarlli R (1960) Two-phase cooling experiments- pressure drop heat transfer burnout measurements. Energia Nucl 7:407–425
14. Dukler AE, Wicks M, Cleveland RG (1964) Frictional pressure drop in two-phase flow. Part A: a comparison of existing correlations for pressure loss and holdup, and Part B: an approach through similarity analysis. AIChE J 10:38–51
15. Owens WL (1961) Two-phase pressure gradient. In: ASME International Developments in Heat Transfer, Part II, pp 363–368
16. Lee J, Mudawar I (2005) Two-phase flow in high-heat-flux micro-channel heat sink for refrigeration cooling applications: part II-heat transfer characteristics. Int J Heat Mass Transf 48:941–955
17. Beattie DRH, Whalley PB (1982) Simple two-phase frictional pressure drop calculation method. Int J Multiph Flow 8:83–87
18. Lin S, Kwok CCK, Li RY, Chen ZH, Chen ZY (1991) Local frictional pressure drop during vaporization for R-12 through capillary tubes. Int J Multiph Flow 17:95–102
19. Chen IY, Yang KS, Chang YJ, Wang CC (2001) Two- phase pressure drop of air-water and R-410A in small horizontal tubes. Int J Multiph Flow 27:1293–1299
20. Yadigaroglu H, Lahey RT Jr (1976) On the various forms of the conservation equations in two-phase flow. Int J Multiph Flow 2:477–494
21. Wang CC (1997) A numerical method for thermally non-equilibrium condensing flow in a double-pipe condenser. Appl Thermal Eng 17:647–660
22. Bhramara P, Rao VD, Sharma KV, Reddy TKK (2009) CFD analysis of two phase flow in a horizontal pipe-prediction of pressure drop. Int J Mech Ind Aerosp Eng 3:81–87
23. Rahimi M, Shabaniana SR, Alsairafi AA (2009) Experimental and CFD studies on heat transfer and friction factor characteristics of a tube equipped with modified twisted tape inserts. Chem Eng Process 48:762–770
24. Moser K, Webb RL, Na B (1998) A new equivalent Reynolds number model for condensation in smooth tubes. Int J Heat Transf 120:410–417
25. Fluent release 6.2.16, Fluent Incorporated (2005)
26. Chen SL, Gerner FM, Tien CL (1987) General film condensation correlations. Exp Heat Transf 1:93–107
27. Kline SJ, McClintock FA (1953) Describing uncertainties in single sample experiments. Mech Eng 75:3–8
28. Collier JG, Thome JR (2001) Convective boiling and condensation. Oxford Science Publications, Oxford
29. Revellin R (2005) Experimental two-phase fluid flow in microchannel. Ph.D. thesis, Ecole Polytechnique Federale De Lausanne, Lyon, France
30. Pope JE (1996) Rules of thumb for mechanical engineers. Gulf professional publishing, Houston
31. Wong TN, Ooi KT (1995) Refrigerant flow in capillary tube: an assessment of the two-phase viscosity correlations on model prediction. Int Commun Heat Mass Transf 22:595–604
32. Fourar M, Bories S (1995) Experimental study of air–water two-phase flow through a fracture (narrow channel). Int J Multiph Flow 21:621–637
33. Davidson WF, Hardie PH, Humphreys CGR, Markson AA, Mumford AR, Ravese T (1943) Studies of heat transmission through boiler tubing at pressures from 500 to 3, 300 Lbs. Trans ASME 65:553–591
34. García F, García R, Padrino JC, Mata C, Trallero JL, Joseph DD (2003) Power law composite power law friction factor correlations for laminar turbulent gas- liquid flow in horizontal pipelines. Int J Multiph Flow 29:1605–1624
35. White FM (2005) Viscous fluid flow. McGraw-Hill, New York
36. Blasius H (1913) Das Ähnlichkeitsgesetz bei Reibungsvorgängen in Flüssikeiten, Forsch. Gebiete Ingenieurw 131
37. Carey VP (1992) Liquid-vapor phase change phenomena. Hemisphere Publishing, New York
38. Chisholm D (1983) Two phase flow in pipelines and heat exchangers. George Godwin in association with The Institution of Chemical Engineers, London
39. Soliman HM (1982) On the annular-to-wavy flow pattern transition during condensation inside horizontal tubes. Can J Chem Eng 60:475–481

40. Smith SL (1969) Void fractions in two-phase flow: a correlation based upon an equal velocity head model. Proc Inst Mech Eng 36:647–664
41. Turner JM, Wallis GB (1965) The separate-cylinders model of two-phase flow, paper no. NYO-3114-6. Thayer's School Eng., Dartmouth College, Hanover
42. Spedding PL, Spence DR (1989) Prediction of holdup in two phase flow. Int J Eng Fluid Mech 2:109–118
43. Woldesemayat MA, Ghajar AJ (2007) Comparison of void fraction correlations for different flow patterns in horizontal and upward inclined pipes. Int J Multiph Flow 33:347–370
44. Honda H, Nozu S, Matsuoka Y, Nakata H (1989) Condensation of R-11 and R-113 in the annuli of horizontal double-tube condensers with an enhanced inner tube. Exp Thermal Fluid Sci 2:173–182
45. Sami SM, Schnotale J (1993) Prediction of forced convective condensation of non-azeotropic refrigerant mixtures inside enhanced surface tubing. Appl Sci Res J 50:149–168
46. Akers WW, Deans A, Crosser OK (1959) Condensing heat transfer within horizontal tubes. Chem Eng Prog Symp Ser 55:171–176
47. Ma X, Briggs A, Rose JW (2004) Heat transfer and pressure drop characteristics for condensation of R113 in a vertical micro-finned tube with wire insert. Int Commun Heat Mass Transf 31:619–627
48. Fukano T, Furukawa T (1998) Prediction of the effects of liquid viscosity on interfacial shear and frictional pressure drop in vertical upward gas-liquid annular flow. Int J Multiph Flow 24:587–603
49. Moeck EO (1970) Annular-dispersed two-phase flow and critical heat flux. AECL 3656:337
50. Fore LB, Beus SG, Bauer RC (2000) Interfacial friction in gas-liquid annular flow: analogies to full and transition roughness. Int J Multiph Flow 26:1755–1769
51. Cousin LB, Dcnton WH, Hewitt GF (1965) Liquid mass transfer in annular two-phase flow. AERE-R4926
52. Wallis GB (1969) One-dimensional two-phase flow. McGraw-Hill, New York
53. Webb D (1970) Studies of the characteristics of downward annular two-phase flow: measurements of entrainment rate, pressure gradient, probability distribution of film thickness and disturbance wave inception. AERE-R6426
54. Whalley PB, Hewitt GF, Hutchinson P (1973) Experimental wave and entrainment measurements in vertical annular two-phase flow. AERE-R7521
55. Whalley PB, Hewitt GF (1978) The correlation of liquid entrainment fraction and entrainment rate in annular two-phase flow. AERE-R9187
56. Hewitt GF, Hall-Taylor NS (1970) Annular two-phase flow. Pergamon Press, Oxford
57. Asali JC, Hanratty TJ, Andreussi P (1985) Interfacial drag and film height for vertical annular flow. AIChE J 31:895–902
58. Azzopardi BJ, Teixeira JCF (1994) Detailed measurements of vertical annular two-phase flow-Part II: gas core turbulence. Trans ASME 116:796–800

Frontiers in Heat and Mass Transfer (FHMT), 3, 013006 (2012)
DOI: 10.5098/hmt.v3.1.3006

Global Digital Central
ISSN: 2151-8629

Frontiers in Heat and Mass Transfer

Available at www.ThermalFluidsCentral.org

A CRITICAL REVIEW OF RECENT INVESTIGATIONS ON FLOW PATTERN AND HEAT TRANSFER DURING FLOW BOILING IN MICRO-CHANNELS

Sira Saisorn[a,b], Somchai Wongwises[b,c*]

[a]*King Mongkut's Institute of Technology Ladkrabang Chumphon Campus Chumphon 86160, Thailand*
[b]*Fluid Mechanics, Thermal Engineering and Multiphase Flow Research Lab. (FUTURE)*
Department of Mechanical Engineering, King Mongkut's University of Technology Thonburi, Bangmod, Bangkok 10140, Thailand
[c]*The Academy of Science, The Royal Institute of Thailand, Sanam Suea Pa, Dusit, Bangkok 10300, Thailand*

ABSTRACT

A summary of recent research on flow boiling in micro-channels is provided in this article. This review aims to survey and identify new findings arising in this important area, which may contribute to optimum design and process control of high performance miniature devices comprising extremely small channels. Several criteria for defining a micro-channel are presented at first and the recent works on micro-scale flow boiling are subsequently described into two parts including flow visualization and two-phase heat transfer. The results obtained from a number of previous studies show that the flow behaviours and heat transfer mechanisms in micro-channels deviate significantly from those in ordinarily sized channels. Future research with numerous aspects of flow boiling phenomena necessary to answer the fundamental questions is still required.

Keywords: *flow boiling, micro-channel, heat transfer*

1. INTRODUCTION

In the past 10 years, investigations on flow boiling heat transfer and flow characteristics in micro-channel flow passages have gained significant attention in engineering community. Flow boiling in micro-channel has been applied to energy and process systems including high heat-flux compact heat exchangers, and cooling devices of various types of equipment such as high performance micro-electronics, high-powered lasers, and so on.

Several advantages can be obtained when micro-channels are selected for applications. In compact heat exchanger implementations, for instance, such small channels can provide a larger contact area with the fluid per unit volume and support high pressure operating conditions. Unfortunately, a comprehensive understanding is still lacking on the trend and parameters dominating the phase-change behavior in micro-channel. The fundamental data corresponding to flow pattern, heat transfer coefficient and pressure drop during flow boiling are therefore essential for designing and operating compact heat exchangers as well as micro-electro-mechanical systems (MEMS).

A scaling analysis of different forces, as recently discussed in Kandlikar (2010), pointed out that surface tension and evaporation momentum forces were significant for two-phase flow phenomena at micro-scale, resulting in the flow behaviors substantially different from those of ordinarily sized channels. Currently, it seems rather vague to identify whether or not the flow passages are micro-channels. Several criteria have been established in order to define a micro-channel.

The classifications with respect to the absolute diameter of channel were presented by Mehendale et al. (2000) and Kandlikar and Grande (2003). Mehendale et al. (2000) defined a channel with a hydraulic diameter ranging from 1 to 100 μm as micro-channel. Kandlikar and Grande (2003), however, divided the range from 10 to 200 μm as micro-channel.

The flow mechanisms in a confined space may be different according to cross-sectional shape. Accordingly, the circular micro-channels cannot give the same results as those in most practical applications which are rectangular in shape and, hence, the micro-channel is not likely to be characterized by only absolute diameter.

The criteria based on different dimensionless parameters have also been proposed in the literature. For instance, the confinement number recommended by Kew and Cornwell (1997) was proposed to be related with some physical aspects of flow boiling. The confinement number is defined as

$$C_o = \frac{D_b}{D_h} \tag{1}$$

where D_h is hydraulic diameter and D_b is nominal bubble size or capillary length which is expressed by

$$D_b = \sqrt{\frac{\sigma}{g(\rho_L - \rho_G)}} \tag{2}$$

The confinement number above 0.5 implies that the micro-scale effects are important for a given channel diameter. In Eq.(2), σ stands for surface tension, g is gravitational acceleration, ρ_L and ρ_G are, respectively, liquid and vapour densities.

Recently, a criterion developed based on flow boiling heat transfer data was proposed by Li and Wu (2010). 4228 data points were collected from the literature. According to their data analysis,

* Corresponding author: E-mail: somchai.won@kmutt.ac.th

the authors found that the transitional threshold from macro- to micro-channels could be represented as a combined non-dimensional number, $\lambda \times Re_L^{0.5} = 200$. λ and Re_L stand, respectively, for Bond number and liquid Reynolds number. The micro-scale effects are dominant when such combined non-dimensional number is lower than 200. The combination of non-dimensional number was also used by Harirchian and Garimella (2010) to propose the transition criterion. They indicated a micro-channel corresponding to the flow conditions for which $\lambda^{0.5} \times Re_L$ is lower than 160.

It is interesting to note from Tibirica and Ribatski (2010) that the channel with a diameter of 2.3 mm was considered as the one in which the transition between macro- and micro-scale flow boiling phenomena took place when halocarbon refrigerants were used as working fluids under Earth's gravity. With visualization study, they detected stratification effects in this channel size. Ong and Thome (2011a) investigated experiments to address the macro-to-micro-scale transition for flow boiling of refrigerants in different channel sizes. They indicated the dependence of the threshold of the transition on flow regime and confinement number. As illustrated in Fig. 1, the lower threshold of macro-scale flow corresponded to confinement number ranging from 0.3 to 0.4 whereas the confinement number of around 1.0 stood for the upper threshold of micro-scale flow. It was noted that the transition region, frequently corresponding to as mini-channels in literature, was located in between the two boundaries.

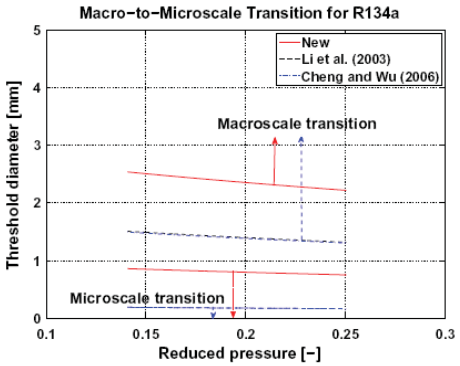

Fig. 1 Transition criterion of Ong and Thome (2011a). "Reprinted from Experimental Thermal and Fluid Science, 35(1), Ong, C.L., and Thome, J.R., Macro-to-microchannel transition in two-phase flow: Part 1-Two-phase flow patterns and film thickness measurements, pp. 37-47 (2011), with permission from Elsevier."

Regarding the experimental data obtained from two-phase gas-liquid adiabatic flow, Chung and Kawaji (2004) found that diameters between 100 and 250 μm seemed to be in the range corresponding to mini-to-micro-scale transitions. Their findings were in agreement with Saisorn and Wongwises (2010).

Despite a number of criteria being proposed, a clear physical criterion that relates the channel diameter to the fluid flow mechanisms is still not available and, hence, further investigation should be performed to meet a more general definition dealing with channel classification.

The foregoing is an introduction and some important tentative criterions which are given in brief. This research field has gained broad interest in the heat transfer community and there have been several major concerns for flow boiling in micro-channels. In this paper, however, the following explorations are carried out to review recent studies on flow patterns and heat transfer characteristics during flow boiling in micro-channels.

2. FLOW BOILING CHARACTERISTICS IN MICRO-CHANNELS

During the past years, a number of investigations pertaining to micro-scale flow phenomena have been published in the literature. Table 1 lists the important investigations on micro-scale flow boiling, recently done by various researchers.

In this section, the recent research works on micro-channel flow boiling are reviewed and are categorized into two main areas. Flow visualization studies are explored and the micro-scale heat transfer characteristics together with the relevant prediction methods are subsequently presented.

2.1. Flow visualization

Lee and Mudawar (2005) conducted flow visualization in rectangular micro-channels with width and depth of 231 μm and 713 μm, respectively. Bubbly/slug flow, slug flow and annular flow were observed for flow boiling of R-134a refrigerant. Not only did the flow regime transition was dependent on vapour quality, the transition behavior was also affected by surface tension and channel configuration.

Kandlikar and Balasubramanian (2005) studied experimentally the flow boiling of water in micro-channels. Hydraulic diameter for each channel was 0.333 mm. The observed flow patterns including bubbly flow, plug flow, churn flow and annular flow tend to appear alternately with time even at a given flow condition. Regarding the experimental data, they indicated the gravitational orientation affecting the flow pattern transitions.

Flow boiling of HCFC123 in micro-channels with different shaped cross-sections was carried out by Yen et al. (2006). They reported that at low vapour quality region, bubbly flow and annular flow were observed in the square micro-channel having hydraulic diameter of 214 μm. In comparison to the square channel, the constitution of flow patterns in the circular channel with nearly the same diameter became more complicated. Capillary flow, representing independent droplets moving along the channel wall, annular flow, bubbly flow and dry-out region were reported for the circular micro-channel. In contrast, the flow patterns at high vapour quality region only comprised annular flow and dry-out region for both circular and square micro-channels.

It should be noted from Jiang and Wong (1999) and Zhang et al. (2002) that bubbly flow was not reported when flow boiling was established in micro-channels with hydraulic diameters ranging from 25 to 60 μm. The channels with triangular cross-sections were used by Jiang and Wong (1999), and those with rectangular cross-sections were examined by Zhang et al. (2002).

Recently, a new type of two-phase flow pattern map for flow boiling in micro-channels was developed by Revellin and Thome (2007). The proposed flow regime map comprises different zones according to the bubble coalescence phenomena. The following are a brief description of each zone located in the flow map.

The isolated bubble (IB) regime corresponds to a relatively high bubble generation rate when compared with the bubble coalescence rate. Either or both of bubbly flow and slug flow are included in this regime. The coalescing bubble (CB) regime is defined when the bubble generation rate is smaller than the bubble coalescence rate. The isolated bubble (IB) flow to coalescing bubble (CB) flow transition is given by

$$x_{IB/CB} = 0.763\left(\frac{Re_{LO}B_o}{We_{GO}}\right)^{0.41} \quad (3)$$

where B_o stands for boiling number, Re_{LO} represents all-liquid Reynolds number and We_{GO} is all-vapour Weber number.

The transition from coalescing bubble flow to annular flow is determined by

DOI: 10.5098/hmt.v3.1.3006 ISSN: 2151-8629

Table 1 Summary of recent investigations on micro-scale flow boiling.

Reference	*Fluid and parameter ranges* G [kg/m^{2}s], q [kW/m^2] P [kPa], T [^{o}C]	*Channel geometry/ substrate/orientation/ diameter* [mm]	*Remarks*
Yang and Shieh (2001)	R-134a G = 300-1600, x = 0.003- 0.92 T_{sat} = 30	Single circular/Pyrex glass/horizontal/ D = 2, 3	Inconsistencies between the flow pattern map established from two-phase air-water and that from two-phase R-134a were addressed.
Lee and Lee (2001)	R-113 G = 50-200, x = 0.15-0.75 q = 0-1.5 P_{sat} = 100	Single rectangular/stainless steel/horizontal/ D_h = 0.78-3.63	Heat transfer coefficient increased with increasing mass flux and vapour quality.
Sumith et al. (2003)	Water G = 23-153, x = 0-0.8 q = 10-715 T_{in} = 97.5, 98	Single circular/stainless steel/vertical D = 1.45	Convective boiling was likely to dominate heat transfer phenomena.
Qu and Mudawar (2003)	Water G = 135-402, x = 0-0.2 T_{in} = 30, 60	21 parallel rectangular/ copper/horizontal D_h = 0.35	Heat transfer mechanisms were compatible with convective boiling contribution.
Huo et al. (2004)	R-114a G = 100-500, x = 0-0.9 q = 13-150 P_{sat} = 800-1200	Single circular/stainless steel/vertical/ D = 2.01, 4.26	Heat transfer mechanism over low vapour quality region was compatible with nucleate boiling contribution. Heat transfer coefficient was higher for the 2.01 mm tube than for the 4.26 mm tube.
Pettersen (2004)	CO_2 G = 190-570, x = 0.12-1 q = 5-20 T_{sat} = 0, 10, 20, 25	25 parallel circular/ aluminum/horizontal/ D = 0.81	The results were discussed according to the dominant role of nucleate boiling over low/moderate vapour quality region. Dry-out effects were obvious at high mass flux and temperature.
Lee and Mudawar (2005)	R-134a G = 127-654, x = 0.26-0.87 q = 159-938 P_{in} = 144-660	53 parallel rectangular/ copper/horizontal/ D_h = 0.35	Bubbly/slug flow, slug flow and annular flow were observed. Different heat transfer mechanisms were addressed for three different vapour quality regions.
Kandlikar and Balasubramanian (2005)	Water G = 120, x = 0.18-0.36 q = 317 T_s = 110-114	6 parallel rectangular/ copper/horizontal and vertical/ D_h = 0.333	Bubbly flow, plug flow, churn flow and annular flow were reported. The gravitational orientation affected the flow pattern transition and heat transfer coefficients.
Yun et al. (2005)	CO_2, R-134a G = 200-400, x = 0-0.9 q= 10 – 20 T_{sat} = 0, 5, 10	6-10 parallel rectangular/ -/horizontal/ D_h = 1.08-1.54	The effect of heat flux on heat transfer coefficient was much more obvious for CO_2 than for R-134a.
Saitoh et al. (2005)	R-134a G = 150-450, x=0-0.2 q = 5-39 T_{sat} = 5, 15	Single circular/-/horizontal/ D = 0.51, 1.12, 3.1	Nucleate boiling was reported in low vapour quality region whereas convective evaporation was dominant in high vapour quality region. The smaller the tube diameter, the higher was the effect of saturation temperature on heat transfer coefficient.
Lie et al. (2006)	R-134a, R-407C G = 200-1500, x = 0.2-0.8 q = 5, 10, 15 T_{sat} = 5, 10, 15	28 parallel circular/copper/ horizontal/ D = 0.83, 2.0	The use of R-407C gave a higher heat transfer coefficient when compared with R-134a.
Yen et al. (2006)	R-123 G = 100-800, x = 0.07-0.8 q = 25-90 P_{in} = 163	Single circular and single square/Pyrex glass/horizontal/ D_h = 0.2	Different shaped cross-sections gave different flow characteristics. The shape of the cross-section had no significant influence on the heat transfer coefficient when high vapour quality region was established.

DOI: 10.5098/hmt.v3.1.3006 ISSN: 2151-8629

Table 1 Summary of recent investigations on micro-scale flow boiling (continued).

Reference	*Fluid and parameter ranges* G [kg/m^{2}s], q [kW/m^2] P [kPa], T [^{o}C]	*Channel geometry/ substrate/orientation/ diameter* [mm]	*Remarks*
Revellin and Thome (2007)	R-134a, R-245fa G = 210-2094, x = 0-0.95 q = 3.1-597 T_{sat} = 26, 30, 35	Single circular/stainless steel/ horizontal/ D = 0.509, 0.79	Two-phase flow regime map was developed, including isolated bubble regime, coalescing bubble regime and annular regime.
Choi et al. (2007a)	CO_2 G = 200-600, x = 0-1 q = 20-40 T_{sat} = -10, -5, 0, 10	Single circular/stainless steel/ horizontal/ D = 1.5, 3	More vigorous nucleate boiling was observed when the smaller diameter tube was used.
Choi et al. (2007b)	R-22, R-134a, CO_2 G = 200-600, x = 0-1 q = 10-40 T_{sat} = 10	Single circular/stainless steel/ horizontal/ D = 1.5, 3	The use of CO_2 caused the heat transfer coefficient higher than the case of R-134a and R-22 fluids.
Agostini et al. (2008a, 2008b)	R-236fa, R-245fa G = 280-1500, x = 0.02-0.78 q = 36-2220 P_{sat} = 141-273	66 parallel rectangular/ silicon/horizontal/ D_h = 0.336	Heat transfer coefficient for R-245fa was dependent on mass flux in comparison to the case for R-236fa. The effect of the saturation pressure on the heat transfer coefficient was obvious for R-236fa.
Lee and Mudawar (2008)	HFE 7100 G = 670-6730 q = 0-7500 P_{out} = 113.8	11-24 parallel rectangular/ copper/horizontal/ D_h = 0.176, 0.2, 0.334, 0.416	Heat transfer coefficient did not monotonously increase with the decrease in hydraulic diameter.
Lee and Garimella (2008)	Water G = 368-738, x = 0-0.2 q = 100-3400 T_{in} = 90.6-95.1	10-60 parallel rectangular/ Silicon/horizontal/ D_h = 0.16-0.54	At high heat flux region, the heat transfer coefficient was nearly independent with heat flux.
Bertsch et al. (2008)	R-134a G = 20.3-81, x = 0-0.85 q = 0-200 T_{sat} = 8.9, 18.7, 29	17 parallel rectangular/ copper/horizontal/ D_h = 1.09	Vapour quality showed significant influence on the heat transfer coefficient whereas the saturation pressure played insignificant role on the heat transfer coefficient. The higher the mass flux, the higher was the heat transfer coefficient.
Shiferaw et al. (2009)	R-134a G = 100-600, x = 0-0.9 q = 16-150 P_{sat} = 600-1200	Single circular/stainless steel/ vertical/ D = 1.1	Heat transfer coefficient increased with increasing heat flux and saturation pressure.
Ong and Thome (2009)	R-134a, R-236fa, R-245fa G = 100-1500, x = 0-1 q = 2.3-250 T_{sat} = 29, 31, 33	Single circular/stainless steel/ horizontal/ D = 1.03	Two-phase flow regime map was developed and worked well for mass flux values larger than 200 kg/m^{2}s and reduced pressure ranging from 1.842 to 7.926. R-134a gave the highest heat transfer coefficient followed by R-236fa and R-245fa, respectively.
Bertsch et al. (2009a)	R-134a, R-245fa G = 20-350, x = 0-0.8 q = 0-220 T_{sat} = 8.9, 18.7, 29	17-33 parallel rectangular/ copper/horizontal/ D_h = 0.54, 1.09	The use of R-134a resulted in high heat transfer coefficient when compared with R-245fa. The heat transfer coefficient was not affected by the variation of the hydraulic diameter.
Choi et al. (2009)	C_3H_8 G = 50-400, x = 0-1 q = 5-20 T_{sat} = 0, 5, 10	Single circular/stainless steel/ horizontal/ D = 1.5, 3	The smaller channel diameter yielded a higher heat transfer coefficient. The heat transfer coefficient increased with increasing saturation temperature.
Tibirica and Ribatski (2010)	R-134a, R-245fa G = 50-700, x = 0.05-0.99 q = 5-55 T_{sat} = 22, 31, 41	Single circular/stainless steel/ horizontal/ D = 2.3	The variation of the heat transfer coefficient with the saturation temperature for R-245fa was more obvious than that for R-134a. R-134a provided high heat transfer coefficients in comparison to R-245fa.

DOI: 10.5098/hmt.v3.1.3006 ISSN: 2151-8629

Table 1 Summary of recent investigations on micro-scale flow boiling (continued).

Reference	*Fluid and parameter ranges* G [kg/m^{2}s], q [kW/m^2] P [kPa], T [^{o}C]	*Channel geometry/ substrate/orientation/ diameter* [mm]	*Remarks*
Arcanjo et al. (2010)	R-134a, R-245fa G = 50-600, x = 0-0.95 T_{sat} = 22, 31, 41	Single circular/stainless steel/ horizontal/ D = 2.32	Slug flow, churn flow and annular flow were observed. The flow pattern transitions were affected by working fluid and saturation temperature.
Celata et al. (2010)	FC-72 G = 500-1500 q = 50-150	Single circular/-/horizontal/ D = 0.48	Stable flows including bubbly/slug flow, slug/annular flow and annular/mist flow were observed at high mass flux and heat flux values
Saisorn et al. (2010)	R-134a G = 200-1000, x = 0.05-0.95 q = 1-83 P_{sat} = 800, 1000, 1300	Single circular/stainless steel/ horizontal/ D = 1.75	Slug flow, throat-annular flow, churn flow, annular flow and annular-rivulet flow were observed and found to influence heat transfer process.
Martin-Callizo et al. (2010)	R-134a G = 100-500, x= 0-0.97 q = 5-45 T_{sat} = 30, 35	Single circular/quartz tube/ vertical/ D = 1.33	Seven two-phase flow patterns were observed including isolated bubbly flow, confined bubbly flow, slug flow, churn flow, slug-annular flow, annular flow and mist flow.
Oh et al. (2011)	R-22, R-134a, R-410A, C_3H_8, CO_2 G = 50-600, x = 0-1 q = 5-40 T_{sat} = 0-15	Single circular/stainless steel/ horizontal/ D = 0.5, 1.5, 3	Heat transfer coefficient increases with the decrease in channel diameter. The heat transfer coefficient of CO_2 was highest in comparison to the other four refrigerants.
Bang et al. (2011)	Water G = 100, x= 0-1 q = 50-160 P_{sat} = 200, 1600	Single circular/stainless steel/ horizontal/ D = 1.73	Heat transfer coefficient was slightly affected by pressure. The dominance of forced convection was reported.
Soupremanien et al. (2011)	Forane®365 HX G = 200-400, x= 0-0.6 q = 25-62 T_{sat} = 56	Single rectangular/stainless steel/horizontal/ D_h = 1.4	Bubbly flow, plug flow, plug/slug flow, churn/annular flow and annular flow were observed. Heat transfer coefficient was influenced by aspect ratio.
Copetti et al. (2011)	R-134a G = 240-930, x= 0-0.8 q = 10-100 T_{sat} = 12, 22	Single circular/stainless steel/ horizontal/ D = 2.62	Heat transfer coefficient was strongly dependent on mass flux only for low heat flux conditions. Flow pattern was reported to play important role on the heat transfer coefficient.
Ong and Thome (2011a, 2011b)	R-134a, R-236fa, R-245fa G = 100-1500, x = 0-1 q = 4.8-250 T_{sat} = 25, 31, 35	Single circular/stainless steel/ horizontal/ D = 1.03, 2.2, 3.04	Flow pattern transition lines were developed to predict both macro-scale and micro-scale flow patterns. The heat transfer coefficient for R-134a showed the highest dependence on heat flux.

$$x_{CB/A} = 0.00014 Re_{LO}^{1.47} We_{LO}^{-1.23} \quad (4)$$

where We_{LO} is all-liquid Weber number.

The proposed correlations take into account different effects including heat flux, viscosity and surface tension which are represented, respectively, by boiling number, Reynolds number and Weber number.

With the data for three refrigerants including R-134a, R-236fa and R-245fa in channels with diameters ranging from 0.509 to 1.03 mm, the Revellin and Thome correlation (2007) was subsequently modified by Ong and Thome (2009) as follows.

The isolated bubble (IB) flow to coalescing bubble (CB) flow transition was modified as

$$x_{IB/CB} = 0.763 \left(\frac{Re_{LO} B_o}{We_{GO}} \right)^{0.39} \quad (5)$$

The transition from coalescing bubble flow to annular flow was modified to account for reduced pressure as follow.

$$x_{CB/A} = \left(\frac{P_r}{P_{sat,R-134a}} \right)^{0.45} 0.00014 Re_{LO}^{1.47} We_{LO}^{-1.23} \quad (6)$$

where P_r stands for reduced pressure and $P_{sat,\ R\text{-}134a}$ represents saturation pressure with respect to refrigerant R-134a. Ong and Thome (2009) also pointed out that their correlations worked well for mass flux values larger than 200 kg /m^{2}s and reduced pressures ranging from 1.842 to 7.926.

Ong and Thome (2011a) continually developed the flow pattern transition lines in order to predict both macro-scale and micro-scale flow patterns as follows.

Isolated bubble/coalescing bubble (IB/CB) was presented by

$$x_{IB/CB} = 0.36 C_o^{0.2} \left(\frac{\mu_G}{\mu_L} \right)^{0.65} \left(\frac{\rho_G}{\rho_L} \right)^{0.9} Re_{GO}^{0.75} B_o^{0.25} We_{LO}^{-0.91} \quad (7)$$

Coalescing bubble/annular (CB/A) was denoted as

$$x_{CB/A} = 0.047 C_o^{0.05} \left(\frac{\mu_G}{\mu_L}\right)^{0.7} \left(\frac{\rho_G}{\rho_L}\right)^{0.6} Re_{GO}^{0.8} We_{LO}^{-0.91} \quad (8)$$

Plug-slug/coalescing bubble (S-P/CB) was expressed in Eq.(9) when $x_{S\text{-}P/CB} < x_{CB/A}$ as shown below.

$$x_{S\text{-}P/CB} = 9 C_o^{0.2} \left(\frac{\rho_G}{\rho_L}\right)^{0.9} Fr_{LO}^{-1.2} Re_{LO}^{0.1} \quad (9)$$

Plug-slug/annular (S-P/A) was established when $x_{S\text{-}P/CB} > x_{CB/A}$ as seen in Eq.(10) .

$$x_{S\text{-}P/A} = x_{CB/A} \quad (10)$$

Notably, Eqs.(9) and (10) are applicable when confinement number is lower than 0.34.

Arcanjo et al. (2010) obtained flow visualization data for flow boiling of R-134a and R-245fa in a horizontal tube having a diameter of 2.32 mm. Slug flow, churn flow and annular flow were observed. According to their report, the flow pattern transitions were affected by working fluid and saturation temperature. Different existing flow pattern maps for micro-channels were discussed and compared with their flow regime maps.

During flow boiling of FC-72 in horizontal circular micro-channel with a diameter of 0.48 mm, Celata et al. (2010) indicated stable flow at high mass flux and heat flux values. In such region, the flow patterns including bubbly/slug flow, slug/annular flow and annular/mist flow were reported.

Saisorn et al. (2010) performed flow visualization study for R-134a refrigerant during flow boiling in a circular channel having a diameter of 1.75 mm. Slug flow, throat-annular flow, churn flow, annular flow and annular-rivulet flow were observed and found to influence the flow boiling heat transfer process as seen in Fig. 2. Slug flow appeared with the lowest heat transfer coefficient in comparison to the other flow regimes. Annular-rivulet flow showed a relatively high heat transfer coefficient but a local dry-out region was observed at high vapour qualities, which has been undesirable for a thermal design approach dealing with a cooling system implemented with small channels. Moderate values of heat transfer coefficient were given by throat-annular flow, churn flow and annular flow which might be good choices for the development of the micro-scale devices. Besides, their flow pattern data were compared with the transition lines by Triplett et al. (1999) for two-phase air-water flow through a 1.45 mm diameter channel. In general, the comparisons showed inconsistencies between the flow pattern map established from two-phase gas-liquid flow and that from phase-change process. Such inconsistencies were also reported by Yang and Shieh (2001) and Martin-Callizo et al. (2010). Yang and Shieh (2001) performed flow visualization with air-water mixture and refrigerant R-134a, and the comparison between such two cases were discussed. Martin-Callizo et al. (2010) conducted the visualization of R-134a during flow boiling in a tube with a diameter of 1.33 mm. Their test section was made from a quartz glass tube coated externally by Indium Tin Oxide (ITO) which was served as the resistive coating over which a potential difference generated by a DC power supply was applied. Their flow pattern data were also compared with the transition lines by Triplett et al. (1999), indicating that the agreement was not satisfactory. However, two-phase gas-liquid flow phenomena tend to be compatible with flow mechanisms based on phase-change process in different aspects. In micro-channels, for instance, Saisorn and Wongwises (2010) reported the fair agreement between their gas-liquid flow pattern data and the transition lines of Garimella et al. (2002) for condensation flow.

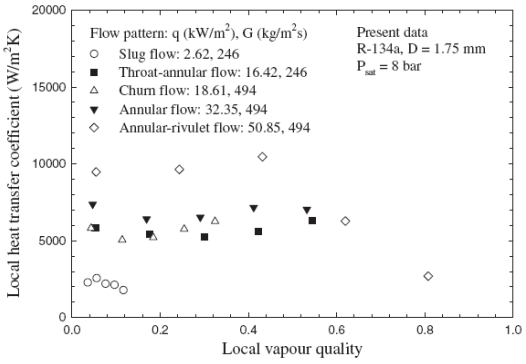

Fig. 2 Flow boiling data of Saisorn et al. (2010). "Reprinted from International Journal of Heat and Mass Transfer, 53(19-20), Saisorn, S., Kaew-On, J., and Wongwises, S., Flow pattern and heat transfer characteristics of R-134a refrigerant during flow boiling in a horizontal circular mini-channel, pp. 4023-4038 (2010), with permission from Elsevier."

Flow boiling visualization study was carried out by Soupremanien et al. (2011). In their work, the test section having hydraulic diameter of 1.4 mm was employed and the Forane® 365 HX was used as working fluid. They observed bubbly flow, plug flow, plug/slug flow, churn/annular flow and annular flow.

2.2. Two-phase heat transfer

Huo et al. (2004) studied experimentally boiling heat transfer of R-134a flowing in 2.01 and 4.26 mm diameter channels. In the range of low vapour quality, the heat transfer coefficient in both tubes increased with increasing heat flux and saturated pressure but was independent of vapour quality. These results were attributed to nucleate boiling being the dominant heat transfer mode. Over other ranges of vapour quality, however, the dominant heat transfer mode was not addressed as a result of inconsistency in the experimental data. Under the same controlled conditions, they found that the nucleate boiling heat transfer coefficient was higher for the 2.01 mm tube than for the 4.26 mm tube.

Flow boiling heat transfer characteristics in micro-channels of 540 mm length with 25 circular flow channels of 0.81 mm diameter were investigated by Pettersen (2004). The author reported that the increase in heat flux resulted in a higher heat transfer coefficient, which was explained according to the dominant role of nucleate boiling over the low/moderate vapour quality region. Another point observed was that the dry-out effects were more noticeable at higher mass flux and temperature, resulting in a substantially reduced heat transfer coefficient at high vapour qualities. The measured heat transfer coefficient data corresponding to low vapour quality region were compared with various heat transfer correlations based on nucleate boiling mechanism.

Kandlikar and Balasubramanian (2004) modified the correlation proposed by Kandlikar (1990) for ordinarily sized channels to extend the prediction to micro-channels which correspond to the neglected Froude number.

For all-liquid Reynolds numbers higher than 100, their correlation can be expressed as shown below.

$$h = \text{larger of} \begin{cases} h_{nb} \\ h_{conv} \end{cases} \quad (11)$$

where the heat transfer coefficient based on nucleate boiling contribution, h_{nb}, and that on forced convective contribution, h_{conv}, are given by Eqs.(12) and (13), respectively.

$$h_{nb} = 0.6683 C_{CO}^{-0.2} (1-x)^{0.8} h_{LO} + 1058.0 B_o^{0.7} (1-x)^{0.8} F_{FI} h_{LO} \quad (12)$$

$$h_{conv} = 1.136C_{CO}^{-0.9}(1-x)^{0.8}h_{LO} + 667.2B_o^{0.7}(1-x)^{0.8}F_{FI}h_{LO} \quad (13)$$

where C_{CO} represents convection number, F_{FI} stands for a fluid-surface dependent parameter which is equal to 1 for all fluids tested with stainless steel tubes, and h_{LO} for all-liquid flow heat transfer coefficient which is found from Eqs.(14) – (16):

$$h_{LO} = \frac{Re_{LO}Pr_L(f/2)(k_L/D)}{1+12.7(Pr_L^{2/3}-1)(f/2)^{0.5}} \quad \text{for } 10^4 \le Re_{LO} \le 5\times 10 \quad (14)$$

$$h_{LO} = \frac{(Re_{LO}-1000)Pr_L(f/2)(k_L/D)}{1+12.7(Pr_L^{2/3}-1)(f/2)^{0.5}} \quad \text{for } 3000 \le Re_{LO} \le 10 \quad (15)$$

$$h_{LO} = \frac{Nuk_L}{D} \quad \text{for } Re_{LO} \le 1600 \quad (16)$$

Pr_L is the liquid Prandtl number and f appearing in Eqs. (14) and (15) is the friction factor determined by:

$$f = [1.58\ln(Re_{LO}) - 3.28]^{-2} \quad (17)$$

It is noted that, for laminar flow in a circular channel with constant surface heat flux, the Nusselt number indicated in Eq. (16) is equal to 4.36. In the case of the transition region, the all-liquid flow heat transfer coefficient is established using a linear interpolation between Re_{LO} of 1600 and 3000.

They also proposed a two-phase heat transfer coefficient for very low Reynolds number ($Re_{LO} \le 100$) which is recommended as:

$$h = h_{nb} = 0.6683C_{CO}^{-0.2}(1-x)^{0.8}h_{LO} + 1058.0B_o^{0.7}(1-x)^{0.8}F_{FI}h_{LO} \quad (18)$$

where h_{LO} is found from Eq. (16).

A number of researchers such as Lee and Lee (2001), Sumith et al. (2003) and Qu and Mudawar (2003) have reported that flow boiling heat transfer is substantially controlled by convective boiling. Inconsistently, there were such publications as Lazarek and Black (1982), Wambsganss et al. (1993), Tran et al. (1996), Kew and Cornwell (1997) and Bao et al. (2000), which indicated nucleate boiling as predominant heat transfer mechanism. Noting that, the analysis of the experimental data based on studies published before 2007 was provided by Thome (2004) and Ribatski et al. (2006).

In addition to nucleate boiling and convective boiling contributions, recently, a three-zone flow boiling model based on the elongated bubble flow regime, was developed by Thome et al. (2004) and Dupont et al. (2004) to predict heat transfer characteristics in micro-channels. The point they make was that heat transfer is controlled primarily by conduction through the evaporation film trapped between the elongated bubble and the tube wall. The prediction is a mechanistic flow boiling heat transfer model comprising heat transfer zones including a pair of liquid slug and elongated bubble zones, followed by vapour slug if dry-out occurs. Each zone is modelled as passing at a fixed location sequentially and cyclically. Rather than nucleate boiling, the heat transfer was proposed to be dominated by conduction through the thin liquid film trapped between the elongated bubble and the tube wall.

To describe the cyclic passage through each zone, a time-averaged local heat transfer coefficient is obtained as follows:

$$h(z) = \frac{t_L}{\tau}h_L(z) + \frac{t_{film}}{\tau}h_{film}(z) + \frac{t_{dry}}{\tau}h_G(z) \quad (19)$$

where the period of bubble generation, τ, which is the reciprocal of the frequency was determined empirically by Dupont et al. (2004). t_L represents the time needed for the liquid slug to pass by a fixed location z along the tube. t_{film} and t_{dry} are the times needed, respectively, for film formation and local wall dry-out. h_{film} stands for the heat transfer coefficient in the film, which is assumed to be stagnant, across which one-dimensional conduction takes place. h_L and h_G are heat transfer coefficients in the liquid and vapour slugs, respectively, and are determined from their local Nusselt numbers. Ribatski et al. (2006) collected the experimental results, dealing with micro-scale flow boiling heat transfer, from the literature and compared them with different prediction methods. Among Zhang et al. (2004), Kandlikar and Balasubramanian (2004), and Thome et al. (2004), Ribatski et al. (2006) concluded, by analysing the selected database, that the three zone flow boiling model developed by Thome et al. (2004) seems to be good choice for flow boiling heat transfer prediction as illustrated in Fig. 3.

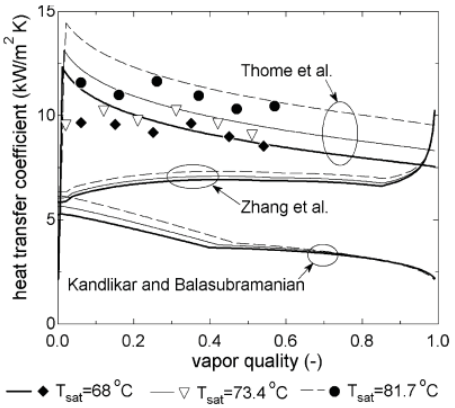

Fig. 3 Comparison of the micro-scale prediction methods and the experimental data of Bao et al. (2000) (Ribatski et al., 2006). "Reprinted from Experimental Thermal and Fluid Science, 31(1), Ribatski, G., Wojtan, L., and Thome, J.R., An analysis of experimental data and prediction methods for two-phase frictional pressure drop and flow boiling heat transfer in micro-scale channels, pp. 1-19 (2006), with permission from Elsevier."

Yun et al. (2005) were concerned with flow boiling heat transfer characteristics in rectangular channels with hydraulic diameters ranging from 1.08 to 1.54 mm. Working fluids tested were CO_2 and R-134a. Generally, the average heat transfer coefficient of CO_2 increased by around 53% as compared with that of R-134a. The effect of heat flux on heat transfer coefficient was much more obvious for CO_2 than for R-134a. The dry-out phenomenon was promoted by an increase in mass flux and it was also noted that the effect of mass flux on heat transfer coefficient was less significant than that of heat flux. As expected, the heat transfer coefficient increased with a decrease in hydraulic diameter.

Heat transfer of refrigerant R-134a during flow boiling in circular channels with different diameters including 0.51, 1.12 and 3.1 mm was studied experimentally by Saitoh et al. (2005). Nucleate boiling was reported in the low vapour quality region whereas convective evaporation was dominant in the high vapour quality region. The latter mechanism was found to be less dominant as the tube diameter decreased. The smaller the tube diameter, the higher was the effect of saturation temperature on heat transfer coefficient.

Effect of gravitational orientation on heat transfer characteristics during flow boiling of water in micro-channels was experimentally investigated by Kandlikar and Balasubramanian (2005). The heat transfer coefficient was affected by the gravitational orientation and found to be compatible with nucleate boiling mechanism.

Lee and Mudawar (2005) carried out experiments to explore flow boiling heat transfer characteristics of R-134a refrigerant in rectangular micro-channels having 231 μm wide and 713 μm deep. In this study, different heat transfer mechanisms were addressed for

Global Digital Central
ISSN: 2151-8629

three different vapour quality regions. According to this finding, they proposed heat transfer correlations for different vapour quality ranges as follows.

For vapour quality ranging from 0 to 0.05, corresponding to bubble nucleation, the relevant correlation as shown in Eq.(20) was developed based only on water flow boiling data of Qu and Mudawar (2003).

$$h_{TP} = 3.856\chi^{0.267} h_L \tag{20}$$

The Martinelli parameter, χ, can be determined according to two-phase flow condition. Laminar liquid-laminar vapour flow and laminar liquid-turbulent vapour flow correspond respectively to Eqs.(21) and (22).

$$\chi_{vv} = \left(\frac{\mu_L}{\mu_G}\right)^{0.5}\left(\frac{1-x}{x}\right)^{0.5}\left(\frac{\rho_G}{\rho_L}\right)^{0.5} \tag{21}$$

$$\chi_{vt} = \left(\frac{f_L Re_G^{0.25}}{0.079}\right)^{0.5}\left(\frac{1-x}{x}\right)^{0.5}\left(\frac{\rho_G}{\rho_L}\right)^{0.5} \tag{22}$$

The heat transfer coefficient for single-phase liquid, h_L, is given by

$$h_L = \frac{Nu_3 k_L}{D_h} \tag{23}$$

where Nu_3 is single-phase Nusselt number for laminar flow with three-sides wall heating and is expressed in terms of aspect ratio (β) or ratio of channel depth to width as shown below.

$$Nu_3 = 8.235\left(1 - 1.883\beta + 3.767\beta^2 - 5.814\beta^3 + 5.361\beta^4 - 2.0\beta^5\right) \tag{24}$$

The correlation for moderate vapour quality range (x = 0.05 - 0.55, bubbly/slug flow) as presented in Eq.(25) was developed from both R-134a and water data points.

$$h_{TP} = 436.48 B_o^{0.522} We_{LO}^{0.351} \chi^{0.665} h_L \tag{25}$$

The annular flow with local dry-out was located in the last vapour quality range (x = 0.55 - 1.0) and the correlation pertaining to this region was based only on R-134a data points as presented below.

$$h_{TP} = \max\left\{\left(108.6\chi^{1.665} h_G\right), h_G\right\} \tag{26}$$

The heat transfer coefficient for single-phase vapour flow, h_G, is evaluated according to vapour flow condition.

For laminar vapour flow:

$$h_G = \frac{Nu_3 k_G}{D_h} \tag{27}$$

For turbulent vapour flow:

$$h_G = 0.023 Re_G^{0.8} Pr_G^{0.4} \tag{28}$$

Yen et al. (2006) experimentally studied flow boiling heat transfer characteristics of HCFC123 in circular and square micro-channels with the same hydraulic diameter of around 210 μm. The heat transfer coefficient for the square channel was relatively high in low vapour quality region when compared with that for the circular channel. In high vapour quality region, however, the shape of the cross-section had no significant influence on the heat transfer coefficient. The corresponding results are illustrated in Fig. 4. The authors explained that the very large number of nucleation sites due to the existence of corners in the square channel resulted in the improved heat transfer coefficients, especially in the region controlled by bubble nucleation mechanism.

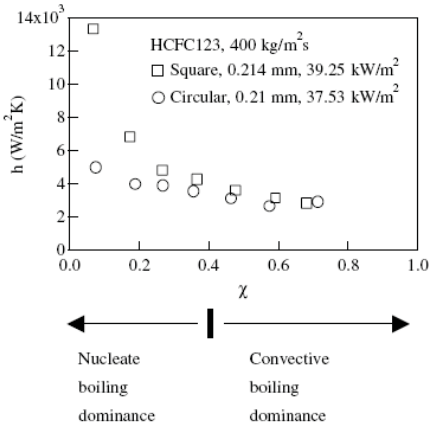

Fig. 4 Heat transfer coefficient data for different shaped cross-sections of Yen et al. (2006). "Reprinted from International Journal of Heat and Mass Transfer, 49(21-22), Yen, T.-H., Shoji, M., Takemura, F., Suzuki, Y., and Kasagi, N., Visualization of convective boiling heat transfer in single microchannels with different shaped cross-sections, pp. 3884-3894 (2006), with permission from Elsevier."

Evaporation heat transfer in tubes was studied experimentally by Lie et al. (2006). A diameter of 0.83 or 2 mm was used for each test section and the working fluids were R-134a and R-407C. The effects of mass flux, vapour quality, saturation temperature and heat flux on the heat transfer coefficient were investigated. Under given experimental conditions, the use of R-407C gave a higher heat transfer coefficient than R-134a.

The experiments with flow boiling of water in a circular tube having a diameter of 1.5 mm were performed by Boye et al. (2007). The wall temperatures of the tube in which the water flows upward were measured using infrared thermography. Nucleate boiling and convective boiling mechanisms were observed in the experiments.

Choi et al. (2007a) reported the heat transfer characteristics of CO_2 through circular channels having diameters of 1.5 and 3 mm. They indicated that nucleate boiling was predominant in the low vapour quality region and a convective boiling heat transfer contribution appeared in moderate and high vapour quality regions. The variation of local heat transfer coefficient with heat flux, mass flux, vapour quality and saturation temperature was discussed. More vigorous nucleate boiling was observed when the smaller diameter tube was used. Flow boiling heat transfer experiments with different refrigerants were continually carried out by Choi et al. (2007b). They indicated that the use of CO_2 caused the heat transfer coefficient to be higher than the case of R-134a and R-22 fluids.

Shiferaw et al. (2007) compared their flow boiling data with existing correlations. Their data points were obtained from experiments with R-134a fluid flowing through circular channels with diameters of 4.26 and 2.01 mm. The comparison revealed that existing correlations did not predict their data very well. Comments and suggestions were provided by the authors for further development of the prediction. Similar experiments were conducted by Shiferaw et al. (2009) to obtain data for a 1.1 mm diameter tube. An insignificant influence of mass flux and vapour quality on heat transfer coefficient was observed. However, the heat transfer coefficient increased with increasing heat flux and saturation pressure.

Heat transfer coefficient data for flow boiling of R-236fa in micro-channels were measured and presented by Agostini et al. (2008a). The channels are 0.223 mm wide and 0.68 mm high. The heat transfer enhancement resulted from the increase in heat flux, and the variation of vapour quality or mass flux had insignificant effect on the heat transfer coefficient. Their next publication referring to Agostini et al. (2008b) concentrated on R-245fa refrigerant during flow boiling condition in the same test section. The results showed that the heat transfer trends were similar to those for R-236fa refrigerant. Notably, the heat transfer coefficient for R-245fa was quite dependent on mass flux in comparison to the case for R-236fa. On the other hand, the effect of the saturation pressure on the heat transfer coefficient was relatively obvious for R-236fa. According to the comparisons based on different experimental conditions, they concluded that R-245fa provided heat transfer performance slightly higher than that for R-236fa.

Lee and Mudawar (2008) carried out experiments to investigate flow boiling in four different rectangular micro-channels. The heat transfer coefficient did not monotonously increase with the decrease in hydraulic diameter. This complex trend was explained with respect to sidewall thickness, channel width and aspect ratio.

The experiments for boiling heat transfer of water flow through rectangular micro-channels were carried out by Lee and Garimella (2008). The channel width ranging from 102 to 997 μm with the channel depth of around 400 μm was considered in this work and working fluid was deionized water. They found that at heat flux larger than 30 W/cm^2, the heat transfer coefficient was nearly independent with heat flux. According to their data and the asymptotic model developed by Steiner and Taborek (1992), the proposed heat transfer correlations were presented as follows.

$$h_{TP} = \frac{Nu_3}{Nu_4}\left[\left(F_{conv}h_L\right)^3 + \left(F_{nb}h_{nb}\right)^3\right]^{\frac{1}{3}} \tag{29}$$

where h_L represents single-phase liquid heat transfer coefficient, proposed by Lee and Garimella (2006), for laminar and thermally developing flow in rectangular micro-channels, and is expressed as

$$h_L = \left[1.766\left(Re_L Pr_L \frac{D_h}{L}\right)^{0.378}\beta^{0.1224}\right]\frac{k_L}{D_h} \tag{30}$$

The convective enhancement factor, F_{conv}, appearing in Eq.(29) can be determined by Eq.(31).

$$F_{conv} = \left(\phi_L^2\right)^{0.2743}\left(\frac{c_{p,TP}}{c_{p,L}}\right)^{0.2743}\left(\frac{k_{TP}}{k_L}\right)^{0.7257} \tag{31}$$

The two-phase frictional multiplier is given in the form of the Lockhart-Martinelli correlation as shown in Eq.(32).

$$\phi_L^2 = 1 + \frac{2566G^{0.5466}D_h^{0.8819}\left(1-e^{-319D_h}\right)}{\chi_{vv}} + \frac{1}{\chi_{vv}^2} \tag{32}$$

The Martinelli parameter for two-phase flow, which is in laminar region, is given by

$$\chi_{vv} = \left(\frac{1-x}{x}\right)^{0.5}\left(\frac{\rho_G}{\rho_L}\right)^{0.5}\left(\frac{\mu_L}{\mu_G}\right)^{0.5} \tag{33}$$

Any two-phase thermophysical properties can be evaluated based on arithmetic mean of those for the two phases.

Regarding Gorenflo (1993) for water, the nucleate boiling heat transfer coefficient is given by the following equation.

$$h_{nb} = 5600\left[1.73P_r^{0.27} + \left(6.1 + \frac{0.68}{1-P_r}\right)P_r^2\right]\left(\frac{q}{20000}\right)^{0.9-0.3P_r^{0.15}} \tag{34}$$

Finally, the nucleate boiling correction factor is obtained by

$$F_{nb} = 4.6809 - 0.6705\log\left(\frac{q}{1\times10^6}\right) + 3.908\left(\frac{D_h}{0.001}\right) \tag{35}$$

Heat transfer characteristics of R-134a for flow boiling in rectangular micro-channels were experimentally investigated by Bertsch et al. (2008). Their test section was micro-channels with a hydraulic diameter of 1.09 mm. Vapour quality showed significant influence on the heat transfer coefficient whereas the saturation pressure played insignificant role on the heat transfer coefficient. The higher the mass flux, the higher was the heat transfer coefficient. Similar to several previous works, the heat transfer coefficient was strongly dependent on the heat flux. With the same experimental apparatus, their next publication referring to Bertsch et al. (2009a) concerned with flow boiling heat transfer phenomena of R-245fa in addition to those of R-134a. In general, the use of R-134a for flow boiling in micro-channels resulted in relatively high heat transfer coefficient compared with R-245fa. Such discrepancy was explained based on the thermodynamic fluid properties. The comparisons between heat transfer results for two different hydraulic diameters of 1.09 and 0.54 mm were carried out for R-134a. The data shown in Fig. 5 revealed that the heat transfer coefficient was not affected by the variation of the hydraulic diameter. The similar manner was also reported by Harirchian and Garimella (2008). In contrast, the obvious effects of heat flux and vapour quality on the heat transfer coefficient were identified. The dominant heat transfer mechanism was considered to be nucleate boiling, due to the experimental data which were well predicted by pool boiling equation of Cooper (1984).

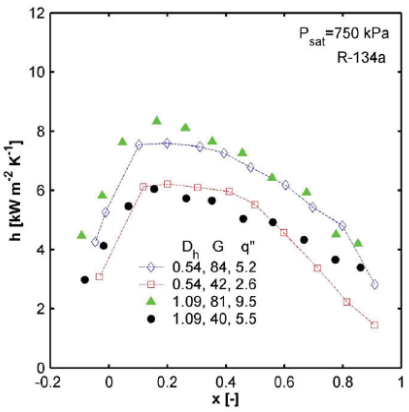

Fig. 5 Heat transfer coefficient data for different hydraulic diameters of Bertsch et al. (2009a). "Reprinted from International Journal of Multiphase Flow, 35(2), Bertsch, S.S., Groll, E.A., and Garimella, S.V., Effects of heat flux, mass flux, vapor quality, and saturation temperature on flow boiling heat transfer in microchannels, pp. 142-154 (2009), with permission from Elsevier."

Bertsch et al. (2009b) proposed a heat transfer correlation for flow boiling in micro-channels. Their correlation was based on the method of Chen (1966), which was done by accounting for nucleate boiling mechanism and two-phase force convection contribution for predicting heat transfer coefficient. The proposed correlation is presented in Eq.(36).

$$h_{TP} = h_{nb}\left(1-x\right) + h_{conv}\left(1 + 80\left(x^2 - x^6\right)e^{-0.6C_o}\right) \tag{36}$$

The nucleate boiling heat transfer coefficient is evaluated using Cooper correlation (1984) as expressed in Eq.(37) and convective heat transfer coefficient is given by Eq.(38).

$$h_{nb} = 55P_r^{0.12-0.2\log R_p}\left(-\log P_r\right)^{-0.55} M^{-0.5} q^{0.67} \tag{37}$$

$$h_{conv} = h_L(1-x) + h_G x \tag{38}$$

Surface roughness parameter, R_p, in Eq.(37) is equal to 1 if the surface roughness is unknown and M denotes molecular weight. The convective heat transfer coefficients for liquid and vapour phases appearing in Eq.(38) can be predicted using Hausen correlation (1943) as shown below.

$$h = \left(3.66 + \frac{0.0668\frac{D_h}{L}RePr}{1+0.04\left(\frac{D_h}{L}RePr\right)^{\frac{2}{3}}} \right)\frac{k}{D_h} \tag{39}$$

As seen in the above equation, liquid-phase heat transfer coefficient is therefore obtained regarding the properties of saturated liquid whereas the similar manner can be done for the vapour-phase heat transfer coefficient.

Three different refrigerants, R-134a, R-236fa and R-245fa, were tested for flow boiling in a 1.03 mm diameter tube by Ong and Thome (2009). Trends apparent in the data were investigated, showing that the heat transfer coefficient depended on heat flux at low vapour quality and on mass flux at high vapour quality. In terms of the refrigerants tested at low vapour quality, R-134a exhibited the highest heat transfer coefficient followed by R-236fa and R-245fa, respectively.

Choi et al. (2009) conducted experiments to obtain the data for two-phase flow vapourization of propane in circular channels. Two different channels with diameters of 1.5 and 3.0 mm were employed in this work. The effects of mass flux, heat flux, channel diameter and saturation temperature on the heat transfer coefficient were addressed. For low vapour quality region, the heat transfer coefficient was less affected by mass flux but substantially dependent on heat flux, showing nucleation-dominant mechanism. At higher quality region, however, an increase of forced convective mechanism was detected. As expected, the smaller channel diameter yielded a higher heat transfer coefficient. The heat transfer coefficient also increased with increasing the saturation temperature. For this work, the modification was done in the basis of Chen correlation (1966). The convective enhancement factor and nucleate boiling correction factor were proposed as shown in Eqs.(40) – (42).

The convective enhancement factor was given by

$$F_{conv} = \max\left(0.5\phi_L, 1\right) \tag{40}$$

where the two-phase multiplier was proposed in the form of the Lockhart-Martinelli correlation with Chisholm parameter expressed as

$$C = 1732.953 Re_{TP}^{-0.323} We_{TP}^{-0.24} \tag{41}$$

The nucleate boiling correction factor was presented in Eq.(42).

$$F_{nb} = 181.458\left(\phi_L^2\right)^{0.002} B_o^{0.816} \tag{42}$$

Sun and Mishima (2009) modified Lazarek and Black correlation (1982) to predict the heat transfer coefficient. Weber number was taken into account in the proposed correlation. Their correlation was not able to predict the trend of the heat transfer coefficient with vapour quality variation. The following is their proposed correlation.

$$h_{TP} = \frac{6Re_{LO}^{1.05} B_o^{0.54} k_L}{D_h We_{LO}^{0.191}\left(\frac{\rho_L}{\rho_G}\right)^{0.142}} \tag{43}$$

Tibirica and Ribatski (2010) presented experimental results for flow boiling heat transfer in a tube having a diameter of 2.3 mm. The results were obtained based on two different refrigerants, R-134a and R-245fa, which were used as working fluids. The heat transfer coefficient generally increased with increasing heat flux, saturation temperature, mass flux and vapour quality. The variation of the heat transfer coefficient with the saturation temperature for R-245fa was more obvious than that for R-134a. Nevertheless, R-134a provided high heat transfer coefficients in comparison to R-245fa.

Lee et al. (2010) collected existing 1623 data points from the literature to develop heat transfer correlations for evaporative micro-channels. The correlations of Lee and Mudawar (2005) were modified in this study as presented in Eqs.(44) – (46).

$$h_{TP} = \frac{3.856\chi^{0.267} h_L}{0.958e^{\left(\frac{-\lambda}{1.537}\right)} + 0.126}; \quad 0 \le x < 0.05 \tag{44}$$

$$h_{TP} = \frac{436.48 B_o^{0.522} We_{LO}^{0.351} \chi^{0.665} h_L}{0.958e^{\left(\frac{-\lambda}{1.537}\right)} + 0.126}; \quad 0.05 \le x < 0.55 \tag{45}$$

$$h_{TP} = \frac{\max\left\{\left(108.6\chi^{1.665} h_G\right), h_G\right\}}{0.958e^{\left(\frac{-\lambda}{1.537}\right)} + 0.126}; \quad 0.55 \le x < 1 \tag{46}$$

Convective boiling heat transfer experiments were carried out by Oh et al. (2011) for tubes with diameters of 0.5, 1.5 and 3.0 mm. There were five refrigerants used in their study, i.e. R-22, R-134a, R-410A, C_3H_8 and CO_2. Based on an insignificant effect of mass flux on the heat transfer coefficient in low vapour quality region, the dominance of nucleate boiling mechanism was indicated. However, forced convective contribution was addressed as dominant in moderate-high quality region due to the mass flux dependency. The smaller diameter tube resulted in the higher heat transfer coefficient, especially at low vapour quality region. The heat transfer coefficient of CO_2 was highest in comparison to the other four refrigerants.

Bang et al. (2011) reported slight effect of pressure on heat transfer coefficient of water during flow boiling in a 1.73 mm diameter channel. The dominance of forced convection was observed during their experiments.

Copetti et al. (2011) presented the experimental work for flow boiling of R-134a in a tube with a diameter of 2.6 mm. Heat transfer characteristics under the variation of different parameters were discussed. They reported the dependence of heat transfer coefficient on heat flux, especially at low vapour quality region. At high quality region, however, the heat flux dependency became lower. The heat transfer coefficient was strongly dependent on mass flux only for low heat flux conditions. Flow pattern was reported to play important role on the heat transfer coefficient.

Influence of the aspect ratio on flow boiling heat transfer characteristics in rectangular channels were reported by Soupremanien et al. (2011). The results showed that for a low aspect ratio of 0.143, the heat transfer coefficient was not dependent on the vapour quality for a heat flux range of 25 to 45 kW/m^2. As heat flux increased above 45 kW/m^2, the heat transfer coefficient tended to decrease with increasing vapour quality. However, the heat transfer coefficient was not affected by the variation of vapour quality when the channel with higher aspect ratio of 0.43 was used in the experiments. Another point to note was that the heat transfer

DOI: 10.5098/hmt.v3.1.3006 ISSN: 2151-8629

coefficient was higher for the aspect ratio of 0.143 than that of 0.43 under low heat flux conditions. The opposite trend was addressed for high heat flux conditions.

Ong and Thome (2011b) experimentally investigated flow boiling heat transfer of three refrigerants in channels of 1.03, 2.20 and 3.04 mm diameters. R-134a, R-236fa and R-245fa were used as working fluids in their study. The channel with higher confinement number, i.e. smaller diameter, gave heat transfer coefficients with lower dependency on heat flux. The heat transfer coefficient was also found to strongly depend on flow pattern. The coalescing bubble flow regime posed heat transfer mechanism compatible with three-zone flow boiling model proposed by Thome et al. (2004) whereas the dominance of forced convection was observed in the annular flow regime. The heat transfer coefficient for R-134a showed the highest dependence on heat flux but R-245fa yielded the lowest heat flux dependency while R-236fa was positioned in between the other two refrigerants. It was noted from the authors that surface roughness played important role on micro-scale flow boiling.

In summary, this emerging field is very attractive and may enable us to develop powerful miniature devices which seem to be unfeasible in the past. Although a number of studies have been reported for micro-channels, micro-scale phenomena with respect to phase-change mechanisms are still open questions for which systematic answers are of importance. Based on this, further investigations should be performed as follows.

1. The existing models and correlations for flow pattern and heat transfer predictions should be examined based on different sources of the experimental data
2. Conduct more experiments to address the macro-to-micro-scale transition for flow boiling of refrigerants in different channel sizes and channel orientations. The threshold of the transition would be addressed according to the dependence of the channel orientation on flow regime and heat transfer characteristics.
3. Heat transfer behaviors in parallel channels are different from those in single channel under a given set of experimental conditions. The discrepancies are possibly due to instabilities resulting from flow reversal in the channels. The details corresponding to instabilities encountered in narrow spaces were reviewed by Tadrist (2007). Referring to Kandlikar et al. (2006), the surface condition was found to influence on the instabilities. The introduction of artificial nucleation cavities fabricated on the micro-channel surface together with inlet header having restriction holes was recommended to obtain a good heat transfer performance without instabilities. The surface effects during flow boiling in micro-channels were also discussed in Mahmoud et al. (2011). Additionally, the effect of conduction heat transfer over the partitions in the parallel channels may cause the difference in the heat transfer characteristics between single and parallel channels. The previous studies imply that the parametric studies regarding the comparisons of the heat transfer performance in single channel and that in parallel channels should be further performed to explain the cause of the discrepancies.
4. Although the topics such as critical heat flux, flow instability and two-phase pressure drop are not included in this paper due to the restricted space, the relevant experimental data are of importance for developing the miniature devices.

3. CONCLUSION

A state-of-the-art review of flow boiling in micro-channels is presented. Recent researches on flow pattern, heat transfer characteristics are described in this paper. Different criteria are presented at first to give definition for micro-channel. The explorations indicate that the existing channel classifications cannot relate the channel diameter to the fluid flow and heat transfer mechanisms. Further works should be conducted to meet a more general definition dealing with the channel classification. Then, flow visualization studies and investigations on heat transfer characteristics are reviewed. Obviously, the research work in this area is still rare so far. As a consequence, a great deal of systematic investigations remain to be done to meet general conclusions needed for the appropriate design and process control of several engineering applications.

ACKNOWLEDGEMENTS

The authors would like to express their appreciation to the Thailand Research Fund, KMITL Research Fund, the Office of Higher Education Commission and the National Research University Project for providing financial support.

NOMENCLATURE

B_o	boiling number, $B_o = q/Gi_{LG}$
C	Chisholm parameter
C_{CO}	convection number, $C_{CO} = (\rho_G/\rho_L)^{0.5}((1-x)/x)^{0.8}$
C_o	confinement number as defined in Eq.(1)
C_p	specific heat at constant pressure (J/kgK)
D	channel diameter (m)
D_b	capillary length (m)
D_h	hydraulic diameter (m)
F	factor
Fr	Froude number, $Fr = G^2/\rho^2 gD$
F_{Fl}	fluid-surface parameter
f	friction factor
G	mass flux (kg/m^2s)
g	gravitational acceleration (m/s^2)
h	heat transfer coefficient (W/m^2K)
i	specific enthalpy (J/kg)
k	thermal conductivity (W/mK)
L	length (m)
M	molecular weight (kg/kmol)
Nu	Nusselt number, $Nu = hD_h/k$
P	pressure (Pa)
P_r	reduced pressure
Pr	Prandtl number, $Pr = \mu C_p/k$
q	heat flux (W/m^2)
Re	Reynolds number, $Re = GD_h/\mu$
R_p	surface roughness parameter
T	temperature (^oC)
t	time (s)
We	Weber number, $We = G^2 D_h/\rho\sigma$
x	vapour quality
z	axial distance (m)

Greek symbols

β	ratio of channel dept to width
χ	Lockhart-Martinelli parameter
ϕ	two-phase multiplier
λ	Bond number, $\lambda = g(\rho_L - \rho_G)D_h^2/\sigma$
μ	dynamic viscosity (Ns/m^2)
ρ	density (kg/m^3)
σ	surface tension (N/m)
τ	pair period (s)

Subscripts

3	three-sided wall heating
4	four-sided wall heating
A	annular flow

CB	coalescing bubble flow
conv	convection boiling contribution
dry	dry-out zone
eq	equivalent
film	liquid film between bubble and wall
G	vapour phase
GO	all-vapour
IB	isolated bubble flow
in	inlet
L	liquid phase
LO	all-liquid
nb	nucleate boiling contribution
out	outlet
s	surface
sat	saturation
TP	two-phase
vt	Laminar liquid-turbulent vapour flow
vv	laminar liquid-laminar vapour flow

REFERENCES

Agostini, B., Thome, J.R., Fabbri, M., Michel, B., Calmi, D., and Kloter, U., 2008a, "High heat flux flow boiling in silicon multi-microchannels – Part I: Heat transfer characteristics of refrigerant R236fa," *International Journal of Heat and Mass Transfer,* 51, 5400-5414.
http://dx.doi.org/10.1016/j.ijheatmasstransfer.2008.03.006

Agostini, B., Thome, J.R., Fabbri, M., Michel, B., Calmi, D., and Kloter, U., 2008b, "High heat flux flow boiling in silicon multi-microchannels – Part II: Heat transfer characteristics of refrigerant R245fa," *International Journal of Heat and Mass Transfer,* 51, 5415-5425.
http://dx.doi.org/10.1016/j.ijheatmasstransfer.2008.03.007

Arcanjo, A.A., Tibirica, C.B., and Ribatski, G., 2010, "Evaluation of flow patterns and elongated bubble characteristics during the flow boiling of halocarbon refrigerants in a micro-scale channel," *Experimental Thermal and Fluid Science,* 34, 766-775.
http://dx.doi.org/10.1016/j.expthermflusci.2010.01.006

Bang, K.H., Kim, K.K., Lee, S.K., and Lee, B.W., 2011, "Pressure effect on flow boiling heat transfer of water in minichannels," *International Journal of Thermal Sciences,* 50, 280-286.
http://dx.doi.org/10.1016/j.ijthermalsci.2010.03.011

Bao, Z.Y., Fletcher, D.F., and Haynes, B.S., 2000, "Flow boiling heat transfer of Freon R11 and HCFC123 in narrow passages," *International Journal of Heat and Mass Transfer,* 43, 3347-3358.
http://dx.doi.org/10.1016/S0017-9310(99)00379-8

Bertsch, S.S., Groll, E.A., and Garimella, S.V., 2008, "Refrigerant flow boiling heat transfer in parallel microchannels as a function of local vapor quality," *International Journal of Heat and Mass Transfer,* 51, 4775-4787.
http://dx.doi.org/10.1016/j.ijheatmasstransfer.2008.01.026

Bertsch, S.S., Groll, E.A., and Garimella, S.V., 2009a, "Effects of heat flux, mass flux, vapor quality, and saturation temperature on flow boiling heat transfer in microchannels," *International Journal of Multiphase Flow,* 35, 142-154.
http://dx.doi.org/10.1016/j.ijmultiphaseflow.2008.10.004

Bertsch, S.S., Groll, E.A., and Garimella, S.V., 2009b, "A composite heat transfer correlation for saturated flow boiling in small channels," *International Journal of Heat and Mass Transfer,* 52, 2110-2118.
http://dx.doi.org/10.1016/j.ijheatmasstransfer.2008.10.022

Boye, H., Staate, Y., and Schmidt, J., 2007, "Experimental investigation and modeling of heat transfer during convective boiling in a minichannel," *International Journal of Heat and Mass Transfer,* 50, 208-215.
http://dx.doi.org/10.1016/j.ijheatmasstransfer.2006.06.017

Celata, G.P., Saha, S.K., Zummo, G., and Dossevi, D., 2010, "Heat transfer characteristics of flow boiling in a single horizontal microchannel," *International Journal of Thermal Sciences,* 49, 1086-1094.
http://dx.doi.org/10.1016/j.ijthermalsci.2010.01.019

Chen, J.C., 1966, "Correlation for boiling heat transfer to saturated fluids in convective flow," I&EC Process Des. Dev., 5, 322-329.

Choi, K.-I., Pamitran, A.S., and Oh, J.-T., 2007a, "Two-phase flow heat transfer of CO_2 vaporization in smooth horizontal minichannels," *International Journal of Refrigeration,* 30, 767-777.
http://dx.doi.org/10.1016/j.ijrefrig.2006.12.006

Choi, K.-I., Pamitran, A.S., Oh, C.-Y., and Oh, J.-T., 2007b, "Boiling heat transfer of R-22, R-134a, and CO_2 in horizontal smooth minichannels," *International Journal of Refrigeration,* 30, 1336-1346.
http://dx.doi.org/10.1016/j.ijrefrig.2007.04.007

Choi, K.-I., Pamitran, A.S., Oh, J.-T., and Saito, K., 2009, "Pressure drop and heat transfer during two-phase flow vaporization of propane in horizontal smooth minichannels," *International Journal of Refrigeration,* 32, 837-845.
http://dx.doi.org/10.1016/j.ijrefrig.2008.12.005

Chung, P.M.-Y., and Kawaji, M., 2004, "The effect of channel diameter on adiabatic two-phase flow characteristics in microchannels," *International Journal of Multiphase Flow,* 30, 735-761.
http://dx.doi.org/10.1016/j.ijmultiphaseflow.2004.05.002

Cooper, M.G., 1984, "Heat flow rates in saturated nucleate pool boiling – A wide ranging examination using reduced properties," *Advances in Heat Transfer,* 16, 157-239.
http://dx.doi.org/10.1016/S0065-2717(08)70205-3

Copetti, J.B., Macagnan, M.H., Zinani, F., and Kunsler, N.L.F., 2011, "Flow boiling heat transfer and pressure drop of R-134a in a mini tube: an experimental investigation," *Experimental Thermal and Fluid Science,* 35, 636-644.
http://dx.doi.org/10.1016/j.expthermflusci.2010.12.013

Dupont, V., Thome, J.R., and Jacobi, A.M., 2004, "Heat transfer model for evaporation in microchannels. Part II: comparison with the database," *International Journal of Heat and Mass Transfer,* 47, 3387-3401.
http://dx.doi.org/10.1016/j.ijheatmasstransfer.2004.01.007

Garimella, S., Killion, J.D., and Coleman, J.W., 2002, "An experimentally validated model for two-phase pressure drop in the intermittent flow regime for circular microchannels," *Journal of Fluids Engineering,* 124, 205-214.
http://dx.doi.org/10.1115/1.1428327

Gorenflo, D., 1993, "Pool Boiling," VDI-Heat Atlas, VDI-Verlag, Dusseldorf, Germany.

Harirchian, T., and Garimella, S.V., 2008, "Microchannel size effects on local flow boiling heat transfer to a dielectric fluid," *International Journal of Heat and Mass Transfer,* 51, 3724-3735.

http://dx.doi.org/10.1016/j.ijheatmasstransfer.2008.03.013

Harirchian, T., and Garimella, S.V., 2010, "A comprehensive flow regime map for microchannel flow boiling with quantitative transition criteria," *International Journal of Heat and Mass Transfer,* 53, 2694-2702.
http://dx.doi.org/10.1016/j.ijheatmasstransfer.2010.02.039

Hausen, H., Warmeuberganges 1943, "Darstellung des in Rohren durch verallgemeinerte Potenzbeziehungen," Z. VDI Beiheft Verfahrenstechnik, 4, 91-102.

Huo, X., Chen, L., Tian, Y.S., and Karayiannis, T.G., 2004, "Flow boiling and flow regimes in small diameter tubes," *Applied Thermal Engineering,* 24, 1225-1239.
http://dx.doi.org/10.1016/j.applthermaleng.2003.11.027

Jiang, L., and Wong, M., 1999, "Phase change in microchannel heat-sinks with integrated temperature sensors," *Journal of Microelectromechanical Systems,* 8, 358-365.
http://dx.doi.org/10.1109/84.809049

Kandlikar, S.G., 1990, "A general correlation for two-phase flow boiling heat transfer coefficient inside horizontal and vertical tubes," *Journal of Heat Transfer,* 112, 219-228.
http://dx.doi.org/10.1115/1.2910348

Kandlikar, S.G., and Grande, W.J., 2003, "Evolution of microchannel flow passages – thermohydraulic performance and fabrication technology," *Heat Transfer Engineering,* 24, 3-17.
http://dx.doi.org/10.1080/01457630304040

Kandlikar, S.G., and Balasubramanian, P., 2004, "An extension of the flow boiling correlation to transition, laminar, and deep laminar flows in minichannels and microchannels," *Heat Transfer Engineering,* 25, 86-93.
http://dx.doi.org/10.1080/01457630490280425

Kandlikar, S.G., and Balasubramanian, P., 2005, "An experimental study on the effect of gravitational orientation on flow boiling of water in 1054 × 197 μm parallel minichannels," *Journal of Heat Transfer,* 127, 820–829.
http://dx.doi.org/10.1115/1.1928911

Kandlikar, S.G., Kuan, W.K., Willistein, D.A., and Borrelli, J., 2006, "Stabilization of flow boiling in microchannels using pressure drop elements and fabricated nucleation sites," *Journal of Heat Transfer,* 128, 389-396.
http://dx.doi.org/10.1115/1.2165208

Kandlikar, S.G., 2010, "Scale effects on flow boiling heat transfer in microchannels: A fundamental perspective," *International Journal of Thermal Sciences,* 49, 1073-1085.
http://dx.doi.org/10.1016/j.ijthermalsci.2009.12.016

Kew, P.A., and Cornwell, K., 1997, "Correlations for the prediction of boiling heat transfer in small-diameter channels," *Applied Thermal Engineering,* 17, 705-715.
http://dx.doi.org/10.1016/S1359-4311(96)00071-3

Lazarek, G.M., and Black, S.H., 1982, "Evaporative heat transfer, pressure drop and critical heat flux in a small diameter vertical tube with R-113," *International Journal of Heat and Mass Transfer,* 25, 945-960.
http://dx.doi.org/10.1016/0017-9310(82)90070-9

Lee, H.J., and Lee, S.Y., 2001, "Heat transfer correlation for boiling flows in small rectangular horizontal channels with low aspect ratios," *International Journal of Multiphase Flow,* 27, 2043-2062.
http://dx.doi.org/10.1016/S0301-9322(01)00054-4

Lee, J., and Mudawar, I., 2005, "Two-phase flow in high-heat-flux micro-channel heat sink for refrigeration cooling applications: Part II – heat transfer characteristics," *International Journal of Heat and Mass Transfer,* 48, 941-955.
http://dx.doi.org/10.1016/j.ijheatmasstransfer.2004.09.019

Lee, P.-S., and Garimella, S.V., 2006, "Thermally developing flow and heat transfer in rectangular microchannels of different aspect ratios," *International Journal of Heat and Mass Transfer,* 49, 3060-3067.
http://dx.doi.org/10.1016/j.ijheatmasstransfer.2006.02.011

Lee, P.-S., and Garimella, S.V., 2008, "Saturated flow boiling heat transfer and pressure drop in silicon microchannel arrays," *International Journal of Heat and Mass Transfer,* 51, 789-806.
http://dx.doi.org/10.1016/j.ijheatmasstransfer.2007.04.019

Lee, J., and Mudawar, I., 2008, "Fluid flow and heat transfer characteristics of low temperature two-phase micro-channel heat sinks – Part 2. Subcooled boiling pressure drop and heat transfer," *International Journal of Heat and Mass Transfer,* 51, 4327-4341.
http://dx.doi.org/10.1016/j.ijheatmasstransfer.2008.02.013

Lee, H.J., Liu, D.Y., Alyousef, Y., and Yao, S., 2010, "Generalized two-phase pressure drop and heat transfer correlations in evaporative micro/minichannels," *Journal of Heat Transfer,* 132, 1-9.
http://dx.doi.org/10.1115/1.4000861

Li, W., and Wu, Z., 2010, "A general criterion for evaporative heat transfer in micro/mini-channels," *International Journal of Heat and Mass Transfer,* 53, 1967-1976.
http://dx.doi.org/10.1016/j.ijheatmasstransfer.2009.12.059

Lie, Y.M., Su, F.Q., Lai, R.L., and Lin, T.F., 2006, "Experimental study of evaporation heat transfer characteristics of refrigerants R-134a and R-407C," *International Journal of Heat and Mass Transfer,* 49, 207-218.
http://dx.doi.org/10.1016/j.ijheatmasstransfer.2005.07.018

Mahmoud, M.M., Karayiannis, T.G., and Kenning, D.B.R., 2011, "Surface effects in flow boiling of R134a in microtubes," *International Journal of Heat and Mass Transfer, 54,* 3334-3346.
http://dx.doi.org/10.1016/j.ijheatmasstransfer.2011.03.052

Martin-Callizo, C., Palm, B., Owhaib, W., and Ali, R., 2010, "Flow boiling visualization of R-134a in a vertical channel of small diameter," *Journal of Heat Transfer,* 132, 1-8.
http://dx.doi.org/10.1115/1.4000012

Mehendale, S.S., Jacobi, A.M., and Ahah, R.K., 2000, "Fluid flow and heat transfer at micro- and meso-scales with application to heat exchanger design," *Applied Mechanics Reviews,* 53, 175-193.
http://dx.doi.org/10.1115/1.3097347

Oh, J.-T., Pamitran, A.S., Choi, K.-I., and Hrnjak, P., 2011, "Experimental investigation on two-phase flow boiling heat transfer of five refrigerants in horizontal small tubes of 0.5, 1.5 and 3.0 mm inner diameters," *International Journal of Heat and Mass Transfer,* 54, 2080-2088.
http://dx.doi.org/10.1016/j.ijheatmasstransfer.2010.12.021

Ong, C.L., and Thome, J.R., 2009, "Flow boiling heat transfer of R134a, R236fa and R245fa in a horizontal 1.030 m m circular channel," *Experimental Thermal and Fluid Science,* 33, 651-663.
http://dx.doi.org/10.1016/j.expthermflusci.2009.01.002

Ong, C.L., and Thome, J.R., 2011a, "Macro-to-microchannel transition in two-phase flow: Part 1-Two-phase flow patterns and film thickness measurements," *Experimental Thermal and Fluid Science,* 35, 37-47.
http://dx.doi.org/10.1016/j.expthermflusci.2010.08.004

Ong, C.L., and Thome, J.R., 2011b, " Macro-to-microchannel transition in two-phase flow: Part 2-Flow boiling heat transfer and critical heat flux," *Experimental Thermal and Fluid Science,* 35, 873-886.
http://dx.doi.org/10.1016/j.expthermflusci.2010.12.003

Pettersen, J., 2004, "Flow vaporization of CO_2 in microchannel tubes," *Experimental Thermal and Fluid Science,* 28, 111-121.
http://dx.doi.org/10.1016/S0894-1777(03)00029-3

Qu, W., and Mudawar, I., 2003, " Flow boiling heat transfer in two-phase microchannel heat sinks; experimental investigation and assessment of correlation methods," *International Journal of Heat and Mass Transfer,* 46, 2755-2771.
http://dx.doi.org/10.1016/S0017-9310(03)00041-3

Revellin, R., and Thome, J.R., 2007, "A new type of diabatic flow pattern map for boiling heat transfer in microchannels," *Journal of Micromechanics and Microengineering,* 17, 788-796.
http://dx.doi.org/10.1088/0960-1317/17/4/016

Ribatski, G., Wojtan, L., and Thome, J.R., 2006, "An analysis of experimental data and prediction methods for two-phase frictional pressure drop and flow boiling heat transfer in micro-scale channels," *Experimental Thermal and Fluid Science,* **31**, 1-19.
http://dx.doi.org/10.1016/j.expthermflusci.2006.01.006

Saisorn, S., and Wongwises, S., 2010, " The effects of channel diameter on flow pattern, void fraction and pressure drop of two-phase air-water flow in circular micro-channels," *Experimental Thermal and Fluid Science,* 34, 454-462.
http://dx.doi.org/10.1016/j.expthermflusci.2009.02.006

Saisorn, S., Kaew-On, J., and Wongwises, S., 2010, " Flow pattern and heat transfer characteristics of R-134a refrigerant during flow boiling in a horizontal circular mini-channel," *International Journal of Heat and Mass Transfer,* 53, 4023-4038.
http://dx.doi.org/10.1016/j.ijheatmasstransfer.2010.05.022

Saitoh, S., Daiguji, H., and Hihara, E., 2005, "Effect of tube diameter on boiling heat transfer of R -134a in horizontal small-diameter tubes," *International Journal of Heat and Mass Transfer,* 48, 4973-4984.
http://dx.doi.org/10.1016/j.ijheatmasstransfer.2005.03.035

Shiferaw, D., Huo, X., Karayiannis, T.G., and Kenning, D.B.R., 2007, "Examination of heat transfer correlations and a model for flow boiling of R134a in small diameter tubes," *International Journal of Heat and Mass Transfer,* 50, 5177-5193.
http://dx.doi.org/10.1016/j.ijheatmasstransfer.2007.07.002

Shiferaw, D., Karayiannis, T.G., and Kenning, D.B.R., 2009, "Flow boiling in a 1.1 mm tube with R134a: Experimental results and comparison with model," *International Journal of Thermal Sciences,* 48, 331-341.
http://dx.doi.org/10.1016/j.ijthermalsci.2008.02.009

Soupremanien, U., Person, S.L., Favre-Marinet, M., and Bultel, Y., 2011, "Influence of the aspect ratio on boiling flows in rectangular mini-channels," *Experimental Thermal and Fluid Science,* 35, 797-809.
http://dx.doi.org/10.1016/j.expthermflusci.2010.06.014

Steiner, D., and Taborek, J., 1992, "Flow boiling heat transfer in vertical tubes correlated by an asymptotic model," *Heat Transfer Engineering,* 13, 43-68.
http://dx.doi.org/10.1080/01457639208939774

Sumith, B., Kaminaga, F., and Matsumura, K., 2003, "Saturated flow boiling of water in a vertical small tube," *Experimental Thermal and Fluid Science,* 27, 789-801.
http://dx.doi.org/10.1016/S0894-1777(02)00317-5

Sun, L., and Mishima, K., 2009, "An evaluation of prediction methods for saturated flow boiling heat transfer in mini-channels," *International Journal of Heat and Mass Transfer,* 52, 5323-5329.
http://dx.doi.org/10.1016/j.ijheatmasstransfer.2009.06.041

Tadrist, L., 2007, "Review on two-phase flow instabilities in narrow spaces," *International Journal of Heat and Fluid Flow, 28*, 54-62.
http://dx.doi.org/10.1016/j.ijheatfluidflow.2006.06.004

Thome, J.R., 2004, "Boiling in microchannels: a review of experiment and theory," *International Journal of Heat and Fluid Flow, 25*, 128-139.
http://dx.doi.org/10.1016/j.ijheatfluidflow.2003.11.005

Thome, J.R., Dupont, V., and Jacobi, A.M., 2004, "Heat transfer model for evaporation in microchannels. Part I: presentation of the model," *International Journal of Heat and Mass Transfer,* 47 3375-3385.
http://dx.doi.org/10.1016/j.ijheatmasstransfer.2004.01.006

Tibirica, C.B., and Ribatski, G., 2010, "Flow boiling heat transfer of R134a and R245fa in a 2.3 mm tube," *International Journal of Heat and Mass Transfer,* 53, 2459-2468.
http://dx.doi.org/10.1016/j.ijheatmasstransfer.2010.01.038

Tran, T.N., Wambsganss, M.W., and France, D.M., 1996, "Small circular- and rectangular-channel boiling with two refrigerants," *International Journal of Multiphase Flow,* 22, 485-498.
http://dx.doi.org/10.1016/0301-9322(96)00002-X

Triplett, K.A., Ghiaasiaan, S.M., Abdel-Khalik, S.I., and Sadowski, D.L., 1999, "Gas-liquid two-phase flow in microchannels Part I: two-phase flow patterns," *International Journal of Multiphase Flow,* 25, 377-394.
http://dx.doi.org/10.1016/S0301-9322(98)00054-8

Wambsganss, M.W., France, D.M., Jendrzejczyk, J.A., and Tran, T.N., 1993, " Boiling heat transfer in a horizontal small-diameter tube," *Journal of Heat Transfer,* 115, 963-972.
http://dx.doi.org/10.1115/1.2911393

Yang, C.-Y., and Shieh, C.-C., 2001, "Flow pattern of air-water and two-phase R-134a in small circular tubes," *International Journal of Multiphase Flow,* 27, 1163-1177.
http://dx.doi.org/10.1016/S0301-9322(00)00070-7

Yen, T.-H., Shoji, M., Takemura, F., Suzuki, Y., and Kasagi, N., 2006, "Visualization of convective boiling heat transfer in single microchannels with different shaped cross-sections," *International Journal of Heat and Mass Transfer,* 49, 3884-3894.
http://dx.doi.org/10.1016/j.ijheatmasstransfer.2005.12.024

Yun, R., Kim, Y., and Kim, M.S., 2005, "Convective boiling heat transfer characteristics of CO_2 in microchannels," *International Journal of Heat and Mass Transfer*, 48, 235-242. http://dx.doi.org/10.1016/j.ijheatmasstransfer.2004.08.019

Zhang, L., Koo, J.M., Jiang, L., Asheghi, M., Goodson, K.E., and Santiago, J.G., 2002, "Measurements and modeling of two-phase flow in microchannels with nearly constant heat flux boundary conditions," *Journal of Microelectromechanical Systems*, 11, 12-19. http://dx.doi.org/10.1109/84.982858

Zhang, W., Hibiki, T., and Mishima, K., 2004, "Correlation for flow boiling heat transfer in mini-channels," *International Journal of Heat and Mass Transfer*, 47, 5749-5763. http://dx.doi.org/10.1016/j.ijheatmasstransfer.2004.07.034

Frontiers in Heat and Mass Transfer (FHMT), 3, 013007 (2012)
DOI: 10.5098/hmt.v3.1.3007

Global Digital Central
ISSN: 2151-8629

Frontiers in Heat and Mass Transfer

Available at www.ThermalFluidsCentral.org

A CRITICAL REVIEW OF RECENT INVESTIGATIONS ON TWO-PHASE PRESSURE DROP IN FLOW BOILING MICRO-CHANNELS

Sira Saisorn[a,b], Somchai Wongwises[b,c*]

[a]*King Mongkut's Institute of Technology Ladkrabang Chumphon Campus Chumphon 86160, Thailand*
[b]*Fluid Mechanics, Thermal Engineering and Multiphase Flow Research Lab. (FUTURE)*
Department of Mechanical Engineering, King Mongkut's University of Technology Thonburi, Bangmod, Bangkok 10140, Thailand
[c]*The Academy of Science, The Royal Institute of Thailand, Sanam Suea Pa, Dusit, Bangkok 10300, Thailand*

ABSTRACT

Two-phase pressure drop during flow boiling has been studied for several decades. Obviously, the publications available on micro-channels are relatively small compared with those for ordinarily sized channels. Although the use of micro-channels yields several advantages, the pressure drop takingp lace in these extremely small channels is higher than that in the ordinarily sized channels because of the increased wall friction. The knowledge of the two-phase pressure drop characteristics in addition to heat transfer phenomena is essential to the design and evaluation of the micro-systems. In this paper, recent research on the flow boiling pressure drop in micro-scale channels is reviewed. The experimental results as well as the relevant prediction methods based on different researchers are presented.

Keywords: *flow boiling, micro-channel, pressure drop, heat transfer*

1. INTRODUCTION

In the past 10 years, investigations on flow boiling heat transfer and flow characteristics in micro-channel flow passages have gained significant attention in engineering community. Because of their large heat transfer surface area, the utilization of micro-channels can result in relatively high heat transfer coefficient when compared with the application of ordinarily sized channels. Flow boiling in micro-channel has been applied to energy and process systems including high heat-flux compact heat exchangers, and cooling devices of various types of equipment such as high performance micro-electronics, high-powered lasers, and so on.

Although there are several advantages arising in micro-channel applications, a considerable penalty is relatively high pressure drop due to the increased wall friction, resulting in the increment of power consumption. The applicable range of the flow in miniature devices is restricted by this main drawback. It is therefore important to understand pressure drop characteristics in addition to heat transfer phenomena in micro-channels, which is of necessity for operating and evaluating the system performance.

A scaling analysis of different forces, as recently discussed in Kandlikar (2010), pointed out that surface tension and evaporation momentum forces were significant for two-phase flow phenomena at micro-scale, resulting in the flow behaviors substantially different from those of ordinarily sized channels.

Currently, it seems rather vague to identify whether or not the flow passages are micro-channels. The followings are some important tentative criterions which are given in brief.

The criteria based on different dimensionless parameters have been proposed in the literature. The confinement number recommended by Kew and Cornwell (1997) was proposed to be related with some physical aspects of flow boiling. The confinement number is defined as

$$C_o = \frac{D_b}{D_h} \tag{1}$$

where D_h is hydraulic diameter and D_b is nominal bubble size or capillary length which is expressed by

$$D_b = \sqrt{\frac{\sigma}{g(\rho_L - \rho_G)}} \tag{2}$$

The confinement number above 0.5 implies that the micro-scale effects are important for a given channel diameter. In Eq.(2), σ stands for surface tension, g is gravitational acceleration, ρ_L and ρ_G are, respectively, liquid and vapour densities.

Based on 4228 data points gathered from the literature, Li and Wu (2010a) showed the transitional threshold from macro- to micro-channels during flow boiling to be represented as a combined non-dimensional number, $B_o \times Re_L^{0.5} = 200$. B_o and Re_L stand, respectively, for Bond number and liquid Reynolds number. The micro-scale effects are dominant when such combined non-dimensional number is lower than 200.

It is interesting to note from Tibirica and Ribatski (2010) that the channel with a diameter of 2.3 mm was considered as the one in which the transition between macro- and micro-scale flow boiling phenomena took place when halocarbon refrigerants were used as working fluids under Earth's gravity. With visualization study, they detected stratification effects in this channel size. Recently, Ong and

* *Corresponding author: E-mail: somchai.won@kmutt.ac.th*

Thome (2011) investigated experiments to address the macro-to-micro-scale transition for flow boiling of refrigerants in different channel sizes. They indicated the dependence of the threshold of the transition on flow regime and confinement number. As illustrated in Fig. 1, the lower threshold of macro-scale flow corresponded to confinement number ranging from 0.3 to 0.4 whereas the confinement number of around 1.0 stood for the upper threshold of micro-scale flow. It was noted that the transition region, frequently corresponding to as mini-channels in literature, was located in between the two boundaries.

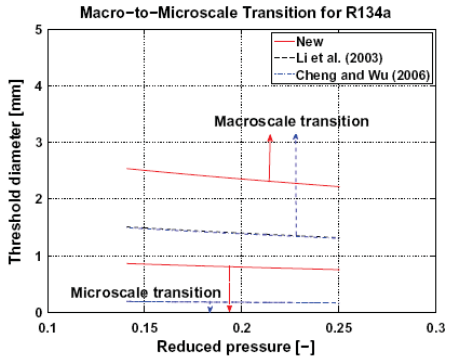

Fig. 1 Transition criterion of Ong and Thome (2011). "Reprinted from Experimental Thermal and Fluid Science, 35(1), Ong, C.L., and Thome, J.R., Macro-to-microchannel transition in two-phase flow: Part 1-Two-phase flow patterns and film thickness measurements, pp. 37-47 (2011), with permission from Elsevier."

Noting from Kandlikar (2010) that as the mass flux substantially increases, the inertia force becomes larger and tends to be of importance as shown in Fig. 2. In the region of very high mass flux, therefore, the inertia force in addition to surface tension and buoyancy (gravity) forces should be taken into account for developing the criteria.

Despite a number of criteria being proposed, a clear physical criterion that relates the channel diameter to the fluid flow mechanisms is still not available and, hence, further investigation should be performed to meet a more general definition dealing with channel classification.

2. TWO-PHASE PRESSURE DROP

Although there are several advantages arising in micro-channel applications, a considerable penalty is relatively high pressure drop, due to the increased wall friction, when compared with the ordinarily sized channels. It is therefore important to understand pressure drop characteristics in addition to heat transfer phenomena in micro-channels, which is of necessity for operating and evaluating the system performance.

Recent studies dealing with flow boiling pressure drop characteristics, excluding flow instability, in micro-channels are reviewed in this section. During the past years, investigations of two-phase pressure drop during micro-scale flow have been published in the literature and Table 1 lists the selected investigations recently done by various researchers.

Two-phase pressure drop across micro-channels were measured by Lee and Mudawar (2005). Flow boiling of R-134a in rectangular channels was established in their study. The measured pressure drops were not well predicted by the existing correlations. To improve the accuracy of the prediction, the parameters including liquid viscosity and surface tension were incorporated in their correlation as seen in Eqs.(3) and (4).

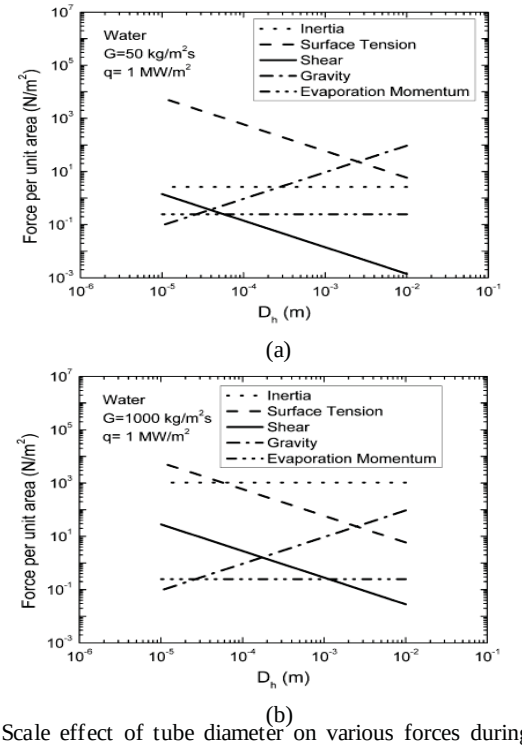

Fig. 2 Scale effect of tube diameter on various forces during flow boiling by Kandlikar (2010). "Reprinted from International Journal of Thermal Science, 49(7), Kandlikar, S.G., Scale effects on flow boiling heat transfer in microchannels: A fundamental perspective, pp. 1073-1085 (2010), with permission from Elsevier."

For laminar liquid-laminar vapour flow:

$$\phi_L^2 = 1 + \frac{2.16 Re_{LO}^{0.047} We_{LO}^{0.6}}{\chi} + \frac{1}{\chi^2} \quad (3)$$

For laminar liquid-turbulent vapour flow:

$$\phi_L^2 = 1 + \frac{1.45 Re_{LO}^{0.25} We_{LO}^{0.23}}{\chi} + \frac{1}{\chi^2} \quad (4)$$

Lee and Garimella (2008) experimentally investigated two-phase pressure drop in rectangular micro-channels. The measured pressure drop strongly depended on heat flux. The comparisons between the experimental data and the existing correlations were discussed. They also proposed a correlation for pressure drop prediction based on the method by Mishima and Hibiki (1996) as follows.

$$\phi_L^2 = 1 + \frac{2566 G^{0.5466} D_h^{0.8819} \left(1 - e^{-319 D_h}\right)}{\chi_{vv}} + \frac{1}{\chi_{vv}^2} \quad (5)$$

For laminar liquid-laminar vapour flow, the Martinelli parameter is expressed as

$$\chi_{vv} = \left(\frac{1-x}{x}\right)^{0.5} \left(\frac{\rho_G}{\rho_L}\right)^{0.5} \left(\frac{\mu_L}{\mu_G}\right)^{0.5} \quad (6)$$

Choi et al. (2008) performed flow boiling pressure drop experiments. R-410A was used as working fluid flowing in stainless steel tubes with diameters of 1.5 and 3 mm. The results indicated that the two-phase pressure drop increased with the increase in mass flux

DOI: 10.5098/hmt.v3.1.3007 ISSN: 2151-8629

Table 1 Summary of recent investigations on pressure drop during micro-scale flow boiling

Reference	Fluid and parameter ranges G [kg/m^{2}s], q [kW/m^2] P [kPa], T [^{o}C]	Channel geometry/ substrate/orientation/ diameter [mm]	Remarks
Lee and Mudawar (2005)	R-134a G = 127-654, x = 0.001-0.25 q = 316-938 P_{in} = 144-660	53 parallel rectangular/ copper/horizontal/ D_h = 0.35	The proposed correlation incorporated liquid viscosity and surface tension effects.
Lee and Garimella (2008)	water G = 368-738, x = 0-0.2 q = 100-3400 T_{in} = 90.6-95.1	10-60 parallel rectangular/ silicon/horizontal/ D_h = 0.16-0.54	Pressure drop strongly depended on heat flux.
Choi et al. (2008)	R-410A G = 300-600, x = 0-1 q = 10-40 T_{in} = 10	Single circular/stainless steel/horizontal/ D = 1.5, 3	Pressure drop increased with increasing mass flux and vapour quality.
Pamitran et al. (2008)	CO_2 G = 200-600 q = 10-30 T_{sat} = -10, -5, 10	Single circular/stainless steel/horizontal/ D = 1.5, 3	Channel diameter, mass flux, surface tension, density and viscosity had influence on pressure drop.
Agostini et al. (2008)	R-236fa G = 276-992, x = 0.5-1.0 q = 1120-2500 T_{sat} = 20.31-34.27	66 parallel rectangular/ silicon/horizontal/ D_h = 0.336	Homogeneous flow model worked well with the measured pressure drop.
Singh et al. (2008)	water G = 82-126, x = 0.29 q = 290-366	Single rectangular/silicon/ horizontal/ D_h = 0.142	Two-phase pressure drop was found to be lower than the single-phase value when a certain mass flux and heat flux range was established.
Lie et al. (2008)	R-134a, R-407C G = 200-400, x = 0.2-0.8 q = 5-15 T_{sat} = 5-15	28 parallel circular/ copper/horizontal/ D = 0.83, 2	The use of R-134a as working fluid caused pressure drop relatively high in comparison to R-407C
Choi et al. (2009)	C_3H_8 G = 50-400, x = 0-1 q = 5-20 T_{sat} = 0, 5, 10	Single circular/stainless steel/horizontal/ D = 1.5, 3	An increase in mass flux or heat flux resulted in higher pressure drop.
Coppetti et al. (2011)	R-134a G = 240-930, x = 0-0.8 q= 10 – 100 T_{sat} = 12, 22	Single circular/stainless steel/horizontal/ D = 2.62	Pressure drop depended on mass flux and vapour quality.
Soupremanien et al. (2011)	Forane®365 HX G = 200-400, x = 0-0.6 q = 25-62 T_{sat} = 56	Single rectangular/stainless steel/horizontal/ D_h = 1.4	Pressure drop characteristics were affected by aspect ratio.
Costa-Patry et al. (2011)	R-236fa, R-245fa G = 499-1100, x = 0.03-0.53 q = 130-1400 T_{sat} = 30.5	135 parallel rectangular/ silicon/horizontal/ D_h = 0.148	The experimental technique was presented to measure the outlet pressure losses.

and vapour quality. The pressure drop was also strongly dependent on the channel diameter.

The two-phase pressure drop experiments similar to Choi et al. (2008) were carried out by Pamitran et al. (2008). The stainless steel tubes having diameters of 1.5 and 3 mm were used as test sections in which flow vapourization of CO_2 was established. According to their experimental data, the pressure drop was in relation with channel diameter, mass flux, surface tension, density and viscosity.

Agostini et al. (2008) carried out experiments to investigate pressure drop of R-236fa and R-245fa during flow boiling in micro-channels. They reported that flow boiling of R-245fa induced pressure drop higher than R-236fa. The prediction method on the basis of homogeneous flow assumption predicted well their measured results.

Singh et al. (2008) investigated two-phase pressure drop characteristics for flow boiling of water in micro-channels with different aspect ratios. All test sections had rectangular cross-section having a constant hydraulic diameter of 142 μm. The experiments were performed for the aspect ratio range of 1.23 to 3.75. The aspect ratio of around 1.56 provided the minimum two-phase pressure drop. Moreover, at this value of aspect ratio, the two-phase pressure drop was found to be lower than the single-phase value when a certain condition was established as presented in Fig. 3.

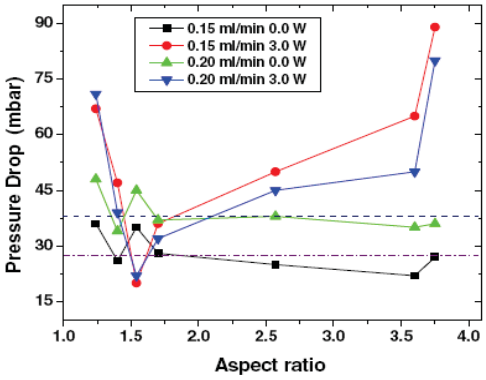

Fig. 3 Pressure drop data of Singh et al. (2008). "Reprinted from Experimental Thermal and Fluid Science, 33(1), Singh, S.G., Kulkarni, A., Duttagupta, S.P., Puranik, B.P., and Agrawal, A., Impact of aspect ratio on flow boiling of water in rectangular microchannels, pp. 153-160 (2008), with permission from Elsevier."

Lie et al. (2008) studied experimentally flow boiling of refrigerants in micro-channels. The frictional pressure drop characteristics of R-134a and R-407C were reported in their work. The results showed the increase in pressure drop with increasing vapour quality and mass flux. The reduction in pressure drop was observed as the saturation temperature was increased. In their study, the pressure drop was less dependent with heat flux. The use of R-134a as working fluid caused pressure drop relatively high in comparison to R-407C. They also proposed pressure drop correlation in the form of friction factor as expressed below.

$$f_{TP} = -0.037 - 147341 Re_{eq}^{-1.859} + 0.039 C_o^{-0.508} + 327726 Re_{eq}^{-1.859} C_o^{-0.508} \quad (7)$$

Re_{eq} in the above equation refers to equivalent Reynolds number expressed as

$$Re_{eq} = \frac{G_{eq} D_h}{\mu_L} \quad (8)$$

The equivalent mass flux, G_{eq}, is determined by

$$G_{eq} = G\left[(1 - x_{in}) + x_{in}\left(\frac{\rho_L}{\rho_G}\right)^{0.5}\right] \quad (9)$$

Pressure drop during flow boiling of propane in horizontal channels was studied by Choi et al. (2009). An increase in mass flux or heat flux resulted in the higher pressure drop. A decrease in channel diameter, corresponding to a higher wall shear stress, leaded to an increase in the pressure drop. They indicated that the lower the saturation temperature, the higher was the pressure drop, which was explained according to the change in density and viscosity. In addition, they developed a pressure drop correlation on the basis of the Lockhart-Martinelli method and the Chisholm parameter was proposed by the following equation.

$$C = 1732.953 Re_{TP}^{-0.323} We_{TP}^{-0.24} \quad (10)$$

Sun and Mishima (2009) analysed 2092 data points collected from several previous studies. They found that in laminar flow region (Re_L < 2000 and Re_G < 2000), the Chisholm parameter was found to be significantly affected by liquid Reynolds number and confinement number, and expressed as follow.

$$C = 26\left(1 + \frac{Re_L}{1000}\right)\left[1 - e^{\left(\frac{-0.153}{0.27C_o + 0.8}\right)}\right] \quad (11)$$

For Re_L > 2000 or Re_G > 2000, the ratio of Re_G to Re_L was found to play dominant role on the Chisholm correlation which was modified as presented below.

$$\phi_L^2 = 1 + \frac{1.79\left(\frac{Re_G}{Re_L}\right)^{0.4}\left(\frac{1-x}{x}\right)^{0.5}}{\chi^{1.19}} + \frac{1}{\chi^2} \quad (12)$$

Zhang et al. (2010) proposed correlations for two-phase flow in micro-channels. The Chisholm parameter needed for pressure drop calculations was correlated by the following equations.

For boiling flow:

$$C = 21\left[1 - e^{\left(\frac{-0.358}{C_o}\right)}\right] \quad (13)$$

For two-phase gas-liquid adiabatic flow:

$$C = 21\left[1 - e^{\left(\frac{-0.674}{C_o}\right)}\right] \quad (14)$$

For two-phase vapour-liquid adiabatic flow:

$$C = 21\left[1 - e^{\left(\frac{-0.142}{C_o}\right)}\right] \quad (15)$$

These correlations were developed based on the method of Mishima and Hibiki (1996). Remarkably, the above correlations are applicable when the experimental conditions comply with the following ranges; 0.014≤ D_h ≤ 6.25 mm, Re_L ≤ 2000 and Re_G ≤ 2000.

Referring to the above three equations, the relevant processes were defined as follows. The gas-liquid adiabatic flow was denoted as two fluids without heat and mass transfers. The vapour-liquid adiabatic flow was dealt only with one fluid appearing in two-phase condition. Flow boiling represented the most complex two-phase flow pertaining to thermal and hydraulic coupling.

The experimental investigation for R-134a refrigerant during flow boiling in a tube having a diameter of 1.75 mm was performed by Saisorn et al. (2010). They reported that the lower liquid viscosity due to the increment of saturation pressure lead to the decrease in frictional pressure drop.

Lee et al. (2010) reported that Bond number and outlet vapour quality played important role on the pressure drop prediction for flow boiling in micro-channels. They also proposed the correlation as seen below.

$$\phi_L^2 = 1 + \frac{121.6\left(1 - e^{-22.7\lambda}\right)x_{out}^{1.85}}{\chi} + \frac{1}{\chi^2} \tag{16}$$

The two-phase pressure drop characteristics in micro-channels were reported by Li and Wu (2010b). Concerning the database containing 769 data points available in the literature, they indicated the significant role of Bond number on the pressure drop prediction, and the Chisholm parameter was modified as follows.

$$C = 11.9B_o^{0.45}; \quad B_o \le 1.5 \tag{17}$$

$$C = 109.4\left(B_o Re_L^{0.5}\right)^{-0.56}; \quad 1.5 < B_o \le 11 \tag{18}$$

For Bond number greater than 11, there was no obvious relationship between the Chisholm parameter and the Bond number. In such region (B_o > 11), however, they recommended the Beattie and Whalley correlation (1982), which is prediction method based on homogeneous flow assumption, as a good choice for predicting the pressure drop. As also reported by Ribatski et al. (2006) and Revellin et al. (2006), the methods on the basis of homogeneous flow model were able to tentatively apply for micro-channels under a certain range of experimental condition. Moreover, the homogeneous flow model was adopted by Chen et al. (2009) and Wang et al. (2010) to predict the pressure drop for two-phase flow through abrupt area change.

The correlation for two-phase pressure change due to sudden expansion in small flow passages was proposed by Wang et al. (2010). With 282 data collected from the literature, their prediction method based on the modified homogeneous model is given by the following equation.

$$\Delta P_e = G^2\sigma_A\left(1-\sigma_A\right)\left[\frac{(1-x)}{\rho_L} + \frac{x}{\rho_G}\right]\left(1+\Omega_1-\Omega_2\right)\left(1+\Omega_3\right) \tag{19}$$

where σ_A represents flow cross-sectional area expansion ratio, 0 < σ_A < 1, and the correction factors, Ω_1, Ω_2, and Ω_3, are expressed as follows.

$$\Omega_1 = \frac{1}{Fr^{0.8}}\left(\frac{We \times B_o}{Re_{LO}}\right)^2\left(\frac{1-x}{x}\right)^{0.3} \tag{20}$$

$$\Omega_2 = 0.2\left(\frac{\mu_G}{\mu_L}\right)^{0.4} \tag{21}$$

$$\Omega_3 = 0.4\left(\frac{x}{1-x}\right)^{0.3} + 0.3e^{\frac{16}{Re_{LO}^{0.1}}} - 0.4\left(\frac{\rho_L}{\rho_G}\right)^{0.2} \tag{22}$$

Instead of using prediction methods, the developed measurement technique, under which flow boiling of R-236fa and R-245fa in rectangular micro-channels having hydraulic diameter of 0.148 mm was studied, was addressed by Costa-Patry et al. (2011) to measure the outlet pressure losses. As presented in Figs. 4 and 5, their measurements indicated that such pressure losses possessed up to 30% of the total pressure drop, tending to be non-negligible.

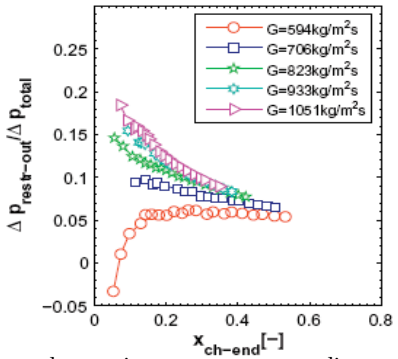

Fig. 4 Pressure drop ratio versus vapour quality at the end of the channel: R-236fa (Costa-Patry et al., 2011). "Reprinted from International Journal of Heat and Fluid Flow, 32(2), Costa-Patry, E., Olivier, J., Nichita, B.A., Michel, B., and Thome, J.R., 2011, Two-phase flow of refrigerants in 85 μm-wide multi-microchannels: Part I – Pressure drop, pp. 451-463 (2011), with permission from Elsevier."

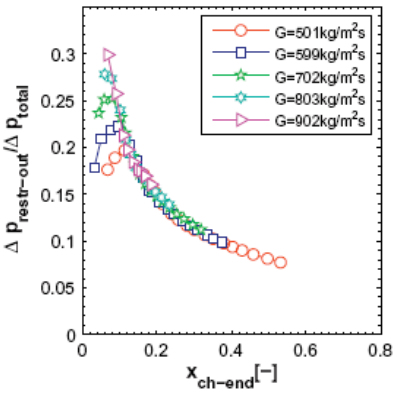

Fig. 5 Pressure drop ratio versus vapour quality at the end of the channel: R-245fa (Costa-Patry et al., 2011). "Reprinted from International Journal of Heat and Fluid Flow, 32(2), Costa-Patry, E., Olivier, J., Nichita, B.A., Michel, B., and Thome, J.R., 2011, Two-phase flow of refrigerants in 85 μm-wide multi-microchannels: Part I – Pressure drop, pp. 451-463 (2011), with permission from Elsevier."

Copetti et al. (2011) reported the two-phase pressure drop results of flow boiling experiment with R-134a flowing in a 2.6 mm diameter tube. The results showed relatively strong dependence of pressure drop on mass flux and vapour quality.

Soupremanien et al. (2011) indicated that aspect ratio had influence on pressure drop characteristics during flow boiling in rectangular channels. The pressure drop became lower as aspect ratio was decreased. In their work, the test sections with the same hydraulic diameter of 1.4 mm were examined.

In summary, this research field is still in its infancy. Although a number of studies have been reported for micro-channels, the pressure drop during micro-scale phenomena with respect to flow boiling mechanisms are still open questions for which systematic answers are of importance. Based on this, further investigations should be performed as follows.

1. Systematic flow boiling experiments should be carried out to obtain the macro-to-micro-scale transition. The threshold of the transition would be addressed according to the dependence of the channel orientation on pressure drop in addition to flow regime and heat transfer characteristics.

Global Digital Central
ISSN: 2151-8629

2. Conduct more investigations for pressure change across inlet and outlet of the micro-channel evaporator to obtain precise prediction methods.
3. The existing models and correlations for two-phase pressure drop prediction should be examined based on different sources of the experimental data
4. Comparisons of flow boiling pressure drop characteristics in parallel channels with those in single channel should be performed under systematic parameters.
5. Void fraction is an important parameter for estimating two-phase pressure drop. Several studies employed the existing correlations, based on ordinarily sized channels, to calculate void fractions which were subsequently used to evaluate the pressure drop in micro-channels. Instead of conventional correlations for macro-scale flow, the prediction method should be developed from the micro-channel flow data. Recently, a small number of investigations were reported for micro-channel void fractions which were experimentally obtained, leading to the correlations. It is noted, however, that the experimental data mainly correspond to adiabatic two-phase gas-liquid flow systems. According to the lacking information, the flow boiling experiments with micro-channels should be designed to obtain the void fraction data for developing an appropriate correlation.
6. Several studies reported that separated flow model predicted well the pressure drop data. In contrast, the homogeneous flow assumption was also found to be in agreement with the measured results as reported by a number of publications. To meet a general conclusion, the systematic experiments during flow boiling in micro-channels should be performed over a wide range of experimental conditions to identify when a given prediction method is applicable to the micro-scale flow boiling.

3. CONCLUSION

Recent studies on pressure drop during micro-scale flow boiling are reviewed in this article to provide information applicable for developing miniature flow devices. Although micro-scale flow has been defined by different criteria, the existing channel classifications cannot relate the channel diameter to the flow boiling mechanisms. On the basis of different previous investigations, the two-phase pressure drop characteristics in micro-channels are not completely compatible with those in ordinarily sized channels. Moreover, the existing two-phase pressure drop predictions are needed to be examined based on different sources of the experimental data.

ACKNOWLEDGEMENTS

The authors would like to express their appreciation to the Thailand Research Fund, KMITL Research Fund, the Office of Higher Education Commission and the National Research University Project for providing financial support.

NOMENCLATURE

B_o	bond number, $B_o = g(\rho_L-\rho_G)D^2/\sigma$
C	Chisholm parameter
C_o	confinement number as defined in Eq.(1)
D	channel diameter (m)
D_b	capillary length (m)
D_h	hydraulic diameter (m)
f	friction factor
G	mass flux (kg/m^2s)
g	gravitational acceleration (m/s^2)
P	pressure (Pa)
ΔP_e	pressure change due to sudden expansion (Pa)
Re	Reynolds number, $Re = GD_h/\mu$
We	Weber number, $We = G^2D_h/\rho\sigma$
x	vapour quality

Greek symbols

χ	Lockhart-Martinelli parameter
ϕ	two-phase multiplier
μ	dynamic viscosity (Ns/m^2)
ρ	density (kg/m^3)
σ	surface tension (N/m)
σ_A	flow cross-sectional area expansion ratio
Ω	correction factors given in Eqs. (20) – (22)

Subscripts

eq	equivalent
G	vapour phase
GO	all-vapour
in	inlet
L	liquid phase
LO	all-liquid
out	outlet
restr-out	outlet restriction
sat	saturation
TP	two-phase
vv	laminar liquid-laminar vapour flow

REFERENCES

Agostini, B., Revellin, R., Thome, J.R., Fabbri, M., Michel, B., Calmi, D., and Kloter, U., 2008, "High heat flux flow boiling in silicon multi-microchannels – Part III: Saturated critical heat flux of R236fa and two-phase pressure drops," *International Journal of Heat and Mass Transfer*, **51**, 5426-5442.
http://dx.doi.org/10.1016/j.ijheatmasstransfer.2008.03.005

Beattie, D.H., and Whalley, P.B., 1982, "Simple two-phase frictional pressure drop calculation method," *International Journal of Multiphase Flow*, **8**, 83-87.
http://dx.doi.org/10.1016/0301-9322(82)90009-X

Chen, I.Y., Tseng, C.-Y., Lin, Y.-T., and Wang, C.-C., 2009, "Two-phase flow pressure change subject to sudden contraction in small rectangular channels," *International Journal of Multiphase Flow*, **35**, 297-306.
http://dx.doi.org/10.1016/j.ijmultiphaseflow.2008.10.008

Choi, K-I., Pamitran, A.S., Oh, C.-Y., and Oh, J.-T., 2008, "Two-phase pressure drop of R-410A in horizontal smooth minichannels," *International Journal of Refrigeration*, **31**, 119-129.
http://dx.doi.org/10.1016/j.ijrefrig.2007.06.006

Choi, K.-I., Pamitran, A.S., Oh, J.-T., and Saito, K., 2009, "Pressure drop and heat transfer during two-phase flow vaporization of propane in horizontal smooth minichannels," *International Journal of Refrigeration*, **32**, 837-845.
http://dx.doi.org/10.1016/j.ijrefrig.2008.12.005

Copetti, J.B., Macagnan, M.H., Zinani, F., and Kunsler, N.L.F., 2011, "Flow boiling heat transfer and pressure drop of R-134a in a mini tube: an experimental investigation," *Experimental Thermal and Fluid Science*, **35**, 636-644.
http://dx.doi.org/10.1016/j.expthermflusci.2010.12.013

Costa-Patry, E., Olivier, J., Nichita, B.A., Michel, B., and Thome, J.R., 2011, "Two-phase flow of refrigerants in 85 μm-wide multi-

microchannels: Part I – Pressure drop," *International Journal of Heat and Fluid Flow*, **32**, 451-463.
http://dx.doi.org/10.1016/j.ijheatfluidflow.2011.01.005

Kandlikar, S.G., 2010, "Scale effects on flow boiling heat transfer in microchannels: A fundamental perspective," *International Journal of Thermal Sciences*, **49**, 1073-1085.
http://dx.doi.org/10.1016/j.ijthermalsci.2009.12.016

Kew, P.A., and Cornwell, K., 1997, "Correlations for the prediction of boiling heat transfer in small-diameter channels," *Applied Thermal Engineering*, **17**, 705-715.
http://dx.doi.org/10.1016/S1359-4311(96)00071-3

Lee, J., and Mudawar, I., 2005, "Two-phase flow in high-heat-flux micro-channel heat sink for refrigeration cooling applications: Part I – pressure drop characteristics," *International Journal of Heat and Mass Transfer*, **48**, 928-940.
http://dx.doi.org/10.1016/j.ijheatmasstransfer.2004.09.018

Lee, P.-S., and Garimella, S.V., 2008, "Saturated flow boiling heat transfer and pressure drop in silicon microchannel arrays," *International Journal of Heat and Mass Transfer*, 51, 789-806.
http://dx.doi.org/10.1016/j.ijheatmasstransfer.2007.04.019

Lee, H.J., Liu, D.Y., Alyousef, Y., and Yao, S., 2010, "Generalized two-phase pressure drop and heat transfer correlations in evaporative micro/minichannels," *Journal of Heat Transfer*, **132**, 1-9.
http://dx.doi.org/10.1115/1.4000861

Li, W., and Wu, Z., 2010a, "A general criterion for evaporative heat transfer in micro/mini-channels," *International Journal of Heat and Mass Transfer*, **53**, 1967-1976.
http://dx.doi.org/10.1016/j.ijheatmasstransfer.2009.12.059

Li, W., and Wu, Z., 2010b, "A general correlation for adiabatic two-phase pressure drop in micro/mini-channels," *International Journal of Heat and Mass Transfer*, **53**, 2732-2739.
http://dx.doi.org/10.1016/j.ijheatmasstransfer.2010.02.029

Lie, Y.M., Su, F.Q., Lai, R.L., and Lin, T.F., 2008, "Experimental study of evaporation pressure drop characteristics of refrigerants R-134a and R-407C in horizontal small tubes," *International Journal of Heat and Mass Transfer*, **51**, 294-301.
http://dx.doi.org/10.1016/j.ijheatmasstransfer.2007.03.046

Mishima, K., and Hibiki, T., 1996, "Some characteristics of air-water two-phase flow in small diameter vertical tubes," *International Journal of Multiphase Flow*, **22**, 703-712.
http://dx.doi.org/10.1016/0301-9322(96)00010-9

Ong, C.L., and Thome, J.R., 2011, "Macro-to-microchannel transition in two-phase flow: Part 1-Two-phase flow patterns and film thickness measurements," *Experimental Thermal and Fluid Science*, **35**, 37-47.
http://dx.doi.org/10.1016/j.expthermflusci.2010.08.004

Pamitran, A.S., Choi, K.-I., Oh, J.-T., and Oh, H.-K., 2008, "Two-phase pressure drop during CO_2 vaporization in horizontal smooth minichannels," *International Journal of Refrigeration*, **31**, 1375-1383.
http://dx.doi.org/10.1016/j.ijrefrig.2008.04.004

Revellin, R., Dupont, V., Ursenbacher, T., Thome, J.R., and Zun, I., 2006, "Characterization of diabatic two-phase flows in microchannels: Flow parameter results for R134a in a 0.5 mm channel," *International Journal of Multiphase Flow*, **32**, 755-774.
http://dx.doi.org/10.1016/j.ijmultiphaseflow.2006.02.016

Ribatski, G., Wojtan, L., and Thome, J.R., 2006, "An analysis of experimental data and prediction methods for two-phase frictional pressure drop and flow boiling heat transfer in micro-scale channels," *Experimental Thermal and Fluid Science*, **31**, 1-19.
http://dx.doi.org/10.1016/j.expthermflusci.2006.01.006

Saisorn, S., Kaew-On, J., and Wongwises, S., 2010, "Flow pattern and heat transfer characteristics of R-134a refrigerant during flow boiling in a horizontal circular mini-channel," *International Journal of Heat and Mass Transfer*, **53**, 4023-4038.
http://dx.doi.org/10.1016/j.ijheatmasstransfer.2010.05.022

Singh, S.G., Kulkarni, A., Duttagupta, S.P., Puranik, B.P., and Agrawal, A., 2008, "Impact of aspect ratio on flow boiling of water in rectangular microchannels," *Experimental Thermal and Fluid Science*, **33**, 153-160.
http://dx.doi.org/10.1016/j.expthermflusci.2008.07.014

Soupremanien, U., Person, S.L., Favre-Marinet, M., and Bultel, Y., 2011, "Influence of the aspect ratio on boiling flows in rectangular mini-channels," *Experimental Thermal and Fluid Science*, **35**, 797-809.
http://dx.doi.org/10.1016/j.expthermflusci.2010.06.014

Sun, L., and Mishima, K., 2009, "Evaluation analysis of prediction methods for two-phase flow pressure drop in mini-channels," *International Journal of Multiphase Flow*, **35**, 47-54.
http://dx.doi.org/10.1016/j.ijmultiphaseflow.2008.08.003

Tibirica, C.B., and Ribatski, G., 2010, "Flow boiling heat transfer of R134a and R245fa in a 2.3 mm tube," *International Journal of Heat and Mass Transfer*, **53**, 2459-2468.
http://dx.doi.org/10.1016/j.ijheatmasstransfer.2010.01.038

Wang, C.-C., Tseng, C.-Y., and Chen, I.Y., 2010, "A new correlation and the review of two-phase flow pressure change across sudden expansion in small channels," *International Journal of Heat and Mass Transfer*, **53**, 4287-4295.
http://dx.doi.org/10.1016/j.ijheatmasstransfer.2010.05.057

Zhang, W., Hibiki, T., and Mishima, K., 2010, "Correlations of two-phase frictional pressure drop and void fraction in mini-channel," *International Journal of Heat and Mass Transfer*, **53**, 453-465.
http://dx.doi.org/10.1016/j.ijheatmasstransfer.2009.09.011

Available online at www.sciencedirect.com

SciVerse ScienceDirect

Journal of the Franklin Institute 349 (2012) 966–984

Journal of The Franklin Institute

www.elsevier.com/locate/jfranklin

A decomposition analysis on convecting–radiating rectangular plate fins for variable thermal conductivity and heat transfer coefficient

Balaram Kundu[a,c], Somchai Wongwises[b,d,*]

[a]*Department of Mechanical Engineering, Jadavpur University, Kolkata 700032, India*
[b]*Fluid Mechanics, Thermal Engineering and Multiphase Flow Research Lab (FUTURE), Department of Mechanical Engineering, King Mongkut's University of Technology Thonburi (KMUTT) Bangmod, Bangkok 10140, Thailand*
[c]*School of Mechanical Engineering, Hanyang University, 17 Haengdang-dong, Sungdong-gu, Seoul, 133-791, Korea*
[d]*The Academy of Science, The Royal Institute of Thailand, Sanam Suea Pa, Dusit, Bangkok 10300, Thailand*

Received 27 February 2011; received in revised form 2 March 2011; accepted 6 December 2011
Available online 13 December 2011

Abstract

The present study concentrates to make a complete thermal analysis on a rectangular fin with its primary surface by taking into consideration of radiation heat exchange with the surrounding along with the convective mode of heat transfer. The one side of the primary surface is heated by a fluid with high temperature which may be required to dissipate heat quickly by a fin array system. To analyze an actual case study, the thermal conductivity of the fin material and convective heat transfer coefficient over the surface are treated as a variable and they are as a function of the local fin surface temperature. With the aforementioned condition, the energy equations for both the fin and primary surface become nonlinear. The decomposition method is suggested to solve these highly nonlinear equations to obtain a closed form temperature distribution. The result of temperature distribution determined by the present analysis is compared with that of the numerical values. With the adaptation of the simplified case, the present method is also compared with the exactly closed form results. From both of these comparisons, an exact matching of results is found. The fin performances, namely, fin efficiency, surface efficiency and augmentation factor are evaluated for a wide range of thermogeometric parameters.

*Corresponding author. Tel.: +66 2 470 9115; fax: +66 2 470 9111.
E-mail addresses: bkundu123@rediffmail.com (B. Kundu), somchai.won@kmutt.ac.th (S. Wongwises).

0016-0032/$32.00 © 2011 The Franklin Institute. Published by Elsevier Ltd. All rights reserved.
doi:10.1016/j.jfranklin.2011.12.002

Nomenclature

A_i	adomian ploynomial
Aug	augmentation factor
Bi	Biot number based on dry surface heat transfer coefficient, $h_0 t/k_{f0}$
g_0, g_1, g_2, g_3	variables, defined in Eq. (20)
h	convective heat transfer coefficient on the fin side, W m^{-2} K^{-1}
h_L	convective heat transfer coefficient on the hot fluid side, W m^{-2} K^{-1}
h_0	constant value of convective heat transfer coefficient on the fin side, W m^{-2} K^{-1}
k	thermal conductivity, W m^{-1} K^{-1}
k_{f0}	thermal conductivity of the fin material corresponding to ambient temperature, W m^{-1} K^{-1}
K_r	thermal conductivity ratio, k_{w0}/k_{f0}
k_{w0}	thermal conductivity of the wall material corresponding to ambient temperature, W m^{-1} K^{-1}
L	length of the fin, m
m_1, m_2, m_3, m_4	parameters see Eqs. (13) and (34)
Nu_L	Nusselt number, $h_L L/k_L$
P	wall length, m
P^*	dimensionless wall length, P/t
q	actual heat transfer rate through the primary surface attached with a fin, W
Q	dimensionless heat transfer rate, see Eq. (25)
q_f	actual heat transfer rate through the fin, W
Q_f	dimensionless heat transfer rate through the fin, see Eq. (29)
q_i	ideal heat transfer rate through the fin-wall system, W
Q_i	dimensionless ideal heat transfer rate, see Eq. (27)
$q_{f\,i}$	ideal heat transfer rate through the fin, W
$Q_{f\,i}$	dimensionless ideal heat transfer rate through the fin, see Eq. (30)
q_0	actual heat transfer rate through the primary surface with considering no fin condition, W
Q_0	dimensionless heat transfer rate, see Eq. (38)
t	semi-fin thickness, m
T_f	Local fin surface temperature ($0 \le x \le L$), K
T_w	Local wall temperature [$L \le x \le (L+w)$], K
T_a	surrounding temperature, K
T_L	hot liquid temperature, K
w	wall thickness, m
x	coordinate, m
X	dimensionless coordinate, x/L
Z_0	dimensionless fin parameter, $\sqrt{Bi}/\psi$

Greek letters

α	coefficient of thermal conductivity, K^{-1}
β	dimensionless variable thermal conductivity parameter, $(T_L - T_a)\alpha$

γ	Temperature ratio, T_L/T_a
δ	dimensionless temperature factor, $T_a/(T_L-T_a)$
ε	dimensionless radiation parameter, $\sigma\varepsilon'(T_L-T_a)^3/h_0$
ε'	emissivity of the fin material
η	surface efficiency
η_f	fin efficiency
λ	variable, see Eq. (28)
σ	Boltzmann constant, W m^{-2} K^{-4}
θ	dimensionless fin temperature, $(T_f-T_a)/(T_L-T_a)$
θ_0	dimensionless tip temperature
τ	dimensionless base temperature
ϕ	dimensionless wall temperature, $(T_w-T_a)/(T_L-T_a)$
Φ	dimensionless wall temperature when there is no fin attached, $(T'_w-T_a)/(T_L-T_a)$
ψ	aspect ratio, t/L
ω	dimensionless wall thickness, w/L

Subscripts

f	fin
w	wall

1. Introduction

The transfer of heat from a heated fluid to surrounding is essentially needed to avoid overheating of the apparatus in industrial applications. A hot fluid flowing through a passage separated it from surrounding air by a solid wall. As the heat transfer coefficient in the air side is low, fins or extended surfaces are attached to the wall to enhance the heat transfer rate. If the hot fluid temperature is very high heat dissipation from the wall and fin surfaces takes place not only due to convection but also radiation mode of heat transfer. Only fin surface is never used in practice. A fin with the attachment of supporting structure, known as fin-wall assembly, is commonly used. To account for the effect of supporting structure, the analysis becomes complicated.

Sparrow and Le [1] studied in a multi-fin array in order to determine the temperature distribution at the fin base and heat flux. Using finite difference formulation Suryanarayana [2] analyzed the heat transfer in an array of longitudinal rectangular fins with insulated tip. Heggs and Stone [3] determined the performance of fin assemblies of longitudinal and annular fins of uniform cross-section. They have used one- and two-dimensional formulation for comparison. In the one-dimensional model, the overall resistance of the fin wall was determined by the analogy of electrical net work. In the two-dimensional analysis, a numerical technique was adopted for obtaining the temperature distribution both in the wall and in the fin. A significant difference between the results predicted by the two types of analysis has been reported. Heggs et al. [4] proposed a semi-analytical solution to evaluate the temperature distribution in the fin array. Recently, performance and optimum design analysis of convective fin arrays attached to

flat and curved primary surfaces has been carried out by Kundu and Das [5]. By an analytical determination, the performance of a fin assembly under dehumidifying conditions was determined by Kundu and Miyara [6] and results have been presented in a comparative ways.

Chung and Zhung [7] demonstrated a novel design for a radiative fin array system. An analysis of heat transfer in rectangular fin arrays was conducted by Elazhary and Soliman [8] with taking into consideration of convection and radiation. The analysis was done based on diffuse nongray surfaces. From the result, they highlighted that convection is more effective mode of heat transfer in fin arrays and the effectiveness of the array decreases as the contribution of the radiative component increases. Recently, Kundu and Aziz [9] determined numerically the performance of a convectively heated rectangular fin with a step change in cross-sectional area when losing heat by simultaneous convection and radiation. Aziz and Khani [10] established an analytic model based on the homototopy analysis method (HAM) for heat transfer in a moving fin of variable thermal conductivity which is losing heat by simultaneous convection and radiation to its surroundings. With the correlation of the fin profile and temperature distribution, the nonlinear heat transfer equation for convective–radiative spines was integrated analytically [11].

From the literature survey mentioned in a summarized way above, a very few works has been devoted to analyze fin-array heat transfer with considering radiation heat exchange. In general, if the supporting wall temperature is high, radiation heat transfer from the supporting wall and fin surfaces cannot be ignored. Due to high temperature variation, thermal conductivity of the wall and fin materials may not be a constant. In addition, there is always possibility to have variable heat transfer coefficients along the fin surface. These have been made to motivate for carrying out the present analysis.

An approximate analytical model has been established to analyze heat transfer through a fin of rectangular fin attached with a flat primary surface. For the analysis, three modes of heat transfer are taken into account. A variable thermal conductivity of the fin as well as wall material has been adopted. The convective heat transfer coefficient is as a power function of temperature taken for an actual analysis. A decomposition method has been applied to solve the governing fin and supporting structure equations to determine the temperature distributions. The surface efficiency and augmentation factor are evaluated. The effects of thermophysical and radiation parameters on fin–wall performances are exhibited.

2. Analysis

A schematic diagram of a plate fin with primary surface is shown in Fig. 1. The present work considers combined convection and radiation modes of heat transfer from a fin of rectangular profile attached to a flat base which is heated by hot liquid with a constant temperature, T_L and convective heat transfer coefficient, h_L. The rectangular fins are attached with the primary surface to the gas side in order to increase the heat transfer rate. The surface temperature of the fin and wall is so high that the radiation mode of heat transfer cannot be neglected. However, there is negligible interaction of radiation heat assumed between wall and fin surfaces. For the high fin surface temperature, variable thermal conductivity is considered. The heat is rejected from the fin surface to the surrounding fluid with a constant temperature T_a. The heat transfer coefficient over the fin surface changes and it is a function of local fin surface temperature. The energy balance

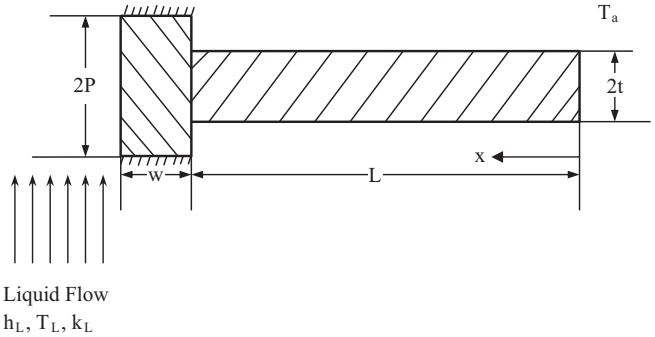

Fig. 1. Diagram of a fin attached with a primary surface.

equation for differential elements of fins and the primary surface for one-dimensional heat conduction is given as

$$\begin{bmatrix} d/dx(k_w dT_w/dx) \\ d/dx(k_f dT_f/dx) - h(T_f - T_a)/t - \sigma\varepsilon_f'(T_f^4 - T_a^4)/t \end{bmatrix} = \begin{bmatrix} 0 \\ 0 \end{bmatrix} \quad \begin{matrix} L \le x \le (L+w) \\ 0 \le x \le L \end{matrix} \tag{1a,1b}$$

The variable thermal conductivity and heat transfer coefficient are assumed in the following:

$$k_f = k_{f0}[1 + \alpha_f(T_f - T_a)]; \quad k_w = k_{w0}[1 + \alpha_w(T_w - T_a)]; \quad h = h_0\theta^n \tag{2}$$

Eq. (1) can be written by Eq. (2) in dimensionless form as

$$\begin{bmatrix} (1+\beta_w\phi)d^2\phi/dX^2 + \beta_w(d\phi/dX)^2 \\ d^2\theta/dX^2 + \beta_f(d\theta/dX)^2 + \beta_f\theta(d^2\theta/dX^2) - Z_0^2\theta(\theta^n + 4\delta^3\varepsilon_f + 6\delta^2\varepsilon_f\theta + 4\delta\varepsilon_f\theta^2 + \varepsilon_f\theta^3) \end{bmatrix} = \begin{bmatrix} 0 \\ 0 \end{bmatrix} \text{for} \quad \begin{matrix} 1 \le X \le (1+\omega) \\ 0 \le X \le 1 \end{matrix} \tag{3a,3b}$$

where

$$\beta_w = \alpha_w(T_L - T_a); \quad \beta_f = \alpha_f(T_L - T_a); \quad Z_0 = \sqrt{Bi}/\psi; \quad Bi = h_0 t/k_{f0};$$
$$\psi = t/L; \quad \gamma = T_L/T_a; \quad \delta = 1/(\gamma - 1); \quad \varepsilon_f = \sigma(T_L - T_a)^3\varepsilon_f'/h_0;$$
$$\varepsilon_w = \sigma(T_L - T_a)^3\varepsilon_w'/h_0; \quad X = x/L; \quad \theta = (T_f - T_a)/(T_L - T_a);$$
$$\text{and} \quad \varphi = (T_w - T_a)/(T_L - T_a) \tag{4}$$

Eq. (3) is subjected to the following boundary conditions:

$$\text{at } X = 0, \quad d\theta/dX = 0 \tag{5a}$$

$$\text{at } X = 1, \quad \theta = \phi \tag{5b}$$

$$\text{at } X = 1, \quad (1+\beta_f\theta)\psi d\theta/dX + Bi(P^* - 1)\theta^{n+1} + Bi\varepsilon_w\phi(P^* - 1)(4\delta^3 + 6\delta^2\varphi + 4\delta\phi^2 + \phi^3) = K_r P^*\psi(1+\beta_w\phi)d\phi/dX \tag{5c}$$

and

$$\text{at } X = 1 + \omega, \quad d\phi/dX = Nu_L(1 - \phi) \tag{5d}$$

where

$$Nu_L = h_L L/k_L; \quad P^* = P/t; \quad \text{and} \quad K_r = k_{w0}k_{f0} \tag{6}$$

The wall temperature can be determined from Eq. (3a) by integrating

$$\beta_w \phi^2 + 2\phi - (m_1 X + m_2) = 0 \tag{7}$$

where m_1 and m_2 are constants determined from boundary conditions. The above equation is a quadratic equation and thus the temperature ϕ can be determined directly. However, for smaller values of β_w, it may not give correct result due to β_w in denominator. Alternatively, the temperature ϕ can be determined by the decomposition method [12] which can give exact results whatever β_w value is selected in the design process. Eq. (7) can be expressed in the following:

$$\phi = (m_1 X + m_2)/2 - (\beta_w/2)\phi^2 \tag{8}$$

The Adomian method consists of calculating ϕ as an infinite series

$$\phi = \sum_{i=0}^{\infty} \phi_i \tag{9}$$

The nonlinear function ϕ^2 is decomposed as

$$\theta^2 = \sum_{i=0}^{\infty} A_i \tag{10}$$

where the Adomian polynomials A_i's are given by

$$A_n(\theta_0, \theta_1, \cdots, \theta_m) = (1/m!) = (d^m/d\zeta^m)\theta^2 \left(\sum \theta_m \zeta^m \right)\Big|_{\zeta = 0} \tag{11}$$

From Eqs. (10) and (11), the Adomian polynomials are written in the following:

$$\begin{aligned} &\begin{bmatrix} A_0 & A_1 & A_2 & A_3 & A_4 & \cdots \end{bmatrix} \\ &\quad = \begin{bmatrix} \varphi_0^2 & 2\phi_0\phi_1 & 2\phi_0\phi_2 + \phi_1^2 & 2\phi_0\phi_3 + 2\phi_1\phi_2 & 2\phi_0\phi_4 + 2\phi_1\phi_3 + \phi_2^2 & \cdots \end{bmatrix} \end{aligned} \tag{12}$$

Using Eqs. (8), (9) and (12), temperature profile in the supporting structure can be written as

$$\begin{aligned} \phi = (m_1 X + m_2) \Bigg[1 - \frac{\beta_w}{2}(m_1 X + m_2) + \frac{\beta_w^2}{2}(m_1 X + m_2)^2 - \frac{5\beta_w^3}{8}(m_1 X + m_2)^3 \\ + \frac{7\beta_w^4}{8}(m_1 X + m_2)^4 - \frac{21\beta_w^5}{16}(m_1 X + m_2)^5 + \cdots \Bigg] \quad (1 \le X \le 1 + \omega) \end{aligned} \tag{13}$$

The temperature distribution in the fin is obtained from Eq. (3b) which is highly nonlinear. For its solution, decomposition method can be employed. To avoid in calculating Adomian polynomials in the Adomian decomposition method, Shang et al. [13] and Biazar et al. [14] implemented variational iteration method (VIM) to solve linear and nonlinear equations. For solving quadratic Riccati differential equations, Legendre wavelet method [15,16] is advantageous because of a fast convergent series of easily computable components found. However, the solution of nonlinear equations with

adopting Adomian decomposition method is still a great interest as convergence becomes rapidly. Introducing the operator $L_X = d^2/dX^2$, Eq. (3b) takes the form below for the Adomian decomposition method

$$L_X\theta = Z_0^2\theta(\theta^n + 4\delta^3\varepsilon_f + 6\delta^2\varepsilon_f\theta + 4\delta\varepsilon_f\theta^2 + \varepsilon_f\theta^3) - \beta_f(d\theta/dX)^2 - \beta_f\theta(d^2\theta/dX^2) \tag{14}$$

Applying inverse operator L_X^{-1} to both sides of Eq. (14) and boundary condition (5a) yields

$$\theta = \theta_0 + Z_0^2 L_X^{-1}[\theta(\theta^n + 4\delta^3\varepsilon_f + 6\delta^2\varepsilon_f\theta + 4\delta\varepsilon_f\theta^2 + \varepsilon_f\theta^3)] - \beta_f L_X^{-1}[(d\theta/dX)^2] - \beta_f L_X^{-1}[\theta(d^2\theta/dX^2)] \tag{15}$$

Three terms of right-hand side in Eq. (15) are nonlinear and they can be decomposed by Adomian polynomials (A_j, B_j and C_j for $j = 0,1,\cdots,\infty$). The temperature terms can then be written in the following:

$$\begin{bmatrix} \theta_1 \\ \theta_2 \\ \vdots \\ \theta_m \end{bmatrix} = \begin{bmatrix} Z_0^2 L_X^{-1} A_0 - \beta_f L_X^{-1} B_0 - \beta_f L_X^{-1} C_0 \\ Z_0^2 L_X^{-1} A_1 - \beta_f L_X^{-1} B_1 - \beta_f L_X^{-1} C_1 \\ \vdots \\ Z_0^2 L_X^{-1} A_{m-1} - \beta_f L_X^{-1} B_{m-1} - \beta_f L_X^{-1} C_{m-1} \end{bmatrix} \tag{16}$$

The Adomian polynomials are computed as follows:

$$\begin{aligned} A_0 &= \theta_0^{n+1} + 6\delta^2\varepsilon_f\theta_0^2 + 4\delta\varepsilon_f\theta_0^3 + \varepsilon_f\theta_0^4; \quad A_1 = Z_0^2\theta_0^2 g_0 g_1 X^2/2!; \\ A_2 &= Z_0^2\theta_0^2 g_0[-\beta_f\theta_0 g_1 X^2/2! + g_1 Z_0^2(4\delta^3\varepsilon_f + \theta_1 g_1 + 3Z_0^2 g_0 g_2)X^4/4!]; \\ A_3 &= \beta_f^2 g_0 g_1 Z_0^2\theta_0^4 X^2/2! - \beta_f Z_0^4\theta_0^3 g_0(3g_0 g_1 + 2\theta_0 g_1^2 + 8\delta^3\varepsilon_f g_1 + 6g_0 g_2)X^4/4! \\ &\quad + Z_0^6 g_0\theta_0^2\lfloor g_1(4\delta^3\varepsilon_f + \theta_0 g_1)^2 + 3\theta_0 g_0 g_1 g_2 + 15g_0 g_2(4\delta^3\varepsilon_f + \theta_0 g_1) \\ &\quad + 15\theta_0 g_0^2 g_3]X^6/6!; \cdots \end{aligned} \tag{17}$$

$$\begin{aligned} &B_0 = 0; \quad B_1 = 0; \quad B_2 = 2Z_0^4\theta_0^2 g_0^2 X^2/2!; \\ &B_3 = -4\beta_f Z_0^4\theta_0^3 g_0^2 X^2/2! + 8Z_0^6 g_0^2\theta_0^2(4\delta^3\varepsilon_f + \theta_0 g_1)X^4/4!; \cdots \end{aligned} \tag{18}$$

and

$$\begin{aligned} &C_0 = 0; \quad C_1 = Z_0^2\theta_0^2 g_0; \quad C_2 = -\beta_f Z_0^2\theta_0^3 g_0 + Z_0^4 g_0\theta_0^2(g_0 + \theta_0 g_1 + 4\delta^3\varepsilon_1)X^2/2; \\ &C_3 = \beta_f^2 Z_0^2\theta_0^3 g_0 - \beta_f Z_0^6 g_0\theta_0^3(5g_0 + 8\delta^3\varepsilon_f + 2\theta_0 g_1)X^2/2! + Z_0^6 g_0\theta_0^2\lfloor 28\delta^3\varepsilon_f g_0 + 7\theta_0 g_0 g_1 \\ &\quad + (4\delta^3\varepsilon_f + \theta_0 g_1)^2 + 3\theta_0 g_0 g_2]X^4/4! \end{aligned} \tag{19}$$

where

$$\begin{bmatrix} g_0 \\ g_1 \\ g_2 \\ g_3 \end{bmatrix} = \begin{bmatrix} 4\delta^3\varepsilon_f + \theta_0^n + 6\delta^2\varepsilon_f\theta_0 + 4\delta\varepsilon_f\theta_0^2 + \varepsilon_f\theta_0^3 \\ (n+1)\theta_0^{n-1} + 12\delta^2\varepsilon_f + 12\delta\varepsilon_f\theta_0 + 4\varepsilon_f\theta_0^2 \\ (n+1)n\theta_0^{n-1} + 12\delta^2\varepsilon_f + 24\delta\varepsilon_f\theta_0 + 12\varepsilon_f\theta_0^2 \\ (n+1)n(n-1)\theta_0^{n-2} + 24\delta\varepsilon_f + 24\varepsilon_f\theta_0 \end{bmatrix} \tag{20}$$

The temperature terms can be determined from Eq. (16) using Adomian polynomials as

$$\theta_1 = Z_0^2 g_0 \theta_0 X^2/2! \tag{21a}$$

$$\theta_2 = -\beta_f Z_0^2 \theta_0^2 g_0 X^2/2! + Z_0^4 g_0 \theta_0 (4\delta^3 \varepsilon_f + \theta_0 g_1) X^4/4! \tag{21b}$$

$$\begin{aligned}\theta_3 = {} & \beta_f^2 Z_0^2 g_0 \theta_0^3 X^2/2! - \beta_f Z_0^4 g_0 \theta_0^2 (3g_0 + 2\theta_0 g_1 \\ & + 8\delta^3 \varepsilon_f) X^4/4! + Z_0^6 g_0 \theta_0 \lfloor (4\delta^3 \varepsilon_f + \theta_0 g_1)^2 + 3\theta_0 g_0 g_2 \rfloor X^6/6\,!\end{aligned} \tag{21c}$$

$$\begin{aligned}\theta_4 = {} & \beta_f^3 Z_0^2 g_0 \theta_0^4 X^2/2! + 3\beta_f^2 Z_0^4 g_0 \theta_0^3 (3g_0 + \theta_0 g_1 + 4\delta^3 \varepsilon_f) X^4/4! \\ & - 3\beta_f Z_0^6 \theta_0^2 g_0 (24\delta^3 \varepsilon_f g_0 + 8\delta^3 \varepsilon_f \theta_0 g_1 + 16\delta^6 \varepsilon_f^2 + 8\theta_0 g_0 g_1 + \theta_0^2 g_1^2 + \theta_0 g_0 g_2) X^6/6! \\ & + Z_0^8 \theta_0 g_0 (64\delta^9 \varepsilon_f^3 + 48\delta^6 \varepsilon_f^2 \theta_0 g_1 + 12\delta^3 \varepsilon_f \theta_0^2 g_1^2 + 72\delta^3 \varepsilon_f \theta_0 g_0 g_2 + \theta_0^3 g_1^3 \\ & + 18\theta_0^2 g_0 g_1 g_2 + 15\theta_0^2 g_0^2 g_3) X^8/8! \\ & \vdots \quad = \quad \vdots\end{aligned} \tag{21d}$$

Thus the temperature distribution in fins is

$$\begin{aligned}\theta = {} & Z_0^2 g_0 \theta_0 (1 - \beta_f \theta_0 + \beta_f^2 \theta_0^2 + \beta_f^3 \theta_0^3 + \cdots) X^2/2! \\ & + Z_0^4 g_0 \theta_0 [4\delta^3 \varepsilon_f + \theta_0 g_1 - \beta_f \theta_0 (3g_0 + 2\theta_0 g_1 + 8\delta^3 \varepsilon_f) \\ & + 3\beta_f^2 \theta_0^2 (3g_0 + \theta_0 g_1 + 4\delta^3 \varepsilon_f) + \cdots] X^4/4! \\ & + Z_0^6 g_0 \theta_0 \lfloor (4\delta^3 \varepsilon_f + \theta_0 g_1)^2 + 3\theta_0 g_0 g_2 - 3\beta_f \theta_0 (24\delta^3 \varepsilon_f g_0 + 8\delta^3 \varepsilon_f \theta_0 g_1 + 16\delta^6 \varepsilon_f^2 \\ & + 8\theta_0 g_0 g_1 + \theta_0^2 g_1^2 + \theta_0 g_0 g_2) + \cdots] X^6/6! \\ & + Z_0^8 \theta_0 g_0 (64\delta^9 \varepsilon_f^3 + 48\delta^6 \varepsilon_f^2 \theta_0 g_1 + 12\delta^3 \varepsilon_f \theta_0^2 g_1^2 + 72\delta^3 \varepsilon_f \theta_0 g_0 g_2 + \theta_0^3 g_1^3 \\ & + 18\theta_0^2 g_0 g_1 g_2 + 15\theta_0^2 g_0^2 g_3) X^8/8! + \cdots\end{aligned} \tag{22}$$

The temperature distribution in fin assemblies expressed in Eqs. (13) and (22) are unknown constants m_1 and m_2 in supporting structure energy equation and θ_0 in fin energy equation. These three unknown can be determined using boundary conditions (5b)–(5d). For a tip temperature θ_0, it is to calculate the fin base temperature from Eqs. (13) and (22) and then equating to ease other, the following expression can be obtained:

$$\begin{aligned}& (m_1 + m_2)\left[1 - \frac{\beta_w}{2}(m_1 + m_2) + \frac{\beta_w^2}{2}(m_1 + m_2)^2 - \frac{5\beta_w^3}{8}(m_1 + m_2)^3 + \frac{7\beta_w^4}{8}(m_1 + m_2)^4 - \frac{21\beta_w^5}{16}(m_1 + m_2)^5 + \cdots\right] \\ & - Z_0^2 g_0 \theta_0 (1 - \beta_f \theta_0 + \beta_f^2 \theta_0^2 + \beta_f^3 \theta_0^3 + \cdots) 1/2! - Z_0^4 g_0 \theta_0 [4\delta^3 \varepsilon_f + \theta_0 g_1 - \beta_f \theta_0 (3g_0 + 2\theta_0 g_1 + 8\delta^3 \varepsilon_f) \\ & + 3\beta_f^2 \theta_0^2 (3g_0 + \theta_0 g_1 + 4\delta^3 \varepsilon_f) + \cdots] 1/4! - Z_0^6 g_0 \theta_0 [(4\delta^3 \varepsilon_f + \theta_0 g_1)^2 + 3\theta_0 g_0 g_2 - 3\beta_f \theta_0 (24\delta^3 \varepsilon_f g_0 \\ & + 8\delta^3 \varepsilon_f \theta_0 g_1 + 16\delta^6 \varepsilon_f^2 + 8\theta_0 g_0 g_1 + \theta_0^2 g_1^2 + \theta_0 g_0 g_2) + \cdots] 1/6! - Z_0^8 \theta_0 g_0 (64\delta^9 \varepsilon_f^3 + 48\delta^6 \varepsilon_f^2 \theta_0 g_1 \\ & + 12\delta^3 \varepsilon_f \theta_0^2 g_1^2 + 72\delta^3 \varepsilon_f \theta_0 g_0 g_2 + \theta_0^3 g_1^3 + 18\theta_0^2 g_0 g_1 g_2 + 15\theta_0^2 g_0^2 g_3) 1/8! + \cdots = 0\end{aligned} \tag{23}$$

From boundary condition (5d), one can write

$$\begin{aligned}& \left[m_1 - \beta_w m_1 (m_1 + m_2 + m_1 \omega) + \frac{3\beta_w^2 m_1}{2}(m_1 + m_2 + m_1 \omega)^2 - \frac{5\beta_w^3 m_1}{2}(m_1 + m_2 + m_1 \omega)^3\right. \\ & \left. + \frac{35\beta_w^4 m_1}{8}(m_1 + m_2 + m_1 \omega)^4 - \frac{63\beta_w^5 m_1}{8}(m_1 + m_2 + m_1 \omega)^5 + \cdots\right] \\ & + Nu_L (m_1 + m_2 + m_1 \omega)\left[1 - \frac{\beta_w}{2}(m_1 + m_2 + m_1 \omega) + \frac{\beta_w^2}{2}(m_1 + m_2 + m_1 \omega)^2\right.\end{aligned}$$

$$-\frac{5\beta_w^3}{8}(m_1+m_2+m_1\omega)^3+\frac{7\beta_w^4}{8}(m_1+m_2+m_1\omega)^4-\frac{21\beta_w^5}{16}(m_1+m_2+m_1\omega)^5+\cdots\Big]$$

$$-Nu_L=0 \tag{24}$$

A generalized Newton–Raphson method can be used to solve Eqs. (23) and (24) simultaneously to determine the unknown constants, m_1 and m_2 for a guess value of θ_0. Using boundary condition (5c), tip temperature θ_0 is evaluated from the previously calculated m_1 and m_2. The final values of these unknowns are estimated by iteration.

The actual heat transfer rate through the fin-supporting structure system is obtained by applying Fourier's law of heat conduction at the liquid side of the primary surface and it can be written in dimensionless form as

$$Q=\frac{q}{2k_{w0}(T_L-T_a)}=P^*\psi(1+\beta_w\phi_{X=1+\omega})\frac{d\phi}{dX}\Big|_{X=1+\omega} \tag{25}$$

Eq. (25) is expanded using Eq. (13) as

$$\begin{aligned}Q=P^*\psi\Big\{&1+\beta_w[m_1(1+\omega)+m_2]-\frac{\beta_w^2}{2}[m_1(1+\omega)+m_2]^2+\frac{\beta_w^3}{2}[m_1(1+\omega)+m_2]^3\\&-\frac{5\beta_w^4}{8}[m_1(1+\omega)+m_2]^4+\frac{7\beta_w^5}{8}[m_1(1+\omega)+m_2]^5-\frac{21\beta_w^6}{16}[m_1(1+\omega)+m_2]^6\Big\}\\&\times\Big\{m_1-\beta_w m_1[m_1(1+\omega)+m_2]+\frac{3\beta_w^2m_1}{2}[m_1(1+\omega)+m_2]^2\\&-\frac{5\beta_w^3m_1}{2}[m_1(1+\omega)+m_2]^3+\frac{35\beta_w^4m_1}{8}[m_1(1+\omega)+m_2]^4\\&-\frac{63\beta_w^5m_1}{8}[m_1(1+\omega)+m_2]^5\Big\}+\cdots\end{aligned} \tag{26}$$

The ideal heat transfer rate through the fin system can be determined by assuming the entire fin–wall surfaces maintaining a uniform temperature which is assumed to be equal to the wall temperature adjacent to the liquid. Mathematically, the ideal heat transfer rate can be expressed in dimensionless form as

$$\begin{aligned}Q_i=\frac{q_i}{2k_{w0}(T_L-T_a)}&=Bi(P^*-1)\left[\lambda^{n+1}+\varepsilon_w\lambda\,(4\delta^3+6\delta^2\lambda+4\delta\lambda^2+\lambda^3)\right]'\\&+\frac{Bi}{\psi}\left[\lambda^{n+1}+\varepsilon_f\lambda(4\delta^3+6\delta^2\lambda+4\delta\lambda^2+\lambda^3)\right]\end{aligned} \tag{27}$$

where

$$\begin{aligned}\lambda=&[m_1(1+\omega)+m_2]-\frac{\beta_w}{2}[m_1(1+\omega)+m_2]^2+\frac{\beta_w^2}{2}[m_1(1+\omega)+m_2]^3\\&-\frac{5\beta_w^3}{8}[m_1(1+\omega)+m_2]^4+\frac{7\beta_w^4}{8}[m_1(1+\omega)+m_2]^5-\frac{21\beta_w^5}{16}[m_1(1+\omega)+m_2]^6+\cdots\end{aligned} \tag{28}$$

The actual heat transfer rate through a fin can be calculated from the following expression:

$$\begin{aligned}Q_f=\frac{q_f}{2k_{w0}(T_L-T_a)}=\psi(1+\beta_f\tau)K_r\Big\{&Z_0^2g_0\theta_0(1-\beta_f\theta_0+\beta_f^2\theta_0^2+\beta_f^3\theta_0^3+\cdots)\\&+Z_0^4g_0\theta_0[4\delta^3\varepsilon_f+\theta_0g_1-\beta_f\theta_0(3g_0+2\theta_0g_1+8\delta^3\varepsilon_f)+3\beta_f^2\theta_0^2(3g_0+\theta_0g_1+4\delta^3\varepsilon_f)\end{aligned}$$

$$+\cdots]1/3! + Z_0^6 g_0\theta_0[(4\delta^3\varepsilon_f + \theta_0 g_1)^2 + 3\theta_0 g_0 g_2 - 3\beta_f\theta_0(24\delta^3\varepsilon_f g_0 + 8\delta^3\varepsilon_f\theta_0 g_1 + 16\delta^6\varepsilon_f^2 + 8\theta_0 g_0 g_1 + \theta_0^2 g_1^2 + \theta_0 g_0 g_2) + \cdots]1/5! + Z_0^8\theta_0 g_0(64\delta^9\varepsilon_f^3 + 48\delta^6\varepsilon_f^2\theta_0 g_1 + 12\delta^3\varepsilon_f\theta_0^2 g_1^2 + 72\delta^3\varepsilon_f\theta_0 g_0 g_2 + \theta_0^3 g_1^3 + 18\theta_0^2 g_0 g_1 g_2 + 15\theta_0^2 g_0^2 g_3)1/7! + \cdots\} \quad (29)$$

where τ is the temperature at the fin base. It can be determined from Eq. (22) by putting $X=1$.

The ideal heat transfer rate through a fin is determined from the following equation:

$$Q_{fi} = \frac{q_{fi}}{2k_{w0}(T_L - T_a)} = \frac{BiK_r\tau}{\psi}\left[\tau^n + \varepsilon_f(4\delta^3 + 6\delta^2\tau + 4\delta\tau^2 + \tau^3)\right] \quad (30)$$

Thus from definition of fin efficiency yields

$$\eta_f = Q/Q_{fi} \quad (31)$$

The performance of a fin attached with the primary surface is conveniently expressed by augmentation factor. It is defined as the ratio of the heat transfer rate to that of the unfinned wall operating under the same condition. The heat transfer rate through the unfinned wall can be determined from the following mathematical steps:

The governing equation in the unfinned wall is given by

$$(1 + \beta_w\Phi)d^2\Phi/dX^2 + \beta_w(d\Phi/dX)^2 = 0 \quad \text{for } 0 \le X \le \omega \quad (32)$$

For the solution of Eq. (32), the following boundary conditions are taken:

$$\text{at } X = 0, \quad (1 + \beta_w\Phi)\frac{d\Phi}{dX} = \frac{Bi}{\psi}\left[\Phi^{n+1} + \varepsilon_w\Phi(4\delta^3 + 6\delta^2\Phi + 4\delta\Phi^2 + \Phi^3)\right] \quad (33a)$$

and

$$\text{at } X = \omega, \quad \frac{d\Phi}{dX} = Nu_L(1-\Phi) \quad (33b)$$

By solving Eq. (32), the following temperature distribution can be obtained:

$$\Phi = (m_3X + m_4)\left[1 - \frac{\beta_w}{2}(m_3X + m_4) + \frac{\beta_w^2}{2}(m_3X + m_4)^2 - \frac{5\beta_w^3}{8}(m_3X + m_4)^3 + \frac{7\beta_w^4}{8}(m_3X + m_4)^4 - \frac{21\beta_w^5}{16}(m_3X + m_4)^5 + \cdots\right] \quad (0 \le X \le \omega) \quad (34)$$

The integration constants m_3 and m_4 are determined from boundary conditions (33). The temperature at $X=0$, Φ_0, is calculated first from Eq. (34) by assuming suitable m_4 value

$$\Phi_0 = m_4 - \beta_w m_4^2/2 + \beta_w^2 m_4^3/2 - 5\beta_w^3 m_4^4/8 + 7\beta_w^4 m_4^5/8 - 21\beta_w^5 m_4^6/16 + \cdots \quad (35)$$

From Eqs. (33a) and (33b), one can get

$$m_3 = \frac{Bi\lfloor\Phi_0^{n+1} + \varepsilon_w\Phi_0(4\delta^3 + 6\delta^2\Phi_0 + 4\delta\Phi_0^2 + \Phi_0^3)\rfloor}{\psi(1 + \beta_w\Phi_0)(1 - \beta_w m_4 + 3\beta_w^2 m_4^2/2 - 5\beta_w^3 m_4^3/2 + 35\beta_w^4 m_4^4/8 - 63\beta_w^5 m_4^5/8 + \cdots)} \quad (36)$$

and

$$m_3[1 - \beta_w(m_3\omega + m_4) + 3\beta_w^2(m_3\omega + m_4)^2/2 - 5\beta_w^3(m_3\omega + m_4)^3/2 + 35\beta_w^4(m_3\omega + m_4)^4/8 - 63\beta_w^5(m_3\omega + m_4)^5/8] - Nu_L[1 - m_3\omega - m_4 + \beta_w(m_3\omega + m_4)^2/2 - \beta_w^2(m_3\omega + m_4)^3/2 + 5\beta_w^3(m_3\omega + m_4)^4/8 - 7\beta_w^4(m_3\omega + m_4)^5/8 + 21\beta_w^5(m_3\omega + m_4)^6/16 - \cdots] = 0 \quad (37)$$

In order to determine the constant m_4, Eq. (37) can be solved by Newton–Raphson iterative method and final m_3 and m_4 are obtained by simultaneous solution of Eqs. (35)–(37) iteratively.

The actual heat transfer rate through unfinned wall can be evaluated from the following expression:

$$Q_0 = \frac{q_0}{2k_{w0}(T_L - T_a)} = P^*\psi\, m_3(1 + \beta_w m_4 - \beta_w^2 m_4^2/2 + \beta_w^3 m_4^3/2 - 5\beta_w^4 m_4^4/8 + 7\beta_w^5 m_4^5/8 - 21\beta_w^6 m_4^6/16)$$
$$(1 - \beta_w m_4 + 3\beta_w^2 m_4^2/2 - 5\beta_w^3 m_4^3/2 + 35\beta_w^4 m_4^4/8 - 63\beta_w^5 m_4^5/8) + \cdots \quad (38)$$

From definition of augmentation factor, it is given by

$$Aug = Q/Q_0 \quad (39)$$

3. Results and discussion

The present analysis is done with considering variable all thermo-physical parameters involved in the heat transfer process to determine analytically thermal performance of a fin attached with a wall. However, the present theoretical model can handle to analyze for an ideal case also where all the thermophysical properties are to be taken constant. For the validation purpose, this ideal condition can be adopted. The temperature distribution in the fin–wall assembly for the ideal condition can be written in nondimensional form as

$$\theta = \frac{K_r P^*\psi\, Nu_L \cosh(Z_0 X)}{\cos Z_0\{(1 + \omega Nu_L)[\psi Z_0 \tanh Z_0 + Bi(P^* - 1)] + K_r P^*\psi Nu_L\}} \quad (0 \le X \le 1) \quad (40)$$

and

$$\phi = \frac{Nu_L(X-1)}{(1+\omega Nu_L)} + \frac{K_r P^*\psi Nu_L(1 - XNu_L + \omega Nu_L + Nu_L)}{(1+\omega Nu_L)\{(1+\omega Nu_L)[\psi z_0 \tanh Z_0 + Bi(P^*-1)] + K_r P^*\psi Nu_L\}} \quad (1 \le X \le 1+\omega) \quad (41)$$

Fig. 2A is drawn for temperature distribution in fin–wall assembly for an ideal case predicted by exact analytical, present analytical and numerical methods. The results obtained from the exact analytical and present analytical methods are matched perfectly whereas a slight deviation in results especially near to the fin tip is found when they are determined by a numerical technique. The finite difference method is used for determining the numerical result. The temperature distribution obtained from the present analytical model with consideration of an actual case is depicted in Fig. 2B. For comparison of results, numerical values have been plotted. A satisfactorily matching of results obtained from both the methods has been found.

The effect of radiation parameter ε_f or ε_w, temperature ratio δ, variable heat transfer coefficient parameter n and variable thermal conductivity parameter β on the temperature distribution in a fin–wall assembly is illustrated in Fig. 3. In Fig. 3A, the influence of radiation is exhibited. The temperature in fin–wall assembly for the condition of no radiation from a fin surface is always higher in comparison to any radiated surface. With the increase in radiation effect, fin array temperature gradually decreases. However, the decreasing effect is slowdown with the increase in radiation parameter. Therefore, the fin surface temperature is extremely dependent on radiation parameter whereas temperature in supporting structure does not have much dependence on it. This fact is due to conduction heat transfer taking place in the supporting structure without losing any heat

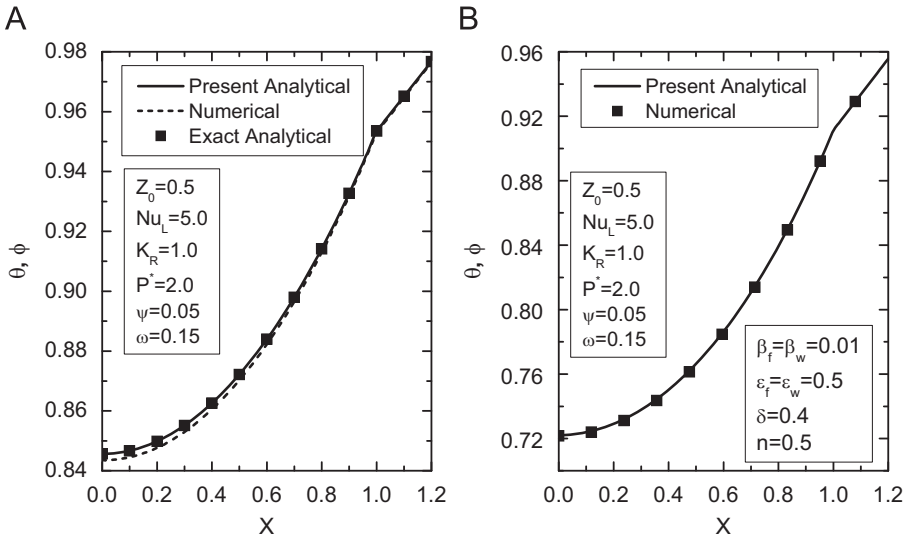

Fig. 2. Temperature distribution in a fin for simplified and actual conditions determined by different methods: (A) simplest study and (B) actual study.

except the boundaries opened to expose to the surrounding. Fig. 3B depicts the effect of temperature ratio parameter δ on temperature distribution in a fin-wall assembly. This parameter has made the same impact with variation of radiation parameters as shown in Fig. 3A. The only difference is temperature dependency effect gradually enhances with the increase in parameter from its zero value. The temperature distribution in a fin assembly is plotted with different values of heat transfer coefficient as illustrated in Fig. 3C. The dependency factor n taken for plotting are 0.5, 2 and 4. The wide range of n value is taken which may be within any practical value. The maximum temperature variation in the fin is found in the case of $n=0.5$. With the increase in n value, variation in temperature in fin assemblies is an incremented function. However, this dependency effect does not have significant impact on the temperature in the supporting structure. The influence of variable thermal conductivity on the temperature distribution has been shown in Fig. 3D. It is obvious from this figure that the variation of thermal conductivity on temperature distribution in the fin assembly may not have any significant change.

Fig. 4 is drawn to show the effect of Nu_L, K_R, P^* and Z_0 on the temperature profile in the fin–wall assembly. Fig. 4A depicts this effect with the variation of Nu_L. An increase in Nu_L means either increase in h_L or decrease in k_L for a constant fin length. For a higher value of Nu_L, convective resistance to the fluid side is to be a lower one and it may be desirable in fin design applications. With the higher Nu_L, the variation of dimensionless temperature in the fin-wall structure is also higher. With the decrease in Nu_L, it decreases as well. For a certain lower value of Nu_L, temperature in fin arrays may be uniform and effectiveness for transferring heat may be a minimum value. The variation of temperature distribution is shown in Fig. 4B with different thermal conductivity ratio K_R. The fin–wall temperature enhances with an increasing K_R value. From temperature distribution, it may be mentioned that for K_R value greater than and equal to one, temperature distribution in the fin and wall structure is clearly distinguishable. But this effect minimizes with the decrease in K_R.

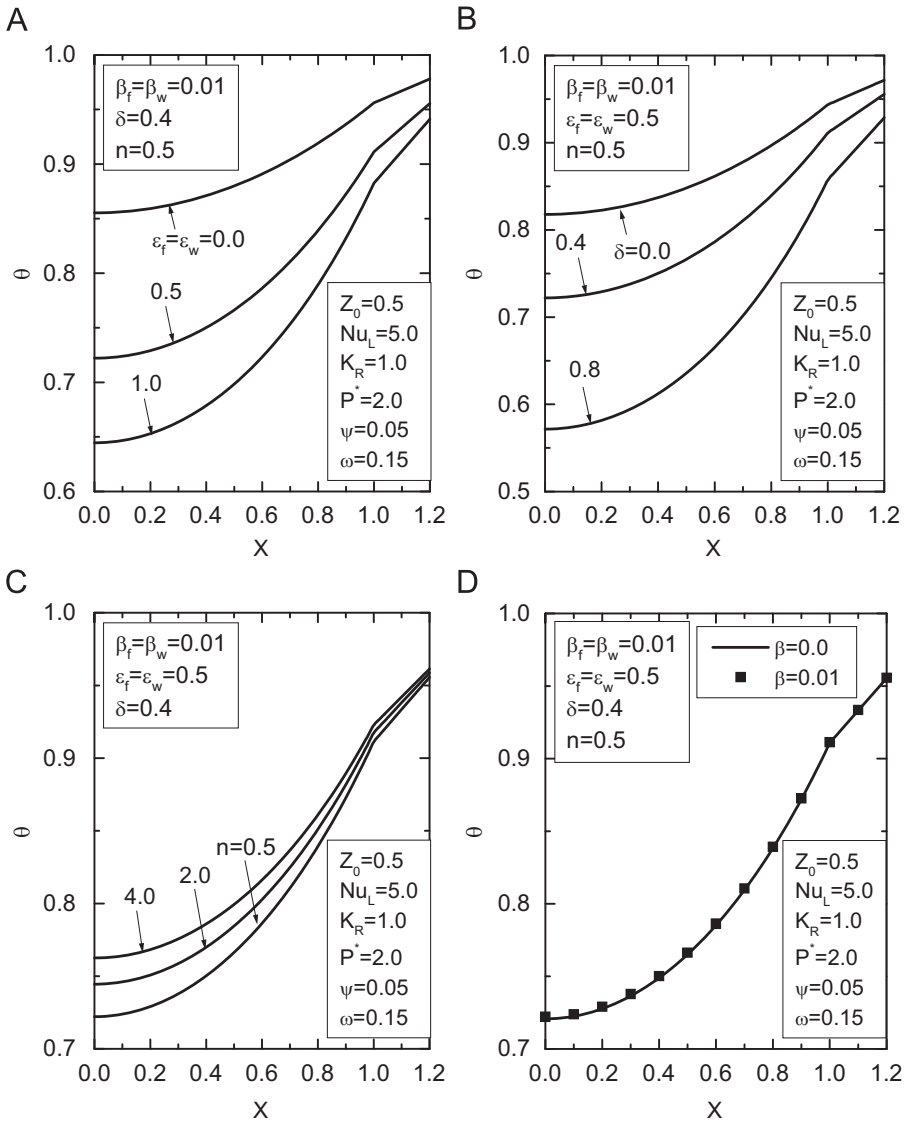

Fig. 3. Effects of different heat transfer parameters on temperature distribution in a fin-wall system: (A) radiation parameter ε, (B) temperature ratio δ, (C) variable heat transfer coefficient parameter n, and (D) variable thermal conductivity parameter β.

The nondimensional wall length P^*effects the temperature distribution in fin arrays as shown in Fig. 4C. With increase in dimensionless wall length, the conductive resistance in the fin array enhances and hence the fin–wall temperature increases. The conductive–convective parameter Z_0 is changed significantly the fin temperature as displayed in Fig. 4D. A smaller value of Z_0 magnifies the fin array temperature. Thus from design point of view, small value of Z_0 and higher value of Nu_L, K_R and P^* may be desirable for the better transfer of heat through a fin–wall assembly.

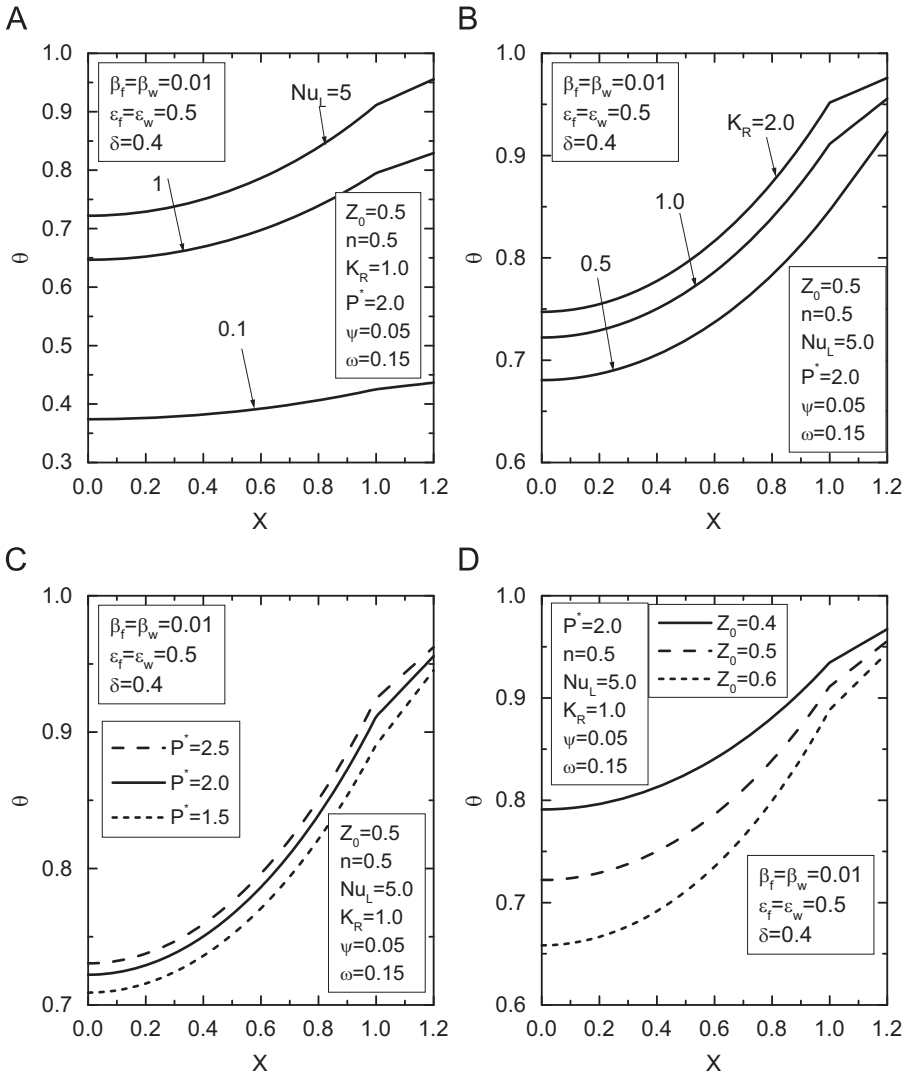

Fig. 4. Effects of thermophysical and geometric parameters on temperature distribution in a fin-wall assembly: (A) radiation parameter ε, (B) Biot number, Bi_L, (C) thermal conductivity ratio, K_R, and (D) conduction–convection parameter, Z_0.

Fin–wall assembly performance, namely, surface efficiency, fin efficiency and augmentation factor are determined based on the present analysis. Fig. 5 is prepared for showing the dependency effect on these performances, by varying δ and Z_0 parameters. The surface efficiency and fin efficiencies decrease with an increasing δ for a constant Z_0 shown in Fig. 5A. The surface efficiency is always lower than the fin efficiency for practical design conditions. However, the nature of curves is almost identical. It may be mentioned that the thermal efficiency of fin–wall system is always less comparison to that of the fin efficiency. Both the surface efficiency and fin efficiency decrement with the increase in Z_0 value. It is less worthy to demonstrate that the difference in efficiencies between fin and

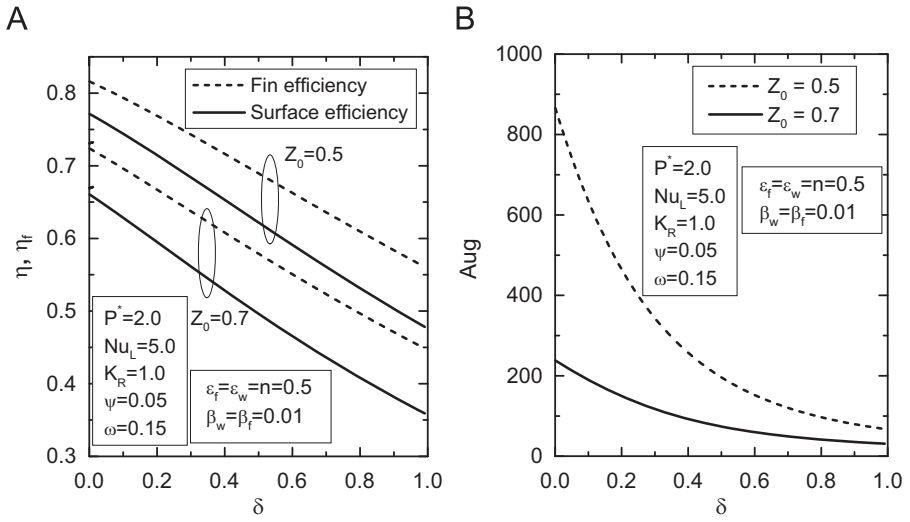

Fig. 5. Performance parameters as a function of δ for different Z_0: (A) fin and surface efficiency and (B) augmentation factor.

surface gradually amplifies with δ but this difference is marginal. The augmentation factor is plotted as a function of δ for different constants Z_0 shown in Fig. 5B. An incremented either δ or Z_0 gives a lower augmentation factor. The diminishing augmentation factor with δ is pronounced at a little value of δ.

Fig. 6 depicts the performances of fin–wall assembly as a function of radiative parameter ε_f. It is obvious that the heat transfer rate is an increasing function with ε_f. The temperature range in the fin–wall is more for an incremented ε_f. Hence, the performances of assembly decline with the radiative parameter. For the lower value of Z_0, decrement of the surface efficiency is always more with that of the fin efficiency for an increase in ε_f. The variation of augmentation factor as a function of ε_f is plotted here for a constant Z_0. The augmentation factor is greatly dependent on the magnitude of Z_0 and the value of ε_f. For a lesser value of Z_0 and ε_f, augmentation factor becomes high due to more heat transfer taken place through the fin-wall than the supporting structure with unfinned condition. The augmentation factor is almost invariable for higher values of Z_0 with variation of ε_f.

Fig. 7 is drawn for showing the fin–wall assembly performances with the variation of index of variable heat transfer coefficient n. It may be mentioned that n value is zero indicating a uniform heat transfer coefficient. With increase in n from its zero value, fin array performances decrease. The decrease in performance namely fin assembly efficiency and fin efficiency are more rapidly with n in comparison to decrease in the augmentation factor. On the other hand, the effect of Z_0 on fin performances is significant especially in the case of augmentation factor.

In every fin design, fin wall plays an important role to augment the heat transfer. Actually depending upon the wall length surface heat transfer coefficient may depend. Fig. 8 is illustrated to execute the effect of projected wall length on fin array performances. An increase in projected wall length decreases both fin efficiency and augmentation factor well which are shown in Figs. 8A and B, respectively. However, the surface efficiency increases with this parameter. It is obvious that for a higher value of wall height, surface

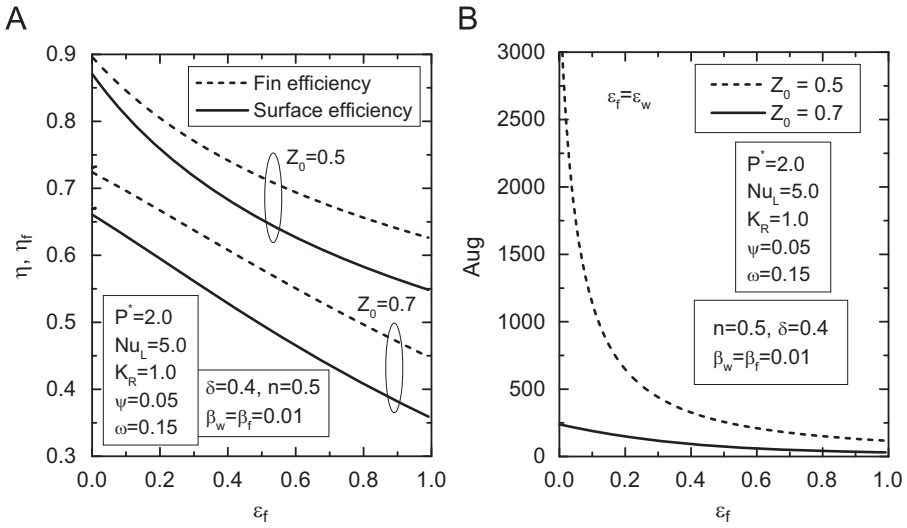

Fig. 6. Effects of radiation parameters ε_f and ε_w on fin performances: (A) fin and surface efficiencies and (B) augmentation factor.

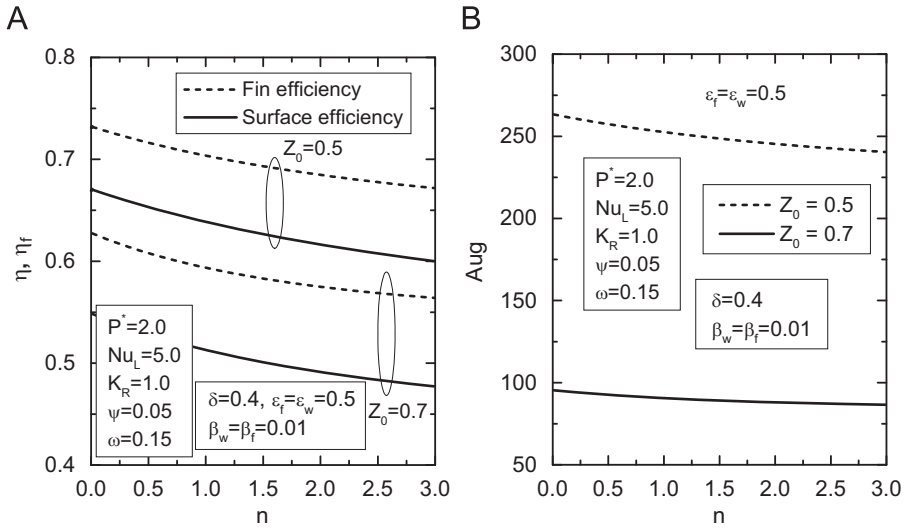

Fig. 7. Effects of variable heat transfer coefficient index n on fin performances: (A) fin and surface efficiencies and (B) augmentation factor.

efficiency is very closer to the fin efficiency. This closeness is dependent also on the magnitude of Z_0 in the design application. The augmentation factor diminishes with the dimensionless wall height P^* as an expected observation. The decremented augmentation factor is a relatively strong function with P^* at lower values of Z_0.

The effect of Nusselt number at the liquid side on the performance of fin array is displayed in Fig. 9. Both surface and fin efficiency decrease with Nu_L due to increase in

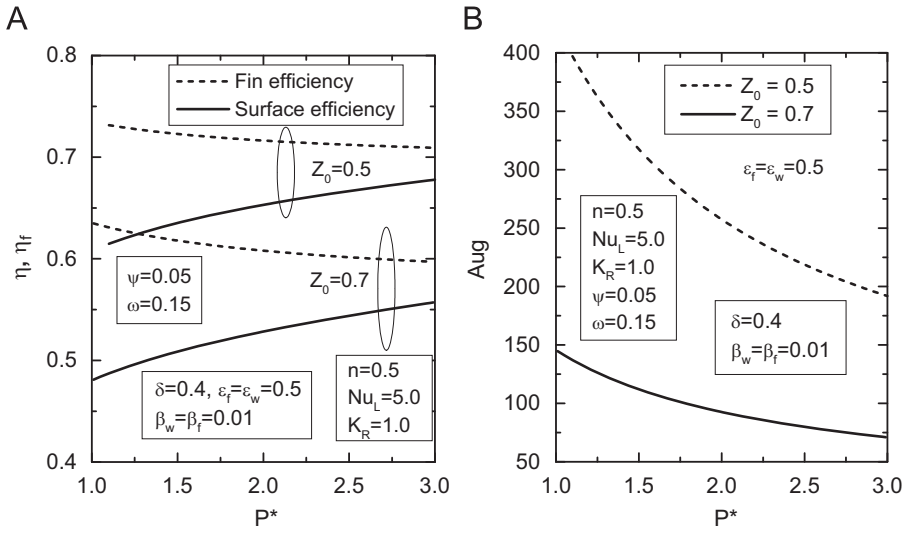

Fig. 8. Fin performances as a function of pitch length P^*: (A) fin and surface efficiencies and (B) augmentation factor.

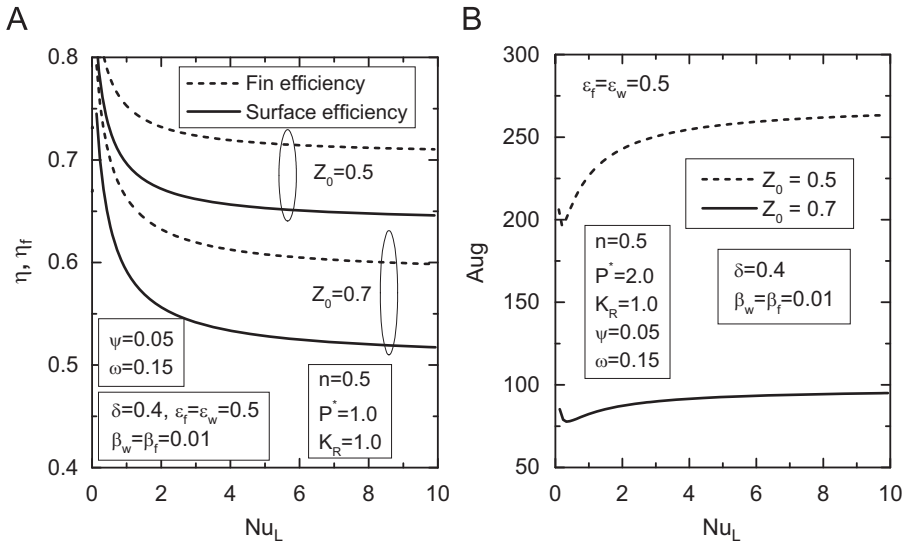

Fig. 9. Variation of fin performances with Biot number Bi_L: (A) fin and surface efficiencies and (B) augmentation factor.

temperature range in the fin–wall assembly. The drop in surface and fin efficiency is more for lower values of Nusselt number. With the increase in Nu_L, this drop rate gradually decreases. The difference between fin and surface efficiency is as an increasing function with Nu_L. On the other hand, AUG decreases with Nu_L for a very small range of Nu_L and then increases monotonically with Nusselt number. But the increment rate depends upon the magnitude of Z_0 also.

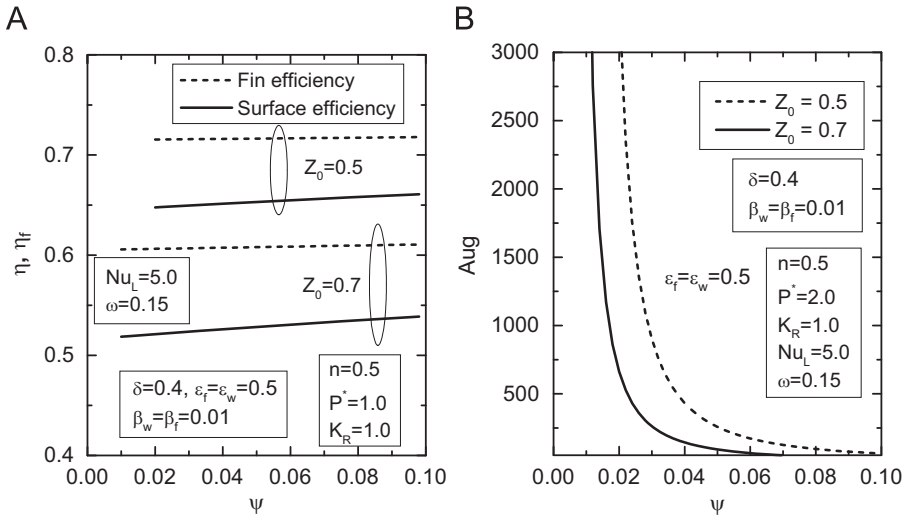

Fig. 10. Variation of fin performances with fin thickness to length ratio ψ: (A) fin and surface efficiencies and (B) augmentation factor.

The fin–wall performance is depicted with the variation of geometrical parameter ψ. The fin and surface efficiency are marginally dependent on this geometric ratio as shown in Fig. 10A. However, this dependency may be treated as a linear. But the fin and surface efficiency are always an increasing function. The augmentation factor with ψ is strongly dependent as shown in Fig. 10B. For higher value of ψ, AUG becomes near to one whatever the design condition is imposed. Naturally for practical utilization of fins, the geometrics of a fin is constructed in such a way that AUG value is high as possible. It may be noted that this is only achievable for a lower value of ψ.

4. Conclusions

From the present analysis, following concluding remarks can be drawn:

1. The proposed approximate analytical model can estimate the temperature distribution and performances of fin–wall assembly under both convective and radiative environments.
2. The analysis has been made into account of the actual situation adopted by considering variable thermophysical parameters.
3. The radiation effect declines both surface temperature and fin–wall performances.
4. With the increase in index of variable heat transfer coefficient n, fin performances decrease slowly.
5. The variable thermal conductivity does not make role significantly on the temperature and fin–wall performances under radiative–convective environment.
6. An increase in Nu_L increases augmentation factor and decreases both the fin and surface efficiencies.
7. The geometrical parameter ψ does not make remarkable impact on fin and surface efficiencies whereas the augmentation factor depends very much upon the ψ.

8. The influence of dimensionless wall height P^* on the fin efficiency and augmentation factor is diminished but the surface efficiency is enhanced as well.

Acknowledgment

The authors must acknowledge King Mongkut's University of Technology Thonburi, the Thailand Research Fund, the Office of the Higher Education Commission and the National Research University Project for providing financial support to complete this work.

References

[1] E.M. Sparrow, L. Lee, Effect of fin base temperature depression in a multi-fin array, ASME J. Heat Transfer 97 (1975) 463–465.
[2] N.V. Suryanarayan, Two-dimensional effects on heat transfer from an array of straight fins, ASME J. Heat Transfer 99 (1977) 129–132.
[3] P.J. Heggs, R.R. Stone, The effects of dimensions of heat flow rates through extended surfaces, ASME J. Heat Transfer 102 (1980) 180–182.
[4] P.J. Heggs, D.B. Ingham, M. Manzoor, The analysis of fin assembly heat transfer by series truncation method, ASME J. Heat Transfer 104 (1982) 210–212.
[5] B. Kundu, P.K. Das, Performance and optimum design analysis of convective fin arrays attached to flat and curved primary surfaces, Int. J. Refrig. 32 (2009) 430–443.
[6] B. Kundu, A. Miyara, An analytical method for determination of the performance of a fin assembly under dehumidifying conditions: A comparative study, Int. J. Refrig. 32 (2009) 369–380.
[7] B.T.F. Chung, B.X. Zhung, A novel design for a radiative fin array system, J. Franklin Inst. 330 (1993) 465–478.
[8] A.M. Elazhary, H.M. Soliman, A nongray analysis of radiating-convecting rectangular plate-fin arrays, Heat Mass Transfer 44 (2008) 413–420.
[9] B. Kundu, A. Aziz, Performance of a convectively heated rectangular fin with a step change in cross-sectional area and losing heat by simultaneous convection and radiation, ASME J. Heat Transfer 132 (2010) 104502-1–104502-6.
[10] A. Aziz, F. Khani, Convection–radiation from a continuously moving fin of variable thermal conductivity, J. Franklin Inst. 348 (2011) 640–651.
[11] A. Razani, H. Zohoor, Optimum dimensions of convective-radiative spines using a temperature correlated profile, J. Franklin Inst. 328 (1991) 471–486.
[12] G. Adomian, in: Non-linear Stochastic System Theory and Application to Physics, Kluwer Academic Publisher, Dordrecht, 1988.
[13] X. Shang, P Wu, X. Shao, An efficient method for solving Emden–Fowler equations, J. Franklin Inst. 346 (2009) 889–897.
[14] J. Biazar, P. Gholamin, K. Hosseini, Variational iteration method for solving Fokker–Planck equation, J. Franklin Inst. 347 (2010) 1137–1147.
[15] P.Y. Tsai, C.K. Chen, An approximate analytic solution of the nonlinear Riccati differential equation, J. Franklin Inst. 347 (2010) 1850–1862.
[16] F. Mohammadi, M.M. Hosseini, A comparative study of numerical methods for solving quadratic Riccati differential equations, J. Franklin Inst. 348 (2011) 158–164.

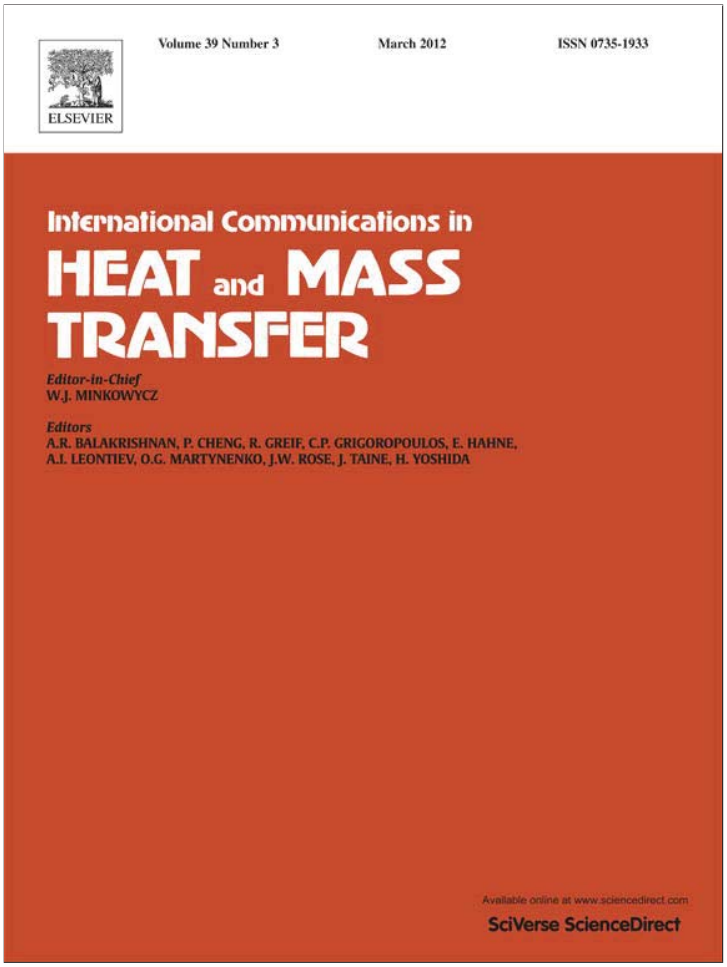

International Communications in Heat and Mass Transfer 39 (2012) 424–431

Contents lists available at SciVerse ScienceDirect

International Communications in Heat and Mass Transfer

journal homepage: www.elsevier.com/locate/ichmt

Investigation of pool boiling of nanofluids using artificial neural networks and correlation development techniques ☆

M. Balcilar [a], A.S. Dalkilic [b,*], A. Suriyawong [c], T. Yiamsawas [c], S. Wongwises [c,d,**]

[a] Computer Engineering Department, Yildiz Technical University, Yildiz, Besiktas, Istanbul 34349, Turkey
[b] Heat and Thermodynamics Division, Department of Mechanical Engineering, Yildiz Technical University, Yildiz, Besiktas, Istanbul 34349, Turkey
[c] Fluid Mechanics, Thermal Engineering and Multiphase Flow Research Lab. (FUTURE), Department of Mechanical Engineering, King Mongkut's University of Technology Thonburi, Bangmod, Bangkok 10140, Thailand
[d] The Academy of Science, The Royal Institute of Thailand, Sanam Suea Pa, Dusit, Bangkok 10300, Thailand

ARTICLE INFO

Available online 31 January 2012

Keywords:
Pool boiling
Heat transfer coefficient
Nanofluid
Modeling
Neural network

ABSTRACT

The nucleate pool boiling heat transfer characteristics of TiO_2 nanofluids are investigated to determine the important parameters' effects on the heat transfer coefficient and also to have reliable empirical correlations based on the neural network analysis. Nanofluids with various concentrations of 0.0001, 0.0005, 0.005, and 0.01 vol.% are employed. The horizontal circular test plate, made from copper with different roughness values of 0.2, 2.5 and 4 μm, is used as a heating surface. The artificial neural network (ANN) training sets have the experimental data of nucleate pool boiling tests, including temperature differences between the temperatures of the average heater surface and the liquid saturation from 5.8 to 25.21 K, heat fluxes from 28.14 to 948.03 kW m^{-2}. The pool boiling heat transfer coefficient is calculated using the measured results such as current, voltage, and temperatures from the experiments. Input of the ANNs are the 8 numbers of dimensional and dimensionless values of the test section, such as thermal conductivity, particle size, physical properties of the fluid, surface roughness, concentration rate of nanoparticles and wall superheating, while the outputs of the ANNs are the heat flux and experimental pool boiling heat transfer coefficient from the analysis. The nucleate pool boiling heat transfer characteristics of TiO_2 nanofluids are modeled to decide the best approach, using several ANN methods such as multi-layer perceptron (MLP), generalized regression neural network (GRNN) and radial basis networks (RBF). Elimination process of the ANN methods is performed together with the copper and aluminum test sections by means of a 4-fold cross validation algorithm. The ANNs performances are measured by mean relative error criteria with the use of unknown test sets. The performance of the method of MLP with 10-20-1 architecture, GRNN with the spread coefficient 0.7 and RBFs with the spread coefficient of 1000 and a hidden layer neuron number of 80 are found to be in good agreement, predicting the experimental pool boiling heat transfer coefficient with deviations within the range of ±5% for all tested conditions. Dependency of output of the ANNs from input values is investigated and new ANN based heat transfer coefficient correlations are developed, taking into account the input parameters of ANNs in the paper.

1. Introduction

The existence of a moving and deforming phase interface affects the heat transfer in two-phase flows concerning gas and liquid phases. Two-phase flows occur during boiler operation in a power plant, nuclear reactors, evaporator performance in refrigeration systems, quenching in materials processing, and condensers in power and refrigeration systems. In this paper, artificial neural network analyses were used as one of the numerical solution techniques to determine the important characteristics of pool boiling heat transfer.

Das and Kishor [1] used a modeling technique based on fuzzy system to determine the heat transfer coefficient in pool boiling of distilled water. They performed an experimental study to develop an empirical correlation for saturated boiling of distilled water from a plain copper heating tube surface at atmospheric and sub-atmospheric pressures. Their experimental data has been compared with those determined from the zero-order adaptive fuzzy model with heat flux as input variable and also Matlab based adaptive neuro-fuzzy inference system (ANFIS) function.

Liu et al., [2] developed a numerical model using artificial neural network (ANN) technology to investigate boiling heat transfer enhancement using additives. Their model was validated by 30 additives tested by the authors and other researchers on the augmentation of boiling heat transfer experimentally.

☆ Communicated by W.J. Minkowycz.
* Corresponding author.
** Correspondence to: S. Wongwises, The Academy of Science, The Royal Institute of Thailand, Sanam Suea Pa, Dusit, Bangkok 10300, Thailand.
E-mail addresses: dalkilic@yildiz.edu.tr (A.S. Dalkilic), somchai.won@kmutt.ac.th (S. Wongwises).

0735-1933/$ – see front matter © 2012 Elsevier Ltd. All rights reserved.
doi:10.1016/j.icheatmasstransfer.2012.01.008

Nomenclature

A	area, m^2
C_p	specific heat, kJ kg^{-1} °C
g	gravitational acceleration, m s^{-2}
h	boiling heat transfer coefficient, W m^{-2} K
h_{fg}	heat of vaporization, kJ kg^{-1}
I	electric current, amps
i	number of test data
k	thermal conductivity, W m^{-1} K^{-1}
Nu	Nusselt number
P	pressure, kPa
P_c	critical pressure, kPa
Pr	Prandtl number
R_a	average roughness, μm
Re	Reynolds number
R_p	particle size, nm
q	heat flux, kW m^{-2}
T_c	critical temperature, K
V	voltage, volts
ΔT	wall superheat, $T_s - T_{sat}$, K

Greek symbols

μ	dynamic viscosity, kg m^{-1} s^{-1}
ρ	density, kg m^{-3}
σ	surface tension, N m^{-1}

Subscripts

exp	experimental
l	liquid phase
s	heating surface
sat	saturation
v	vapor phase

Scalabrin et al., [3] studied the heat transfer modeling of flow boiling inside horizontal tubes at saturation conditions using eight pure fluids and a constant composition ternary mixture. ANNs were used to characterize conventional heat transfer surfaces. Their model's performance was validated by five conventional correlations. Scalabrin et al., [4] investigated the flow boiling inside horizontal smooth tubes for mixtures. They proposed a new modeling technique for the heat transfer. They improved their model to mixtures in their former work. Directly-accessible physical quantities controlling the phenomenon were selected for the correlation architectures considered for the ANN functions. They stated that they obtained considerable increase of prediction capability with respect to the conventional methods by means of their numerical model.

Wang et al., [5] developed a generalized neural network correlation for boiling heat transfer coefficient of R22 and its alternative refrigerants R134a, R407C and R410A inside horizontal smooth tubes using the experimental data in the literature. The inputs of the neural network consisted of four kinds of dimensionless parameter groups from existing generalized correlations, while the output was a Nusselt number. As a result of their analyses, the input parameter group based on the Gungor–Winterton [6] correlation has the highest predictability in the tested groups.

Suriyawong and Wongwises [7] studied nucleate pool boiling heat transfer of TiO_2–water nanofluids experimentally. Nanofluids with various concentrations of 0.00005, 0.0001, 0.0005, 0.005, and 0.01 vol.% were employed in their study. The experiments were performed to explore the effects of nanofluids concentration as well as heating surface material and roughness on nucleate pool boiling characteristics and the heat transfer coefficient under ambient pressure. Their results showed that based on the copper heated surface which was tested with a concentration of 0.0001 vol.%, higher nucleate pool boiling heat transfer coefficient was obtained when compared with the base fluid.

Trisaksri and Wongwises [8] investigated nucleate pool boiling heat transfer of a refrigerant-based-nano-fluid at different nanoparticle concentrations and pressures. TiO_2 nanoparticles were mixed with the refrigerant HCFC 141b at 0.01, 0.03 and 0.05 vol%. Pool boiling experiments of nano-fluid were conducted and compared with that of the base refrigerant. Their results indicated that the nucleate pool boiling heat transfer deteriorated with increasing particle concentrations, especially at high heat fluxes.

The correct prediction of refrigerant boiling heat transfer performance is important for the design of evaporators. Information on the pool boiling characteristics of refrigerant-based nanofluids is still limited. Moreover, there remains room for further research, especially on the point at which the presence of the nanoparticle can enhance or deteriorate heat transfer. As a consequence, the main aim of the present study was to have reliable empirical correlations, based on numerical and experimental studies, to cover the wide range important parameters on the pool boiling. The effect of various TiO_2–water nanoparticle concentrations using a copper-based heating material with various surface roughness values on the boiling heat transfer coefficient is considered in the numerical analyses to achieve the main aim thoroughly. In addition to this, the effect of input parameters (thermal conductivity, particle size, physical properties of the fluid, surface roughness, concentration rate of nanoparticles and wall superheating) on the output parameters (heat flux and pool boiling heat transfer coefficient) is shown and discussed as a primary study on this subject in the literature.

2. Sample preparation and experimental apparatus

In the present study, nanofluids provided by a commercial source (DEGUSSA, VP Disp. W740x) are used as working fluid. The detailed image of dispersed TiO_2 nanoparticles in water, taken by Transmission electron microscopy (TEM), details of preparation of nanofluids and details of experimental apparatus can be seen from Suriyawong and Wongwises [7].

3. Data reduction

3.1. Experimental pool boiling heat transfer coefficient

Experimental investigations were carried out to observe the boiling characteristics using the flat plate heater. The heat fluxes, q (W m^{-2}), were calculated from the following equation:

$$q = \frac{IV}{A} \tag{1}$$

where I is the current (amps), V is the voltage (volts), and A is the heating surface area (m^2).

The average boiling heat transfer coefficient, h_b (W m^{-2} °C), is defined as:

$$h_b = \frac{q}{(T_s - T_{sat})} \tag{2}$$

where T_s is the average heater surface temperature (°C) calculated from Eq. (3), and T_{sat} is the liquid saturation temperature (°C):

$$T_s = \frac{\sum_{i=1}^{4} T_i \sum_{i=1}^{4} x^2{}_i - \sum_{i=1}^{4} x_i \sum_{i=1}^{4} x_i T_i}{4\sum_{i=1}^{4} x^2{}_i - \left(\sum_{i=1}^{4} x_i\right)^2} \tag{3}$$

where T_i is the local temperature (°C) and x is the position of the temperature measurement (m) on the test section. The examples of the

axial temperature distribution in the copper test section can be seen from Suriyawong and Wongwises [7].

The uncertainties of the heat flux, heating surface temperature and heat transfer coefficient are ±2.2%, ±3.7% and ±11.6%, respectively.

3.2. Calculation procedure for the Generalized Artificial Neural Networks (ANNs) model

ANNs are such factors that can utilize machine learning for the duty of considered necessary mapping of the inputs to the outputs. A dataset is divided into three parts such as training, testing and validation. ANNs determine a function between the inputs and outputs generalizing the training group. The success of this group is calculated using the test group. The training duration of ANNs is determined by the validation group. When the training group has over-fitting as a result of long time training, ANNs memorize the training group and its success on the test group reduces. The optimum point for the stop of training is determined by using a validation group. Performance of ANNs is measured by the success of the prediction. There are many described ANN types and their architectures (different size of layers, neuron numbers and spread coefficients) related to function approximation in the literature. The most known methods are multi-layer perceptron (MLP), radial basis functions networks (RBF), generalized regression neural networks (GRNN) and artificial neural fuzzy inference system (ANFIS), which is the combination of fuzzy logic decision systems and ANNs. Schematic diagrams of artificial intelligence models used in the analysis, obtained by Matlab software, and detailed information can be seen from the authors' previous publication [9].

Nelder and Mead developed a simplex method to determine a local minimum of a function of several variables. It is a good alternative method when the differential of the fitness function is complex either analytically or numerically. A simplex forms triangle for two variables and function values at the three vertices of this triangle are compared by means of the pattern search method. The new vertex is found by replacing with the rejected worst vertex where f (x, y) is largest. Then, the search is continued when the new vertex is formed. A sequence of triangles, which might have different shapes, is generated by each iteration when values at the vertices get smaller and smaller. Reduction of the size of the triangles is performed and the coordinates of the minimum point are found. The Nelder–Mead technique was proposed by Nelder and Mead [10] and is a technique for minimizing a fitness function in a many-dimensional space. Operators in Nelder–Mead algorithm is shown in [11].

The least square (LS) method is one of the standard approaches to the approximate solution of over-determined systems or inexactly specified systems of equations in an approximate sense. It can be used when the sets of equations in which there are fewer unknowns than equations. LS means that the overall solution minimizes the sum of the squares of the errors made in solving every single equation instead of solving the equations exactly. The data fitting is the most important application of LS. The minimization of the sum of squared residuals is sensed by the best fit in the LS and a residual causes the difference between an observed value and the value provided by a model. LS match with the maximum probability criterion if there is a normal distribution of the experimental errors.

LS problems consist of linear least squares and non-linear least squares (NLS) depending on whether or not the residuals are linear in all unknowns. Most statistical regression analyses have linear LS problems; it has a closed form solution. The non-linear problem, usually solved by iterative refinement, has no closed solution. The system is approximated by a linear one at each iteration in order to have similar results for the core calculation in both cases. The Non-Linear Least Square (NLS) method allows determination of the most optimal non-linear function coefficients, in order to fit data collected from an experimental environment to a non-linear function (non-linear curve fitting). This method tries to minimize the mean square error, beginning from the first estimated values determined by the user. Mathematical basis of the investigated methods and details are shown in [11].

3.3. Correlation development

Rhosenow [12] proposed the following equations from Eqs. (4)–(7) for pool nucleate boiling considering surface characteristics. His correlations are widely accepted in the literature. Narayan et al. [13] used Eq. (4) to investigate the effect of surface orientation on pool boiling heat transfer of nanoparticle suspensions. They stated that m should be taken as 1 for water in Eq. (4). Suriyawong and Wongwises [7] also used Eq. (4) to study nucleate pool boiling heat transfer characteristics of TiO_2–water nanofluids at very low concentrations. Taylor and Phelan [14] benefitted from Eq. (5) to prepare their review on the pool boiling of nanofluids. Bang and Chang [15] used Rhosenow [12]'s equations of 6 and 7 to determine boiling heat transfer performance and phenomena of Al_2O_3–water nanofluids from a plain surface in a pool

$$\frac{C_{p,l}(T_s-T_{sat})}{h_{fg}\mathrm{Pr}_l^{\,m}} = C_{sf}\left(\frac{q}{\mu_l h_{fg}}\sqrt{\frac{\sigma}{g(\rho_l-\rho_v)}}\right)^{0.33} \tag{4}$$

$$q = \mu_l h_{fg}\left[\frac{\sigma}{g(\rho_l-\rho_v)}\right]^{-1/2}\left(\frac{1}{C_{sf}}\right)^{1/r}\mathrm{Pr}_l^{\,s/r}\left[\frac{C_{p,l}(T_s-T_{sat})}{h_{fg}}\right] \tag{5}$$

$$Nu = \frac{1}{C_{sf}}\mathrm{Re}^{(1-n)}\mathrm{Pr}_l^{\,-m} \tag{6}$$

$$h = \left(\frac{1}{C_{sf}}\right)\left[\frac{C_{p,l}q}{h_{fg}}\right]\left[\frac{q}{\mu_l h_{fg}}\left(\frac{\sigma}{g(\rho_l-\rho_v)}\right)^{1/2}\right]^{-n}\left[\frac{Cp_l\mu_l}{k_l}\right]^{-(m+1)} \tag{7}$$

Zhaohu et al., [16] developed some correlation structures similar with Eqs. (8) and (9) to investigate the nucleate pool boiling heat transfer coefficients of pure HFC134a, HC290, HC600a and their binary and ternary mixtures.

$$h = \frac{AP_c^{\,B}}{M^C T_c^{\,D}}(ER_a)^{F\left(1-\frac{P}{P_c}\right)}\frac{\left(\frac{P}{P_c}\right)^G}{\left[1-H\left(\frac{P}{P_c}\right)\right]^I}\mathrm{q}^J \tag{8}$$

$$h = A\mathrm{q}^B \tag{9}$$

It should be noted that Cornwell and Houston [17] developed convective type correlation for the nucleate pool boiling on horizontal tubes. Das et al., [18,19] benefitted from Cornwell and Houston [17]'s correlation to determine pool boiling characteristics of nanofluids and developed correlations for the smooth and rough surfaces and also various nanoparticles concentrations separately.

3.4. Error analysis

The error analyses' calculation procedure for the average values of the experimental and calculated results regarding with R square error, proportional error and Mean square error (MSE) can be seen from authors' previous publication [9].

4. Results and discussion

The experiments of the present study were done at the Fluid Mechanics, Thermal Engineering and Multiphase Flow Research Lab. (FUTURE) in KMUTT for the determination of heat transfer

enhancement during pool boiling of nanofluids. The heat transfer enhancement obtained by the use of nanoparticles, pool boiling curve in the form of relationships between heat flux and $T_s - T_{sat}$ and in the form of relationships between heat flux and heat transfer coefficient can be seen from Suriyawong and Wongwises [7]. This numerical research studied the heat transfer characteristic of nucleate pool boiling at atmospheric pressure using distilled water and TiO_2–water nanofluids at various concentration levels as working fluids by means of various methods of Artificial Neural Networks. Special attention was paid on the accuracy of the measurements during experiments as can be seen from authors' previous publications on two-phase flow in the literature. Discussion of the results will be given in turn as follows:

Numerical analysis of artificial intelligence includes 7 dimensional input parameters, such as thermal conductivity (k, W m^{-1} K^{-1}), particle size (nm), density (ρ, kg m^{-3}), dynamic viscosity (μ, kg m^{-1} s^{-1}), specific heat at constant pressure, (C_p, kJ kg^{-1} K^{-1}), roughness of heating surface (Ra, μm) and wall superheat ($\Delta T = T_s - T_{sat}$), and 1 dimensionless input parameter of nanoparticle concentration (%), 2 dimensional output parameters such as pool boiling heat transfer coefficient (h, kW m^{-2} K^{-1}) and heat flux (q, kW m^{-2}).

Regarding the elimination process of several artificial neural network (ANN) methods such as multi-layer perceptron (MLP), radial basis networks (RBF) and generalized regression neural network (GRNN), train and test sets are determined by the way of 4-fold cross validation. According to 4-fold cross validation, all data points are divided into 4 different sets randomly. The first set is determined as test and the others are determined as train set. After this iteration the second set is determined test and the other is train too. Hence all individual sets are determined test receptively. At the train section, %20 of train data is selected as validation set to prevent over-fitting. The best value of ANNs control parameters is determined using 4-fold cross validation in training phase.

During the calculation process of pool boiling heat transfer coefficient and heat flux, the most agreeable multi-layer perceptron (MLP) has 2 hidden layers. First hidden layer has 20 neurons and second hidden layer has 10 neurons. The most agreeable spread numbers (s_p) were found as 1000 and hidden layers neurons were 80 for the radial basis function networks (RBF). The most agreeable spread numbers (s_p) were found as 0.7 for the generalized regression neural networks (GRNN). Table 1 shows the best predictive method for the pool boiling heat transfer coefficient and heat flux accurately according to the their low average values of all test points' results using several error analysis methods. According to Table 1, the method of multi-layer perceptron (MLP) for the heat flux and the method of generalized regression neural network (GRNN) were found as the most predictive methods with their higher R^2 values than others.

Table 1
Elimination of ANN methods according to the error rates for the determination of heat flux and pool boiling heat transfer coefficient.

Output 1 – q (kW m^{-2})			
ANN Methods	Error Analysis		
	R square	Proportional (%)	Square law
MLP	0.916	23.2994	6251.2506
GRNN	0.8846	23.3829	8543.5481
RBF	0.8989	37.8096	7401.877
Output 2 – h (kW m^{-2} K^{-1})			
ANN Methods	Error Analysis		
	R square	Proportional (%)	Square law
MLP	0.8638	23.9805	28.1906
GRNN	0.8795	19.3751	23.3867
RBF	0.8472	24.05128	29.2348

The performance comparisons of the investigated ANN methods were shown in Figs. 1–3 for the heat flux and in Figs. 4–6 for the pool boiling heat transfer coefficient regarding the surface roughness of the heater separately. From these figures, all tested ANN methods seem to have similar results with each other by means of satisfactory results with their deviations within the range of ±30% for the estimated pool boiling heat transfer coefficient and the estimated heat flux, respectively.

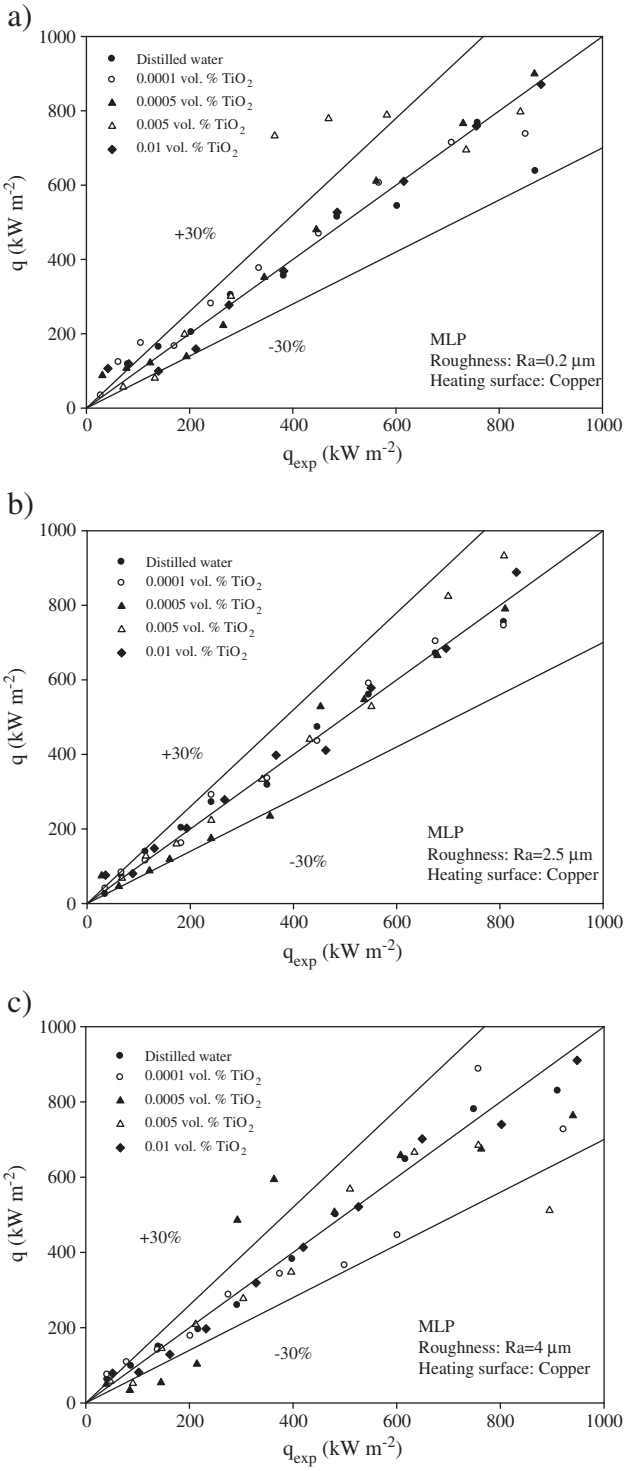

Fig. 1. Comparison of experimental and numerical heat fluxes obtained from artificial neural network prediction method of MLP for the various surface roughness values of heater.

Table 2 shows the most predictive combinations of input parameters, whose deviations are quite low, according to the error rates for the determination of pool boiling heat transfer coefficient (h) and heat flux (q) using the method of multi-layer perceptron (MLP) with 10-20-1 architecture which was found as the most successful architecture as a results of the analyses. They also show the dependency of the each input parameters on the outputs of the study separately according to the error rates of the test group of ANN, as a result of

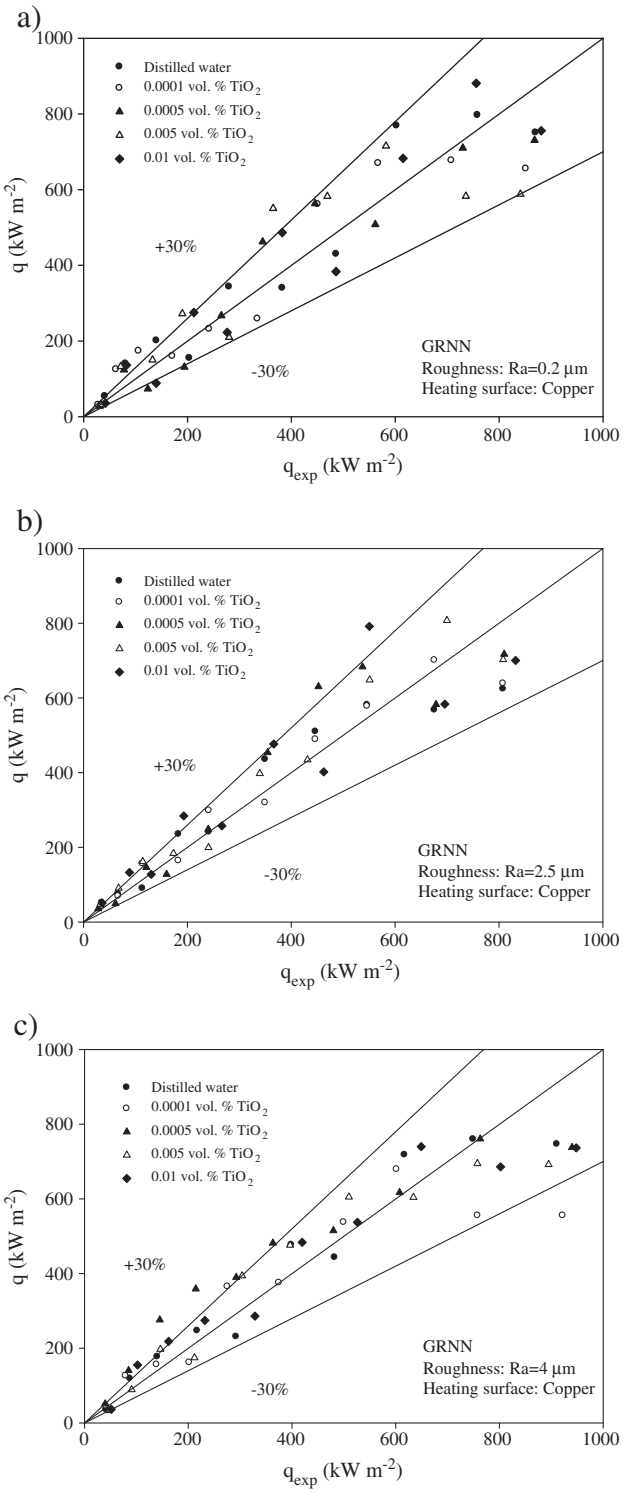

Fig. 2. Comparison of experimental and numerical heat fluxes obtained from artificial neural network prediction method of GRNN for the various surface roughness values of heater.

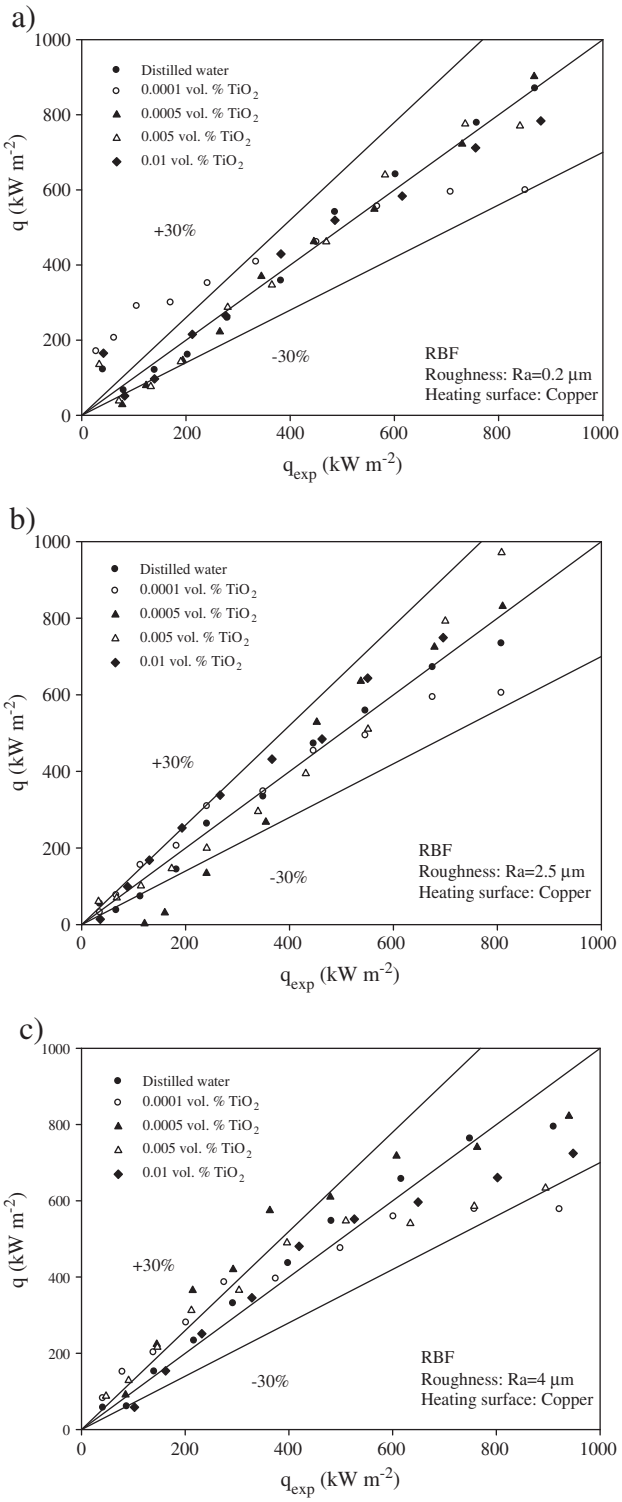

Fig. 3. Comparison of experimental and numerical heat fluxes obtained from artificial neural network prediction method of RBF for the various surface roughness values of heater.

the most predictive ANN method of the MLP 10-20-1 architecture for the operating conditions shown in all figures. The input parameters are shown with numbers in this table as follows: thermal conductivity (I), particle size (II), liquid density of the fluid (III), liquid dynamic viscosity (IV), liquid specific heat at constant pressure (V), roughness of heating surface (VI), nanoparticle concentration (VII) and wall superheat (VIII). When the input parameter number is 1, wall superheat (VIII) seems to be the most dominant parameter on

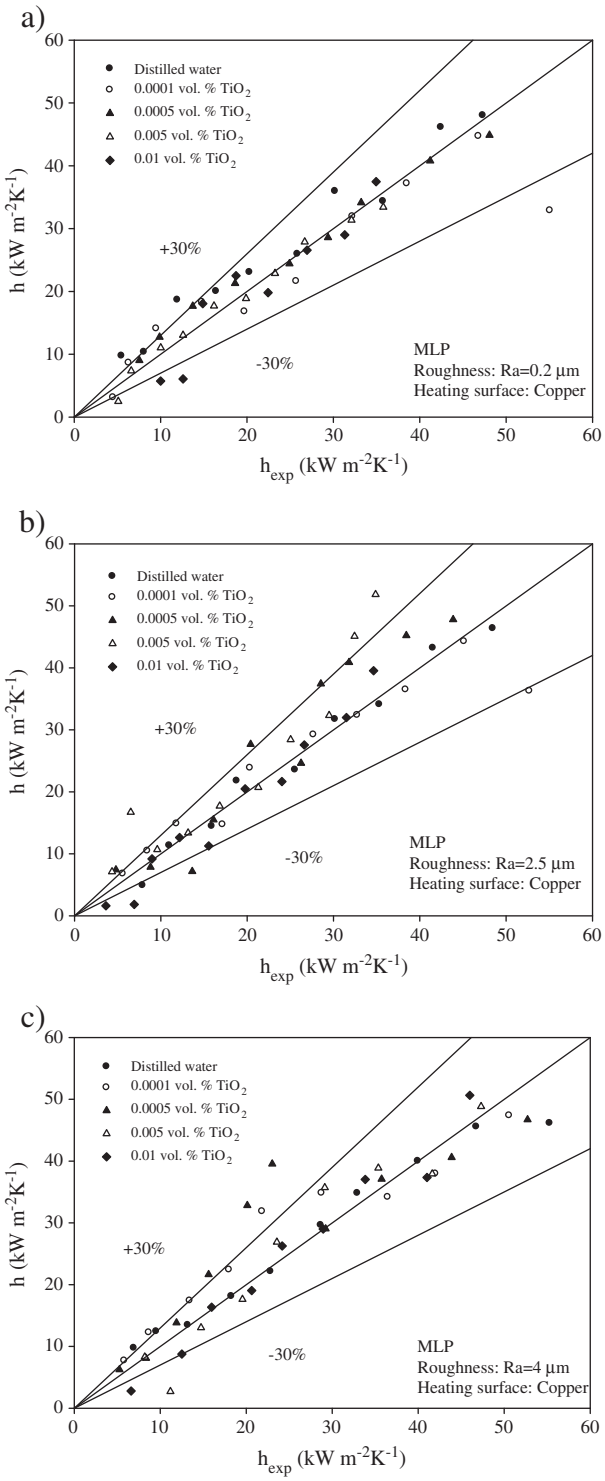

Fig. 4. Comparison of experimental and numerical pool boiling heat transfer coefficients obtained from artificial neural network prediction method of MLP for the various surface roughness values of heater.

the prediction of pool boiling heat flux and heat transfer coefficient with the deviations of 0.6087% and 50.85% in Table 2 respectively. When the input parameter number is 3, liquid dynamic viscosity (IV), roughness of heating surface (VI) and wall superheat (VIII) seem to be dominant on the prediction of heat flux with the deviation of 0.8474% and liquid density of the fluid (III), nanoparticle concentration (VII) and wall superheat (VIII) have the success on the heat transfer coefficient with the deviation of 0.7827% in Table 2. It shows that the accuracy of the estimated output values by means of input values increases with increasing added proper input parameters due to the result of the learning process of the artificial intelligence. As a result, it is possible to derive many results from this table on the input combinations' performance.

The correlation development study's results are shown in Table 3 and also in Fig. 7. The main frames of the proposed correlations are shown from Eqs. (4)–(9), which have many possible dominant parameters on the pool boiling heat transfer coefficient. Artificial

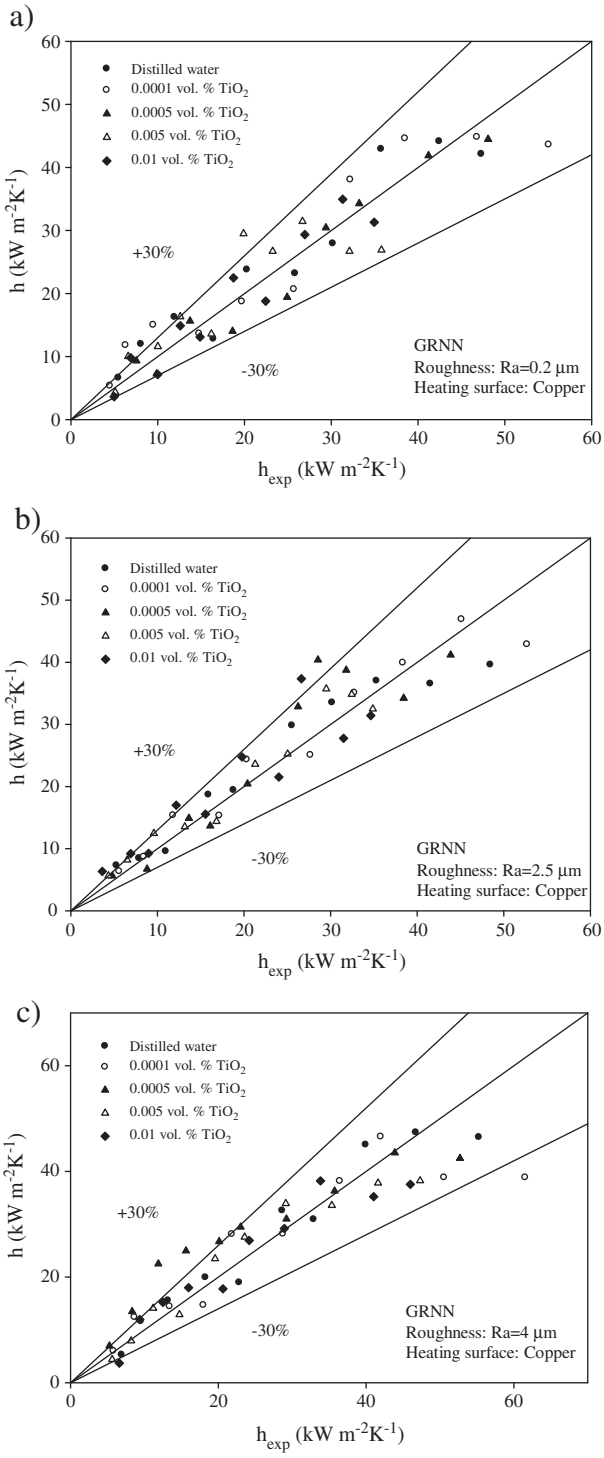

Fig. 5. Comparison of experimental and numerical pool boiling heat transfer coefficients obtained from artificial neural network prediction method of GRNN for the various surface roughness values of heater.

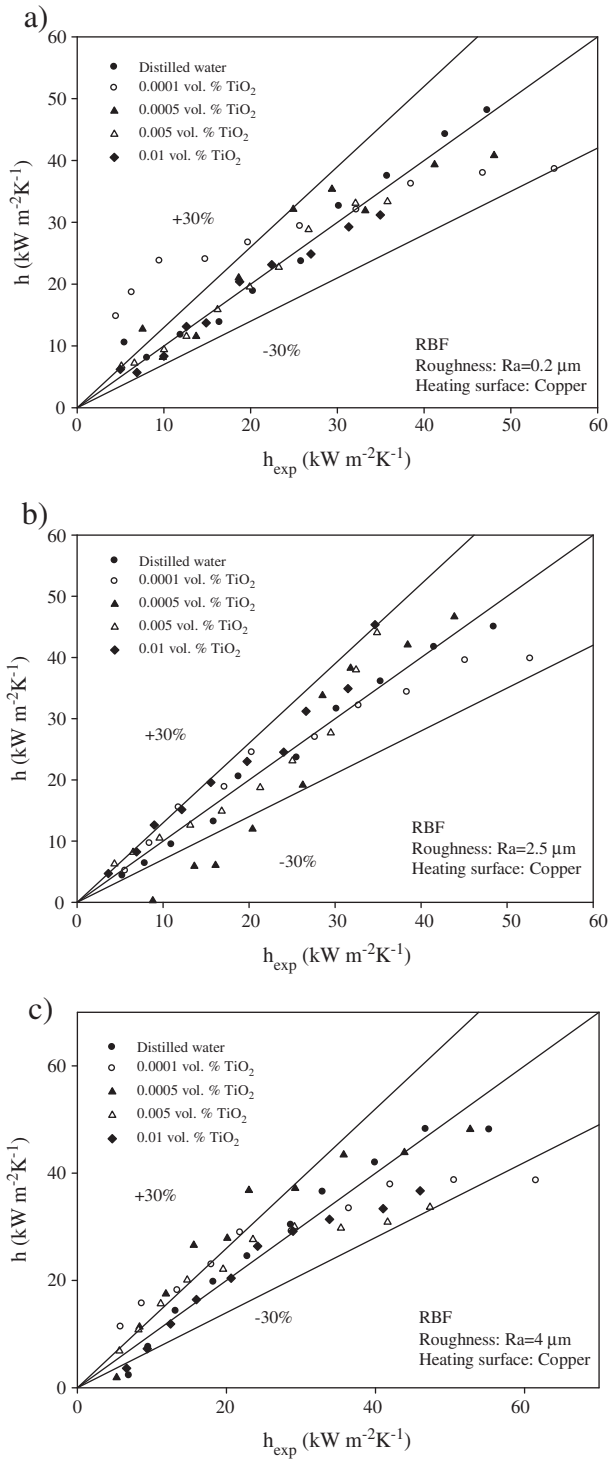

Fig. 6. Comparison of experimental and numerical pool boiling heat transfer coefficients obtained from artificial neural network prediction method of MLP for the various surface roughness values of heater.

intelligence decided the coefficients of these significant parameters step by step in Table 3 and their error rates can be seen in the same Table. All of the data obtained from the optimization methods of pool boiling heat transfer coefficient fall between the deviations of ± 30% in Table 3. It can be seen that Eq. (7) has the best proposed correlation formula by means of NLS method of optimization analyses according to all error criteria calculated by Eqs. (10)–(12) on the prediction of the pool boiling heat transfer coefficient and its results are shown in Fig. 7. It should be noted that measured heat flux is used in Eqs. (7) and (9).

Table 2
Dependency analyses regarding with the inputs on the output as heat flux of the artificial neural networks.

INPUTS								Input Number	OUTPUTS
I	II	III	IV	V	VI	VII	VIII		R^2 – q
							X	1	0.6087
					X		X	2	0.6328
			X		X		X	3	0.8474
X			X		X		X	4	0.8970
X			X		X	X	X	5	0.8992
X		X	X		X	X	X	6	0.9122
X	X	X	X		X	X	X	7	0.9152
X	X	X	X	X	X	X	X	8	0.9160
I	II	III	IV	V	VI	VII	VIII	Input Number	R^2 – h
							X	1	0.5085
						X	X	2	0.5190
		X				X	X	3	0.7827
		X		X		X	X	4	0.7842
X		X		X		X	X	5	0.7958
X		X	X	X		X	X	6	0.8082
X		X	X	X	X	X	X	7	0.8223
X	X	X	X	X	X	X	X	8	0.8795

5. Conclusion

The numerical pool boiling heat transfer coefficient and heat flux values with the measured values by means of artificial intelligence methods were compared in this paper. It should be noted that there is no research on the content of this paper considering its parameters in current literature. For that reason, the results of this study are expected to fill this gap in the literature.

The artificial neural network (ANN) methods of multi-layer perceptron (MLP), radial basis networks (RBF) and the generalized regression neural network (GRNN) are found to be capable of predicting the heat transfer coefficient and heat flux for the pool boiling of water–TiO_2 nano-fluid within the range of ± 30% and also within the slightly small error rates.

The performance of the method of multi-layer perceptron (MLP), radial basis function networks (RBF) and the generalized regression neural network (GRNN) on the correlation development have the similar and satisfactory results with their deviations with the average R^2 values about 92% for the estimated pool boiling heat transfer coefficient using the artificial neural network methods of unconstrained nonlinear minimization Nelder–Mead algorithm (NM) and the nonlinear least squares algorithm (NLS). It should be noted that these artificial intelligence methods have better results on the prediction of pool boiling heat transfer coefficient and heat flux than the empirical models and correlations proposed in the authors' previous publications.

Pool boiling heat flux of nano-fluid in the paper are found to be dependent on the nano-liquid dynamic viscosity (IV), roughness of heating surface (VI) and wall superheat (VIII) while liquid density of the fluid (III), nanoparticle concentration (VII) and wall superheat (VIII) are for the pool boiling heat transfer coefficient strongly according to the results of analysis.

Acknowledgements

The second author wishes to thank King Mongkut's University of Technology Thonburi for providing him with a Post-doctoral fellowship. The third, fourth and fifth authors wish to thank the Thailand Research Fund, the Office of Higher Education Commission and the National Research University Project for financial support.

Table 3
Error rates for the correlation development study.

Optimization methods	Proposed Correlations	Error Analysis		
		R square	Proportional (%)	Square law
NM	$h = \left(\frac{1}{45.49}\right)\left[\frac{C_{pl}q}{h_{fg}}\right]\left[\frac{q}{\mu_l h_{fg}}\left(\frac{\sigma}{g(\rho_l-\rho_v)}\right)^{1/2}\right]^{-0.2445}\left[\frac{Cp_l\mu_l}{k_l}\right]^{-1.179}$	0.9294	11.9546	13.5719
NLS	$h = \left(\frac{1}{7741.22}\right)\left[\frac{C_{pl}q}{h_{fg}}\right]\left[\frac{q}{\mu_l h_{fg}}\left(\frac{\sigma}{g(\rho_l-\rho_v)}\right)^{1/2}\right]^{-0.248}\left[\frac{Cp_l\mu_l}{k_l}\right]^{-1.989}$	0.938	11.1037	11.8737
NM	$h = \frac{1.1132P_c^{0.24}}{M^{0.312}T_c^{0.417}}(0.478R_a)^{0.03\left(1-\frac{p}{p_c}\right)}\frac{\left(\frac{p}{p_c}\right)^{0.318}}{\left[1-0.61\left(\frac{p}{p_c}\right)\right]^{-0.012}}q^{0.737}$	0.9258	12.6739	14.1924
NLS	$h = \frac{0.544P_c^{0.411}}{M^{0.817}T_c^{0.747}}(0.716R_a)^{0.03\left(1-\frac{p}{p_c}\right)}\frac{\left(\frac{p}{p_c}\right)^{0.058}}{\left[1-0.629\left(\frac{p}{p_c}\right)\right]^{-0.849}}q^{0.737}$	0.9258	12.6739	14.1924
NM-NLS	$h = 0.311q^{0.738}$	0.92	12.4595	15.3066

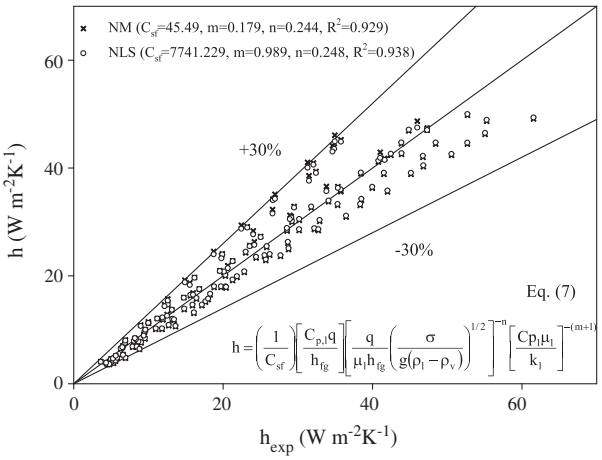

Fig. 7. Comparisons of experimental convective heat transfer coefficients with the most predictive proposed correlation obtained from optimization methods using 150 number of experimental data points.

References

[1] M.K. Das, N. Kishor, Adaptive fuzzy model identification to predict the heat transfer coefficient in pool boiling of distilled water, Expert Systems with Applications 36 (2009) 1142–1154.

[2] T. Liu, X. Sun, X. Li, H. Wang, Neural network analysis of boiling heat transfer enhancement using additives, International Journal of Heat and Mass Transfer 45 (2002) 5083–5089.

[3] G. Scalabrin, M. Condosta, P. Marchi, Modeling flow boiling heat transfer of pure fluids through artificial neural networks, International Journal of Thermal Sciences 45 (2006) 643–663.

[4] G. Scalabrin, M. Condosta, P. Marchi, Mixtures flow boiling: modeling heat transfer through artificial neural networks, International Journal of Thermal Sciences 45 (2006) 664–680.

[5] W.J. Wang, L.X. Zhao, C.L. Zhang, Generalized neural network correlation for flow boiling heat transfer of R22 and its alternative refrigerants inside horizontal smooth tubes, International Journal of Heat and Mass Transfer 49 (2006) 2458–2465.

[6] K.E. Gungor, R.H.S. Winterton, A general correlation for flow boiling in tubes and annuli, International Journal of Heat Mass Transfer 29 (1986) 351–358.

[7] A. Suriyawong, S. Wongwises, Nucleate pool boiling heat transfer characteristics of TiO_2–water nanofluids at very low concentrations, Experimental Thermal and Fluid Science 34 (2010) 992–999.

[8] V. Trisaksri, S. Wongwises, Nucleate pool boiling heat transfer of TiO_2–R141b nanofluids, International Journal of Heat and Mass Transfer 52 (2009) 1582–1588.

[9] M. Balcilar, A.S. Dalkilic, S. Wongwises, Artificial neural network (ANN) techniques for the determination of condensation heat transfer characteristics during downward annular flow of R134a inside a vertical smooth tube, International Communications in Heat and Mass Transfer 38 (2011) 75–84.

[10] J.A. Nelder, R. Mead, A simplex method for function minimization, Computer Journal 7 (1965) 308–313.

[11] M. Balcilar, A.S. Dalkilic, B. Bolat, S. Wongwises, Investigation of empirical correlations on the determination of condensation heat transfer characteristics using computational numerical methods during downward annular flow of R134a inside a vertical smooth tube, Journal of Mechanical Science and Technology 25 (2011) 1–20.

[12] W.M. Rhosenow, A method of correlating heat transfer data for surface boiling of liquids, Transactions of ASME 74 (1952) 969–975.

[13] G.P. Narayan, K.B. Anoop, G. Sateesh, S.K. Das, Effect of surface orientation on pool boiling heat transfer of nanoparticle suspensions, International Journal of Multiphase Flow 34 (2008) 145–160.

[14] R.A. Taylor, P.E. Phelan, Pool boiling of nanofluids: comprehensive review of existing data and limited new data, International Journal of Heat and Mass Transfer 52 (2009) 5339–5347.

[15] I.C. Bang, S.H. Chang, Boiling heat transfer performance and phenomena of Al_2O_3–water nano-fluids from a plain surface in a pool, International Journal of Heat and Mass Transfer 48 (2005) 2407–2419.

[16] S. Zhaohu, G. Maoqiong, L. Zhijian, W. Jianfeng, Nucleate pool boiling heat transfer coefficients of pure HFC134a, HC290, HC600a and their binary and ternary mixtures, International Journal of Heat and Mass Transfer 50 (2007) 94–104.

[17] K. Cornwell, S.D. Houston, Nucleate pool boiling on horizontal tubes: a convection-based correlation, International Journal of Heat Mass Transfer 37 (1994) 303–309.

[18] S.K. Das, N. Putra, W. Roetzel, Pool boiling characteristics of nano-fluids, International Journal of Heat and Mass Transfer 46 (2003) 851–862.

[19] S.K. Das, N. Putra, W. Roetzel, Pool boiling of nano-fluids on horizontal narrow tubes, International Journal of Multiphase Flow 29 (2003) 1237–1247.

International Journal of Heat and Mass Transfer 55 (2012) 3138–3146

Contents lists available at SciVerse ScienceDirect

International Journal of Heat and Mass Transfer

journal homepage: www.elsevier.com/locate/ijhmt

A dispersion model for predicting the heat transfer performance of TiO_2–water nanofluids under a laminar flow regime

Weerapun Duangthongsuk [a,b], Somchai Wongwises [b,c,*]

[a] Department of Mechanical Engineering, South-East Asia University, Bangkok, Thailand
[b] Fluid Mechanics, Thermal Engineering and Multiphase Flow Research Laboratory (FUTURE), Department of Mechanical Engineering, King Mongkut's University of Technology Thonburi, Bangmod, Bangkok 10140, Thailand
[c] The Academy of Science, The Royal Institute of Thailand, Sanam Suea Pa, Dusit, Bangkok 10300, Thailand

ARTICLE INFO

Article history:
Received 22 April 2011
Received in revised form 3 February 2012
Accepted 3 February 2012
Available online 22 March 2012

Keywords:
Nanofluids
Heat transfer performance
Thermal conductivity
Dispersion model

ABSTRACT

Nanofluids are a suspension of particles with ultrafine size in a conventional base fluid that increases the heat transfer performance of the original base fluid. They show higher thermal performance than base fluids especially in terms of the thermal conductivity and heat transfer coefficient. During the last decade, many studies have been carried out on the heat transfer and flow characteristics of nanofluids, both experimentally and theoretically. The purpose of this article is to propose a dispersion model for predicting the heat transfer coefficient of nanofluids under laminar flow conditions. TiO_2 nanoparticles dispersed in water with various volume fractions and flowing in a horizontal straight tube under constant wall heat flux were used. In addition, the predicted values were compared with the experimental data from He et al. [14]. In the present study, the results show that the proposed model can be used to predict the heat transfer behaviour of nanofluids with reasonable accuracy. Moreover, the results also indicate that the predicted values of the heat transfer coefficient obtained from the present model differ from those obtained by using the Li and Xuan equation by about 3.5% at a particle volume fraction of 2.0%.

1. Introduction

Conventional heat transfer fluids such as oil, water and ethylene glycol have inherently poor thermal properties. Thus, over the past ten years, many researchers have attempted to rectify the poor heat transfer properties of these fluids, in particular their thermal conductivity. In general, solids have several hundred-fold greater thermal conductivity than common fluids. In order to overcome this problem, ultrafine solid particles can be suspended in base fluids to increase their thermal performance. The earliest studies of the thermal performance of liquids with a nanoparticle suspension were reported by Masuda et al. [1] in 1993. However, the term nanofluids was introduced by Choi [2] in 1995, and subsequently gained popularity. Nanofluids were expected to be ideally suited for practical application because they have a substantially higher thermal conductivity and convective heat transfer coefficient relative to the base fluids.

Over the past decade, many researchers have reported the heat transfer and flow behaviour of various types of nanofluids, especially their thermal conductivity and heat transfer coefficient. A number of researchers have attempted to investigate the thermal behaviour of nanofluids both theoretically and experimentally. The available literature with respect to the heat transfer performance and flow characteristics of nanofluids is summarized elsewhere [3–5]. However, such reviews are not up to date. Recent papers dealing with the heat transfer and flow features of nanofluids both experimentally and theoretically are summarized below.

He et al. [6] experimentally studied the heat transfer and flow behaviours of TiO_2–distilled water nanofluids flowing through a vertical pipe in an upward direction under a constant heat flux in both a laminar and a turbulent flow regime. The experimental results showed that the local heat transfer coefficient increased with increasing particle concentration in both laminar and turbulent flow regimes in a given condition. They also showed that the pressure drop of the nanofluids was similar to that of the base fluid.

Nguyen et al. [7] experimentally investigated the heat transfer coefficient of an Al_2O_3–water nanofluid flowing through a small liquid cooling system of microprocessors under a turbulent flow regime. The results showed a much higher heat transfer coefficient for nanofluids than for the base liquid, with a nanofluid with a 36 nm particle diameter giving a higher heat transfer coefficient than that with a 47 nm particle diameter.

* Corresponding author at: Fluid Mechanics, Thermal Engineering and Multiphase Flow Research Laboratory (FUTURE), Department of Mechanical Engineering, King Mongkut's University of Technology Thonburi, Bangmod, Bangkok 10140, Thailand. Tel: +662 470 9115; fax: +662 470 9111.
E-mail address: somchai.won@kmutt.ac.th (S. Wongwises).

0017-9310/$ - see front matter © 2012 Elsevier Ltd. All rights reserved.
doi:10.1016/j.ijheatmasstransfer.2012.02.016

Nomenclature

C_p	specific heat, J/kgK
d	nanoparticle diameter, m
D	tube diameter, m
h	heat transfer coefficient, W/m^{2}K
k	thermal conductivity, W/mK
L	length of the test tube, m
Nu	Nusselt number
Pe	Peclet number
Pr	Prandtl number
q	heat flux, W/m^2
R	tube radius, m
Re	Reynolds number
T	temperature, K
u	mean velocity, m/s

Greek symbols

β	dispersion coefficient, W/mK
ϕ	volume fraction
κ_B	Boltzmann constant (1.3807×10^{-23} m^2 kg/ s^{2}K)
ρ	density, kg/m^3
α	thermal diffusivity, m^2/s
μ	viscosity, kg/ms

Subscript

ave	average
o	inlet
p	particles
nf	nanofluid
w	water or wall

Ko et al. [8] reported on an experiment in which the viscosity and pressure drop of CNT nanoparticles was dispersed in distilled water flowing through a horizontal tube. The effect of the CNT concentrations and preparation methods on the viscosity of nanofluids was also reported. Under laminar flow conditions, the results indicated that the nanofluids had larger friction factors than the base fluid. In contrast, under turbulent flow conditions, the friction factor of the nanofluids was very close to that of the base fluids.

Chein and Chuang [9] reported the performance of the microchannel heat sink (MCHS) using CuO–water nanofluids as coolants. At a low flow rate, the experimental results showed that nanofluids absorbed more energy than the base fluid. However, there was no contribution from heat absorption when the flow rate was high.

Duangthongsuk and Wongwises [10,11] studied the effect of thermophysical properties on the prediction of the heat transfer coefficient and also reported the heat transfer performance and friction characteristics of a TiO_2–water nanofluid. The results indicated that a number of thermophysical models have an insignificant effect on the calculated Nusselt number of the nanofluid. Moreover, the results also showed that the presence of nanoparticles leads to a higher heat transfer coefficient than that of water and that the pressure drop of the nanofluid is similar to that of the base fluid.

Nguyen et al. [12] studied the heat transfer performance of Al_2O_3–water nanofluids in a confined and submerged jet impinging on a horizontal and circular heated surface. The experimental results indicated that nanofluids with high particle fractions (6.0 vol.% and even 2.8 vol.%) do not seem to be appropriate for heat transfer enhancement purposes under such a configuration. Moreover, their results also showed that the use of nanofluids does not increase heat transfer, and in the worst cases, there was a clear decrease in the heat transfer coefficient. Thus, the use of nanofluids does not always guarantee enhancement of heat transfer.

Izadi et al. [13] numerically investigated the hydrodynamics and thermal behaviours of an Al_2O_3–water nanofluid flowing through an annulus under a laminar flow regime, using a single-phase model. The numerical results showed that the convective heat transfer coefficient increased with increasing particle concentration. Moreover, the results also indicated that the particle volume concentration has no significant effect on the dimensionless axial velocity, but does affect the temperature profile.

He et al. [14] numerically studied the convective heat transfer of a nanofluid with TiO_2 nanoparticles dispersed in water under laminar flow conditions. A single-phase model and combined Euler and Lagrange method (Discrete method) were used to determine the effects of volume concentrations, Reynolds number and aggregate sizes on the convective heat transfer and flow behaviour of the nanofluid. Their results indicated that the nanofluid significantly enhanced the Nusselt number, especially in the entrance region. Moreover, the numerical results were consistent with experimental data.

Bianco et al. [15] numerically investigated the heat transfer performance of an Al_2O_3–water nanofluid flowing through a circular tube under a laminar flow regime. A single-phase model and two-phase model were employed to describe the heat transfer coefficient of the nanofluid. The results showed that the heat transfer coefficient increased with increasing particle volume fraction as well as Reynolds number and was higher than that of the base fluid. Moreover, there was an approximately 11% difference in the average heat transfer coefficient between the single-phase and two-phase model.

Kumar et al. [16] used a single-phase thermal dispersion model to analyse the thermal properties and flow field of a nanofluid numerically. The results showed that suspended nanoparticles increased the heat capacity and surface area of the conventional base liquid, which led to an increase in the Nusselt number, especially at high volume fractions.

The review of literature shown above includes all studies of nanofluids flowing in channels, both experimental and theoretical. However, most of the models used involved commercial software and few compared the simulation results with the experimental data. In the present study, main concern is to develop a mathematical model to describe the convective heat transfer characteristics of nanofluids under a laminar flow conditions, and then compare the results with experimental data. This dispersion model is different from that proposed by He et al. [14] which is based on single phase method and combined Euler and Lagrange method.

2. Mathematical model and data reduction

2.1. Mathematical model

There are two different approaches to analysing the heat transfer enhancement of nanofluids. One is the two-phase model and the other is the single-phase model. Although the former describes the functions of both the liquid phase and solid phase in the heat transfer process, it requires a long time for computation and a high performance computer. The second model, assuming that both the liquid and particle phases are in thermal equilibrium and flow at the same velocity, is simpler and requires less computation time. However, although the behaviour of a nanofluid is more similar to a liquid than solid–liquid mixtures, several factors such as gravity, Brownian forces, friction between the liquid and solid particles, sedimentation and dispersion may coexist in the main flow of

nanofluids. So, this means that the slip velocity between the fluid and solid particles may not be zero and random movement of the particles in the main flow must be taken into account [17]. This model was first introduced by Taylor [18] in 1953. However, Xuan and Li [17] were the first to apply this model to describing the heat transfer characteristics of nanofluids under constant wall temperature boundary conditions. As mentioned above, the purpose of this work was to use the modified single-phase model (Dispersion model) to investigate the heat transfer performance of nanofluids flowing through a horizontal tube under a laminar flow regime and constant wall heat flux boundary conditions. On the basis of this model, the governing equation under steady state conditions and a negligible axial temperature gradient is as follows:

$$u\frac{\partial T}{\partial x}=\frac{1}{r}\frac{\partial}{\partial r}\left[\alpha_{nf}+\frac{\beta}{(\rho Cp)_{nf}}\right]r\frac{\partial T}{\partial r} \tag{1}$$

where u is the velocity of nanofluid which is assumed constant along the test section, α_{nf} is the thermal diffusivity of the nanofluid, and β is the thermal dispersion coefficient, which considers the contribution of hydrodynamic dispersion and the irregular movement of the ultra-fine particles.

Unfortunately, to date, there has been no theoretical or experimental work on the dispersion coefficient of nanofluids. However, the dispersion coefficient (β) appearing in Eq. (1) can be calculated by Einstein–Strokes's equation, which was introduced by Buongiorno [19]. The form of this equation is as follows:

$$\beta=\frac{\kappa_B T_{nf}}{3\pi\mu_{nf}d_P} \tag{2}$$

in which κ_B is Boltzmann's constant (1.3807×10^{-23} m^2 kg/s^{2}K) and d_P is the nanoparticle diameter (m). In general, the dispersion coefficient for water-based nanofluids at room temperature ranges between 4×10^{-10} to 4×10^{-12} m^2/s [19].

In order to find the solution for Eq. (1), the following boundary conditions are required:

$$T=T(r,x)$$
$$T(r,0)=T_0 \tag{3}$$
$$\frac{\partial T}{\partial r}(0,x)=0 \tag{4}$$
$$\frac{\partial T}{\partial r}(r,x)=\frac{q_w}{k} \tag{5}$$

where T_0 is the inlet temperature of fluid (K), q_w is the wall heat flux and k is the thermal conductivity of the nanofluid.

Applying the following dimensionless parameters

$$\theta=\frac{T-T_0}{T_w-T_0} \tag{6}$$
$$\bar{r}=r/R \quad \text{and} \quad \bar{x}=x/L \tag{7}$$

and rearranging the left-hand side and right-hand side of Eq. (1), we obtain the following expressions:

$$u\frac{\partial T}{\partial x}=\frac{u(T_w-T_0)}{L}\frac{\partial\theta}{\partial\bar{x}} \tag{8}$$

and

$$\frac{1}{r}\frac{\partial}{\partial r}\left[\frac{k^*_{eff}}{\rho Cp}\right]r\frac{\partial T}{\partial r}=\frac{1}{R^2\bar{r}}\frac{\partial}{\partial\bar{r}}\left[\frac{k^*_{eff}}{\rho Cp}\bar{r}(T_w-T_0)\frac{\partial\theta}{\partial\bar{r}}\right] \tag{9}$$

where $k^*_{eff}=\alpha_{nf}+\beta$

Substituting Eqs. (8) and (9) into Eq. (1) yields,

$$\frac{u(T_w-T_0)}{L}\frac{\partial\theta}{\partial\bar{x}}=\frac{1}{R^2\bar{r}}\frac{\partial}{\partial\bar{r}}\left[\frac{k^*_{eff}}{\rho Cp}\bar{r}(T_w-T_0)\frac{\partial\theta}{\partial\bar{r}}\right] \tag{10}$$

By rearranging Eq. (10), we obtain

$$\frac{u}{L}\frac{\partial\theta}{\partial\bar{x}}=\frac{1}{R^2\bar{r}}\frac{\partial}{\partial\bar{r}}\left[\frac{k^*_{eff}}{\rho Cp}\bar{r}\frac{\partial\theta}{\partial\bar{r}}\right] \tag{11}$$

Rearranging the above equation yields

$$\frac{uL}{L^2}\frac{\partial\theta}{\partial\bar{x}}=\frac{1}{R^2\bar{r}}\frac{k^*_{eff}}{\rho Cp}\frac{\partial}{\partial\bar{r}}\bar{r}\frac{\partial\theta}{\partial\bar{r}} \tag{12}$$

let

$$\frac{k^*_{eff}}{\rho Cp}=\alpha^*_{eff} \tag{13}$$

Substituting Eq. (13) into Eq. (12), we obtain

$$\frac{uL}{\alpha^*_{eff}}\frac{\partial\theta}{\partial\bar{x}}=\frac{L^2}{R^2\bar{r}}\frac{\partial}{\partial\bar{r}}\left[\bar{r}\frac{\partial\theta}{\partial\bar{r}}\right] \tag{14}$$

Let

$$\frac{uL}{\alpha^*_{eff}}=Pe^* \tag{15}$$

Substituting Eq. (15) into Eq. (14), yields

$$Pe^*\frac{R^2}{L^2}\frac{\partial\theta}{\partial\bar{x}}=\frac{1}{\bar{r}}\frac{\partial}{\partial\bar{r}}\left[\bar{r}\frac{\partial\theta}{\partial\bar{r}}\right] \tag{16}$$

let

$$Pe^*\frac{R^2}{L^2}=\overline{Pe} \tag{17}$$

Substituting the above equation into Eq. (16) yields

$$\overline{Pe}\frac{\partial\theta}{\partial\bar{x}}=\frac{1}{\bar{r}}\frac{\partial}{\partial\bar{r}}\left[\bar{r}\frac{\partial\theta}{\partial\bar{r}}\right] \tag{18}$$

Applying the separation method yields

$$\theta(\bar{r},\bar{x})=R_1(\bar{r})X_1(\bar{x})+R_2(\bar{r})+X_2(\bar{x}) \tag{19}$$

The new boundary conditions are expressed as follows:

$$\theta(\bar{r},0)=0 \tag{20}$$
$$\theta(0,\bar{x})=\text{finite} \tag{21}$$
$$\frac{\partial\theta}{\partial\bar{r}}(1,\bar{x})=1 \tag{22}$$

By rearranging Eq. (18), we obtain

$$\frac{\partial\theta}{\partial\bar{x}}=R_1\frac{dX_1}{d\bar{x}}+\frac{dX_2}{d\bar{x}} \tag{23}$$

and

$$\frac{\partial}{\partial\bar{r}}\bar{r}\frac{\partial\theta}{\partial\bar{r}}=\frac{d}{d\bar{r}}\bar{r}X_1\frac{dR_1}{d\bar{r}}+\frac{d}{d\bar{r}}\bar{r}\frac{dR_2}{d\bar{r}} \tag{24}$$

Substituting Eqs. (23) and (24) into Eq. (18), we obtain

$$\overline{Pe}\left[R_1\frac{dX_1}{d\bar{x}}+\frac{dX_2}{d\bar{x}}\right]=\frac{X_1}{\bar{r}}\frac{d}{d\bar{r}}\bar{r}\frac{dR_1}{d\bar{r}}+\frac{1}{\bar{r}}\frac{d}{d\bar{r}}\bar{r}\frac{dR_2}{d\bar{r}} \tag{25}$$

By arranging Eq. (25), we obtain

$$\overline{Pe}R_1\frac{dX_1}{d\bar{x}}=\frac{X_1}{\bar{r}}\frac{d}{d\bar{r}}\bar{r}\frac{dR_1}{d\bar{r}} \tag{26}$$

Rearranging again yields

$$\frac{\overline{Pe}}{X_1}\frac{dX_1}{d\bar{x}}=\frac{1}{R_1\bar{r}}\frac{d}{d\bar{r}}\bar{r}\frac{dR_1}{d\bar{r}}=-\lambda^2 \tag{27}$$

According to Eq. (27), rearranging yields

$$\frac{1}{R_1\bar{r}}\frac{d}{d\bar{r}}\bar{r}\frac{dR_1}{d\bar{r}}+\lambda^2=0$$

$$\frac{1}{R_1\bar{r}}\left[\bar{r}\frac{d^2R_1}{d\bar{r}^2}+\frac{dR_1}{d\bar{r}}\right]+\lambda^2=0$$

$$\frac{1}{R_1}\frac{d^2R_1}{d\bar{r}^2}+\frac{1}{R_1\bar{r}}\frac{dR_1}{d\bar{r}}+\lambda^2=0$$

$$\frac{d^2R_1}{d\bar{r}^2}+\frac{1}{\bar{r}}\frac{dR_1}{d\bar{r}}+\lambda^2R_1=0 \tag{28}$$

The general solution of the above equation is

$$R_1=C_1J_0(\lambda\bar{r})+C_2Y_0(\lambda\bar{r}) \tag{29}$$

The remaining term in Eq. (27) is

$$\frac{\overline{Pe}}{X_1}\frac{dX_1}{d\bar{x}}+\lambda^2=0$$

$$\frac{1}{X_1}dX_1+\frac{\lambda^2}{\overline{Pe}}d\bar{x}=0 \tag{30}$$

The general solution of this equation is

$$X_1=C_3e^{-\lambda^2\bar{x}/\overline{Pe}} \tag{31}$$

The remaining term in Eq. (25) is

$$\overline{Pe}\frac{dX_2}{d\bar{x}}=\frac{1}{\bar{r}}\frac{d}{d\bar{r}}\bar{r}\frac{dR_2}{d\bar{r}}=C_4 \tag{32}$$

$$X_2=\frac{C_4}{\overline{Pe}}\bar{x}+C_5 \tag{33}$$

and

$$R_2=\frac{C_4}{4}\bar{r}^2+C_5\ln\bar{r}+C_6 \tag{34}$$

Substituting Eq. (21) into Eq. (29), we obtain

$$R_1=C_1J_0(0)+C_2Y_0(0)$$
$$C_2=0$$

Substituting Eq. (21) into Eq. (34) yields

$$C_5=0$$

From the above expressions, Eq. (19) can be changed as follows:

$$\theta(\bar{r},\bar{x})=C_1C_3e^{-\lambda_n^2\bar{x}/\overline{Pe}}J_0(\lambda_n\bar{r})+\frac{C_4}{4}\bar{r}^2+C_6+\frac{C_4}{\overline{Pe}}\bar{x} \tag{35}$$

Substituting Eq. (20) into Eq. (35), we obtain

$$0=C_1C_3J_0(\lambda_n\bar{r})+\frac{C_4}{4}\bar{r}^2+C_6 \tag{36}$$

From the linearly independent relation, this yields

$$C_6=0$$

Differentiating Eq. (35) yields

$$\frac{\partial\theta}{\partial\bar{r}}=C_1C_3e^{-\lambda_n^2\bar{x}/\overline{Pe}}(-\lambda_n)J_1(\lambda_n\bar{r})+\frac{C_4}{2}\bar{r} \tag{37}$$

Substituting Eq. (22) into Eq. (37), we obtain

$$1=-\lambda_nC_1C_3e^{-\lambda_n^2\bar{x}/\overline{Pe}}J_1(\lambda_n)+\frac{C_4}{2}$$
$$C_4=2 \tag{38}$$

where λ_n are eigen values that are the positive roots of the $J_1(\lambda_n)=0$

Then, substituting $C_4=2$ into Eq. (36), we obtain

$$0=C_1C_3J_0(\lambda_n\bar{r})+\frac{\bar{r}^2}{2}$$
$$-\frac{\bar{r}^2}{2}=\sum_{n=0}^{\infty}C_nJ_0(\lambda_n\bar{r}) \tag{39}$$

Rearranging the above equation yields

$$-\frac{\bar{r}^2}{2}=C_0J_0(\lambda_n\bar{r})+\sum_{n=1}^{\infty}C_nJ_0(\lambda_n\bar{r}) \tag{40}$$

Considering a part of Eq. (40)

$$-\frac{\bar{r}^2}{2}=\sum_{n=1}^{\infty}C_nJ_0(\lambda_n\bar{r})$$

Multiplying the above equation by $\bar{r}J_0(\lambda_n\bar{r})d\bar{r}$ and then integrating from 0 to 1, yields

$$-\int_0^1\frac{\bar{r}^2}{2}\bar{r}J_0(\lambda_n\bar{r})d\bar{r}=\int_0^1\sum_{n=1}^{\infty}C_nJ_0(\lambda_n\bar{r})\bar{r}J_0(\lambda_n\bar{r})d\bar{r}$$
$$-\frac{1}{2}\int_0^1\bar{r}^2\bar{r}J_0(\lambda_n\bar{r})d\bar{r}=\frac{1}{2}\sum_{n=1}^{\infty}C_nJ_0^2(\lambda_n) \tag{41}$$

Taking the right-hand term of Eq. (41) into account and applying the method of bypass integration, we obtain

$$w=\bar{r}^2,\quad dw=2\bar{r}d\bar{r}\quad\text{and}\quad dv=\bar{r}J_0(\lambda_n\bar{r})d\bar{r}$$

This yields

$$v=\int dv=\int\bar{r}J_o(\lambda_n\bar{r})d\bar{r}=\frac{1}{\lambda_n}\int\lambda_n\bar{r}J_o(\lambda_n\bar{r})d\bar{r}=\frac{1}{\lambda_n}\bar{r}J_1(\lambda_n\bar{r})$$

Applying the relation $\int wdv=wv-\int vdw$ yields

$$\int_0^1\bar{r}^2\bar{r}J_0(\lambda_n\bar{r})d\bar{r}=\frac{\bar{r}}{\lambda_n}\bar{r}J_1(\lambda_n\bar{r})\Big|_0^1-\int_0^1\frac{\bar{r}}{\lambda_n}J_1(\lambda_n\bar{r})2\bar{r}d\bar{r}$$
$$=\frac{1}{\lambda_n}J_1(\lambda_n)-\frac{2}{\lambda_n^2}\int_0^1\lambda_n\bar{r}^2J_1(\lambda_n\bar{r})d\bar{r}$$
$$=-\frac{2}{\lambda_n^2}\bar{r}^2J_2(\lambda_n\bar{r})\Big|_0^1$$
$$\int_0^1\bar{r}^2\bar{r}J_0(\lambda_n\bar{r})d\bar{r}=-\frac{2}{\lambda_n^2}J_2(\lambda_n)$$

Substituting the above equation into Eq. (41), we obtain

$$-\frac{1}{2}\frac{2}{\lambda_n^2}J_2(\lambda_n\bar{r})=\frac{1}{2}J_0^2(\lambda_n)\sum_{n=1}^{\infty}C_n$$
$$C_n=\sum_{n=1}^{\infty}\frac{2}{\lambda_n^2}\frac{J_2(\lambda_n)}{J_0^2(\lambda_n)} \tag{42}$$

since

$$J_{v+1}(x)=\frac{2v}{x}J_v(x)-J_{v-1}(x)$$

And given $v=1$, we obtain

$$J_2(x)=\frac{2}{x}J_1(x)-J_0(x)$$

Rearranging Eq. (42) yields

$$C_n=\sum_{n=1}^{\infty}\frac{2}{\lambda_n^2}\left[\frac{2}{\lambda_n}J_1(\lambda_n)-J_0(\lambda_n)\right]\frac{1}{J_0^2(\lambda_n)}$$
$$C_n=-\sum_{n=1}^{\infty}\frac{2}{\lambda_n^2}\frac{J_0(\lambda_n)}{J_0^2(\lambda_n)}=-\sum_{n=1}^{\infty}\frac{2}{\lambda_n^2}\frac{1}{J_0(\lambda_n)} \tag{43}$$

The remaining term in Eq. (40) is

$$-\frac{\bar{r}^2}{2}=C_0J_0(\lambda_n\bar{r})$$

Multiplying by $\bar{r}J_0(\lambda_n\bar{r})d\bar{r}$ and integration from 0 to 1 yields

$$-\frac{1}{2}\int_0^1 \bar{r}^2\bar{r}J_0(\lambda_n\bar{r})d\bar{r} = C_0\int_0^1 J_0(\lambda_0\bar{r})\bar{r}J_0(\lambda_0\bar{r})d\bar{r}$$

Applying the relations $J_0(\lambda_n\bar{r}) = 0$ and $J_0(\lambda_0\bar{r}) = 1$ yields

$$-\frac{1}{2}\frac{\bar{r}^4}{4}\Big|_0^1 = C_0\frac{\bar{r}^2}{2}\Big|_0^1$$

$$C_0 = -\frac{1}{4} \tag{44}$$

Eventually, the final solution of Eq. (19) is as follows:

$$\theta = \frac{T-T_0}{T_w-T_0} = \frac{2\bar{x}}{\overline{Pe}} + \frac{\bar{r}^2}{2} - \frac{1}{4} - 2\sum_{n=1}^{\infty} e^{-\lambda_n^2\bar{x}/\overline{Pe}}\frac{J_0(\lambda_n\bar{r})}{\lambda_n^2 J_0(\lambda_n)} \tag{45}$$

For the constant heat flux boundary condition, the heat transfer equation at the tube wall is defined as follows:

$$q_w = k_{eff}^*\frac{\partial T}{\partial r}\Big|_{r=R}$$

By rearranging the above equation, we obtain

$$\frac{q_w R}{k_{eff}^*} = (T_w - T_o) \tag{46}$$

Substituting the above equation into Eq. (45) yields

$$\frac{T-T_0}{\frac{q_w R}{k_{eff}^*}} = \frac{2\bar{x}}{\overline{Pe}} + \frac{\bar{r}^2}{2} - \frac{1}{4} - 2\sum_{n=1}^{\infty} e^{-\lambda_n^2\bar{x}/\overline{Pe}}\frac{J_0(\lambda_n\bar{r})}{\lambda_n^2 J_0(\lambda_n)} \tag{47}$$

In this situation, the wall heat flux is known. So, the variation in wall temperature along the test section can be expressed as follows:

$$\frac{T_w-T_0}{\frac{q_w R}{k_{eff}^*}} = \frac{2\bar{x}}{\overline{Pe}} + \frac{1}{2} - \frac{1}{4} - 2\sum_{n=1}^{\infty} e^{-\lambda_n^2\bar{x}/\overline{Pe}}\frac{J_0(\lambda_n)}{\lambda_n^2 J_0(\lambda_n)}$$

$$\frac{T_w-T_0}{\frac{q_w R}{k_{eff}^*}} = \frac{2\bar{x}}{\overline{Pe}} + \frac{1}{4} - 2\sum_{n=1}^{\infty} \frac{e^{-\lambda_n^2\bar{x}/\overline{Pe}}}{\lambda_n^2} \tag{48}$$

By applying the energy balance

$$\rho A_t u Cp(T_b - T_o) = q_w A_w$$

From the above equation, the variation in bulk fluid temperature along the test section can be expressed as follows:

$$T_b(x) - T_o = \frac{2q_w x}{\rho RuCp} \tag{49}$$

Multiplying the above equation by $\frac{Rk_{eff}^*}{Rk_{eff}^*}$ yields

$$T_b(x) - T_o = \frac{2q_w x}{\rho RuCp}\frac{Rk_{eff}^*}{Rk_{eff}^*} = \frac{2xk_{eff}^*}{\rho uCpR^2}\frac{q_w R}{k_{eff}^*} \tag{50}$$

Dividing this equation by $\frac{q_w R}{k_{eff}^*}$, we obtain

$$\frac{T_b(x) - T_o}{\frac{q_w R}{k_{eff}^*}} = \frac{2xk_{eff}^*}{\rho uCpR^2} \tag{51}$$

where $x = \bar{x}L$

Subtracting Eq. (51) from Eq. (48), we obtain

$$\frac{T_w - T_b(\bar{x})}{\frac{q_w R}{k_{eff}^*}} = \frac{2\bar{x}}{\overline{Pe}} + \frac{1}{4} - 2\sum_{n=1}^{\infty}\frac{e^{-\lambda_n^2\bar{x}/\overline{Pe}}}{\lambda_n^2} - \frac{2\bar{x}Lk_{eff}^*}{\rho uCpR^2} \tag{52}$$

Considering the first term of the right hand side of Eq. (52) and applying the relations in Eq. (17), yields

$$\frac{2\bar{x}}{\overline{Pe}} = \frac{2\bar{x}}{Pe^*}\frac{L^2}{R^2}$$

By rearranging the above equation, we obtain

$$\frac{2\bar{x}}{\overline{Pe}} = \frac{2\bar{x}L^2}{R^2}\frac{\alpha_{eff}^*}{uL} = \frac{2\bar{x}L^2}{R^2uL}\frac{k_{eff}^*}{\rho Cp} = \frac{2\bar{x}Lk_{eff}^*}{R^2u\rho Cp} \tag{53}$$

Substituting the above equation into Eq. (52) yields

$$\frac{T_w - T_b(\bar{x})}{\frac{q_w R}{k_{eff}^*}} = \frac{1}{4} - 2\sum_{n=1}^{\infty}\frac{e^{-\lambda_n^2\bar{x}/\overline{Pe}}}{\lambda_n^2} \tag{54}$$

From the Newton Cooling laws:

$$h = \frac{q_w}{(T_w - T_b)}$$

On rearranging, we obtain

$$\frac{T_w - T_b}{q_w} = \frac{1}{h}$$

Substituting the above equation into Eq. (54), the analytical correlation of the local Nusselt number of the nanofluid is obtained as follows:

$$\frac{k_{eff}^*}{h_x R} = \frac{1}{4} - 2\sum_{n=1}^{\infty}\frac{e^{-\lambda_n^2\bar{x}/\overline{Pe}}}{\lambda_n^2}$$

$$\frac{2k_{eff}^*}{h_x D} = \frac{1}{4} - 2\sum_{n=1}^{\infty}\frac{e^{-\lambda_n^2\bar{x}/\overline{Pe}}}{\lambda_n^2}$$

$$\frac{h_x D}{k_{eff}^*} = Nu_x = \frac{8}{1 - 8\sum_{n=1}^{\infty}\frac{e^{-\lambda_n^2\bar{x}/\overline{Pe}}}{\lambda_n^2}} \tag{55}$$

Moreover, the average heat transfer coefficient can be calculated using the following equation:

$$h_{ave} = \frac{1}{L}\int_{x_1}^{x_2} h_x dx \tag{56}$$

In order to calculate the local heat transfer coefficient Eq. (55) along the test section, the distance along the test tube is divided into numerous sections. The eigenvalues (λ_n) are the positive roots of the equation of $J_1(\lambda_n) = 0$. The $\overline{Pe}$ number that appears in Eq. (55) can be calculated using Eq. (17).

Finally, the average heat transfer coefficient obtained from the present model was compared with the correlation proposed by Li and Xuan [20] as follows:

Table 1
The thermophysical properties of nanofluids used in the present study.

Properties	Particle volume fraction (%)						
	0	**0.24**	**0.6**	**1.18**	**2.0**	**4.0**	**6.0**
ρ (kg/m^3)	998	1004.2	1016.9	1035.3	1061.3	1124.7	1188.2
Cp (J/kgK)	4180.8	4174	4160	4140	4111.5	4042.1	3972.7
μ (kg/ms)	0.000922	0.000927	0.000937	0.000951	0.000971	0.00103	0.00108
k (W/mK)	0.592	0.595	0.601	0.610	0.623	0.655	0.689

$$h_{nf} = 0.4328(k_{nf}/D)(1.0 + 11.285\phi^{0.754}Pe_d^{0.218})Re_{nf}^{0.333}\mathrm{Pr}_{nf}^{0.4} \quad (57)$$

The physical properties such as the density, viscosity, and specific heat and thermal conductivity of the nanofluid were calculated using the following published correlations:

The density and specific heat were calculated from equations in Pak and Cho [21], which are as follows:

$$\rho_{nf} = \phi\rho_p + (1-\phi)\rho_w \quad (58)$$

and

$$Cp_{nf} = \phi Cp_p + (1-\phi)Cp_w \quad (59)$$

Brinkman [22] suggested an equation to calculate the viscosity of the suspension, which is defined as follows:

$$\mu_{nf} = \frac{1}{(1-\phi)^{2.5}}\mu_w \quad (60)$$

Similarly, one well-known equation for calculating the thermal conductivity of a nanofluid is the Hamilton and Crosser [23] model, which is expressed in the following form:

$$k_{nf} = \left[\frac{k_p + (n-1)k_w - (n-1)\phi(k_w - k_p)}{k_p + (n-1)k_w + \phi(k_w - k_p)}\right]k_w \quad (61)$$

$$n = 3/\psi \quad (62)$$

where n is the empirical shape factor and ψ is the sphericity, defined as the ratio of the surface area of a sphere (with the same volume as the given particle) to the surface area of the particle. The sphericity is 1 and 0.5 for the spherical and cylindrical shapes, respectively. Moreover, ϕ is the volume concentration, k is the thermal conductivity.

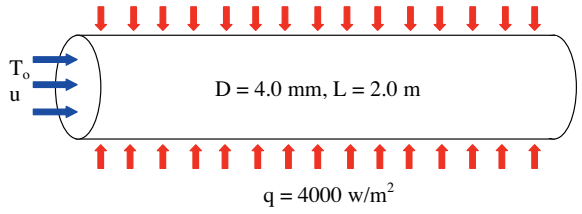

Fig. 1. Schematic diagram of the simulation domain.

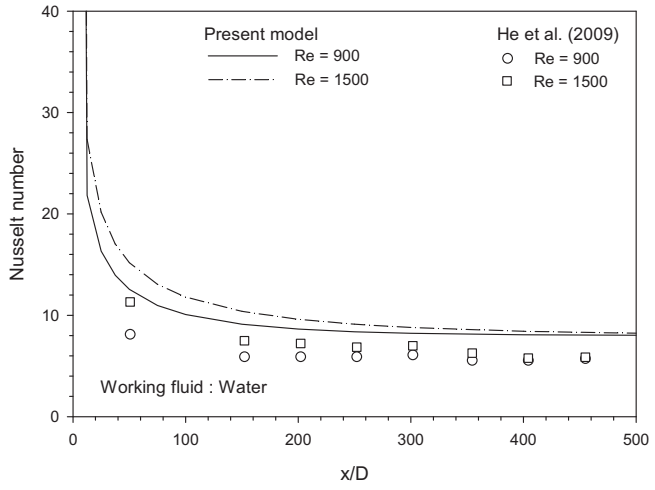

Fig. 2. Comparison of the Nusselt number between the measured data of He et al. [14] and the predicted values for water.

It should be noted that the above equation can be used to estimate the Nusselt number of a nanofluid under constant heat flux boundary conditions. However, other aspects of the heat transfer condition can be seen in Xuan and Li [17]. It is evident that the dispersion effect of the nanoparticles resulting from their random

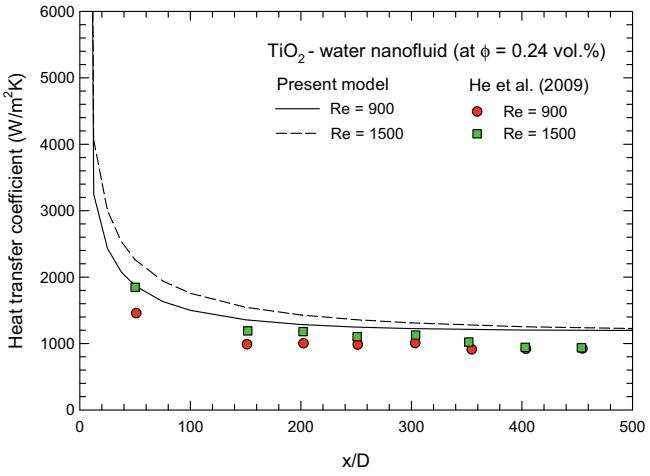

(a) at particle concentration of 0.24 vol.%

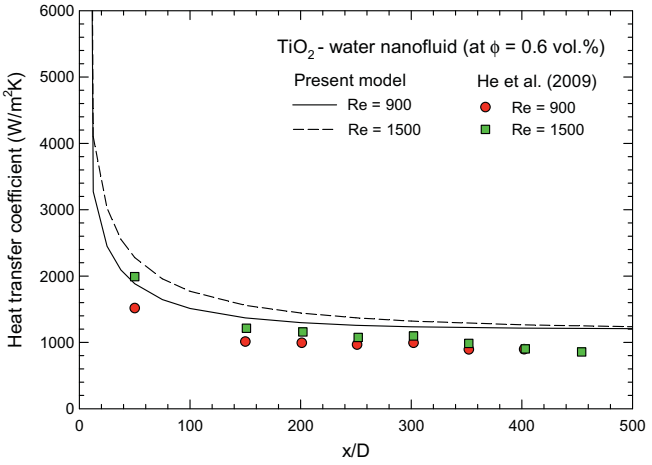

(b) at particle concentration of 0.60 vol.%

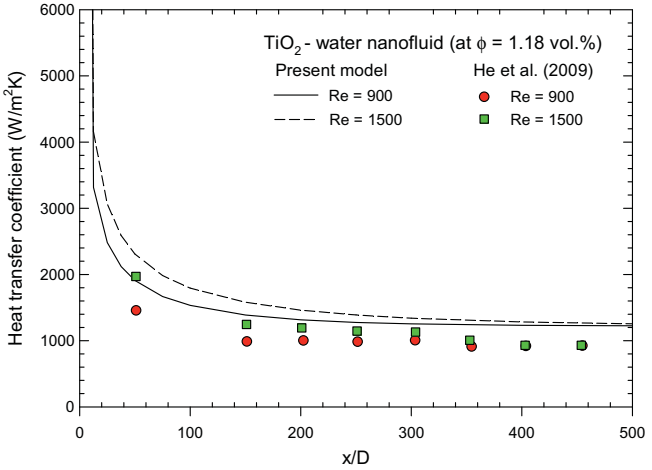

(c) at particle concentration of 1.18 vol.%

Fig. 3. Comparison of the predicted local heat transfer coefficients with those obtained from measured data of He et al. [14] for nanofluids with various volume fractions and Reynolds number.

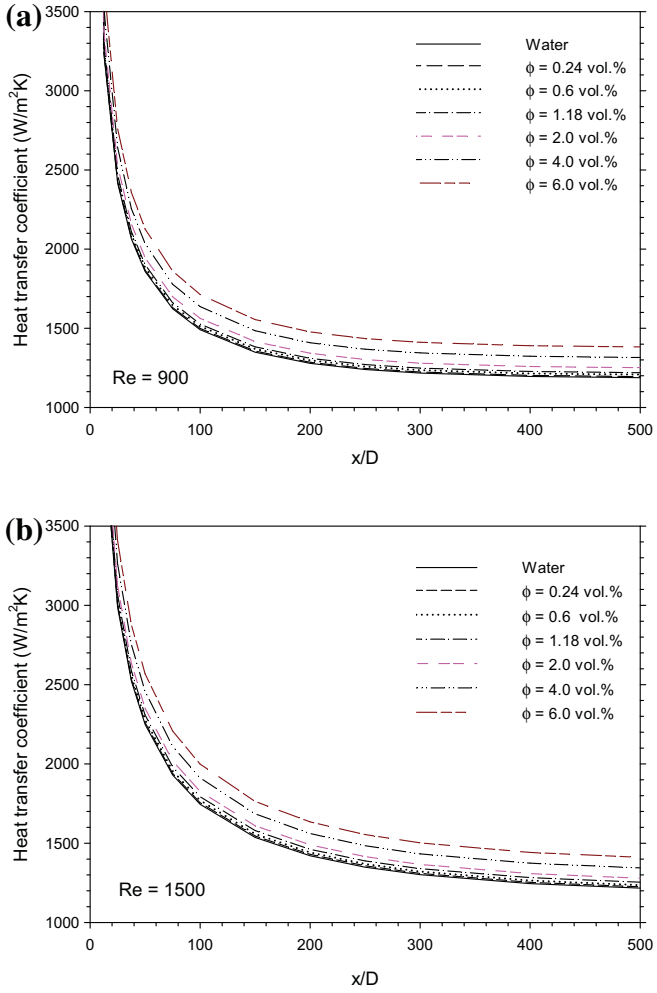

Fig. 4. Local heat transfer coefficient obtained from the present model as a function of particle concentrations at Reynolds number of 900 and 1500.

movement should be included in the model. However, a comparison of this model with the experimental data is still lacking, and was thus the main objective of this study.

2.2. Simulation conditions

For comparison with available experimental data, the data of He et al. [14] were used. In their study, a straight pipe with a 2.0 m length and 4.00 mm inner diameter was used as a test section. TiO_2 nanoparticles dispersed in water with volume concentrations of 0.24%, 0.6% and 1.18% were used to determine the heat transfer coefficient of a nanofluid. The wall heat flux was kept constant at 4000 W/m^2. Similarly, the Reynolds number was kept constant at 900 and 1500. The thermophysical properties of nanofluids used in the present study are shown in Table 1 and the geometrical configuration used in the simulation is shown in Fig. 1.

3. Results and discussion

Fig. 2 shows a comparison of the Nusselt number obtained from the simulation results and the experimental data of He et al. [14]. The data are obtained from pure water. It can be seen that the proposed model gives about a 25% higher predicted Nusselt number than the measured data.

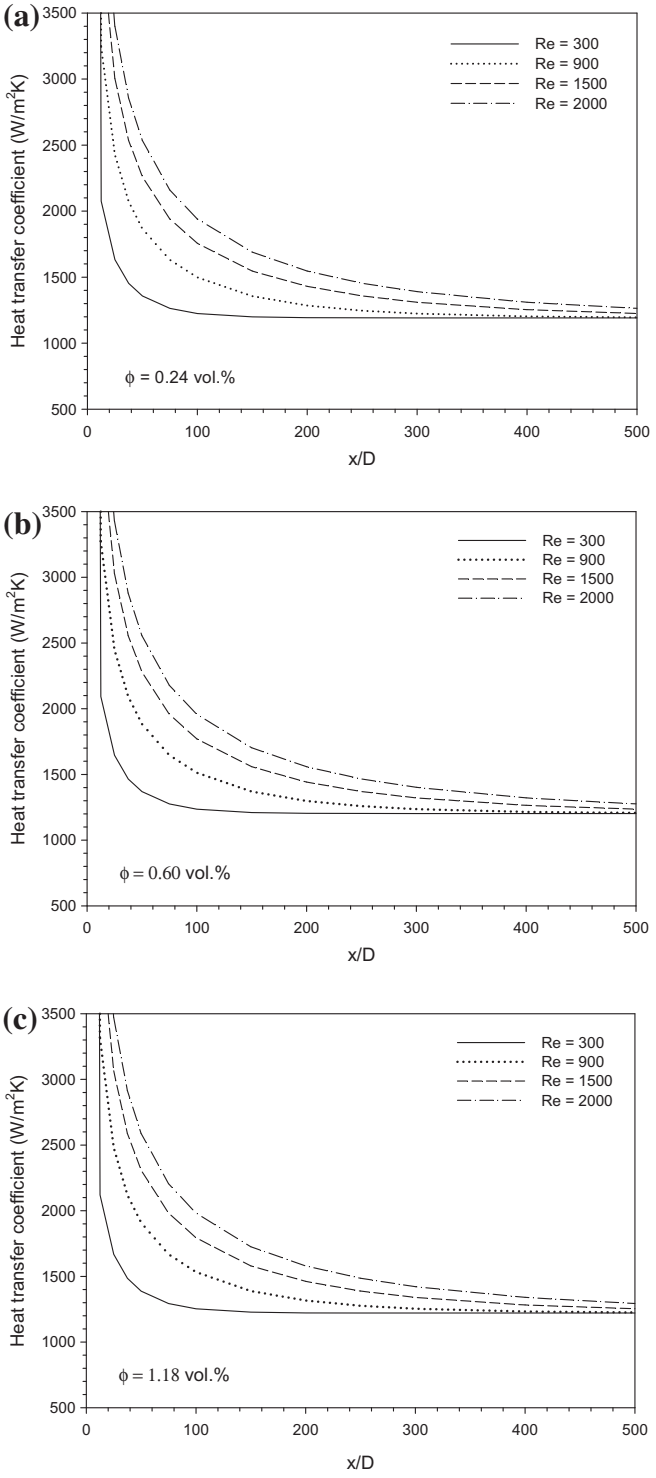

Fig. 5. Local heat transfer coefficient obtained from the present model as a function of Reynolds number at various particle concentration (a) 0.24 vol.%. (b) 0.6 vol.% (c) 1.18 vol.%.

Similarly, Fig. 3a–c shows a comparison of the predicted heat transfer coefficient of nanofluids obtained from the present model and the measured values of He et al. [14]. As shown in Fig. 3, the data from the present model give a 25–30% larger heat transfer coefficient than the experimental data. However, although the present model shows moderate over-prediction of the heat transfer coefficient compared with the measured data, this approach is easier and consumes less computational time compared with

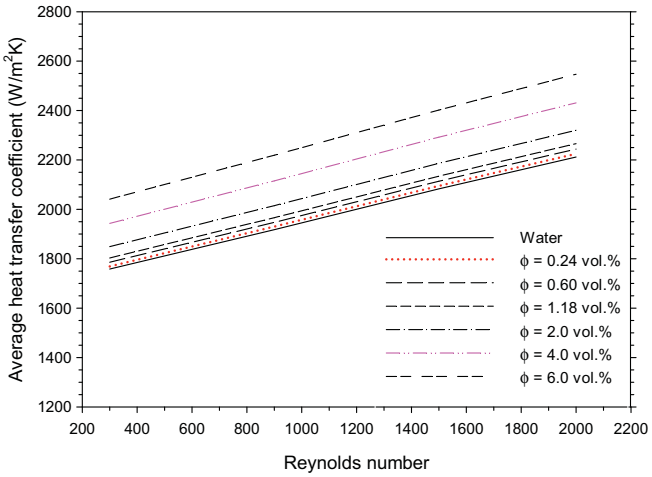

Fig. 6. Predicted average heat transfer coefficient as a function of Reynolds number and particle concentrations.

other models proposed by a number of researchers using commercial software.

Fig. 4a and b shows the effect of particle concentration on the heat transfer coefficient of nanofluids for a Re of 900 and 1500. The results indicate that the heat transfer coefficient of nanofluids increases with increasing particle volume fractions and decreases with increasing tube length, as expected. This behavior occurs because adding nanoparticles to a base fluid leads to an increase in the thermal conductivity of the base liquid. Moreover, the chaotic movement of nanoparticles in the main flow brings to large energy exchange process [24].

Fig. 5a–c shows the variation in the local heat transfer coefficient obtained from the present model as a function of Reynolds number at a particle volume fraction of 0.24, 0.6 and 1.18 vol.%, respectively. The increasing of the Reynolds number leads to an increasing of heat transfer rate and results in an increase in the heat transfer coefficient.

Similarly, Fig. 6 also shows the average heat transfer coefficient as a function of Reynolds number and particle concentrations. The simulation results show that the average heat transfer coefficient of nanofluids increases with increasing Reynolds number as well as with particle concentration. The reason for this is given in the preceding section.

Fig. 7a–c shows a comparison of the predicted average heat transfer coefficient obtained from the proposed model and the calculated values from obtained from Li and Xuan [2] for particle volume fractions of 0.6, 1.0 and 2.0%, respectively. At Reynolds numbers ranging between 1200 and 2000, the use of the present model to evaluate the heat transfer coefficient of nanofluids gives different values compared with the Li and Xuan correlation [20], by around 13% (at ϕ = 1.0 vol.%) and 3.5% (at ϕ = 2.0 vol.%).

Besides the difference in the nanoparticles used in both studies, the proposed model is also analyzed by the means of analytical approach whereas the Li and Xuan correlation was established based on their experimental data. Therefore it is impossible that both results will be equal. In general, for experimental approach, the complicated phenomena such as agglomeration, random movement of the nanoparticle, the slip velocity between the solid–liquid mixture, sedimentation and deposition on the tube wall will be coexisting in the main flow. These phenomenon rather differ from the assumption used in the present model which cause some different between the proposed model and the Li and Xuan correlation. However there is a good agreement with respect to the shapes of the heat transfer coefficient profile.

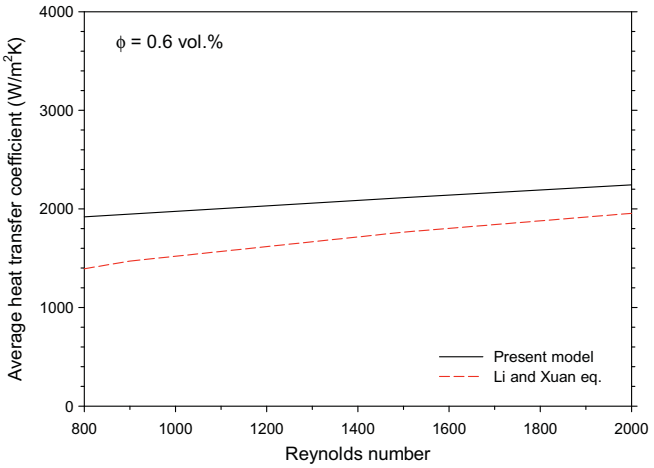

(a) at particle concentration of 0.60 vol.%

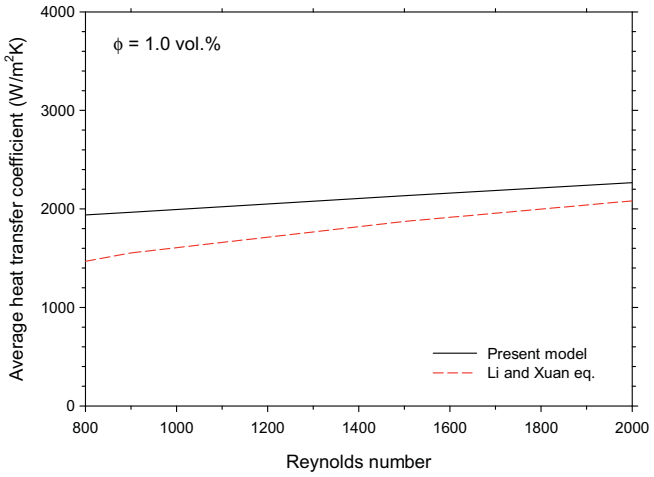

(b) at particle concentration of 1.0 vol.%

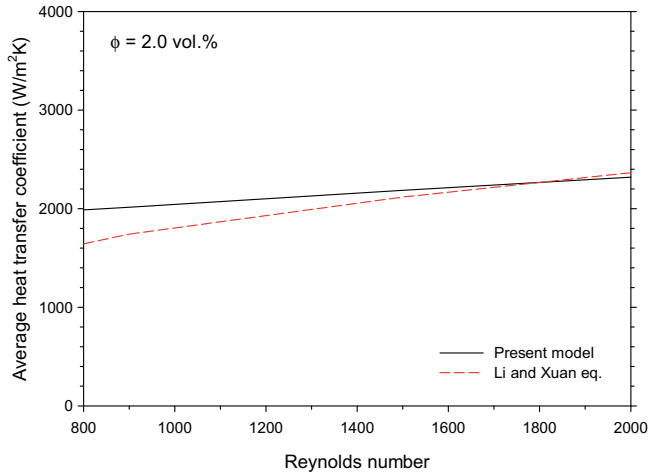

(c) at particle concentration of 2.0 vol.%

Fig. 7. Comparison of the average heat transfer coefficient of nanofluids between present model and the Li and Xuan correlation.

4. Conclusions

In the present study, the dispersion model for predicting the heat transfer performance of TiO_2–water nanofluids flowing under a laminar flow regime and constant heat flux is proposed. The Einstein–Strokes's equation is used to calculate the dispersion coefficient of nanofluids. The results from the present model are

compared with the data of He et al. [14]. The simulation results indicate that the heat transfer coefficient obtained from the proposed model is higher than the experimental data by around 25–30%. However, the advantages of this model are that it is easy to use, easy to understand and that it consumes less computational time. The model results also show that the heat transfer coefficient of nanofluids increases with increasing Reynolds number and particle concentration. In contrast, the heat transfer coefficient decreases with increasing length of the test tube. Moreover, the results from the present model differ from those obtained using the Li and Xuan correlation [20] by approximately 3.5% at a particle concentration of 2.0 vol.%.

Acknowledgments

The authors would like to express their appreciation to the Thailand Research Fund (TRF), the office of the Higher Education Commission and the National Research University Project for providing financial support.

References

[1] H. Masuda, A. Ebata, K. Teramae, N. Hishinuma, Alteration of thermal conductivity and viscosity of liquid by dispersing ultra-fine particles (dispersion of Al_2O_3, SiO_2 and TiO_2 ultra-fine particles), Netsu Bussei (Japan) 7 (4) (1993) 227–233.
[2] S.U.S. Choi, Enhancing thermal conductivity of fluids with nanoparticle, ASME FED 231 (1995) 99.
[3] W. Duangthongsuk, S. Wongwises, A critical review of convective heat transfer of nanofluids, Renew. Sust. Energ. Rev. 11 (2007) 797–817.
[4] V. Trisaksri, S. Wongwises, Critical review of heat transfer characteristics of the nanofluids, Renew. Sust. Energ. Rev. 11 (3) (2007) 512–523.
[5] X.Q. Wang, A.S. Mujumdar, Heat transfer characteristics of nanofluids: a review, Int. J. Thermal Sci. 46 (2007) 1–19.
[6] Y. He, Y. Jin, H. Chen, Y. Ding, D. Cang, H. Lu, Heat transfer and flow behavior of aqueous suspensions of TiO_2 nanoparticles (nanofluids) flowing upward through a vertical pipe, Int. J. Heat Mass Transfer 50 (2007) 2272.
[7] C.T. Nguyen, G. Roy, C. Gauthier, N. Galanis, Heat transfer enhancement using Al_2O_3–water nanofluid for electronic liquid cooling system, Appl. Thermal Eng. 28 (2007) 1501.
[8] G.H. Ko, K. Ho, K. Lee, D.S. Kim, C. Kim, Y. Sohn, M. Choi, An experimental study on the pressure drop of nanofluids containing carbon nanotubes in the horizontal tube, Int. J. Heat Mass Transfer 50 (2007) 4749.
[9] R. Chein, J. Chuang, Experimental microchannel heat sink performance studies using nanofluids, Int. J. Thermal Sci. 46 (1) (2007) 57.
[10] W. Duangthongsuk, S. Wongwises, Effect of thermophysical properties models on the prediction of the convective heat transfer coefficient for low concentration nanofluid, Int. Commun. Heat Mass Transfer 35 (2008) 1320.
[11] W. Duangthongsuk, S. Wongwises, Heat transfer enhancement and pressure drop characteristics of TiO_2–water nanofluid in a double-tube counter flow heat exchanger, Int. J. Heat Mass Transfer 52 (2009) 2059–2067.
[12] C.T. Nguyen, N. Galanis, G. Polidori, S. Fohanno, C.V. Popa, A.L. Bechec, An experimental study of a confined and submerged impinging jet heat transfer using Al_2O_3–water nanofluid, Int. J. Thermal Sci. 48 (2009) 401–411.
[13] M. Izadi, A. Behzadmehr, D. Jajali-Vahida, Numerical study of developing laminar forced convection of a nanofluid in an annulus, Int. J. Thermal Sci. (2009) 1–11.
[14] Y. He, Y. Men, Y. Zhao, H. Lu, Y. Ding, Numerical investigation into the convection heat transfer of TiO_2 nanofluids flowing through a straight tube under the laminar flow conditions, Appl. Thermal Eng. 29 (2009) 1965–1972.
[15] V. Bianco, F. Chiacchio, O. Manca, S. Nardini, Numerical investigation of nanofluids forced convection in circular tubes, Appl. Thermal Eng. 29 (17–18) (2009) 3632–3642.
[16] S. Kumar, S.K. Prasad, J. Banerjee, Analysis of flow and thermal field in nanoflui using a single phase thermal dispersion model, Appl. Math. Model. 34 (3) (2010) 573–592.
[17] Y. Xuan, Q. Li, Heat transfer emhancement of nanofluids, Int. J. Heat Fluid Flow 21 (2000) 58–68.
[18] G.I. Taylor, Dispersion of soluble matter in solvent flowing through a tube, Proc. Royal Soci. (London) A219 (1953) 186–203.
[19] J. Buongiorno, Convective transport in nanofluids, Transaction of the ASME, J. Heat Transfer 128 (2006) 240–250.
[20] Q. Li, Y. Xuan, Convective heat transfer and flow characteristics of Cu-water nanofluid, Sci. China (Ser. E) 45 (4) (2002) 408–416.
[21] B.C. Pak, Y.I. Cho, Hydrodynamic and heat transfer study of dispersed fluids with submicron metallic oxide particles, Exp. Heat Transfer 11 (1998) 151–170.
[22] H.C. Brinkman, The viscosity of concentrated suspensions and solution, J. Chem. Phys. 20 (1952) 571–581.
[23] R.L. Hamilton, O.K. Crosser, Thermal conductivity of heterogeneous two-component systems, Indust. Eng. Chem. Fundament. 1 (3) (1962) 187–191.
[24] Y. Xuan, W. Roetzel, Conceptions for heat transfer correlation of nanofluids, Int. J. Heat Mass Transfer 43 (2000) 3701–3707.

International Journal of Air-Conditioning and Refrigeration
Vol. 20, No. 1 (2012) 1250001 (11 pages)

DOI: 10.1142/S2010132512500010

World Scientific
www.worldscientific.com

EXPERIMENTAL INVESTIGATION OF R134a FLOWING THROUGH ADIABATIC HELICALLY COILED CAPILLARY TUBES

JATUPORN KAEW-ON[*,†], SAKARIN CHINGULPITAK[†] and SOMCHAI WONGWISES[†,‡,§]

[*]*Physics Department, Thaksin University*
Papayom, Phattalung 93110, Thailand

[†]*Fluid Mechanics, Thermal Engineering and Multiphase Flow Research Laboratory (FUTURE)*
Department of Mechanical Engineering
King Mongkut's University of Technology Thonburi
Bangmod, Bangkok 10140, Thailand

[‡]*The Academy of Science, The Royal Institute of Thailand*
Sanam Suea Pa, Dusit, Bangkok 10300, Thailand
[§]*somchai.won@kmutt.ac.th*

Received 5 August 2011
Accepted 29 November 2011
Published 31 March 2012

The effects of the relevant parameters on the flow characteristic of R134a flowing through adiabatic helical capillary tubes were experimentally studied. The capillary tubes' diameter, coil diameter, and parameters relating to flow conditions such as inlet pressures and degree of subcooling were the major parameters investigated. The test section was made from copper tubing with inner diameters of 1.07, 1.27, and 1.62 mm. The coil diameters were 25, 50, and 100 mm. The local pressure and temperature distributions along the length of the capillary tubes were measured at inlet pressures ranging from 10 to 14 bar, mass flow rates from 8 to 20 kg/h, and degrees of subcooling from 0.5°C to 15°C. The metastable flow and the delay of vaporization of R134a are also presented and discussed. The results showed that the capillary diameter had more of a significant effect on the mass flow rate than the other variables.

Keywords: Capillary; pressure drop; R134a; subcooling; temperature; two-phase flow.

Nomenclature

AD : Average deviation, %
C_p : Specific heat, J kg^{-1} K^{-1}
D : Coil diameter, mm
d : Capillary diameter, mm
i : Enthalpy, J kg^{-1}
L : Capillary tube length, m
$\dot{m}$: Mass flow rate, kg s^{-1}
MD : Mean deviation, %
P : Pressure, Pa
p : Pitch of coil, mm
T : Temperature, °C

Greek Letters

μ : Viscosity, Pa s
π : Dimensionless parameter
ρ : Density, kg m^{-3}
σ : Surface tension, N m^{-1}

Subscripts

aprox : Approximately
cond : Condenser
crit : Critical point
in : Inlet
l : Liquid phase
out : Outlet
sat : Saturation
sub : Subcooled
v : Vapor phase

1. Introduction

A capillary tube is one of the expansion devices that are widely used in household refrigerators and window-type air conditioners. Normally, it is a long hollow tube of drawn copper with an inside diameter of between 0.5 and 2.0 mm and a length from 2 to 6 m that is connected at the outlet of the condenser and the inlet of the evaporator. The advantages of a capillary tube are its simplicity, low expense, zero maintenance cost, and that it has no moving parts. Moreover, it allows the pressures between the condenser and evaporator to equalize during the off cycle, thus decreasing the starting torque requirements of the compressor. Consequently, a capillary tube is suitable for household refrigerators or freezers, where the cooling load and refrigerant charge remain slightly constant.

Over the years, there have been a number of studies on the flow characteristic of refrigerants in capillary tubes. However, it should be noted that the studies found in the literature focused on the flow in horizontal tubes. Information on helically coiled capillary tubes is still limited, especially with regard to experimental data.

To the best of the authors' knowledge, up to now there has been minimal experimental investigation carried out by researchers on this issue. The available papers regarding experimental investigation of refrigerant flow in coiled capillary tubes are summarized as follows:

Kim *et al.*[1] studied the performance of R22, R407C, and R410A in several capillary tubes for air conditioners. They performed tests at 40°C, 45°C, and 50°C of the condensing temperature, and 1.5°C, 5°C, and 10°C of the subcooling temperature. They used the Buckingham π theorem to develop the correlation for predicting the mass flow rate through the capillary tubes. They concluded that the mass flow rates of R407C were greater by 4.0%, and those of R410A were greater by 23%, than those of R22. The mass flow rates in helical capillary tubes were smaller compared with those of straight tubes, especially in the cases of smaller the coil diameters. The deviation of experimental results for R22, R407C, and R410A from the dimensionless correlation in this study was between $\pm 12\%$ for all test conditions.

Zhou and Zhang[2] experimentally and numerically investigated the mass flow rate of R22 flowing through a capillary coil tube. They found that the mass flow rate of the refrigerant with coil diameter of 40 mm is approximately 10% less than that of a straight tube. They also found that the change in mass flow rate for coil diameters beyond 300 mm was insignificant.

Park *et al.*[3] studied the flow characteristics of coil capillary tubes in order to develop a generalized correlation for the mass flow rate through coil capillary tubes. The resulting correlation showed good predictions with the present database for R22, R407C, and R410A in the straight and coil capillary tubes, yielding average and standard deviations of 0.24% and 4.4%, respectively.

Khan *et al.*[4] investigated the flow of R134a inside an adiabatic helical capillary tube. The main study parameters were capillary tube diameter, length, coil pitch, and inlet subcoolings. They concluded that the effect of coiled capillary tubes reduces the mass flow rate by 5% to 15%, as compared to those of straight capillary tubes operating under similar conditions. They also proposed a correlation to predict the mass flow rate in spiral coil capillary tubes. Khan *et al.*[4] found that the correlation could predict more than 91% of the mass flow rate. The data were in agreement with measured data in an error band of $\pm 10\%$.

Mittal *et al.*[5] studied the coiling effect on the flow of R407C in an adiabatic helical capillary tube. They observed that coiling the capillary tube had a strong effect on the mass flow rate of R407C through the tube. They also found that the mass flow rates in coiled capillary tubes were 5%−10% less than those in straight ones. The correlations based on the

Buckingham π theorem were developed for predicting mass flow rates in straight and helically coiled capillary tubes. The error band of comparison between experimental data and their correlation was $\pm 10\%$.

Over the years, many studies have focused on the horizontal capillary tube while coiled capillary tube has received comparatively little attention. Experimental investigation in coiled capillary tubes has not attracted much attention despite its importance in real practical use. Although some information is currently available on this issue, there still remains room to discuss. In particular, detailed investigation is lacking on the effects of various relevant parameters on flow characteristics, specifically local pressure and local temperature distributions along the capillary tube. In this paper, the main concern was to study the influence of parameters such as inlet pressure, degree of subcooling, capillary tube diameters, and coil diameters on local pressure, local temperature distribution, and mass flow rate along the capillary tube length. The behavior of the flashing process and the delay of refrigerant vaporization are also presented.

2. Experimental Apparatus and Method

The experiment used a vapor-compression refrigeration system that included a capillary tube as the expansion device. Figure 1 shows a schematic diagram of the test apparatus. It consisted of the main refrigeration system components: Compressor, condenser, capillary tube, evaporator, and other accessory parts: the oil separator, liquid receiver, filter/drier, sight glass, subcooler, and accumulator. A two-cylinder single stage reciprocating compressor, driven by an electric motor, was used to circulate the refrigerant. The speed of the motor was varied so as to provide a wide range of mass flow rates by means of an inverter. The Alco AW-55824 helical oil separator was used to minimize the effect of lubricating oil on refrigerant flow through capillary tube. The efficiency of oil separation was approximately 99%. Compact plate heat exchangers were used as a condenser, evaporator, and subcooler.

An electric heater and a separate refrigeration system were installed in the water tank so as to control the water temperature. The hot water was supplied from a hot water tank by the circulating pump and passed through the flow meter and evaporator. The downstream pressure of the test section was controlled by adjusting the temperature and the flow rate of hot water. A condenser was used to reject heat to the water coming from a cold water tank. The upstream pressure of the test section was set by varying the flow rate of water to the subcooler.

The upstream pressure of the test section was regulated by adjusting the temperature of cold water. The degree of refrigerant subcooling entering the test section was set by varying the flow rate of

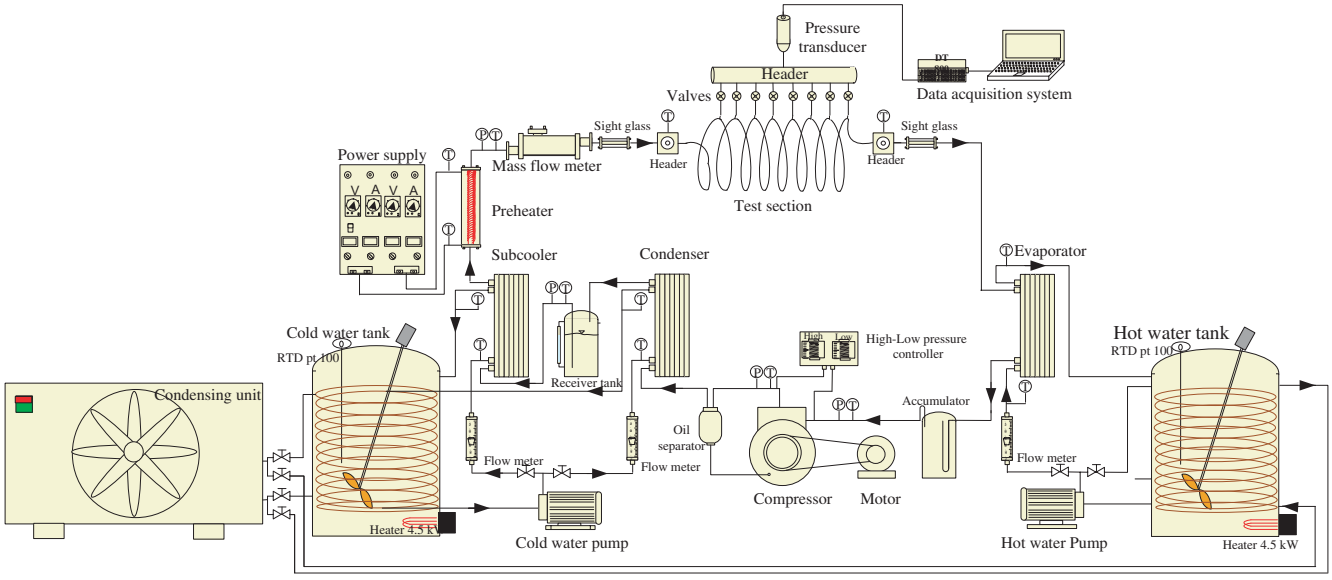

Fig. 1. Schematic diagram of the experimental apparatus.

water to the subcooler. The test runs were chosen to cover a wide range of working conditions of an air conditioner. The upstream pressures were set at 10, 12 and 14 bar, while the downstream pressures were varied between 3.5 to 4.5 bar. The degree of subcooling was varied from 0.5°C to 10.5°C.

The pressure distribution inside the capillary tube was measured by the pressure transducer calibrated from 0 to 22 bar within a ±20 mbar accuracy. The T-type thermocouple with an accuracy of ±0.1°C was installed to measure the temperature distribution along the test section. A total of nine thermocouples were soldered on the outer surface wall of the capillary tube at nine sections along the test tube to measure the outer wall temperatures. These outer wall temperatures were used to determine the inner wall temperatures based on heat conduction through the wall. The flow rate of the refrigerant through the capillary tube was measured by a coriolis mass flow meter (ABB FCM2000) with an accuracy of ±0.25%.

The details of the dimension of the test capillary tubes are presented in Fig. 2. The inlet pressure and inlet temperature were measured at the inlet header. Similarly, the outlet pressure and outlet temperature were obtained from the outlet header. Seven points of the capillary tube were drilled for the installation of pressure taps. Also, the seven T-type thermocouples were installed in the same sections as the pressure taps. The thermocouples were insulated with the Aeroflex standard sheet to reduce the effect of heat transfer on the measurement errors. The range of experimental conditions tested and the details of test sections are listed in Table 1.

3. Results and Discussion

The results are divided in three sections. First, the flow characteristics inside the capillary tubes are discussed. Next, the profiles of pressure and temperature distributions along the adiabatic helical capillary tubes are presented. Finally, the geometric and test conditions' effects on the mass flow rate of the refrigerant are shown and discussed in detail.

3.1. *Flow characteristics inside the capillary tube*

Figure 3 shows the measured pressure profiles and saturation pressure profiles along the capillary tube for a capillary diameter of 1.27 mm, coil diameter of 50 mm, condenser outlet pressure of 12 bar, and degree of subcooling of 8.5°C. The saturation pressures were calculated from measured temperatures, obtained from the T-type thermocouples installed in the same sections as the pressure tabs along the capillary tubes. As shown in Fig. 3, the refrigerant entered the capillary tube as a subcooled liquid. The measured pressure gradually decreased towards the end of the tube, at which point it rapidly decreased. On the other hand, the measured temperatures along the tube were nearly constant, but suddenly decreased at the end of the tube. The coincident point of the measured pressure and saturation pressure is called the theoretical flash point. The saturation pressure remains constant after it has passed the theoretical flash point, but then rapidly decreases. The delay in refrigerant vaporization is called the metastable region. Therefore, this phenomenon confirmed that refrigerant flow inside the capillary tube can be divided into three regions: Subcooled liquid region, metastable liquid region, and metastable two-phase region. In the subcooled liquid region, the measured pressure was higher than the saturation pressure. However, in the metastable liquid region, the measured pressure was lower than the near-constant saturation pressure. This behavior indicated that the refrigerant existed

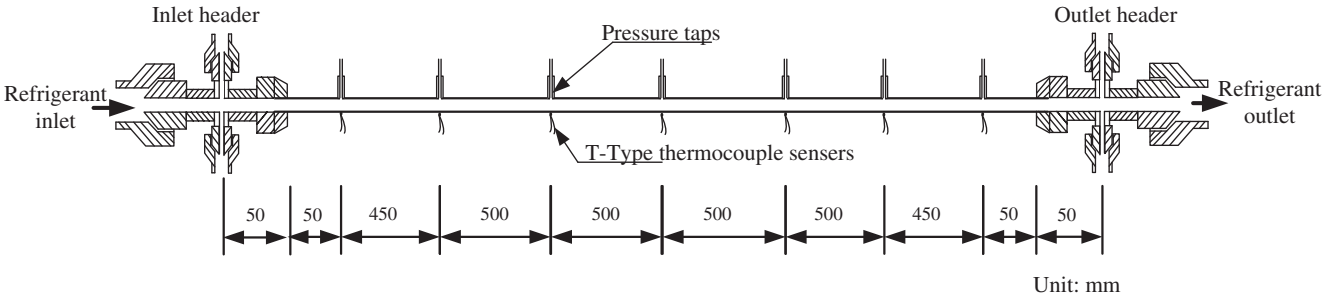

Fig. 2. Schematic diagram of the test section.

Table 1. The details of test sections and experimental conditions.

Items	Details
Refrigerant	R134a
Capillary diameter (mm)	1.07, 1.27, 1.62
Coil diameter (mm)	25, 50, 100
Capillary length (m)	3.05
Inlet pressure (bar)	10, 12, 14
Degree of subcooling	0.5−10.5

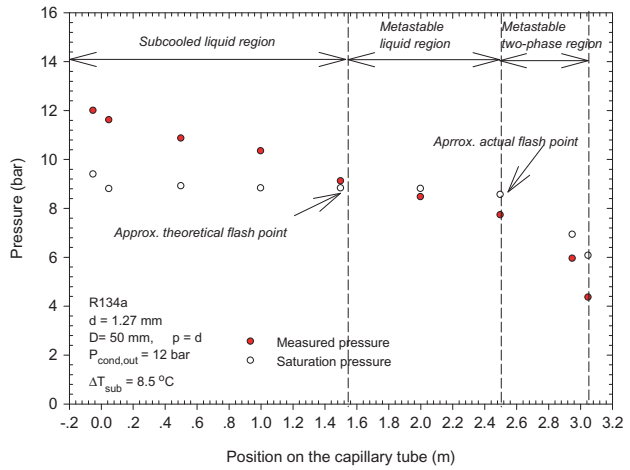

(a)

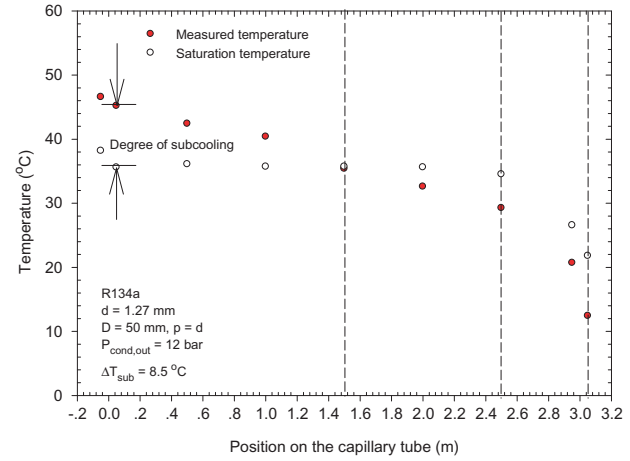

(b)

Fig. 3. Flow phenomena inside the capillary tube (a) pressure distribution and (b) temperature distribution.

in a liquid state, and lead to nonthermodynamic equilibrium. Therefore, the flow phenomenon in this region was called the metastable liquid flow. In the metastable two-phase region, the measured temperature suddenly decreased. This was a result of the velocity of the refrigerant greatly increasing when the liquid refrigerant changed to a liquid−vapor mixture. This phenomenon led to a decrease in refrigerant pressure and temperature. In addition, it was also found that the measured pressure was lower than the saturation pressure. As described above, this means that the state of refrigerant was a two-phase (liquid/vapor) mixture and did not exist in thermodynamic equilibrium. This flow phenomenon was consistent with the results of Valladares.[6]

3.2. *Pressure and temperature distributions*

Figure 4 presents the relevant influence parameters on pressure and temperature distributions along the adiabatic helical capillary tube length. The experiment was conducted for capillary diameters of 1.07, 1.27, and 1.52 mm, subcooling temperature ranges of 2.5°C to 10.5°C, and inlet pressures of 10, 12, and 14 bar. The coil diameters were 25, 50, and 100 mm. The results and discussion of the main relevant effects on the variation of pressure along the helical capillary tube length are as follows:

3.2.1. *Effect of inlet pressure on pressure and temperature distributions*

The variations of refrigerant pressure and temperature along the capillary tube at different inlet pressure are depicted in Fig. 4(a). The pressure and temperature drop was enhanced by increasing the inlet pressure. The possible reason for this could be that the enlargement of inlet pressure led to an increased difference between inlet and outlet pressure, which resulted in an increase of refrigerant mass flow rate and velocity. Consequently, the frictional and acceleration-related pressure drop inside the capillary tube was increased. It was also found that temperature distribution was directly related to pressure distribution. This was due to the fact that the increase in saturation pressure resulted in an increase of saturation temperature, at the same degree of subcooling and capillary tube configuration.

3.2.2. *Effect of degree of subcooling on pressure and temperature distributions*

The effect of degree of subcooling on pressure and temperature distributions along the capillary tube at the same inlet pressure and capillary tube configuration

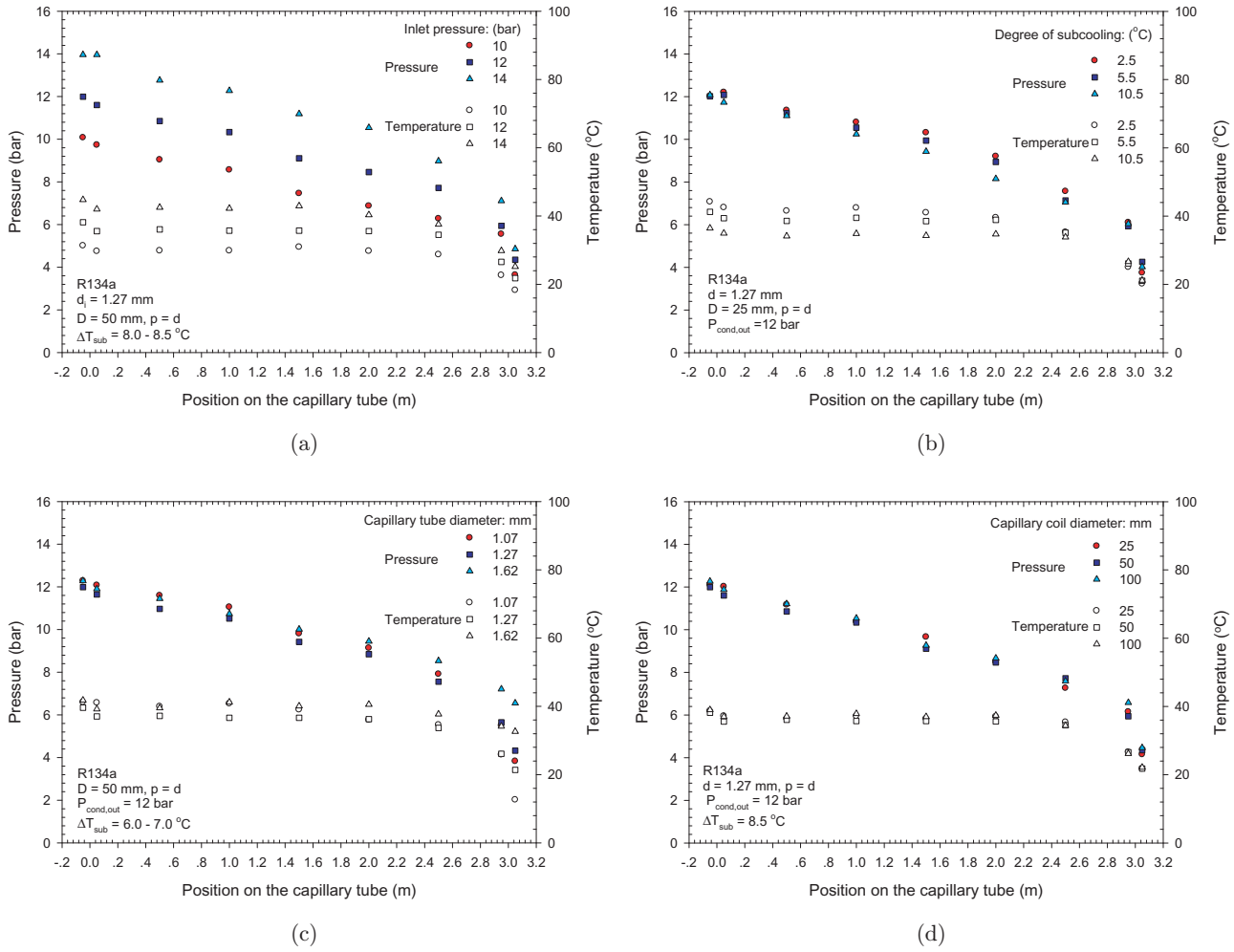

Fig. 4. Effect of the relevant parameter on the pressure and temperature distribution along the capillary length: (a) Effect of inlet pressure, (b) effect of degree of subcooling, (c) effect of capillary tube diameter, and (d) effect of coil diameter.

is presented in Fig. 4(b). The results show that the average pressure and temperature along the capillary tube was reduced as the degree of subcooling decreased. This was due to the fact that the density and velocity of refrigerant is boosted as the degree of subcooling increased, which resulted in an increase in frictional pressure drop inside the helical capillary tube. However, at the end of the capillary tube, the pressure drop was highest when the degree of subcooling was low. This may be due to a decrease in acceleration-related pressure when the quality at the end of the capillary tube is higher.

3.2.3. *Effect of capillary tube diameter on pressure and temperature distributions*

As shown in Fig. 4(c), the pressure and temperature drop along the capillary tube was decreased with an increase in the capillary tube diameter. This was due to the fact that the frictional pressure drop was increased by decreasing the capillary tube diameter. The reason for the variation of temperature at different capillary tube diameters is similar to that described above.

3.2.4. *Effect of coil diameter on pressure and temperature distributions*

The effect of coil diameter on pressure and temperature distribution is presented in Fig. 4(d). The results show that decrease in pressure and temperature was similar for all test conditions. Thus, it can be concluded that coil diameter has no significant effect on pressure and temperature distribution.

3.3. *The mass flow rate*

The coriolis mass flow meter (ABB FCM2000), with an accuracy of $\pm 0.25\%$, was installed to measure the mass flow rate of the refrigerant flowing through the capillary tubes. The effect of capillary tube geometry, such as tube diameter and coil diameter, as well as the operating conditions, such as inlet pressure and degree of subcooling on the mass flow rate of the refrigerant through adiabatic helical capillary tubes, were investigated. The results from the experimental investigation are as follow:

3.3.1. *Effect of degree of subcooling on mass flow rate*

Figure 5 plots the variations of mass flow rate against the degree of subcooling for various conditions. These figures show that for all conditions, the mass flow rate increased with an increased degree of subcooling. This phenomenon can be explained by the fact that the increase in mass flow rate was a result of increased liquid length for high inlet subcooling, since resistance of the liquid flow was less than that for the two-phase flow.

3.3.2. *Effect of inlet pressure on mass flow rate*

The variation of mass flow rates for capillary inlet pressures of 10, 12, and 14 bar with varying degrees of subcooling is presented in Fig. 5(a). The results show that for a given capillary diameter, the mass flow rate increased with an increase in the inlet pressure. At higher inlet pressures, the driving force

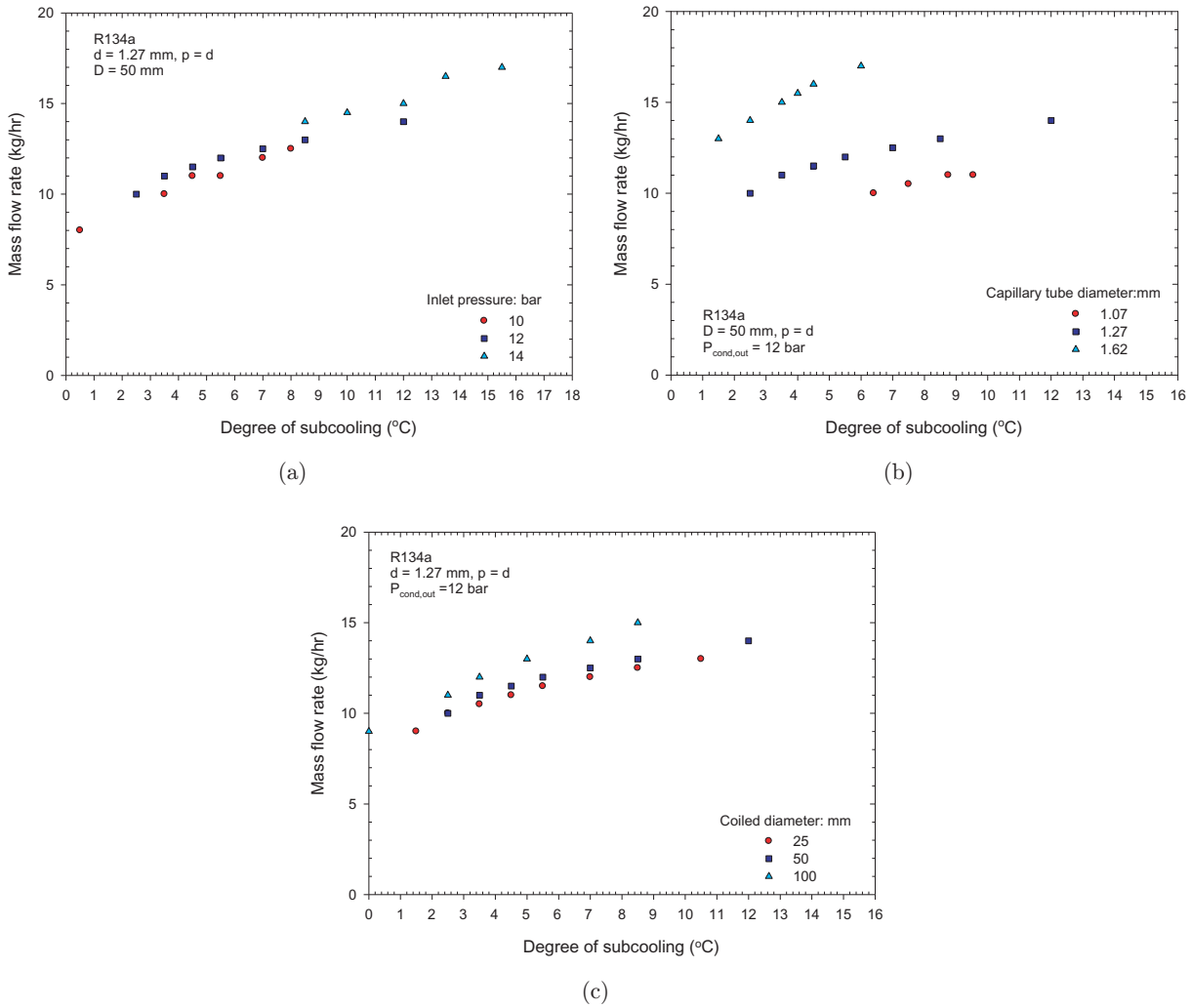

Fig. 5. Effect of the relevant parameter on the mass flow rate of the R134a through the capillary tubes: (a) Effect of inlet pressure, (b) effect of capillary tube diameter, and (c) effect of coil diameter.

was also higher and resulted in an increase of mass flow rate. As seen in Fig. 5(a), at identical degrees of subcooling, increasing inlet pressure from 10 to 12 bar increases the mass flow rate by 5% to 10%.

3.3.3. *Effect of capillary tube diameter on mass flow rate*

Figure 5(b) presents mass flow rates and degrees of subcooling for capillary tube diameters of 1.07, 1.27, and 1.62 mm, inlet pressure of 12 bar, and coil diameter of 50 mm. The effect of capillary tube diameter on refrigerant mass flow rate is clearly seen and significant. The results show that the mass flow rates dramatically increased with an increase in capillary tube diameter. Figure 5(b) shows that for 6.5°C of subcooling, as the capillary tube diameter was increased from 1.07 mm to 1.27 mm, and from 1.27 mm to 1.62 mm, the refrigerant mass flow rate increased by 26.3% and 41.7%, respectively. This was due to smaller frictional effects as the internal diameter of the capillary tube increased.

Table 2. The relevant dimensionless parameters.

π-group	Dimensionless parameters	Consideration	References
π_1	$\pi_1 = (P_{in} - P_{sat})/P_{crit}$	Inlet pressure	Choi *et al.*,[9,10] Zhang[11]
π_2	$\pi_2 = \Delta T_{sub}/T_{crit}$	Subcooling	Choi *et al.*,[9,10] Zhang[11]
π_3	$\pi_3 = L/d$	Tube geometry	ASHRAE,[7] Melo *et al.*,[8] Kim *et al.*,[1] Choi *et al.*,[9,10] Zhang,[11] Mittal *et al.*[5]
π_4, π'_4	$\pi_4 = \rho_l/\rho_v, \pi'_4 = \rho_v/\rho_l$	Density	ASHRAE,[7] Choi *et al.*,[9,10] Zhang,[11] Mittal *et al.*[5]
π_5, π'_5	$\pi_5 = (\mu_l - \mu_v)/\mu_v, \pi'_5 = \mu_v/\mu_l$	Viscosity	ASHRAE,[7] Choi *et al.*,[9,10] Zhang,[11] Mittal *et al.*[5]
π_6	$\pi_6 = \sigma/(P_{in}d)$	Bubble growth	Choi *et al.*,[9,10] Zhang[11]
π_7	$\pi_7 = \rho_l i_{vl}/P_{sat}$	Vaporization	Choi *et al.*,[9,10] Zhang[11]
π_8	$\pi_8 = \dot{m}/(d^2\sqrt{\rho_l P_{in}})$	Mass flow rate	Choi *et al.*,[9,10] Zhang[11]
π_9	$\pi_9 = \dot{m}/(d\mu_l)$	Mass flow rate	ASHRAE,[7] Melo *et al.*,[8] Kim *et al.*,[1] Mittal *et al.*[5]
π_{10}	$\pi_{10} = d^2\rho_l P_{in}/\mu_l^2$	Inlet pressure	ASHRAE,[7] Melo *et al.*,[8] Kim *et al.*,[1] Mittal *et al.*[5]
π_{11}	$\pi_{11} = d^2\rho_l^2 Cp_l \Delta T_{sub}/\mu_l^2$	Subcooling	ASHRAE,[7] Melo *et al.*,[8] Kim *et al.*,[1] Mittal *et al.*[5]
π_{12}	$\pi_{12} = d^2 h_{lv}\rho_l^2/\mu_l^2$	Vaporization	Kim *et al.*,[1] Mittal *et al.*[5]
π_{13}	$\pi_{13} = d\rho_l\sigma/\mu_l^2$	Bubble growth	Kim *et al.*,[1] Mittal *et al.*[5]
π_{14}	$\pi_{14} = D/d$	Geometry	Mittal *et al.*[5]

Table 3. The summary of the existing correlations for predicting the mass flow rate.

No	Author(s)	Correlation	Conditions
1	ASHRAE[7]	$\pi_9 = 1.8925\pi_3^{-0.484}\pi_4^{0.773}\pi_5^{0.265}\pi_{10}^{1.369}\pi_{11}^{0.0187}$	Straight tube, R134a, R22, R410A
2	Melo *et al.*[8]	$\pi_9 = 1.95\pi_3^{-0.528}\pi_{10}^{0.448}\pi_{11}^{0.164}$	Straight tube, R12, R134a, R600a
3	Kim *et al.*[1]	$\pi_9 = 1.5104\pi_3^{-0.3785}\pi_{10}^{0.5351}\pi_{11}^{0.1074}\pi_{12}^{-0.1596}\pi_{13}^{0.096}$	Helical and Straight tube, R22, R407C, R410A
4	Choi *et al.*[9]	$\pi_8 = 1.313 \times 10^{-3}\pi_1^{-0.087}\pi_2^{0.188}\pi_3^{-0.412}\pi_4^{-0.834}\pi_5^{0.199}\pi_6^{-0.368}\pi_7^{0.992}$	Straight tube, R12, R22
5	Choi *et al.*[10]	$\pi_8 = 0.5782 \times 10^{-4}\pi_1^{-0.315}\pi_2^{0.369}\pi_3^{-0.344}\pi_4^{-0.034}\pi_5^{0.040}\pi_6^{-0.458}\pi_7^{0.376}$	Straight tube, R12, R22, R134a, R152a, R407C, R410A
6	Zhang[11]	$\pi_8 = 1/[1 + \exp(2.956h - 0.064)]h = 1/[1 + \exp(0.654 - 5.371\pi_1 + 7.332\pi_2 - 9.541 \times 10^{-4}\pi_3 - 0.1588\pi_4 + 2.277 \times 10^{-2}\pi_5 - 5.202 \times 10^4\pi_6 + 1.731 \times 10^{-2}\pi_7)]$	Straight tube, R12, R134a, R22, R290, R407C, R410A, and R600a
7	Mittal *et al.*[5]	$\pi_9 = 0.0087\pi_3^{-0.351}\pi_4'^{-0.507}\pi_5'^{-1.235}\pi_{10}^{1.538}\pi_{11}^{0.003}\pi_{12}^{-0.463}\pi_{13}^{-0.965}\pi_{14}^{0.098}$	Helical tube R407C

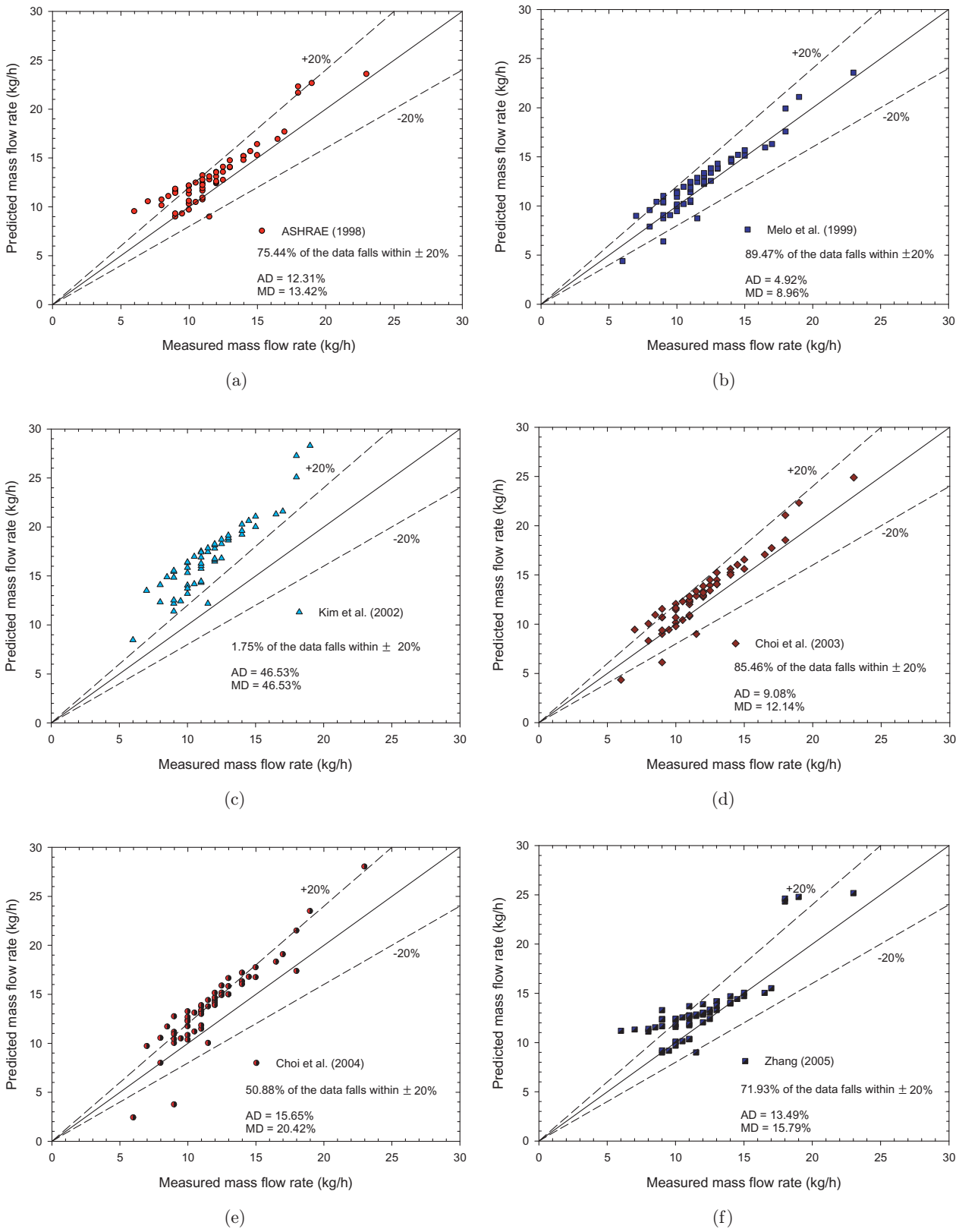

Fig. 6. Comparison of the present measured mass flow rate with existing correlations: (a) ASHARE,[7] (b) Melo *et al.*,[8] (c) Kim *et al.*,[1] (d) Choi *et al.*,[9] (e) Choi *et al.*,[10] (f) Zhang,[11] and (g) Mittal *et al.*[5]

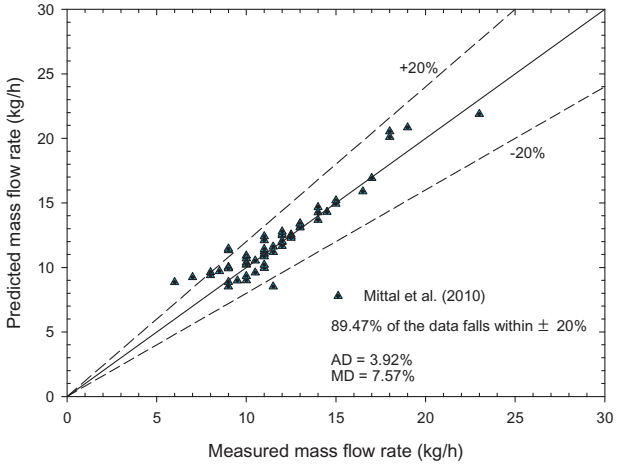

(g)

Fig. 6. (*Continued*)

Table 4. The percentage of the data falls within ±20% and deviations of the predicted and measured mass flow rate.

Correlation	% of the data falls within ±20%	Average deviation (%)	Mean deviation (%)
ASHRAE[7]	75.44	12.31	13.42
Melo *et al.*[8]	**89.47**	**4.92**	**8.96**
Kim *et al.*[1]	1.75	46.53	46.53
Choi *et al.*[9]	85.96	9.08	12.14
Choi *et al.*[10]	50.88	15.65	20.42
Zhang[11]	71.93	13.49	15.75
Mittal *et al.*[5]	**89.47**	**3.92**	**7.57**

3.3.4. *Effect of coil diameter on mass flow rate*

The variation of mass flow rates with coil diameters of 25, 50, and 100 mm is presented in Fig. 5(c). It can be clearly observed that the refrigerant mass flow rate increased with an increase in coil diameter. For 8.5°C of subcooling, as the coil diameter increased from 25 mm to 50 mm, and from 50 mm to 100 mm, the refrigerant mass flow rate increased by 7.5% and 15%, respectively.

3.3.5. *Comparison with the mass flow rate correlations*

The correlations for predicting the refrigerant mass flow rate in the capillary tube have been proposed by several researchers. In general, these correlations are presented as a function of the dimensionless parameters. The summary of the most common dimensionless parameters with descriptions is presented in Table 2. The seven selected mass flow rate correlations, proposed by ASHRAE,[7] Melo *et al.*,[8] Kim *et al.*,[1] Choi *et al.*,[9] Choi *et al.*,[10] Zhang[11] and Mittal *et al.*,[5] are presented as equations in Table 3. Comparisons of the measured mass flow rates with the predicted mass flow rates are shown in Fig. 6. The deviations obtained from the comparisons are summarized in Table 4. The correlations of Mittal *et al.*[5] presented the best predictions with average and mean deviations of 3.92% and 7.57%.

4. Conclusion

In this paper, the flow characteristics of R134a flowing through adiabatic helical capillary tubes were experimentally investigated. Copper tubes with inside diameters of 1.07 mm, 1.27 mm, and 1.62 mm, with coil diameters of 25 mm, 50 mm, and

100 mm, and length of 3.05 m, were used as the test sections. Conclusions can be drawn as follows:

(1) The refrigerant flow inside the capillary tube can be divided into three regions: Subcooled liquid region, metastable liquid region, and metastable two-phase region. The subcooled liquid region was extended by increasing the inlet pressure and degree of subcooling.
(2) The effect of relevant parameters on pressure and temperature distributions showed that the average pressure and temperature along the capillary tube was reduced as the degree of subcooling decreased. Additionally, the pressure and temperature drop along the capillary tube decreased by increasing the capillary tube diameter.
(3) Capillary diameter, capillary coil diameter, degree of refrigerant subcooling, and condensing pressure had varying effects on refrigerant mass flow rate in adiabatic capillary tubes. The results show that capillary diameter has more of a significant effect on mass flow rate than the other variables. For instance, at 6.5°C of subcooling, as the capillary tube diameter increased from 1.07 mm to 1.27 mm, and from 1.27 mm to 1.62 mm, the refrigerant mass flow rate increased by 26.3% and 41.7%, respectively. Similarly, at 8.5°C of subcooling, as the coil diameter increased from 25 mm to 50 mm, and from 50 mm to 100 mm, the refrigerant mass flow rate increased by 7.5% and 15%, respectively.
(4) The Mittal *et al.*[5] correlation gives the best predictions with the average deviation of 3.92% and the mean deviation of 7.57%.

Acknowledgments

The authors would like to acknowledge the Thailand Research Fund, The Office of the Higher Education Commission and The National Research University project for financial support.

References

1. S. G. Kim, M. S. Kim and S. T. Ro, Experimental investigation of the performance of R22 R407C and R410A in several capillary tubes for air-conditioners, *Int. J. Ref.* **25** (2002) 521−531.
2. G. Zhou and Y. Zhang, Experimental investigation on hysteresis effect of refrigerant flowing through a coiled adiabatic capillary tube, *Energy Convers. Manage.* **47** (2006) 3084−3093.
3. C. Park, S. Lee, H. Kang and Y. Kim, Experimentation and modeling of refrigerant flow through coiled capillary tubes, *Int. J. Ref.* **30** (2007) 1168−1175.
4. M. K. Khan, R. Kumar and P. K. Sahoo, An experimental study of the flow of R-134a inside an adiabatic spirally coiled capillary tube, *Int. J. Ref.* **31** (2008) 970−978.
5. M. K. Mittal, R. Kumar and A. Gupta, An experimental study of the flow of R-407C in an adiabatic helical capillary tube, *Int. J. Ref.* **33** (2010) 840−847.
6. O. G. Valladares, Numerical simulation and experimental validation of coiled adiabatic capillary tubes, *Appl. Therm. Eng.* **27** (2007) 1062−1071.
7. *ASHRAE Handbook*: *Refrigeration/SI edition*, Chapter 45 (ASHRAE, 1998).
8. C. Melo, R. T. S. Ferreira, C. B. Neto, J. M. Goncalves and M. M. Mezavila, An experimental analysis of adiabatic tubes, *Appl. Therm. Eng.* **19** (1999) 669−684.
9. J. Choi, Y. Kim and H. Y. Kim, A generalized correlation for refrigerant mass flow rate through adiabatic capillary tube, *Int. J. Ref.* **26** (2003) 881−888.
10. J. Choi, Y. Kim and J. T. Chung, An empirical correlation and rating charts for the performance of adiabatic capillary tubes with alternative refrigerants, *Appl. Therm. Eng.* **24** (2004) 29−41.
11. C. L. Zhang, Generalized correlation of refrigerant mass flow rate through adiabatic capillary tubes using artificial neural network, *Int. J. Ref.* **28** (2005) 506−514.

Isı Bilimi ve Tekniği Dergisi, 32, 1, 19-31, 2012
J. of Thermal Science and Technology
©2012 TIBTD Printed in Turkey
ISSN 1300-3615

HEAT TRANSFER ENHANCEMENT DURING DOWNWARD LAMINAR FLOW CONDENSATION OF R134A IN VERTICAL SMOOTH AND MICROFIN TUBES

Ahmet Selim DALKILIÇ*, İsmail TEKE* and Somchai WONGWISES**
*Yildiz Technical University Mechanical Engineering Faculty Department of Mechanical Engineering
34349 Beşiktaş, İstanbul, Turkey, dalkilic@yildiz.edu.tr
**King Mongkut's University of Technology Thonburi Engineering Faculty Department of Mechanical Engineering
10140 Bangmod, Bangkok, Thailand, somchai.won@kmutt.ac.th

(Geliş Tarihi: 04. 08. 2010, Kabul Tarihi: 08. 11. 2010)

Abstract: This paper presents an experimental comparison of the laminar film condensation heat transfer coefficients of R134a in vertical smooth and micro-fin tubes having inner diameters of 7 mm and lengths of 500 mm. Condensation experiments were performed at a mass flux of 29 kg m^{-2} s^{-1}. The pressures were between 0.8 and 0.9 MPa. The original smooth tube heat transfer model was modified by a well-known friction factor to account for the heat transfer enhancement effects due to the presence of micro-fins on the internal wall surface during annular flow regime conditions. Alterations of the local heat transfer coefficient, and condensation rate along the tube length during downward condensing film were determined, considering the effects of the temperature difference between the saturation temperature and the inner wall temperature of the test tubes, and the condensing temperature on these items. The results show that the interfacial shear stress is found to have significance for the laminar condensation heat transfer of R134a under the given conditions due to its better predictive performance than the classical solution neglecting the interfacial shear stress effect. A comparison of the condensation heat transfer coefficients was also done according to the condensing pressures. New empirical correlations of the condensation heat transfer coefficient belonging to the test tubes are proposed for practical applications.
Keywords: Condensation, Heat transfer coefficient, Downward flow, Laminar flow, Micro-fin tube, Nusselt theory, Annular flow.

İÇ YÜZEYİ PÜRÜZSÜZ VE MİKRO KANATLI DÜŞEY BORULARDA R134A'NIN LAMİNER AKIŞINDAKİ YOĞUŞMASI SIRASINDA MEYDANA GELEN ISI TRANSFERİ İYİLEŞMESİNİN ARAŞTIRILMASI

Özet: Bu çalışmada, iç çapı 7 mm ve uzunluğu 500 mm olan iç yüzeyi pürüzsüz ve mikro kanatlı borular içinde akan R134a'nın laminar film yoğuşması ısı transferi katsayısının deneysel karşılaştırılması sunulmuştur. Yoğuşma deneyleri 29 kg $m^{-2}s^{-1}$ kütlesel akılarında yapılmıştır. Basınçlar 0.8-0.9 MPa değerleri arasındadır. Halka akışı şartlarında geçerli olan iç yüzeyi pürüzsüz boruya ait olan ısı transferi modeli, literatürde yaygın olarak kullanılan bir sürtünme katsayısı ile boru iç yüzeyindeki mikro kanatların varlığından ötürü meydana gelen ısı transferi iyileşmesini hesaba katacak şekilde modifiye edilmiştir. Düşey olarak yoğuşan film esansındaki yerel ısı transferi katsayılarındaki değişim ve boru boyunca oluşan yoğuşma miktarı, doyma sıcaklığı ile boru iç yüzeyindeki sıcaklık farkı ve yoğuşma sıcaklığı da dikkate alınarak bulunmuştur.Sonuçlar arayüzey kayma gerilmesinin çalışmada belirtilen şartlarda R134a'nın laminer yoğuşma ısı transferi üzerinde öneme sahip olduğunu ve önerilen modelin arayüzey kayma gerilmesinin etkisinin ihmal edildiği geleneksel çözümden daha iyi sonuçlar vermesiyle göstermiştir. Ayrıca, yoğuşma basınçlarına göre ısı transferi katsayıları da karşılaştırılmıştır. Pratik uygulamalar için test edilen borulara ait yeni amprik yoğuşma ısı transferi eşitlikleri önerilmiştir.
Anahtar Kelimeler: Yoğuşma, Isı transferi katsayısı, Düşey akış, Laminer akış, Micro kanatlı boru, Nusselt teorisi, Halka akış.

NOMENCLATURE

A_i	tube inside surface area, m^2
A_{mf}/A_s	augmentation ratio
c_p	specific heat capacity at constant pressure, J $kg^{-1}K^{-1}$
d	inside diameter of tube, m
Exp	experiment
G	mass flux, kg $m^{-2}s^{-1}$
g	gravitational acceleration, m s^{-2}
h	heat transfer coefficient, W $m^{-2}K^{-1}$
i	specific enthalpy, j kg^{-1}

i_{fg}	latent heat of condensation, J kg^{-1}
i_{fg}'	correction factor included latent heat of condensation, J kg^{-1}
k	thermal conductivity, W $m^{-1}K^{-1}$
l	tube length, m
L	characteristic length
l_f	fin length, m
m	mass flow rate, kg s^{-1}
n	number of fins per unit length
Nu	Nusselt number
P	pressure, MPa
Pr	Prandtl number
Re	Reynolds number
Q	heat transfer rate, W
T	temperature, °C
u	axial velocity, m s^{-1}
w	tube thickness, m
x	vapour quality
y	wall coordinate
z	axial coordinate
$\Delta T_{r,sat}$	$T_{r,sat}$-T_{wi} , K

Greek symbols

δ	film thickness, m
δ*	dimensionless film thickness
μ	dynamic viscosity, kg $m^{-1}s^{-1}$
ρ	density, kg m^{-3}
ρ_g*	fictitious vapour density defined by Carey (1992), kg m^{-3}
β	spiral angle, rad
τ	shear stress, N m^{-2}

Subscripts

avg	average
cond	condensate
corr	correlation
eq	equivalent
exp	experimental
F	frictional term
G	gravitational term
g	gas/vapour
i	inlet
l	liquid
M	momentum term
o	outlet
ph	preheater
r	refrigerant
sat	saturation
T	total
TS	test section
w	water
wi	inner wall

INTRODUCTION

The taking cognisance of the need to increase the thermal performance of heat exchangers, thereby effecting savings of energy, material and cost, as well as a consequential mitigation of environmental degradation, has led to the development and use of many heat transfer enhancement techniques. In general, enhancement techniques can be divided into two groups: active and passive. Active techniques require external forces, e.g., electrical field, acoustic or surface vibration. Passive techniques require special surface geometries, such as rough surface, extended surface for liquids etc., or fluid additives. Both techniques have been used by researchers for 140 years to increase heat transfer rates in heat exchangers. If two or more of these techniques are utilised together to achieve enhancement, this is referred to as compound enhancement.

The usage of micro-fin tubes has increased the heat transfer performance of tubes with relatively low pressure drop increases in commercial and air conditioning applications since the 1980s. Micro-fins improve heat transfer in both single-phase and two-phase applications, and are one of the most efficient and common heat transfer enhancement mechanisms for heat exchangers due to their superior heat transfer performance.

Many experimental investigations have been performed to determine the effects of fin geometry, tube diameter, refrigerant, etc., on the condensation heat transfer and pressure drop performance of micro-fin tubes. The presence of the micro-fins inside the tube enhances the heat transfer by providing an increased surface area. They cause not only uniform liquid film distribution around the circumference of the tube, but also turbulence induced in the liquid film.

Many studies on condensation have been done with horizontal micro-fin tubes. Wang and Honda (2003), Cavallini et al. (1999), Chamra et al. (1996), and Schlager (1990) have proposed correlations and theoretical models to predict the heat transfer, and they have made intensive comparisons of previously proposed correlations with a large body of experimental data at the same time. Helically grooved, 18° helix angled, horizontal micro-fin tubes have been used in air conditioners recently, because of their better heat transfer performance compared to smooth tubes.

However, there are few studies on the condensation of R134a with down flow in vertical micro-fin tubes. Briggs et al. (1998) have used large diameter tubes around 20.8 mm with CFC113. The Shah (1979) correlation has commonly been used by researchers for turbulent condensation conditions.

The flow pattern occurring in many real convective condensation applications is that of an annular flow along a tube length, which is characterised by a phase interface separating a thin liquid film from the gas flow in the core region. Researchers, in relation to both analytical and experimental work, have paid attention to this flow regime due to its practical importance.

The first theoretical solution for predicting heat transfer coefficients was proposed by Nusselt (1916). A linear temperature profile through a laminar film flowing downwards without entrainment on a vertical plate was assumed, waves and an interfacial shear effect between the phases were neglected in his analysis. Nusselt-type analysis can be used for convective condensation in round tubes under these conditions. Detailed information on the studies in the literature regarding modifications of the Nusselt theory can be seen in the authors' previous publications (Dalkilic et al., 2009a, 2009b).

Carey (1992) developed a theoretical model to investigate convective condensation in round tubes during an annular flow regime. He modified Nusselt's theory (1916) by taking into account the interfacial shear stress and new simplified equations. An iterative technique for the calculation of the interfacial shear and the determination of the local heat transfer coefficients were proposed in this study. Any alteration of the thermo-physical properties of the refrigerant for condensation was also neglected due to the small pressure drop along the test tube. But it is reported that the analysis in his study cannot be applicable to fully or partially turbulent film flow.

Dalkilic et al. (2009a) used Carey's (1992) theoretical model for the downward condensation of R134a to investigate the local and average heat transfer coefficients in a vertical smooth tube at low mass flux conditions. The calculated results obtained from the modified Nusselt model incorporating interfacial shear stress, the modified Nusselt model with the McAdams correction factor (1954), and the classical Nusselt model (1916), were compared with the experimental data. Comparisons with the data for laminar flow at low mass flux show that the modified Nusselt model without a correction factor predicts the data well. Experimental results show that the interfacial shear stress that was incorporated into the modified Nusselt model (1916) affects the condensation process of R134a in a vertical smooth tube.

The most common passive heat transfer enhancement technique nowadays for condensers is the use of helical micro-fin tubes. In the present study, tests are performed in smooth and micro-fin tubes with the same dimensions and conditions for the purpose of comparison. The helical micro-fin tube, which was produced for commercial usage, used as test tube has a 0.5 m length, 7.94 mm outside diameter, 18° helix angle and 50 fins. To the best of the authors' knowledge, there has been insufficient work dealing with condensation heat transfer of HFC-134a in small diameter micro-fin tubes during downward flow. Although some information is currently available, there still remains room for further research. Moreover, it should also be noted that the reported mass fluxes, heat fluxes, condensation pressures and dimensions of the test tube do not include the parameters presently studied (except for the authors' previous publications (Balcilar et al. (2010a, 2010b), Dalkilic et al. (2007, 2008, 2009, 2010)). The aim of the present study is to determine the heat transfer enhancement, comparing smooth and micro-fin tubes, and investigate the alteration of the local heat transfer coefficients, film thicknesses, and condensation rates along the test tubes. In addition to this, the effect of different experimental parameters such as condensing temperature difference between saturation and wall inlet temperature of the test tube, condensation pressure on the convective heat transfer coefficient of R134a and condensation rate are also shown and then discussed. Moreover, new correlations for the condensation heat transfer coefficient are proposed for practical applications for smooth and micro-fin tubes separately.

EXPERIMENTAL SETUP

A schematic diagram of the test apparatus is shown in Figure 1. The refrigerant loop consists of an evaporator, test section and condenser loop. The refrigerant is circulated by a gear pump controlled by an inverter. The refrigerant flows in series through the bypass line, a coriolis type refrigerant flow meter which has a sensitivity of 0.1%, an evaporator, a separator, and a sight glass tube, and then enters the test section. The evaporator controls the inlet quality before entering the test section, and consists of a plate heat exchanger designed to supply heat to adjust the inlet quality for the vaporisation of the refrigerant. The circulated water flow rate of the evaporator is measured by a turbine-type flow meter which has a sensitivity of 2%. After exiting the test section, the vapour phase of R134a, which comes from the liquid-gas separator, continues to the condenser. The flow rate of liquid R134a from the liquid-gas separator is measured in a vessel to check the condition of the apparatus. A plate heat exchanger is used as a condenser. The liquid phase of R134a, from the condenser and separator, is collected in a reserve tank which has a water coil to balance the pressure of liquid R134a. There is another sight glass to check the saturated liquid R134a before the refrigerant pump. The pressures are measured by pressure transducers which have sensitivities of 0.5%.

The test section is a vertical counter-flow tube-in-tube heat exchanger with refrigerant flowing in the inner tube and cooling water flowing in the annulus. The inner and outer tubes are made from copper having inner diameters of 7 mm and 16 mm, respectively. The length of the heat exchanger is 0.5 m. A thermostat is used to control the inlet temperature of the water. The flow rate of cooling water is measured using a turbine-type flow meter which has a sensitivity of 1%. The pressure drop is measured by a differential pressure transducer, which has a sensitivity of 0.05%, installed between the inlet and outlet of the test section. The temperatures of the inlet and outlet of the test section are measured by pt100 sensors and T-type thermocouples. A band-type heater is

wrapped around the copper tube line from the exit of the evaporator to the inlet of the test tube to control the system pressure of the refrigerant flow.

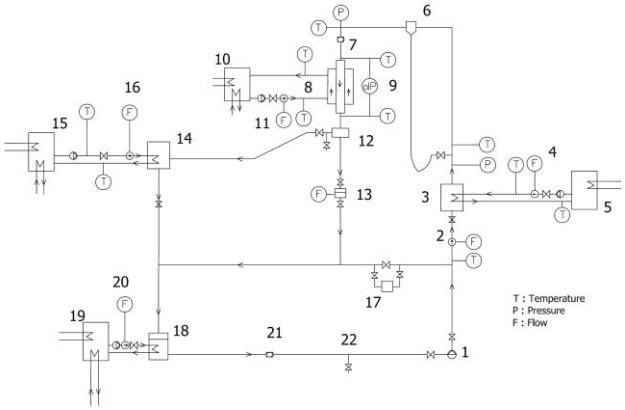

1- Refrigerant Pump 2- Coriolis Flow Meter 3- Evaporator 4- Turbine Flow Meter 5- Thermostat System 6- Liquid/Gas Separator 7- Sight Glass 8- Test Section 9- Differential Pressure Transmitter 10- Thermostat System 11- Turbine Flow Meter 12- Liquid/Gas Separator 13- Scaled Vessel 14- Condenser 15- Thermostat System 16- Rotameter 17- Filter/Dryer 18- R134a Reserve Tank 19- Thermostat System 20- Rotameter 21- Sight Glass 22- R134a Charging Point

Figure 1. Schematic diagram of experimental apparatus.

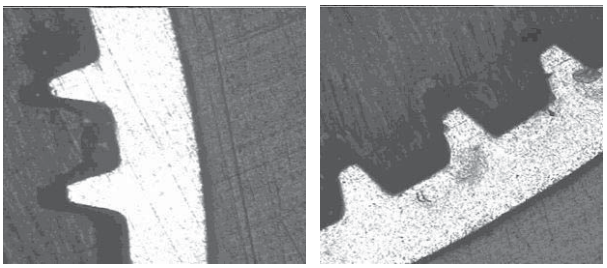

(a) Cross-section of the micro-fin tube by electron microscope (100x) (Dalkilic, 2007)

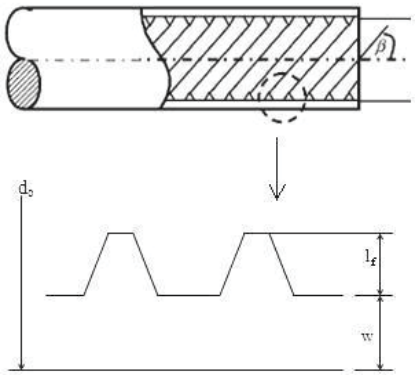

(b) Schematic cross-section of the micro-fin tube (Dalkilic and Wongwises, 2009t)

Figure 2. Detailed cross-section of the test tube.

A Panasonic-Nais PLC device was used to record and collect data from all flow meters, pressure transducers and differential pressure transmitters. The computer programme collected 10 types of data and recorded the average values each second using an MS Excel programme spreadsheet.

Figure 2 shows detailed cross section of the tested micro-fin tube which was produced for commercial usage and its geometric parameters can be seen in Table 1.

Table 1. Geometry of the tested micro-fin tube.

Test tube	Micro-fin tube
l (mm)	500
d_o (mm)	7.94
w (mm)	0.28
l_f (mm)	0.15
ß (°)	18
n	100
A_{mf}/A_s	1.38

DATA REDUCTION

The data reduction of the measured results can be analysed as follows:

The Inlet Vapour Quality of The Test Section ($x_{TS,i}$)

$$x_{TS,i} = \frac{i_{TS,i} - i_{l@T_{TS,i}}}{i_{fg@T_{TS,i}}} \quad (1)$$

where $i_{l@T_{TS,i}}$ is the specific enthalpy of the saturated liquid based on the inlet temperature of the test section, $i_{fg@T_{TS,i}}$ is the specific enthalpy of vaporization based on the inlet temperature of the test section, $i_{TS,i}$ is the refrigerant specific enthalpy at the test section inlet and is given by:

$$i_{TS,i} = i_{ph,i} + \frac{Q_{ph}}{m_r} \quad (2)$$

where $i_{ph,i}$ is the inlet specific enthalpy of the liquid refrigerant before entering the pre-heater, m_r is the mass flow rate of the refrigerant, and Q_{ph} is the heat transfer rate in the pre-heater:

$$Q_{ph} = m_{w,ph} c_{p,w} (T_{w,i} - T_{w,o})_{ph} \quad (3)$$

where $m_{w,ph}$ is the mass flow rate of the water entering the preheater, cp,w is the specific heat of water, $(T_{w,i} - T_{w,o})_{ph}$ is the temperature difference between inlet and outlet positions of the preheater.

The Outlet Vapour Quality of The Test Section ($x_{TS,o}$)

$$x_{TS,o} = \frac{i_{TS,o} - i_{l@T_{TS,o}}}{i_{fg@T_{TS,o}}} \quad (4)$$

where $i_{TS,o}$ is the refrigerant specific enthalpy at the test section outlet, $i_{l@T_{TS,o}}$ is the specific enthalpy of the saturated liquid based on the outlet temperature of the test section, and $i_{fg@T_{TS,o}}$ is the specific enthalpy of vaporization. The outlet specific enthalpy of the refrigerant flow is calculated as follows:

$$i_{TS,o} = i_{TS,i} - \frac{Q_{TS}}{m_{ref}} \quad (5)$$

where the heat transfer rate, Q_{TS}, in the test section is obtained from:

$$Q_{TS} = m_{w,TS} c_{p,w} (T_{w,o} - T_{w,i})_{TS} \quad (6)$$

where $m_{w,TS}$ is the mass flow rate of the water entering the test section, and $(T_{w,o} - T_{w,i})_{TS}$ is temperature difference between outlet and inlet position of the test section.

The Average Heat Transfer Coefficient

$$h_{exp} = \frac{Q_{TS}}{A_{wi}(T_{r,sat} - T_{wi})} \quad (7)$$

where h_{exp} is the experimental average heat transfer coefficient, Q_{TS} is the heat transfer rate in the test section, T_{wi} is the average temperature of the inner wall, $T_{r,sat}$ is the saturation temperature of the refrigerant, and A_{wi} is the inside surface area of the test section:

$$A_{wi} = \pi d l \quad (8)$$

where d is the inside diameter of the test tube. l is the length of the test tube. It should be noted that the increase in tube area (A_{mf}/A_s) in Table 1 is considered for the surface area of the micro-fin tube during calculation process.

THE LAMINAR ANNULAR FILM CONDENSATION MODEL

Figure 3 shows the steady-state physical model of downward film condensation of R134a in a vertical tube. The assumptions were made as follows: laminar film flow; saturated state for the vapour of R134a; condensed film of R134a along the tube surface; constant physical properties corresponding to inlet pressure and temperature conditions; no entrainment. A Nusselt-type analysis is valid under these assumptions for the internal convective condensation in a round tube. The interfacial shear effect at the liquid-vapour interface is taken account due to the much greater vapour velocity than the film velocity. It should be noticed that the inertia and downstream diffusion contributions were also neglected.

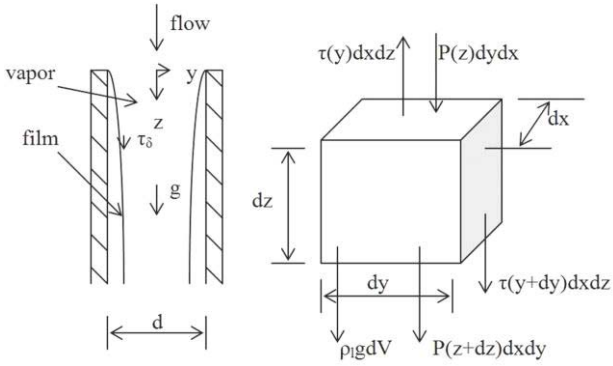

Figure 3. System model for analysis of downward condensation (Dalkilic et al., 2009a).

The differential element's force balance in the control volume is given as follows:

$$\rho_l g dx dy\, dz + \tau_\delta(y+dy)dxdz + P(z)dxdy = \tau_\delta(y)dxdz + P(z+dz)dxdy \quad (9)$$

The hydrostatic pressure gradient, the frictional pressure gradient and the momentum pressure gradient composes the total two-phase pressure gradient and it can be seen as:

$$\left(\frac{dP}{dz}\right)_T = \left(\frac{dP}{dz}\right)_G + \left(\frac{dP}{dz}\right)_F + \left(\frac{dP}{dz}\right)_M \quad (10)$$

where the hydrostatic pressure gradient is:

$$\left(\frac{dP}{dz}\right)_G = \rho g g \quad (11)$$

The interfacial shear stress causes the occurrence of the frictional pressure gradient in the vapour (Carey, 1992) and it can be expressed as follows:

$$\left(\frac{dP}{dz}\right)_F = -\frac{4\tau_\delta}{(d-2\delta)} \quad (12)$$

As a result of the one-dimensional two-phase separated-flow analysis, the momentum pressure gradient can be calculated as follows:

$$\left(\frac{dP}{dz}\right)_M = -G^2 \frac{d}{dz}\left[\frac{x^2}{\rho_g \alpha} + \frac{(1-x)^2}{\rho_l (1-\alpha)}\right] \quad (13)$$

Eq. (14) is obtained from Eq. (13) under the following assumptions: liquid density of R134a is much greater than its vapour density; the variation in vapour quality is bigger than the variation in the void fraction along the test tube (Carey, 1992):

$$\left(\frac{dP}{dz}\right)_M = -\frac{2xdG^2}{\rho_g(d-2\delta)}\frac{dx}{dz} \quad (14)$$

Carey (1992) modified this by means of the usual idealisation on pressure gradient According to his theory; pressure gradient has an equal value in the vapour phase and in the liquid film as expected. A fictitious vapour density is defined to facilitate analysis of the momentum transport in the liquid film, as reported below (Carey, 1992):

$$\rho_g^* g = \rho_g g - \frac{4\tau_\delta}{d-2\delta} - \frac{2xdG^2}{\rho_g(d-2\delta)}\left(\frac{dx}{dz}\right) \quad (15)$$

The velocity gradient can be obtained from Eq. (16) using interfacial shear stress as follows:

$$\frac{du}{dy} = \frac{(\delta - y)(\rho_l - \rho_g^*)g}{\mu_l} + \frac{\tau_\delta}{\mu_l} \quad (16)$$

Integration of Eq. (16) gives Eq. (17) using u=0 at y=0:

$$u = \frac{(\rho_l - \rho_g^*)g}{\mu_l}\left(y\delta - \frac{y^2}{2}\right) + \frac{\tau_\delta y}{\mu_l} \quad (17)$$

The liquid flow rate can be derived from the velocity profile as follows:

$$\dot{m} = \pi d\delta u_{avg}\rho_l = \left[\frac{(\rho_l - \rho_g^*)g\delta^2}{3\mu_l} + \frac{\tau_\delta\delta}{2\mu_l}\right]\pi d\delta\rho_l \quad (18)$$

Eq. (19) can be expressed from the overall mass and energy balance in the case of a falling film without sub-cooling (Carey, 1992):

$$k_l\left(\frac{T_{r,sat} - T_{wi}}{\delta}\right)\pi ddz = i_{fg}d\dot{m} \quad (19)$$

The energy balance in Eq. (19) yields quality gradient as (Carey, 1992):

$$\dot{q} = h_l\pi d\Delta z\Delta T_{sat} = \dot{m}_{cond} i_{fg} \quad (20)$$

$$\frac{dx}{dz} = \frac{4q''}{DGi_{fg}} = \frac{4h_l(T_{r,sat} - T_{w,i})}{DGi_{fg}} \quad (21)$$

Eq. (19) can be rearranged using Eq. (21): (δ=0, x=0)

$$\delta^4 + \frac{4}{3}\frac{\tau_\delta\delta^3}{(\rho_l - \rho_g^*)g} = \frac{4k_l\mu_l(T_{r,sat} - T_{wi})z}{\rho_l(\rho_l - \rho_g^*)gi_{fg}} \quad (22)$$

The film thickness equation, belong to Nusselt's analysis (Nusselt, 1916), can be obtained when the interfacial shear stress effects are omitted as shown in Eq. (23):

$$\delta(z) = \left[\frac{4\mu_l k_l z(T_{r,sat} - T_{wi})}{gi_{fg}\rho_l(\rho_l - \rho_g)}\right]^{1/4} \quad (23)$$

Application of the correction factor to the latent heat of vaporisation per unit mass can be seen from Eq. (24) as follows:

$$i_{fg}' = i_{fg}\left[1 + \left(\frac{3}{8}\right)\frac{c_{pl}(T_{r,sat} - T_{wi})}{i_{fg}}\right] \quad (24)$$

The film heat transfer coefficient is shown in Eq. (25) assuming a linear temperature distribution in the film region as:

$$h_l(z) = \frac{k_l}{\delta(z)} \quad (25)$$

The vapour flow can be behaved as a single phase flow in the tube as an approach due to the thin film and the much greater mean velocity of vapour than the liquid velocity at the interface caused by the high viscosity of the liquid phase compared to the vapour phase. Furthermore, vapour velocity is assumed to be zero between the phases in calculations. The interfacial shear can be obtained by means of the conventional single phase correlation with these assumptions (Carey, 1992):

$$\tau_\delta = f_g\left(\frac{\rho_g u_g^2}{2}\right) = f_g\left(\frac{G^2x^2}{2\rho_g(1-4\delta/d)}\right) \quad (26)$$

The friction factor can be expressed for round smooth tubes as (Carey, 1992):

$$f_g = 0.079\left[\frac{Gx(d-\delta)}{\mu_g(1-4\delta/d)}\right]^{-0.25} \quad (27)$$

Cavallini et al. (1997b) proposed a friction factor for round micro-fin tubes including their fin parameters as follows:

$$f_g = \frac{[1.74 - 2.\log(2Rx_f)]^{-2}}{4} \quad (28)$$

where geometry enhancement factor of micro-fin tube in comparison to the smooth tube is expressed in Eq. (29) as (Cavallini, 1997b):

$$Rx_f = \frac{0.18\left(\frac{l_f}{d}\right)}{(0.1 + \cos\beta)} \quad (29)$$

It is possible for the McAdams correction factor (1954) to be used to consider the effects of the waviness and rippling in the film regarding the increase in heat transfer. It can be used for downward laminar film condensation, and it corrects the Nusselt's equation (1916) in terms of the above explanation as follows:

$$h_{wave} = 1.2\frac{k_l}{\delta(z)} \quad (30)$$

Carey (1992) offered an iterative technique for the determination of film heat transfer coefficient and interfacial shear using specified mass flux, tube wall inlet temperature, and condensation pressure and thermo physical properties. Firstly, a value for a film thickness is guessed, the quality gradient is obtained from Eqs. (21) and (25). The interfacial shear stress value is calculated by means of Eqs. (26) and (28), and Eq. (15) gives the fictitious vapour density.

The substitution of the estimated film thickness values, calculated fictitious vapour density and interfacial shear values are performed into Eq. (22). These values are updated and the film thickness value repeatedly estimated until convergence. The level of accuracy judges the acceptable values of estimated film thickness and calculated film heat transfer coefficient. Figure 4 shows this procedure step by step in detail.

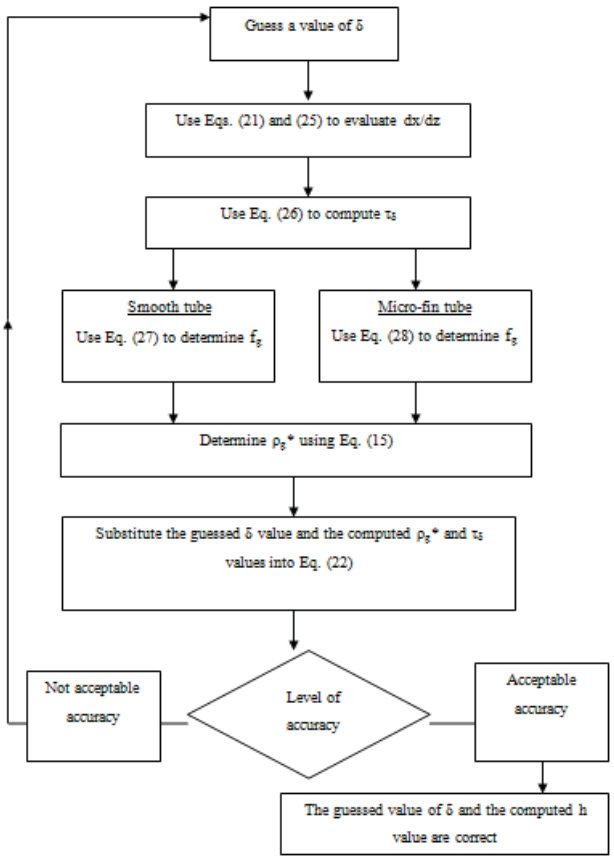

Figure 4. Flow chart of iteration process.

It should be noted that it is possible Nusselt's theory (1916) to be used for both condensation on vertical flat surfaces and condensation outside tubes and also inside the tubes if the tubes are large in diameter, compared with the film thickness. Nusselt (1916) proposed the average convective heat transfer coefficient as follows ($0<Re_l<30$):

$$h_{Nusselt} = 0.943\left[\frac{\rho_l(\rho_l-\rho_g)gi_{fg}k_l^3}{\mu_l l(T_{r,sat}-T_{wi})}\right]^{1/4} \quad (31)$$

RESULTS AND DISCUSSION

The experiments of smooth and micro-fin tubes were done using R134a in tubes at the mass flux of 29 kg $m^{-2}s^{-1}$ and pressures between 0.8-0.9 MPa. The modified Nusselt theory including the interfacial shear effect was used in the calculations of all local heat transfer coefficients. Figures 5-8 show the effect of the temperature difference between the saturated temperature of R134a and inner wall temperature of the micro-fin tube ($\Delta T_{r,sat}$) and the condensation pressure on the local heat transfer coefficients, film thickness and condensation rates along the micro-fin tube's length.

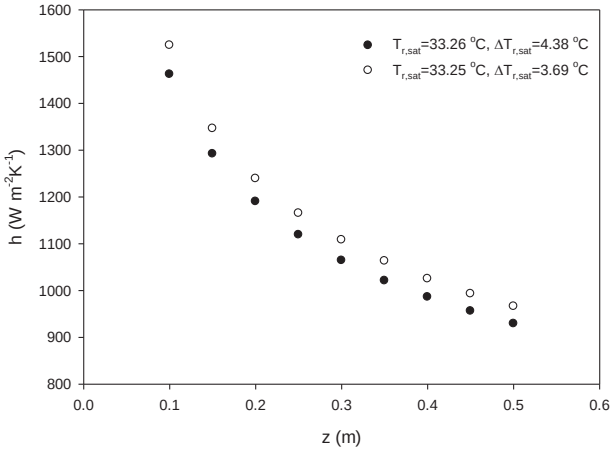

Figure 5. Comparison of local heat transfer coefficients of micro-fin tube at different $\Delta T_{r,sat}$ for the mass flux of 29 kg $m^{-2}s^{-1}$ and a constant condensation temperature.

The decrease in the local condensation heat transfer coefficient and condensation rate of micro-fin tube along the tube length, calculated by the proposed model, can be seen from Figures 5 and 6. It is because of this that the film thickness and hence total condensation rate increase from the top to the bottom of the test tube through the direction of gravity. There is high local condensation rate along the tube length at the tube entrance caused by high vapour velocity and high interfacial shear. It decreases along the tube length with decreasing vapour velocity due to an increase in condensation rate. Oh and Revankar (2005) have the similar characteristics of trend lines in their study.

The effect of pressure, in other saying, the effect of the saturation temperature on the local heat transfer coefficients and condensation rate along the tube length for the micro-fin tube, calculated by the proposed model, can be seen from Figures 7 and 8. Low condensation pressures, in other saying, high temperature differences and change of physical properties at low pressure induce higher local heat transfer coefficients than those of high condensation pressure. These results and the general trend are found

to be compatible with the Nusselt (1916) theory in which the average and local heat transfer coefficients are proportional to $\Delta T_{r,sat}^{-0.25}$ and $z^{-0.25}$.

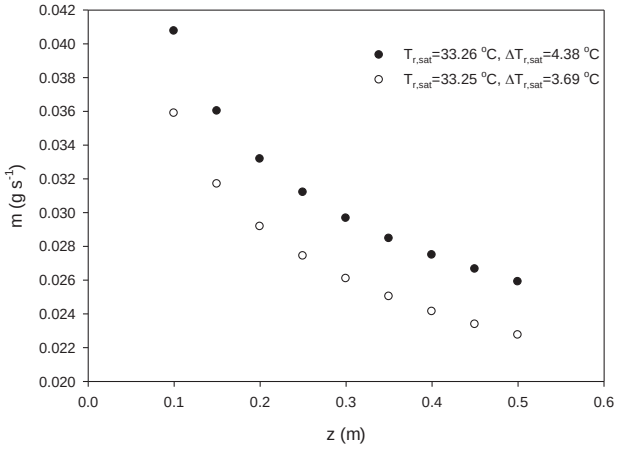

Figure 6. Comparison of local condensation rates of micro-fin tube at different $\Delta T_{r,sat}$ for the mass flux of 29 kg m^{-2}s^{-1} and a constant condensation temperature.

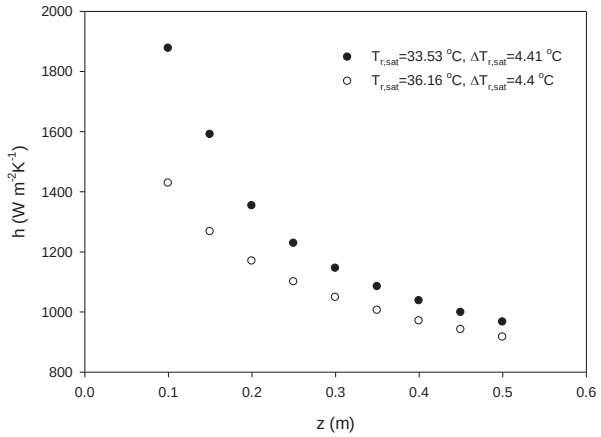

Figure 7. Comparison of local heat transfer coefficients of micro-fin tube at different condensation temperatures (33.53 and 36.16 °C) for the mass flux of 29 kg m^{-2}s^{-1} and $\Delta T_{r,sat}$=4.4 °C.

The data shown in all figures and tables were collected in an annular flow regime in Hewitt and Robertson's (1969) flow pattern map, and also checked by sight glasses at the inlet and outlet of the test section.

The determination of the film heat transfer coefficient for the laminar flow at low mass flux for the smooth and micro-fin tubes was performed by means of the modified Nusselt theory (Carey, 1992), the McAdams correlation (1954) and the classical Nusselt theory (1916).

The modified Nusselt theory in Eq. (22) including the interfacial shear stress effect is found to be the most suitable model for the experimental data from the micro-fin tube according to the analysis of Figure 9. Besides this, it can be also understood from Figure 9 that the investigated experimental conditions do not require the usage of McAdams correction factor (1954) in Eq. (30) to take account the wave effect at the vapour-liquid interface occurred by low mass flux. In addition to this, the classical Nusselt theory in Eq. (31) overestimates the heat transfer coefficients considering the deviation of 30%.

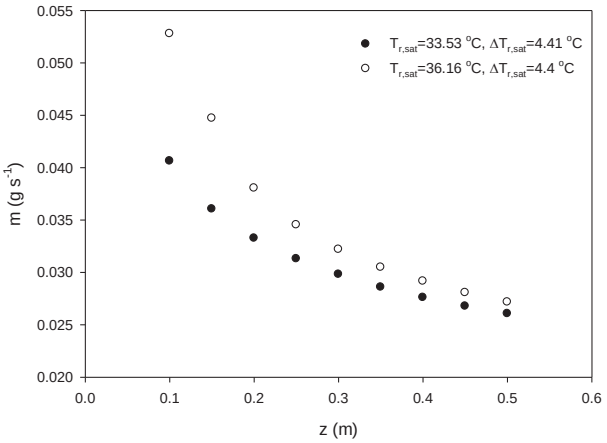

Figure 8. Comparison of local condensation rates of micro-fin tube at different condensation temperatures (33.53 and 36.16 °C) for the mass flux of 29 kg m^{-2}s^{-1}and $\Delta T_{r,sat}$=4.4 °C.

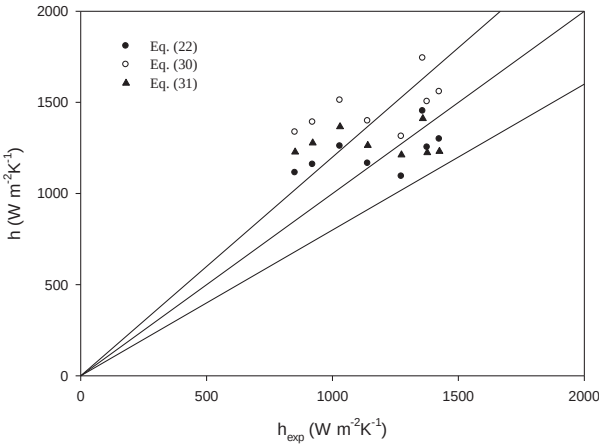

Figure 9. Comparisons between the experimental and calculated condensation heat transfer coefficients for the micro-fin tube under the experimental conditions: G=29 kg m^{-2}s^{-1}, P= 0.8-0.9 MPa, $T_{r,sat}$= 31.73-35.28 ºC, $\Delta T_{r,sat}$= 1.67-4.4 °C, x_{avg} = 0.82-0.99.

The enhancement on the condensation heat transfer coefficients using smooth and micro-fin tubes at the approximately similar experimental conditions, shown in Table 2, such as mass flux, condensing pressure, vapour quality, $\Delta T_{r,sat}$ can be seen from Figure 10. According to the result of analysis, the heat transfer enhancement of 60-82% is gained by means of the usage of micro-fin in comparison to the smooth tube.

Figure 11 shows the effect of the condensation pressure on the heat transfer coefficients. According to Figure 11, the average experimental condensation heat transfer coefficients obtained from Eq. (7) decrease with increasing system pressure as expected.

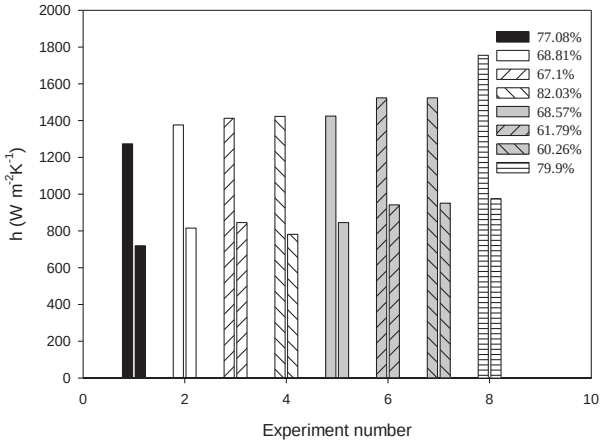

Figure 10. Comparisons between the experimental condensation heat transfer coefficients for the smooth and micro-fin tubes under the experimental conditions:
G=29 kg $m^{-2}s^{-1}$, P= 0.8-0.9 MPa, $T_{r,sat}$= 31.08-36.16 ºC, $\Delta T_{r,sat}$= 2.71-4.86 °C, x_{avg} = 0.8-0.99.

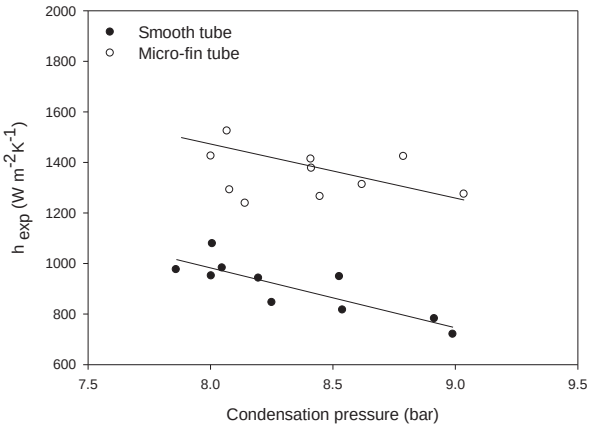

Figure 11. Comparison of average experimental convective heat transfer coefficients of the smooth and micro-fin tubes for the mass flux of 29 kg $m^{-2}s^{-1}$ at pressures of 0.77-0.90 MPa.

Bellinghausen and Renz's (1992) method is used to present correlations for the smooth (Dalkilic, 2009a) and micro-fin tubes separately. Although their correlation's accuracy seems poor with their data (Bellinghausen and Renz, 1992) it can be used in Nusselt-type analysis for the conditions of laminar film with stagnant vapour and a wave-free interface in a smooth tube. Therefore, the low mass flux data (29 kg $m^{-2}s^{-1}$) were used. It should be noted that these correlations simplify the calculations for practical applications. The comparison of the results from the present correlation with the experimental data is shown in Figure 12. The majority of the data fall within ±25% of the proposed correlation.

Table 2. Numerical values used in Figure 10.

Exp. number	Tube type	$T_{r,sat}$ (°C)	G (kg $m^{-2}s^{-1}$)	x	$\Delta T_{r,sat}$ (°C)	h (W $m^{-2}K^{-1}$)	Augmentation rate (h, %)
1	Smooth	35.982	28.434	0.936	3.989	719.413	77.08
1	Micro-fin	36.169	28.664	0.938	4.405	1273.982	
2	Smooth	34.084	28.65	0.99	3.609	815.385	68.81
2	Micro-fin	33.537	28.432	0.8	4.419	1376.521	
3	Smooth	32.836	28.73	0.88	3.69	845.127	67.1
3	Micro-fin	33.527	28.478	0.88	4.56	1412.718	
4	Smooth	35.669	29.74	0.85	4.861	781.32	82.03
4	Micro-fin	35.141	28.72	0.84	4.676	1422.693	
5	Smooth	32.83	28.73	0.88	3.699	845.127	68.57
5	Micro-fin	31.723	29.75	0.82	4.457	1424.652	
6	Smooth	32.59	28.903	0.938	3.09	941.773	61.79
6	Micro-fin	32.019	28.57	0.925	2.904	1523.75	
7	Smooth	31.73	28.79	0.97	2.76	950.782	60.26
7	Micro-fin	32.019	28.57	0.925	2.904	1523.75	
8	Smooth	31.082	28.972	0.864	3.04	975.225	79.9
8	Micro-fin	31.174	28.81	0.98	2.719	1755.282	

The correlations are presented as:

For the smooth tube (Dalkilic et al. (2009a):

$$\delta^*=7.4.Re_l^{0.018} \quad (32)$$

For the micro-fin tube:

$$\delta^*=6.19.Re_l^{0.018} \quad (33)$$

$$h_l=(k_l/L).(1/\delta^*) \quad (34)$$

Liquid Reynolds number:

$$Re_l = \dot{m}/(\pi.d.\mu_l) \quad (35)$$

Liquid Nusselt number:

$$Nu_l=1/\delta^* \quad (36)$$

Dimensionless film thickness:

$$\delta^*=\delta/L \quad (37)$$

Characteristic length:

$$L=(\delta_l^2/g)^{1/3} \quad (38)$$

Nusselt number:

$$Nu_l=h_l.L/k_l \quad (39)$$

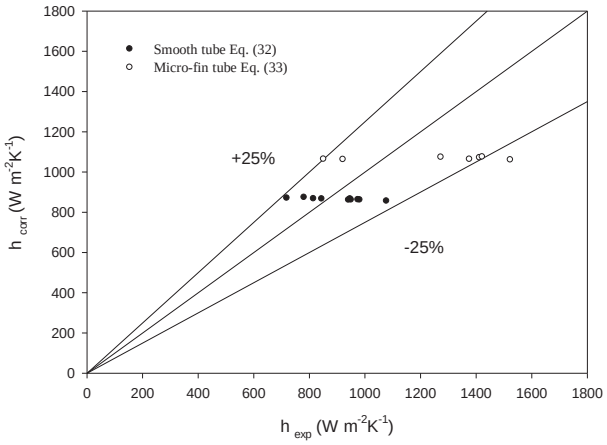

Figure 12. Comparison of the experimental convective heat transfer coefficient with the present heat transfer correlations for the smooth tube and micro-fin tubes.

CONCLUSION

Generally, horizontal micro-fin tubes are used to enhance convective heat transfer during in-tube condensation. According to the review of literature, only a few experimental works (Dalkilic and Wongwises, 2009) have been done for the heat transfer and flow characteristics inside enhanced vertical tubes. There isn't any previous work with the content and parameters in the literature apart from the present paper. Therefore, the present study has a large importance for the development of new types of compact heat exchangers in all industrial fields.

The investigation of the convective heat transfer coefficient of R134a during condensation in vertical downward flow at a low mass flux in smooth and micro-fin tubes was presented in the paper. It should be noted that research on the various parameters used in the present study is still limited. The results from this study are expected to fill the gap in the literature due to the insufficient works regarding condensation inside vertical micro-fin tubes in the literature. The accurate and repeatable heat transfer data for the condensation of R134a in a downward flow at a low mass flux inside smooth and micro-fin tubes were obtained. Detailed investigation and discussion were performed on the effects of various relevant parameters such as condensing temperature, condensation temperature difference, vapour quality and mass flux on the heat transfer.

The investigation of the local and average heat transfer coefficients in vertical smooth and micro-fin tubes at low mass flux conditions were done by means of the theoretical model from Carey (1992). Cavallini et al. (1997b)'s friction factor was added to the model for the micro-fin tube's calculations. The experimental data was compared with the calculated results obtained from the modified Nusselt model incorporating the interfacial shear stress, along with the modified Nusselt model with McAdams correction factor and also with the classical Nusselt model.

As an expected result, the condensation rate reaches the highest value at the pipe entrance where the highest local heat transfer coefficients exist. The film thickness is highest at the end of the tube where the local heat transfer coefficients are lowest. This result also shows the experiments' accuracy and validity.

According to the comparisons with laminar flow at low mass flux data, the modified Nusselt model without a correction factor predicts the data well. As a result of the analysis, the interfacial shear stress that was incorporated into the modified Nusselt model affects the condensation process of R134a in a vertical smooth and micro-fin tube. The classical Nusselt theory and the McAdams heat transfer coefficient cannot predict the data well.

Convective condensation heat transfer coefficients of micro-fin tube are found to be 1.6-1.82 times higher than the smooth tube at the similar experimental conditions.

New correlations for the determination of condensation heat transfer coefficients are proposed belong to the tested tubes separately for practical applications, and as a result of this study, it is possible to simply calculate the condensation heat transfer coefficient with an interfacial shear effect during downward laminar flow in vertical smooth and micro-fin tubes at low mass flux conditions.

ACKNOWLEDGEMENTS

The present study was financially supported by Yildiz Technical University. The first author wishes to thank KMUTT for providing him with a Post-doctoral fellowship, while the third author wish to acknowledge the support provided by the Thailand Research Fund. The authors also wish to thank Wieland-Wilke AG (Ulm, Germany) for valuable donation of the micro-fin tube used in the present study.

REFERENCES

Balcilar, M., Dalkilic, A.S., Wongwises, S., Artificial Neural Network (ANN) Techniques for the Determination of Condensation Heat Transfer Characteristics during Downward Annular Flow of R134a inside a Vertical Smooth Tube, *Int. Communications in Heat and Mass Transfer*, "Accepted for Publication-Article in Press", 2010. (a)

Balcilar, M., Dalkilic, A.S., Wongwises, S., Determination of Condensation Heat Transfer Characteristics of R134a by means of Artificial Intelligence Method, *ASME International Mechanical Engineering Congress and Exposition*, 12-18, 2010. (b)

Bellinghausen. R, Renz, U., Heat Transfer and Film Thickness During Condensation of Steam Flowing at High Velocity in a Vertical Pipe, *Int. J. of Heat and Mass Transfer* 35, 683-689, 1992.

Briggs, A., Kelemenis, C., Rose, J.W., Condensation of CFC-113 with Down Flow in Vertical, Internally Enhanced Tubes, *Proceedings of 11th IHTC*, 23-28, 1998.

Carey, V.P., *Liquid-Vapor Phase Change Phenomena*, Hemisphere Publishing, 1992.

Cavallini, A., Del Col, D., Doretti, L., Longo, G.A., Rossetto, L.A., A New Computational Procedure for Heat Transfer and Pressure Drop during Refrigerant Condensation inside Enhanced Tubes, *Enhanced Heat Transfer* 6, 441-456, 1999. (a)

Cavallini, A., Del Col, D., Doretti, L., Longo, G.A., Rossetto, L., Pressure Drop During Condensation and Vaporisation of Refrigerants Inside Enhanced Tubes, *Heat and Technology* 15, 3-10, 1997. (b)

Chamra, L.M., Webb, R.L., Randlett, M.R., Advanced Micro-fin Tubes for Condensation, *Int. Journal of Heat and Mass Transfer* 39, 1839-1846, 1996.

Dalkilic, A.S., Yildiz, S., Wongwises, S., Experimental Investigation of Convective Heat Transfer Coefficient During Downward Laminar Flow Condensation of R134a in a Vertical Smooth Tube, *Int. Journal of Heat and Mass Transfer* 52, 142-150, 2009. (a)

Dalkilic, A.S., Wongwises, S., Intensive Literature Review of Condensation Inside Smooth and Enhanced Tubes, *Int. Heat and Mass Transfer* 52, 3409-3426, 2009. (b)

Dalkilic, A.S., Laohalertdecha, S., Wongwises, S., Effect of Void Fraction Models on the Two-phase Friction Factor of R134a During Condensation in Vertical Downward Flow in a Smooth Tube, *Int. Communications in Heat and Mass Transfer* 35, 921-927, 2008. (c)

Dalkilic, A.S., Laohalertdecha, S., Wongwises, S., Two-phase Friction Factor in Vertical Downward Flow in High Mass Flux Region of Refrigerant HFC-134a During Condensation, *Int. Communications in Heat and Mass Transfer* 35, 1147-1152, 2008. (d)

Dalkilic, A.S., Laohalertdecha, S., Wongwises, S., Effect of Void Fraction Models on the Film Thickness of R134a During Downward Condensation in a Vertical Smooth Tube, *Int. Communications in Heat and Mass Transfer* 36, 172-179, 2009. (e)

Dalkilic, A.S., Laohalertdecha, S., Wongwises, S., Experimental Investigation on Heat Transfer Coefficient of R134a During Condensation in Vertical Downward Flow at High Mass Flux in a Smooth Tube, *Int. Communications in Heat and Mass Transfer* 36, 1036-1043, 2009. (f)

Dalkilic, A.S., Agra, O., Teke, I., Wongwises, S., Comparison of Frictional Pressure Drop Models During Annular Flow Condensation of R600a in a Horizontal Tube at Low Mass Flux and of R134a in a Vertical Tube at High Mass Flux, *Int. Journal of Heat and Mass Transfer* 53, 2052-2064, 2010. (g)

Dalkilic, A.S., Wongwises, S., An Investigation of a Model of the Flow Pattern Transition Mechanism in Relation to the Identification of Annular Flow of R134a in a Vertical Tube Using Various Void Fraction Models and Flow Regime Maps, *Experimental Thermal and Fluid Science* 34, 692-705, 2010. (h)

Dalkilic, A.S., Laohalertdecha, S., Wongwises, S., Validation of Void Fraction Models and Correlations Using a Flow Pattern Transition Mechanism Model in Relation to the Identification of Annular Vertical Downflow In-tube Condensation of R134a, *Int. Communications in Heat and Mass Transfer* 37, 827-834, 2010. (i)

Dalkilic, A.S., Laohalertdecha, S., Wongwises, S., Experimental Study of the Condensation Heat Transfer Coefficients in High Mass Flux Region in Annular Flow Regime of HFC-134a Inside the Vertical Smooth tube, *Heat Transfer Engineering* 32, 1-12, 2011. (j)

Dalkilic, A.S., Laohalertdecha, S., Wongwises, S., New Experimental Approach on the Determination of Condensation Heat Transfer Coefficient Using Frictional Pressure Drop and Void Fraction Models in a Vertical Tube, *Energy Conversion and Management* 51, 2535-2547, 2010. (k)

Dalkilic, A.S. Dalkilic, Wongwises, S., A Performance Comparison of Vapour Compression Refrigeration System Using Various Alternative Refrigerants, *Int. Communications in Heat and Mass Transfer* 37, 1340-1349, 2010. (l)

Dalkilic, A.S., Teke, I., Wongwises, S., Experimental Analysis for the Determination of the Convective Heat Transfer Coefficient by Measuring Pressure Drop Directly During Annular Condensation Flow of R134a in a Vertical Smooth Tube, *Int. J. of Heat and Mass Transfer*, "Accepted for Publication-Article in Press". (m)

Dalkilic, A.S., Laohalertdecha, S., Wongwises, S., A Comparison of the Void Fraction Correlations of R134a During Condensation in Vertical Downward Laminar Flow in a Smooth and Microfin Tube, *ASME Proceedings of the Micro/Nanoscale Heat Transfer International Conference* Parts A-B, 1029-1040, 2008. (n)

Dalkilic, A.S., Laohalertdecha, S., Wongwises, S., Two-phase Friction Factor Obtained From Various Void Fraction Models of R-134a During Condensation in Vertical Downward Flow at High Mass Flux, *ASME Proceedings of the ASME Summer Heat Transfer Conference* 2, 193-206, 2009. (o)

Dalkilic, A.S., Laohalertdecha, S., Wongwises, S., Experimental Investigation on the Condensation Heat Transfer and Pressure Drop Characteristics of R134a at High Mass Flux Conditions During Annular Flow Regime Inside a Vertical Smooth Tube, *ASME Summer Heat Transfer Conference* 19-23, 2009. (p)

Dalkilic, A.S., Agra, O., Experimental Apparatus for the Determination of Condensation Heat Transfer Coefficient for R134a and R600a Flowing Inside Vertical and Horizontal Tubes, *ASME Summer Heat Transfer Conference* 19-23, 2009. (r)

Dalkilic, A.S., Laohalertdecha, S., Wongwises, S., Experimental Research on the Similarity of Annular Flow Models and Correlations for the Condensation of R134a at High mass Flux Inside Vertical and Horizontal Tubes, *ASME International Mechanical Engineering Congress and Exposition* 13-19, 2009. (s)

Dalkilic, A.S., Wongwises, S., A Heat Transfer Model for Co-current Downward Laminar Film Condensation of R134a in a Vertical Micro-fin Tube During Annular Flow Regime, *the Eleventh UK National Heat Transfer Conference* 6-8, 2009. (t)

Dalkilic, A.S., Laohalertdecha, S., Wongwises, S., Comparison of Condensation Frictional Pressure Drop Models and Correlations During Annular Flow of R134a Inside a Vertical Tube, *ASME-ATI-UTI Thermal and Environmental Issues in Energy Systems* 16-19, 2010. (u)

Dalkilic, A.S., Wongwises, S., Experimental Study on the Flow Regime Identification in the Case of Co-current Condensation of R134a in a Vertical Smooth Tube, *ASME International Heat Transfer Conference* 8-13, 2010. (v)

Dalkilic, A.S., Wongwises, S., Comparison of Various Alternative Refrigerants for Vapour Compression Refrigeration Systems, *ASME/JSME 8th Thermal Engineering Joint Conference* 13-17, 2011. (y)

Dalkilic, A.S., Düşey borularda yoğuşmada ısı taşınım katsayısının araştırılması, *Ph.D. Thesis*, Yildiz Technical University, Istanbul, Turkey, 2007. (z)

Hewitt, G.F., Robertson, D.N., Studies of Two-phase Flow Patterns by Simultaneous X-ray and Flash Photography, *Rept AERE-M2159, UKAEA, Harwell*, 1969.

McAdams, W.H., *Heat Transmission*, 3rd ed., McGraw-Hill, New York Univ. Calif. (Berkeley) Pub. Eng., 443-461, 1954.

Nusselt, W., Die Oberflachen Kondenastion des Wasserdamfes, *Zeitschrift des Vereines Deutscher Ingenieure* 60, 541-546, 569-575, 1916.

Oh, S., Revankar, A., Analysis of the Complete Condensation in a Vertical Tube Passive Condenser, *Int. Communications in Heat and Mass Transfer* 32, 716-727, 2005.

Schlager, L.M., Pate, M.B., Bergles, A.E., Evaporation and Condensation Heat Transfer and Pressure Drop in Horizontal, 12.7-mm Microfin Tubes with Refrigerant 22, *J. of Heat Transfer* 12, 1041-1047, 1990.

Shah, M.M., A General Correlation for Heat Transfer During Film Condensation Inside Pipes, *Int. J. of Heat and Mass Transfer* 22, 547-556, 1979.

Wang, H.S., Honda, H., Condensation of Refrigerants in Horizontal Microfin Tubes: Comparison of Prediction Methods for Heat Transfer, *Int. J. of Refrigeration* 26, 452-460, 2003.

Ahmet Selim DALKILIÇ is currently a Research Assistant of Mechanical Engineering at Yildiz Technical University, İstanbul, Turkey. He received his Ph.D. Degree in Mechanical Engineering from the same university. His current research interest is on enhanced heat transfer, convection heat transfer, condensation, evaporation, boiling heat transfer of new refrigerants and mixture refrigerants and applications in heat exchangers. Dr. Ahmet Selim Dalkılıç is the member of Innovation Explorer for Scientific Researchers Community sponsored by Elsevier and American Society of Mechanical Engineers (ASME). He has been serving as a volunteer associate editor for Scientific Journals International (SJI) - Journal of Mechanical, Aerospace and Industrial Engineering.

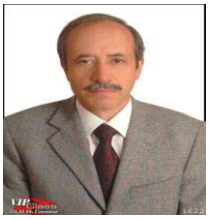

İsmail TEKE is currently a professor of mechanical engineering at Yıldız Technical Üniversity,İstanbul, Turkey. He received his PhD degree in mechanical engineering from the same üniversity in 1981. His current research interest is on two phase flow and heat exchangers.

Somchai Wongwises is currently a professor of mechanical engineering at King Mongkut's University of Technology Thonburi, Bangmod, Thailand. He received his Doktor-Ingenieur (Dr.-Ing.) in mechanical engineering from the University of Hannover, Germany, in 1994. His research interests include two phase flow, heat transfer enhancement, and thermal system design. He is the head of the Fluid Mechanics, Thermal Engineering and Multiphase Flow Research Labarotory (FUTURE). He has been serving as an editor for Experimental Thermal and Fluid Science.

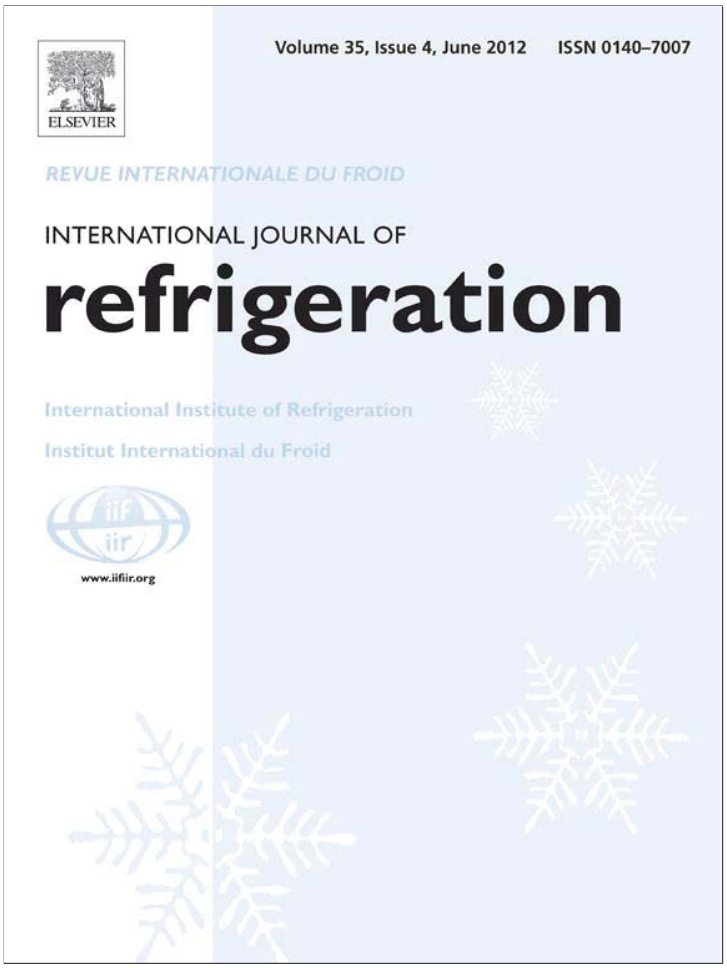

INTERNATIONAL JOURNAL OF REFRIGERATION 35 (2012) 740–749

Available online at www.sciencedirect.com

SciVerse ScienceDirect

journal homepage: www.elsevier.com/locate/ijrefrig

Review

A review of numerical modelling studies on short-tube orifice performance with applications to air-conditioning systems

Kitti Nilpueng [a,b], *Somchai Wongwises* [b,c,*]

[a] *Department of Mechanical Engineering, South-East Asia University, Bangkok, Thailand*
[b] *Fluid Mechanics, Thermal Engineering and Multiphase Flow Research Lab (FUTURE), Department of Mechanical Engineering, King Mongkut's University of Technology Thonburi, Bangmod, Bangkok 10140, Thailand*
[c] *The Academy of Science, The Royal Institute of Thailand, Sanam Suea Pa, Dusit, Bangkok 10300, Thailand*

ARTICLE INFO

Article history:
Received 25 August 2011
Received in revised form
20 January 2012
Accepted 20 January 2012
Available online 3 February 2012

Keywords:
Expansion valve
Flow rate
Critical pressure
Temperature variation

ABSTRACT

The manufacturers of air conditioners need a precise method for calculating the critical flow rate of refrigerant through the short-tube orifice, and they must select the proper size of short-tube orifice at given operating conditions in order to achieve optimum system performance. The present study divides the research into two main groups: studies conducted under the semi-empirical model and those conducted under the theoretical model. The former model has been developed based on the single-phase orifice equation with the correction factor. The latter model applies the proper governing equations, including conservation of mass, momentum, and energy, to determine the refrigerant flow mechanism inside the short-tube orifice. Because these equations are rather difficult to solve, only a few studies have been conducted. This paper describes the details of the numerical modelling of refrigerant flow characteristics through the short-tube orifice reported in previous publications as well as the guideline for future research.

Etudes sur la modélisation numérique effectuées sur la performance des orifices des tubes courts dans le contexte du conditionnement d'air : passage en revue

Motsclés : détendeur ; débit ; pression critique ; variation de température

* *Corresponding author*. Department of Mechanical Engineering, King Mongkut's University of Technology Thonburi, Bangmod, Bangkok 10140, Thailand. Tel.: +662 4709115; fax: +662 4709111.
E-mail address: somchai.won@kmutt.ac.th (S. Wongwises).
0140-7007/$ – see front matter © 2012 Elsevier Ltd and IIR. All rights reserved.
doi:10.1016/j.ijrefrig.2012.01.019

Nomenclature

A	cross-section area of short-tube orifice, m^2
C	discharge coefficient
C_c	correction factor for chamfering
C_p	specific heat at constant pressure, $kJ\,kg^{-1}\,K^{-1}$
C_{tp}	correction factor for two-phase flow
DEPTH	chamfer depth, mm
D	diameter, m
D_{ref}	reference short-tube diameter, m
D_R	normalized diameter
EVAP	normalized downstream pressure
f	fanning friction factor
F_{GL}	interfacial fictional force per unit volume between vapour and liquid, $N\,m^{-3}$
F_{WL}	interfacial fictional force per unit volume between tube wall and liquid phase, $N\,m^{-3}$
G	mass flux, $kg\,m^{-2}\,s^{-1}$
G_{cr}	critical mass flux, $kg\,m^{-2}\,s^{-1}$
g_c	dimensional gravity constant, $1.296 \times 10^{10}\ s^2\,N\,h^{-2}\,kN^{-1}$
h	enthalpy, $kJ\,kg^{-1}$
k	slip ratio
L	length, m
$\dot{m}$	mass flow rate, $kg\,s^{-1}$
P	pressure, Pa
P_f	adjusted downstream pressure, Pa
P_R	normalized upstream pressure
s	entropy, $kJ\,kg^{-1}\,K^{-1}$
SUBC	normalized subcooling
T	temperature, °C
t_R	normalized upstream temperature
u	fluid velocity, $m\,s^{-1}$
u_L	liquid velocity, $m\,s^{-1}$
u_G	vapour velocity, $m\,s^{-1}$
We_d	Weber number, $G^2D/\rho_L\sigma$
x	quality
z	incremental axial length, mm

Greek symbols

ρ	density, $kg\,m^{-3}$
β	short-tube orifice diameter to the tube diameter ratio
υ	specific volume, $m^3\,kg^{-1}$
μ	viscosity, $kg\,m^{-1}\,s^{-1}$
σ	surface tension, $N\,m^{-1}$
Φ	correction factor
Γ	inter-phase mass transfer rate per unit volume, $kg\,m^{-3}\,s^{-1}$
ϕ_{tp}^2	two-phase multiplier

Subscripts

c	critical
down	downstream
f	liquid phase
g	gas-phase
ref	reference
sat	saturation
up	upstream

1. Introduction

A short-tube orifice is a type of expansion device popularly used in residential and automotive air conditioners. It is made from extremely small bore hollow brass with length-to-diameter ratios ranging between 3 and 20. The benefits of a short-tube orifice over a thermostatic expansion valve are the low starting torque of the compressor as the pressures across the short-tube orifice equalize during the off-cycle, simplicity, low initial cost, and absence of any moving parts. However, it has been found that after the size of a short-tube orifice is selected to install into an air-conditioning system, it will be suitable for only one design condition. That is, the mass flow rate and pressure drop would not be adequate under different operating conditions. In addition, the refrigerant flow inside the short-tube orifice should be choked in order to obtain an appropriate distribution of refrigerant under working conditions. This is because, under a non-choked flow condition, the refrigerant mass flow rate discharged into the evaporator will decrease when the evaporator pressure increases with an increase in evaporator load. Conversely, the mass flow rate increases as the evaporator pressure decreases under a decrease in evaporator load. This flow behaviour is inappropriate for air-conditioning systems. Thus, to obtain the optimum performance of the air-conditioning system, engineers must identify proper short-tube orifice size at a given operating condition or quantify the critical flow rate that can be produced through the short-tube orifice.

In the past decade, several short-tube orifice models were developed to calculate the refrigerant flow behaviour inside the short-tube orifice. The models can be divided into two main groups: semi-empirical models and theoretical models. The aim of this paper is to describe the detail of the numerical modelling of refrigerant flow characteristics through the short-tube orifice of previous publications and to suggest guidelines for future research.

2. Semi-empirical models

The semi-empirical models are generated in the form of simple equations with the correction factor created from experimental data. During the past decade, it can be seen that most previous researchers have developed short-tube orifice flow models based on a single-phase orifice equation (ASME, 1971). The single-phase orifice equation is expressed as follows:

$$\dot{m} = CA\sqrt{\frac{2\rho(P_{up} - P_{down})}{(1-\beta^4)}} \tag{1}$$

where C is the discharge coefficient, A is the cross-sectional area of a short-tube orifice, ρ is the density of fluid, P_{up} is

upstream pressure, P_{down} is downstream pressure, and β is the ratio of the orifice diameter to the upstream tube diameter.

Mei (1982) proposed two short-tube orifice models with degrees of subcooling over 22.2 °C and below 22.2 °C for HCFC-22 flow through short-tube orifices. The refrigerant mass flux can be estimated by

$$G = C\left[2\rho\left(P_{up} - P_{down}\right)\right]^{1/2} \tag{2}$$

For $\Delta T_{sub} < 22.2\ ^{\circ}C$

$$C = -0.007364\left(\sqrt{\Delta P} - \sqrt{1034.2}\right) + 0.0108\Delta T_{sub} + 0.40 \tag{3}$$

For $\Delta T_{sub} > 22.2\ ^{\circ}C$

$$C = 0.9175 - 0.00585\Delta T_{sub} \tag{4}$$

The correlation of the orifice coefficient (C) was presented as a function of degree of subcooling (ΔT_{sub}) and pressure difference between upstream and downstream (ΔP).

Aaron and Domanski (1990) developed the single-phase orifice equation with a correction factor of adjusted saturation pressure for the purpose of predicting the mass flow rate of HCFC-22 through short-tube orifices. In their model, the discharge coefficient (C) is set equal to unity, while the velocity of approach factor ($1-\beta^4$) is neglected, as shown below.

$$\dot{m} = C_c A\sqrt{2\rho(P_1 - P_2)} \tag{5}$$

where

$$P_2 = P_{sat}\left[1 + 12.599\mathrm{SUB}^{1.293} - 0.1229\exp\left(-0.0169(L/D)^2\right) - 0.04753\mathrm{EVAP}^{0.6192}\right] \tag{6}$$

$$\mathrm{SUB} = \left(T_{sat} - T_{fliud}\right)/T_{sat} \tag{7}$$

$$\mathrm{EVAP} = \left(P_{sat} - P_{down}\right)/P_{sat} \tag{8}$$

A correlation of the chamfered inlet is applied to a short-tube orifice with a chamfered inlet.

$$C_c = 1 + 0.0551(L/D)^{0.5844}(\mathrm{DEPTH}/D)^{0.2967} \tag{9}$$

where DEPTH is the inlet chamfer depth.

The models for calculating the flow rate of saturated liquid and two-phase flow of CFC-12, HCFC-22, HFC-134a, and HFC-407C though a short-tube orifice were developed by Kim et al. (1994), Kim and O'Neal (1994) and Payne and O'Neal (1998). The adjusted downstream pressure correlation was proposed as a function of the upstream pressure, downstream pressure, upstream temperature, diameter, and length-to-diameter ratio. The flow rate can be estimated with the following equation:

$$\dot{m} = C_c C_{tp} A\sqrt{2\rho\left(P_{up} - P_f\right)} \tag{10}$$

where P_f is the pressure before the flashing point, which correlates with the degree of subcooling, the ratio of length to diameter, diameter, and downstream pressure.

$$P_f = P_{sat}\left[b_1 + b_2\left(P_{up}/P_c\right)^{b_3}(L/D)^{b_4}\mathrm{SUBC}^{b_5} + b_6\left(P_{up}/P_c\right)^{b_7} + b_8\exp\left(b_9(D/D_{ref})(L/D)^{b_{10}}\right) + b_{11}\mathrm{EVAP}\right] \tag{11}$$

$$C_c = 1 + \pi_1(L/D)^{\pi_2}(\mathrm{DEPTH}/D)^{\pi_3} \tag{12}$$

Table 1 – Coefficient of correction factor. Reproduced with permission of ASHRAE Transactions: symposia, from Two-phase flow of HFC134a and CFC12 through short tube orifices, Kim, Y.C., O'Neal, D.L., Yuan, Y., 1994; permission conveyed through Copyright Clearance Center, Inc.", "Reproduced with permission of ASHRAE Transactions, from Two-phase flow of R-22 through short tube orifices, Kim, Y., O'Neal, D.L., 100, 1994; permission conveyed through Copyright Clearance Center, Inc.", "Reproduced with permission of ASHRAE Transactions, from Mass flow characteristics of R407C through short-tube orifices, Payne, W.V., O'Neal, D.L., 104 (3), 1998; permission conveyed through Copyright Clearance Center, Inc.

Coefficient	CFC-12	HCFC-22	HFC-134a	HFC-407C (Pure)	HFC-407C (1.1% oil)
a_1	–	–	−2.6519	−4.45974577	−4.349745770
a_2	–	–	5.7705	10.69467130	10.454571210
a_3	–	–	−0.4474	−0.55303036	−0.663120121
a_4	–	–	0.3820	0.39429366	0.323273661
b_1	1.0011	1.0050	1.0156	0.963034325	0.980538238
b_2	11.3523	5.7367	10.0612	4.286408416	4.957604391
b_3	−0.2176	−0.485	−0.3296	−0.278235435	−0.309919995
b_4	−0.2150	−0.179	−0.1758	−0.043090943	−0.116219951
b_5	1.0643	0.9948	1.0831	0.916226528	0.906610038
b_6	0.0000	0.268	0.0000	0.071794702	0.227476573
b_7	0.0000	2.716	0.0000	0.499098698	0.186773583
b_8	−0.1905	−0.226	−0.1802	−0.208417565	−0.398196082
b_9	−0.00615	−0.021	−0.00214	−0.034680678	−0.030711793
b_{10}	2.4291	2.0000	2.9596	1.844061084	1.587754176
b_{11}	−0.0437	−0.092	−0.0745	−0.091235910	−0.134132834
π_1	–	0.02655	–	–	–
π_2	–	0.070775	–	–	–
π_3	–	0.22684	–	–	–

$$SUBC = (T_{sat} - T_{up})/T_c \tag{13}$$

$$EVAP = (P_c - P_{down})/P_c \tag{14}$$

For two-phase flow, the correlation (C_{tp}), which includes the effect of upstream quality and short-tube geometry, was added into his model.

$$C_{tp} = \frac{1}{(1 + a_1 x_{up})\left(1 + a_2 (L/D)^{a_3} Y^{a_4 \mathrm{Ln}(L/D)}\right)} \tag{15}$$

$$Y = \frac{x_{up}}{(1 - x_{up})}\left(\frac{\rho_f}{\rho_g}\right)^{0.5} \tag{16}$$

The model for HFC-407C is divided into two cases: pure refrigerant and oil–refrigerant mixtures. Table 1 shows the correction coefficient of various refrigerants used in the flow model.

For practical application, flow charts of HCFC-22 derived from the empirical correlations were generated by Kim and O'Neal (1994) and Aaron and Domanski (1990). Four flow charts, which are a function of upstream pressure, inlet quality, degree of subcooling, short-tube diameter, short-tube length, and chamfer depth, were proposed. The mass flow rate was calculated using the following equation:

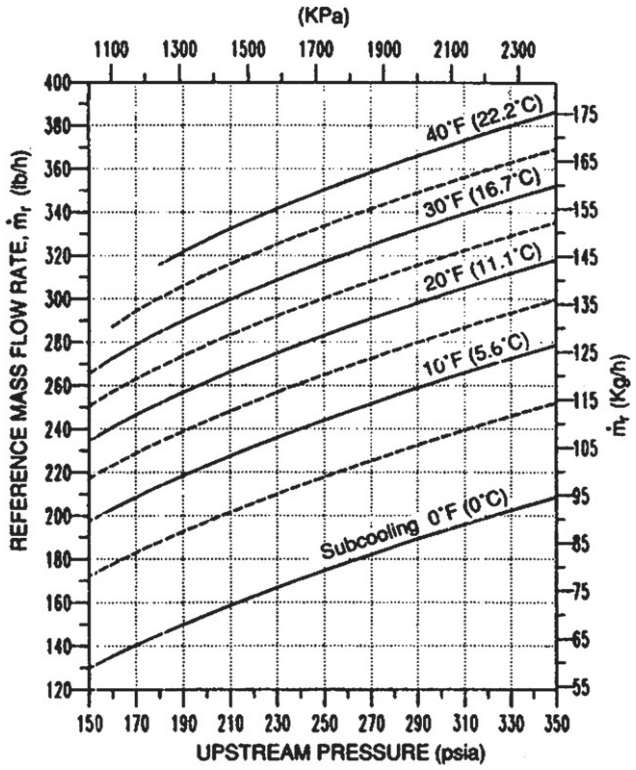

Fig. 1 – Reference mass flow rate for short-tube orifice with HCFC-22: L = 12.70mm and D = 1.35mm. Reproduced with permission of ASHRAE Transactions, from Experimentation analysis and correlation of refrigerant-22 flow through short tube restrictors, Aaron, A.A., Domanski, P.A., 96 (1), 1990; permission conveyed through Copyright Clearance Center, Inc.

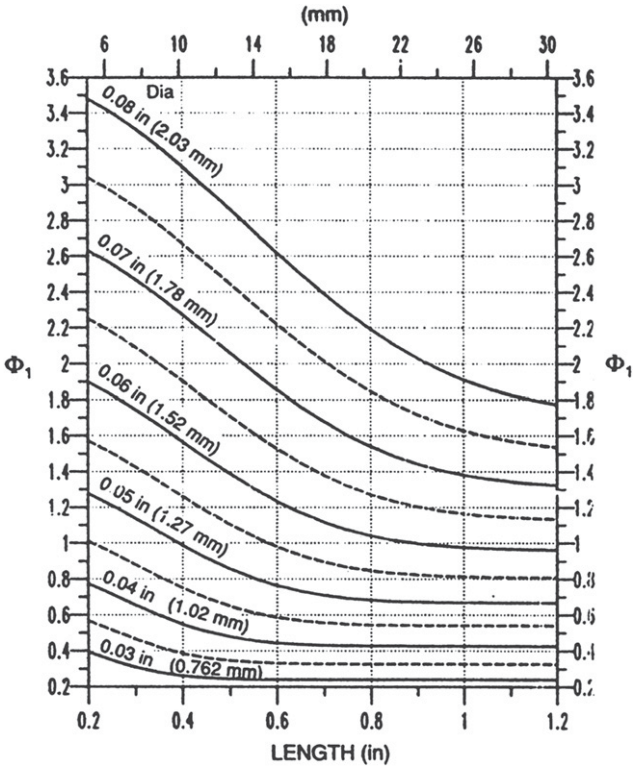

Fig. 2 – Correction factor for short-tube orifice configuration with HCFC-22. Reproduced with permission of ASHRAE Transactions, from Experimentation analysis and correlation of refrigerant-22 flow through short tube restrictors, Aaron, A.A., Domanski, P.A., 96 (1), 1990; permission conveyed through Copyright Clearance Center, Inc.

$$\dot{m}_a = \dot{m}_r \Phi_1 \Phi_2 \Phi_3 \tag{17}$$

where $\dot{m}_a$ is the actual mass flow rate, $\dot{m}_r$ is the reference mass flow rate, Φ_1 is the correction factor for short-tube geometry, Φ_2 is the correction factor for the degree of subcooling or quality, and Φ_3 is the correction factor for the inlet chamfer. The calculated mass flow rate obtained from the flow charts agreed with the actual value. However, Kim and O'Neal (1994), and Aaron and Domanski (1990) reported that the accuracy of calculation cannot be guaranteed when extrapolating beyond the operating conditions of the flow chart. The selection charts for HCFC-22 are shown in Figs. 1–4.

Singh et al. (2001) developed a model for predicting the mass flow rate of HFC-134a inside a short-tube orifice over a wide range of inlet and outlet conditions, that is, liquid, two phase, and vapour. The flow model could be divided into four regimes, namely liquid inlet–liquid outlet flow, liquid inlet–two-phase outlet flow, two-phase inlet–two-phase outlet flow, and single-phase inlet–single-phase outlet flow. However, for predicting the mass flow rate under the choke flow condition, the models were combined together as shown below.

$$\dot{m} = (1 - x_{up})^{c_8} c_1 D^2 \sqrt{2\rho(P_{up} - P_{down}K)} + x_{up}^{c_9} c_{10} P_{up} D^2 M \sqrt{\gamma_{up}/(RT_{up})} \tag{18}$$

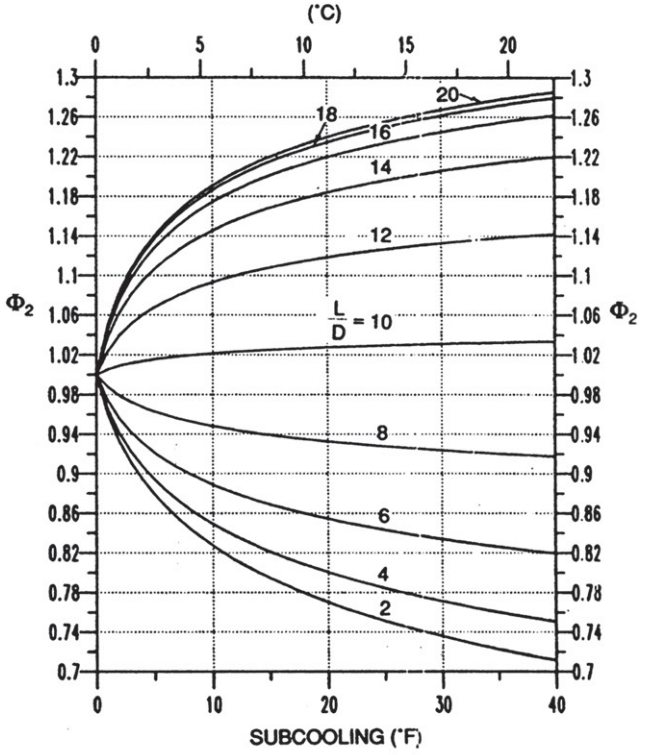

Fig. 3 – Correction factor for inlet subcooling with HCFC-22. Reproduced with permission of ASHRAE Transactions, from Experimentation analysis and correlation of refrigerant-22 flow through short tube restrictors, Aaron, A.A., Domanski, P.A., 96 (1), 1990; permission conveyed through Copyright Clearance Center, Inc.

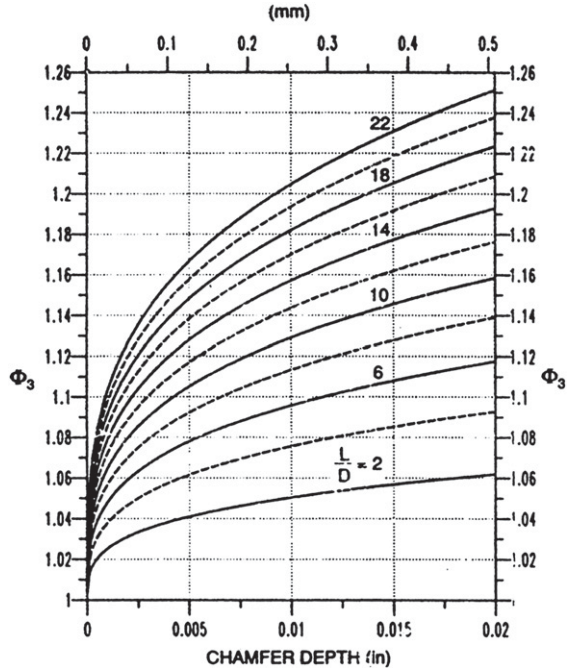

Fig. 4 – Correction factor for chamfering with HCFC-22. Reproduced with permission of ASHRAE Transactions, from Experimentation analysis and correlation of refrigerant-22 flow through short tube restrictors, Aaron, A.A., Domanski, P.A., 96 (1), 1990; permission conveyed through Copyright Clearance Center, Inc.

$$K = c_2\left(\frac{S}{T_c}\right)c_3 + D^{c_4}L^{c_5} + c_6L + c_7\left(\frac{P_c - P_{down}}{P_c}\right) \quad (19)$$

where D is the short-tube orifice diameter, L is the short-tube orifice length, S is inlet subcooling, M is the Mach number, and R is the gas constant. The coefficients included in the model are presented in Table 2.

Kim et al. (2002) have developed the mass flow rate correlation of HCFC-22 through a flexible short-tube orifice, and they presented the single-phase orifice model with a correction factor for the HCFC-22. For each flexible short tube, the proposed flow model is divided into moduli of elasticity of 7063 kPa and 9860 kPa.

$$\dot{m} = CA\sqrt{2\gamma_c\rho(P_{up} - P_f)} \quad (20)$$

$$P_f = P_{sat}\left[b_1 + b_2(PRA)^{b_3}SUB^{b_4} + b_5EVAP^{b_6}\right] \quad (21)$$

where SUB is normalized subcooling, $(T_{sat} - T_{up})/T_c$. EVAP is the normalized downstream pressure, and $(P_c - P_{down})/P_c$. PRA is the ratio of upstream pressure to critical pressure (P_{up}/P_c). γ_c is a dimensional constant, $1.296 \times 10^{10}\ s^2\,N\,h^{-2}\,kN^{-1}$. The coefficients of the correction factor of this model appear in Table 3. The non-linear regression technique was used to determine a correlation between adjusted pressure and normalized parameters.

Liu et al. (2004) formulated a flow model to estimate the mass flow rate of R744 through a short-tube orifice. The upstream pressure, upstream temperature, diameter, and length-to-diameter ratio were included in the adjusted downstream pressure correlation. The mass flow rate was calculated with the followed equation:

$$\dot{m} = A\sqrt{2\rho(P_{up} - P_f)} \quad (22)$$

Table 2 – Coefficient in the mass flow model. Reprinted from HVAC&Research, 7, Singh, G.M., Hrnjak, P.S., Bullard, C.W., Flow of refrigerant R134a through orifice tubes, pp. 245–262 (2001), with permission from Taylor & Francis.

Coefficient	
c_1	0.265249714
c_2	−0.11497189
c_3	0.041465780
c_4	−0.006578346
c_5	0.0039000541
c_6	0.0000218672
c_7	0.0362919356
c_8	1.7562517005
c_9	0.4970578018
c_{10}	25π

Table 3 – Coefficient of the correction factor. Reprinted from HVAC&Research, 8(2), Kim, Y.C., Payne, W.V., O'Neal, D.L., Farzad, M., Refrigerant flow through flexible short tube orifices, pp. 179–190 (2004), with permission from Taylor & Francis.

Coefficient	Modulus of elasticity 7063 kPa	Modulus of elasticity 9860 kPa
b_1	0.9187	1.0434
b_2	10.4091	7.4048
b_3	−0.0500	0.0191
b_4	1.1787	1.0421
b_5	−0.0276	−0.1683
b_6	0.9241	−0.7797

$$P_f = P_c\left|0.77213 + 0.86505D_R^{0.42405} - 0.40453P_R^{-4.7025}t_R^{0.12293} + 0.00006(L/D)^{1.6326}\right| \quad (23)$$

where D_R is normalized diameter, (D/D_p), $(D_p = 7.03\ \text{mm})$, and P_R is normalized upstream pressure, (P_{up}/P_c). t_R is normalized upstream temperature $(t_{up} - t_c)/t_c)$.

Tu et al. (2006) presented a semi-empirical flow model for the liquid inlet–two-phase outlet flow of HFC-134a through a micro-scale short-tube orifice based on a single-phase orifice equation with an adjusted discharge coefficient. The discharge coefficient was correlated with downstream vapour quality.

$$\dot{m} = (1 + C_x x_{out})C_d A\sqrt{2\rho\Delta P} \quad (24)$$

where x_{out} is the downstream vapour quality and C_x and C_d are empirical constants. C_d was 0.7 and 0.68 for short-tube diameters of 52 and 31 μm, respectively, and the value of C_x is 0.416.

Nilpueng and Wongwises (2009) proposed a flow model for a small size short-tube orifice ($D = 0.605$–1.2 mm) under critical flow. The flow model is expressed as

Table 4 – Dimensionless π term of the generalized correlation. Reprinted from International Journal of Refrigeration, 27, Choi, J., Chung, J.T., Kim, Y., A generalized correlation for two-phase flow of alternative refrigerants through short tube orifices, pp. 393–400 (2004), with permission from Elsevier.

π term	Parameter	Inlet condition
π_1	$\dot{m}/D^2\sqrt{\rho_f P_{in}}$	Subcooled/two-phase
π_2	$(P_c - P_{in})/P_c$	Subcooled/two-phase
π_3	$(P_c - P_{down})/P_c$	Subcooled/two-phase
π_4	$(P_c - P_{sat})/P_c$	Subcooled
π_5	$\Delta T_{sub}/T_c$	Subcooled
π_6	L/D	Subcooled/two-phase
π_7	ρ_f/ρ_g	Subcooled
π_8	$(\mu_f - \mu_g)/\mu_g$	Subcooled/two-phase
π_9	σ/DP_{in}	Subcooled
π_{10}	$x_{in}/(1 - x_{in})$	Two-phase
π_{11}	ρ_{mean}/ρ_f	Two-phase

$$\dot{m} = A\sqrt{2\rho(P_{up} - P_f)} \quad (25)$$

$$P_f = P_{sat}\left[0.201 + 0.421P_R^{-0.204}(L/D)^{0.218}T_R^{0.398} + 0.244P_R^{-0.458} + 0.203\exp 0.00031D_R(L/D)^{1.55}\right] \quad (26)$$

where D_R is normalized diameter (D/D_{ref}), $(D_{ref} = 0.961\ \text{mm})$, and P_R is normalized upstream pressure (P_{up}/P_c). T_R is normalized upstream temperature $(T_{sat} - T_{up})/T_c)$. The calculated results showed good agreement with the measured results with a mean deviation $(1/n\sum_1^n[|\dot{m}_{meas} - \dot{m}_{cal}| \times 100/\dot{m}_{meas}])$ of 6.3%.

Due to the fact that the semi-empirical models were generated based on their own database, each model cannot be used beyond its condition. Therefore, Choi et al. (2004) developed a generalized correlation in a simple form to calculate the mass flow rate of alternative refrigerants inside short-tube orifices. The relevant parameters consisted of three groups: operating condition, short-tube orifice geometry, and refrigerant property. They developed their correlation based on the dimensional analysis, and produced the correlation in the power law form of dimensionless parameters. The generalized correlation for calculating the refrigerant mass flow rate through the short tube falls into two groups: the subcooled inlet condition and the two-phase inlet condition.

For the subcooled inlet condition

$$\pi_1 = 0.1378\pi_2^{-0.950}\pi_3^{0.033}\pi_4^{0.769}\pi_5^{0.082}\pi_6^{-0.099}\pi_7^{-0.104}\pi_8^{0.554}\pi_9^{-0.034} \quad (27)$$

For the two-phase inlet condition

$$\pi_1 = 0.0720\pi_2^{-0.090}\pi_3^{0.406}\pi_6^{-0.149}\pi_8^{-0.099}\pi_{10}^{-0.013}\pi_{11}^{0.283} \quad (28)$$

Table 4 lists and defines the dimensionless π groups included in the generalized correlation. The coefficient and exponents of the independent Pi-groups are determined from a non-linear regression method. Extensive experimental data for CFC-12, HCFC-22, HFC-134a, HFC-407C, HFC-410A, and HFC-502 were used to create the correlation. The results indicate that the present correlation yielded a good agreement with the database with standard deviations of 6.1% and 5% for subcooled inlet conditions and two-phase inlet conditions, respectively.

3. Theoretical models

As described in the earlier section, the semi-empirical models can be used to calculate the mass flow rate through a short-tube orifice, but they cannot be used to indicate the physical meaning of refrigerant flow mechanism. To fulfil this shortcoming, other researchers have proposed two-phase critical flow models to simulate the refrigerant flow behaviour.

The present study compared eight critical flow models by Kim and O'Neal, (1995) with the measured mass flow rates of HCFC-22 and HFC-134a, and divided these models into three groups: (1) homogeneous equilibrium models (HEM), (2) homogeneous frozen models (HFM), and (3) non-homogeneous equilibrium models (NEM). The details of each group of models are described below.

3.1. Homogeneous equilibrium model

This model was generated based on the following assumption: the liquid–vapour mixture is homogeneous, the vapour and liquid velocities are equal, and both phases exist in thermal equilibrium. Based on the interfacial mass transfer between the liquid and vapour phases ($\partial x/\partial P$), the models were divided into three groups: isenthalpic flow path (Lahey and Moody, 1977), isentropic flow path (Lahey and Moody, 1977), and Fanno line (Sajben, 1961). The critical mass flux can be determined by the following model.

3.1.1. Isenthalpic homogeneous equilibrium model

$$G_{cr} = \left(\frac{-1}{\frac{dv_f}{dP} - \left(\frac{v_{fg}}{h_{fg}}\right)\frac{dh_f}{dP} + x\left(\frac{dv_{fg}}{dP} - \left(\frac{v_{fg}}{h_{fg}}\right)\frac{dh_{fg}}{dP}\right)} \right)^{1/2} \tag{29}$$

where v_f is the specific volume of the liquid phase, P is pressure, x is quality, v_{fg} is the difference between vapour and liquid specific volume, and h_{fg} is the difference between vapour and liquid enthalpy. A thermodynamic relation of $h = h_f + xh_{fg}$ was used to calculate the interfacial mass transfer path.

3.1.2. Isentropic homogeneous equilibrium model

$$G_{cr} = \left(\frac{-1}{\frac{dv_f}{dP} - \left(\frac{v_{fg}}{s_{fg}}\right)\frac{ds_f}{dP} + x\left(\frac{dv_{fg}}{dP} - \left(\frac{v_{fg}}{s_{fg}}\right)\frac{ds_{fg}}{dP}\right)} \right)^{1/2} \tag{30}$$

where s_f is the entropy of the liquid phase and s_{fg} is the difference between vapour and liquid enthalpy. $\partial x/\partial P$ was determined by the relation $s = s_f + xs_{fg}$.

3.1.3. Sajben homogeneous equilibrium model

In this model, the assumptions of the flow are adiabatic with friction in a constant area (Fanno line), which was derived from the following equations:

$$\frac{G^2\bar{v}^2}{2} + \frac{h_{fg}\bar{v}}{v_{fg}} - \left[h_t - \left(h_f - \frac{h_{fg}}{v_{fg}}v_f\right)\right] = 0 \tag{31}$$

$$h_t = h_f + xh_{fg} + \frac{u_m^2}{2} = \text{const} \tag{32}$$

Therefore, the critical mass flux was calculated by

$$G_{cr} = \left(\frac{h_{fg}/v_{fg}}{\frac{d\left(h_f - h_{fg}\left(v_f/v_{fg}\right)\right)}{dP} + \left[(1-x)v_f + xv_g\right]\left[\frac{d\left(h_{fg}/v_{fg}\right)}{dP} - 1\right]} \right)^{1/2} \tag{33}$$

3.2. Homogeneous frozen model (HFM)

The homogeneous frozen model was established with the following assumptions: the two-phase flow is homogeneous, the average velocities of each phase are equal, and no mass transfer occurs between phases ($\partial x/\partial P = 0$). The models used in this work were proposed by Wallis (1969) and Smith (1963).

3.2.1. Wallis homogeneous frozen model

Based on the above assumptions, Wallis (1969) presented the mass flux equation of refrigerant flow rate through a short-tube orifice as follows:

$$G_{cr} = \left[-\left(x\frac{dv_g}{dP} + (1-x)\frac{dv_f}{dP} \right)^{-1} \right]^{1/2} \tag{34}$$

3.2.2. Smith homogeneous frozen model

In this model, the pressure–volume relation for an isentropic process was included as follows:

$$P\left[\bar{v} - v_f(1-x)\right]^{\Gamma} = \text{constant} \tag{35}$$

$$\Gamma = \frac{xC_{pg} + (1-x)C_f}{xC_{vg} + (1-x)C_f} \tag{36}$$

Therefore, the governing equation for the model was given by

$$G_c = \left[\frac{xC_{pg} + (1-x)C_f}{xC_{vg} + (1-x)C_f} \left(\frac{P}{xv_g}\right) \right]^{1/2} \tag{37}$$

where C_{pg} is the specific heat at a constant pressure of vapour, C_{vg} is the specific heat at a constant volume of vapour, and C_f is the specific heat of the liquid. Under incompressible liquid flow, the specific heat of liquid was approximated by specific heat at the constant pressure of liquid.

3.3. Non-homogeneous equilibrium model

In non-homogeneous equilibrium models, the velocities of the two phases were not equal. Therefore, the slip ratio was included for calculating the critical mass flow rate inside a short-tube orifice. The other assumptions of the models were the presence of a thermodynamic equilibrium with no heat and no mass transfer between the phases as well as no friction. Two models with different slip ratios, which were used to predict the critical mass flux through a short-tube orifice, were presented.

3.3.1. Fauske non-homogeneous equilibrium model (Fauske, 1962)

$$G_{cr} = \left[\frac{-g_c k}{A}\right]^{1/2} \tag{38}$$

$$A = \left[(1 - x + kx)x\right]\frac{dv_g}{dP} + \left[v_g(1 + 2kx - 2x) + v_f\left(2kx - 2k - 2xk^2 + k^2\right)\right]\frac{dx}{dP} + k\left[1 + x(k-2) - x^2(k-1)\right]\frac{dv_f}{dP} \tag{39}$$

The interfacial mass transfer ($\partial x/\partial P$) was estimated based on the isenthalpic flow path, and the slip ratio was calculated by

$$k = \left(\frac{v_g}{v_f}\right)^{1/2} \tag{40}$$

where k is the slip ratio, v_f is the specific volume of the liquid phase, and v_g is the specific volume of the vapour phase.

3.3.2. *Moody non-homogeneous equilibrium model (Moody, 1965)*

$$G_{cr} = \left[\frac{-2g_c\left(\upsilon_f + x\upsilon_{fg}\right)}{a(ad+2be)}\right]^{1/2} \tag{41}$$

$$a = k\upsilon_f + x\left(\upsilon_g - k\upsilon_f\right) \tag{42}$$

$$b = \frac{1}{k^2} + x\left(1 - \frac{1}{k^2}\right) \tag{43}$$

$$d = \left[\frac{1}{k^2 s_{fg}}\frac{\partial s_g}{\partial P} - \frac{1}{s_{fg}}\frac{\partial s_f}{\partial P} - \frac{s_{fg}k^2}{k^4 s_{fg}}\right] + x\left[\frac{1}{k^4 s_{fg}}\frac{\partial\left(s_{fg}k^2\right)}{\partial P} - \frac{1}{s_{fg}}\frac{\partial s_{fg}}{\partial P}\right] \tag{44}$$

$$e = \left[s_{fg}\frac{\partial}{\partial P}\left(\frac{k\upsilon}{s_{fg}}\right) + \left(\frac{k\upsilon_f}{s_{fg}}\right)\frac{\partial s_g}{\partial P} - \left(\frac{\upsilon_g}{s_{fg}}\right)\frac{\partial s_f}{\partial P}\right] + x\left[s_{fg}\frac{\partial}{\partial P}\left(\frac{\upsilon_g}{s_{fg}}\right) - s_{fg}\frac{\partial}{\partial P}\left(\frac{k\upsilon_f}{s_{fg}}\right)\right] \tag{45}$$

Moody (1965) used the criterion of minimum value of the specific kinetic energy to estimate the slip ratio. The resulting expression for the slip ratio was given by

$$k = \left(\frac{\upsilon_g}{\upsilon_f}\right)^{1/3} \tag{46}$$

Based on the experimental results, Kim and O'Neal, (1995) stated that a lack of equilibrium due to a short time of expansion and homogeneous mist flow at the exit plane appeared in the short-tube orifice. The lack of equilibrium indicated that the flow was consistent with the assumptions of the homogeneous frozen model. In addition, a comparison between the calculated results obtained from the critical flow models and the experimental data showed that the homogeneous frozen model gave the best agreement, except at outlet qualities below 0.06.

Yang and Zhang (2005) developed a non-equilibrium, two-fluid model for predicting refrigerant flow behaviour inside a short-tube orifice. Their model is based on the following assumptions: (1) one-dimensional steady flow; (2) constant cross-section flow area; (3) adiabatic flow, and (4) neglect the gravitational force. The governing equations, which consisted of mass, momentum, and energy equations for each phase, are represented by the following equations:

Vapour phase mass equation

$$\frac{\partial}{\partial z}(\varphi\rho_G u_G) = \Gamma_G \tag{47}$$

Liquid phase mass equation

$$\frac{\partial}{\partial z}[(1-\varphi)\rho_L u_L] = \Gamma_L \tag{48}$$

Vapour phase momentum equation

$$\frac{\partial}{\partial z}(\varphi p) + \frac{\partial}{\partial z}\left(\varphi\rho_G u_G^2\right) = F_{GL} + F_{Gi} \tag{49}$$

Total momentum equation

$$\frac{\partial p}{\partial z} + \frac{\partial}{\partial z}\left(\varphi\rho_G u_G^2\right) + \frac{\partial}{\partial z}\left[(1-\varphi)\rho_L u_L^2\right] = -F_{WL} + F_{GL} + F_{LG} + F_{Gi} + F_{Li} \tag{50}$$

Total energy equation

$$\frac{\partial}{\partial z}\left[\varphi\rho_G u_G\left(h_G + \frac{u_G^2}{2}\right)\right] + \frac{\partial}{\partial z}\left[(1-\varphi)\rho_L u_L\left(h_L + \frac{u_L^2}{2}\right)\right] = 0 \tag{51}$$

Energy equation of bubble growth

$$\alpha_i(T_L - T_G)A_i = GA\ dx(h_G - h_L) + xGA\ dh_G \tag{52}$$

where Γ_L is the liquid phase mass transfer rate per unit volume, Γ_G is the vapour phase mass transfer rate per unit volume, F_{GL} and F_{LG} are interfacial frictional forces per unit volume between vapour and liquid, and F_{WL} is the frictional force between the tube wall and liquid phase. α_i is the interfacial heat transfer coefficient, a_i is the interfacial area per unit volume, and A_i is the interfacial area. The supplementary equations in terms of the empirical correlations, including the interfacial frictional force, momentum transfer, heat transfer, bubble diameter, and void fraction in different flow patterns, were included in the model as follows:

(1) The steady-state inter-phase frictional force (F_{LG}, F_{GL})

$$F_{LG} = -F_{GL} = 3C_{fi}\varphi^{1/2}\rho_G(u_G - u_L)|u_G - u_L|/D \tag{53}$$

where C_{fi} is the interfacial frictional factor.

$$C_{fi} = 0.005[1 + 75(1-\varphi)] \tag{54}$$

(2) Interfacial momentum transfer (F_{Gi}, F_{Li})

$$F_{Gi} = -\eta\Gamma_G(u_G - u_L) \tag{55}$$

$$F_{Li} = -(1-\eta)(u_L - u_G) \tag{56}$$

(3) Frictional force per unit volume (F_{WL})

$$F_{WL} = \phi_{tp}^2(dp/dz)F_{Lo} \tag{57}$$

where $(dp/dz)F_{Lo}$ is the friction pressure drop, assuming that the total flow rate is liquid and can be calculated from

$$(dp/dz)F_{Lo} = \frac{f_{Lo}G^2}{(2\rho D)} \tag{58}$$

$$f_{Lo} = (0.79\ln Re_{Lo} - 1.64)^{-2} \tag{59}$$

Table 5 – Interfacial area and heat transfer coefficient at different flow pattern. Reprinted from International Journal of Refrigeration, 28, Yang, L., Zhang, C-L., Two-fluid model of refrigerant two-phase flow through short tube orifice, pp. 419–427 (2005), with permission from Elsevier.

Flow regime	Correlations
Bubble flow	$a = N\pi d^2 = \sqrt[3]{36N\pi\varphi^2}$, $\varphi = N\pi d^3/6$ $\alpha_i = k_L(2 + 0.6Re_b^{1/2}Pr_L^{1/3})/d$
Churn-turbulent	$a = a_b + (a_b - a_a)\cdot(\varphi - \varphi_b)/(\varphi_b - \varphi_a)$ $\alpha_i = (\alpha_b)_{\varphi_b}\cdot\alpha_a/(\alpha)_{\varphi_b}$
Annular flow	$a = 4\varphi^{1/2}/D$ $\alpha_i = 0.5C_{fi}\rho_L c_{pL}(u_G - u_L)Pr^{-2/3}$

The empirical two-phase multiplier can be estimated by

$$\phi_{tp}^2 = \left(\frac{1-x}{1-\varphi}\right)^{1.75} \tag{60}$$

The Yang and Zhang (2005) study divided the correlation of interfacial area and heat transfer coefficient into three flow patterns: bubbly flow, churn-turbulent flow, and annular flow (Table 5). They solved the governing equations through the central difference discretization method, and thus computed and presented the mass flow rate, velocity, and temperature distribution of refrigerants through short-tube orifices. In addition, their study verified the effect of non-equilibrium behaviour on the mass flow rate by comparing the predicted results between a two-fluid model and a homogeneous equilibrium model. Based on the measured mass flow rates of HFC-134a, CFC-12, HCFC-22, HFC-410A, and HFC-407C, they found that the two-fluid model gave an acceptable prediction with experimental data with deviation of ±20%, while the homogeneous equilibrium model underestimated the predicted results obtained from two-fluid model by 25–30%. This indicated that the non-equilibrium behaviour coexisted during the flow of refrigerant through the short-tube orifice. However, for the flow of supercritical carbon dioxide (CO_2) through a short-tube orifice, Zhang and Yang (2005) reported that the non-homogeneous and non-equilibrium behaviour was unimportant. They also concluded that the accuracy of the two-fluid model was similar to that of the homogeneous equilibrium model. Therefore, in this case, Zhang and Yang (2005) recommended the homogeneous equilibrium model for calculating the mass flow rate inside the short-tube orifice.

Simulation of the fluid-dynamic flow characteristics of carbon dioxide through short-tube orifices was presented by Garcia-Valladares (2006). To predict the mass flow rate and pressure distribution inside a short-tube orifice, the continuity equation, momentum equation, energy equation, and entropy equation were developed. The hypothesis of the mathematical model was one-dimensional flow, thermodynamic equilibrium between phases, and adiabatic flow. The present review found that the mass flow rate, pressure, and enthalpy at the outlet section can be estimated from the following equations:

- Continuity equation

$$\dot{m}_{i+1} = \dot{m}_i - \frac{A\Delta z}{\Delta t}\left(\bar{\rho}_{tp} - \bar{\rho}_{tp}^0\right) \tag{61}$$

where

$$\rho_{tp} = \varepsilon_g \rho_g + (1-\varepsilon_g)\rho_1 \tag{62}$$

- Momentum equation

$$p_{i+1} = p_i - \frac{\Delta z}{A}\left(\Phi\frac{\bar{f}}{4}\frac{\bar{\dot{m}}^2}{2\bar{\rho}_{tp}A^2}\pi D + \bar{\rho}_{tp}Ag\sin\theta + \frac{\bar{\dot{m}} - \bar{\dot{m}}^0}{\Delta t} + \frac{\left[\dot{m}\left(x_g v_g + (1-x_g)\right)v_1\right]_i^{i+1}}{\Delta z}\right) \tag{63}$$

- Energy equation

$$h_{i+1} = \frac{-a\dot{m}_{i+1} + b\dot{m}_i + cA\Delta z/\Delta t}{\dot{m}_{i+1} + \dot{m}_i + \bar{\rho}_{tp}^0 A\Delta z/\Delta t} \tag{64}$$

$$a = \left(x_g v_g + (1-x_g)v_1\right)_{i+1}^2 + g\sin\theta\Delta z - h_i \tag{65}$$

$$b = \left(x_g v_g + (1-x_g)v_1\right)_i^2 - g\sin\theta\Delta z + h_i \tag{66}$$

$$c = 2\left(\bar{p}_i - \bar{p}_i^0\right) - \bar{\rho}_{tp}^0\left(h_i - 2\bar{h}_i^0\right) - \left(\overline{\rho v_i^2} - \bar{\rho}^0\bar{v}_i^{0^2}\right) \tag{67}$$

where v_1 is the specific volume of the liquid phase, x is the quality, v_g is the specific volume of the vapour phase, Δz is a spatial discretization step, Δt is a temporal discretization step, $\bar{v}_i^0$ is the average specific volume at the previous instant, $\bar{h}_i^0$ is average enthalpy at the previous instant, $\bar{f}$ is the average friction factor, $\dot{m}$ is the mass flow rate, and Φ is the two-phase frictional multiplier. In order to solve the above equations, additional information regarding the friction factor and the two-phase frictional multiplier was necessary, and can be determined with the following equations:

- friction factor

$$f = 0.316Re^{-1/4} \quad \text{for } Re \le 2\times10^4 \tag{68}$$

$$f = 0.184Re^{-1/5} \quad \text{for } Re > 2\times10^4 \tag{69}$$

- two-phase frictional multiplier

$$\Phi_{f,lo}^2 = 1 + 4.2\left(\Gamma^2 - 1\right)\left[\frac{B}{We_D}x_g^{0.875}\left(1-x_g\right)^{0.875} + x_g^{1.75}\right] \tag{70}$$

where

$$\Gamma^2 = \frac{f_{go}v_g}{f_{lo}v_1} \tag{71}$$

Table 6 – Criteria for selecting B. Reprinted from Applied Thermal Engineering, 26, Garcia-Valladares, Numerical simulation of trans-critical carbon dioxide (R744) flow through short tube orifices, pp. 144–151 (2006), with permission from Elsevier.

Γ	G (kg m^{-2} s^{-1})	B
≤9.5	≤500	4.8
	500 < G < 1900	2400/G
	≥1900	55/$G^{0.5}$
9.5 < Γ < 28	≤600	520/($\Gamma G^{0.5}$)
	>600	21/Γ
≥28	–	15,000/($\Gamma^2 G^{0.5}$)

where Γ is a dimensionless physical property coefficient, We_D is the Weber number, f_{go} is the friction factor for vapour only, and f_{lo} is the friction factor for liquid only. Table 6 presents the criteria for selecting the coefficient B. In addition, to verify the critical flow condition, the invalidity of entropy equation and $dp/dz \to \infty$ at the short-tube outlet plane were used as the criterion. The results showed good agreement between the numerical simulation and experimental data.

4. Conclusions

This paper presented the details of numerical modelling of two-phase refrigerant flow inside the short-tube orifice. The models can be divided into two groups: semi-empirical models and theoretical models. The present review thus gives the following conclusions for each model:

- The semi-empirical models, which are generated from the single-phase orifice equation, are utilized by most previous researchers. Researchers prefer them because they are easy to create; however, the accuracy of each model is valid only for the testing conditions.
- To cover the wide range of the calculation of mass flow rate under various operating conditions and refrigerants, a generalized correlation in a simple form can be developed through a dimensional analysis. However, the empirical correction factors obtained from this correlation do not imply any physical significance.
- The theoretical model, which is developed from the continuity, momentum and energy equation under the proper assumptions, can describe the physical meaning of refrigerant flow behaviour inside the short-tube orifice. The calculated results obtained from this model agreed well with the experimental data.
- The theoretical model is attractive, because it can show the physical meaning of the refrigerant along the short-tube orifice. Yet the theoretical model is rather difficult to solve when complicated equations and correlations are included. As a result, only a few published studies have used theoretical models, and it is still not clear which one is the best. Therefore, further development of the theoretical model for refrigerant flow through the short-tube orifice is still required.

Acknowledgements

The authors would like to express their appreciation to the Thailand Research Fund (TRF), the Commission of Higher Education and the National Research University Project for providing financial support for this study.

REFERENCES

Aaron, A.A., Domanski, P.A., 1990. Experimentation analysis and correlation of refrigerant-22 flow through short tube restrictors. ASHRAE Trans. 96 (1), 729–742.

ASME, 1971. Fluid Meters – Their Theory and Application, sixth ed. American Society of Mechanical Engineers, New York.

Choi, J., Chung, J.T., Kim, Y., 2004. A generalized correlation for two-phase flow of alternative refrigerants through short tube orifices. Int. J. Refrigeration 27, 393–400.

Fauske, H.K., 1962. Contribution to the Theory of Two-phase, One Component Critical Flow. ANL-6633. ANL Lab., Argonne.

Garcia-Valladares, O., 2006. Numerical simulation of trans-critical carbon dioxide (R744) flow through short tube orifices. Appl. Therm. Eng., 144–151.

Kim, Y., O'Neal, D.L., 1994. Two-phase flow of R-22 through short tube orifices. ASHRAE Trans. 100, 323–334.

Kim, Y., O'Neal, D.L., 1995. A comparison of critical flow models for estimating two-phase flow of HCFC22 and HFC134a through short tube orifices. Int. J. Refrigeration 18, 447–455.

Kim, Y.C., O'Neal, D.L., Yuan, Y., 1994. Two-phase flow of HFC134a and CFC12 through short tube orifices. ASHRAE Trans.: Symposia, 582–591.

Kim, Y.C., Payne, W.V., O'Neal, D.L., Farzad, M., 2002. Refrigerant flow through flexible short tube orifices. HVAC&R Res. 8 (2), 179–190.

Lahey, R.T., Moody, E.J., 1977. The Thermal–Hydraulic of a Boiling Water Nuclear Reactor. American Nuclear Society, Hinsdale, Illinois.

Liu, J.P., Niu, Y.M., Chen, J.P., Chen, Z.J., Feng, X., 2004. Experimental and correlation of R744 two-phase flow through short tubes. Exp. Therm. Fluid Sci. 28, 565–573.

Mei, V.C., 1982. Short tube refrigerant flow restrictors. ASHRAE Trans. 88 (2), 157–169.

Moody, F.J., 1965. Maximum flow rate of a single component two-phase mixture. J. Heat Transf., Trans. ASME, 134–142.

Nilpueng, K., Wongwises, S., 2009. Flow pattern, mass flow rate, pressure distribution, and temperature distribution of two-phase flow of HFC-134a inside short-tube orifices. Int. J. Refrigeration 32, 1864–1875.

Payne, W.V., O'Neal, D.L., 1998. Mass flow characteristics of R407C through short-tube orifices. ASHRAE Trans. 104 (3), 197–209.

Sajben, M., 1961. Adiabatic flow of flashing liquid in pipe. J. Basic Eng. 83, 619–631.

Singh, G.M., Hrnjak, P.S., Bullard, C.W., 2001. Flow of refrigerant R134a through orifice tubes. HVAC&R Res. 7 (3), 245–262.

Smith, R.V., 1963. Some idealized solution for chocking, two-phase flowing hydrogen, nitrogen and oxygen. Adv. Cryog. Eng. 8, 563–573.

Tu, X., Hrnjak, P.S., Bullard, C.W., 2006. Refrigerant 134a liquid flow through micro-scale short tube orifices with/without phase change. Exp. Therm. Fluid Sci. 30 (3), 253–262.

Wallis, G.B., 1969. One-dimensional Two-phase Flow. McGraw Hill Book.

Yang, L., Zhang, C.-L., 2005. Two-fluid model of refrigerant two-phase flow through short tube orifice. Int. J. Refrigeration 28, 419–427.

Zhang, C.-L., Yang, L., 2005. Modeling of supercritical CO_2 flow through short tube orifice. J. Fluid Eng., Trans. ASME, 1194–1198.

Convective Heat Transfer of Al_2O_3-water Nanofluids in a Microchannel Heat Sink

Weerapun Duangthongsuk[a,b] Ahmet Selim Dalkilic[c] and Somchai Wongwises[b,d*]

[a]*Department of Mechanical Engineering, South-East Asia University, Bangkok , Thailand;* [b]*Fluid Mechanics, Thermal Engineering and Multiphase Flow Research Lab. (FUTURE), Department of Mechanical Engineering, King Mongkut's University of Technology Thonburi, Bangmod, Bangkok, Thailand;* [c]*Heat and Thermodynamics Division, Department of Mechanical Engineering, Yildiz Technical University, Yildiz, Istanbul, 34349, Turkey;* [d]*The Academy of Science, The Royal Institute of Thailand, Sanam Suea Pa, Dusit, Bangkok 10300, Thailand*

Abstract: The research presents an experimental study on the heat transfer and pressure drop characteristics of Al_2O_3-water nanofluids flowing through a microchannel heat sink (MCHS). The effects of Reynolds number and particle concentrations on the heat transfer and flow behavior are investigated. Comparison of the heat transfer coefficient obtained from water-cooled MCHS and nanofluids-cooled MCHS is also presented. MCHS with rectangular flow channel made from aluminum with dimension of 50x50 mm is used as the test section. Al_2O_3-water nanofluids with particle concentrations of 1.0, 2.0 and 3.0 wt.% are tested. Two electric heaters each with a capacity of 50 W are used to supply heat to the test section. The results indicate that the heat transfer performance of MCHS increases with increasing Reynolds number as well as particle concentrations. Compared with pure water, the results indicate that at particle concentration of 3.0 wt%, the heat transfer coefficient for nanofluid-cooled MCHS is range between 1,100-1,700 W/m^{2}K which is higher than that of water by about 7 – 15%. The pressure drop is between 8 and 25 kPa which is close to the water.

Keywords: Heat transfer coefficient, microchannel heat sink, nanofluid, pressure drop.

1. INTRODUCTION

The concept of nanofluid is to disperse some solid particles with nanometer size in conventional heat transfer fluids such as water, oil and ethylene glycol. This concept was carried out by Masuda *et al*., [1] who studied the heat transfer performance of liquids with solid nanoparticles suspension in 1993. However, the term "nanofluid" was first introduced by S.U.S Choi [2] in 1995, and successively gained popularity. A number of researchers reported that nanofluids gave higher heat transfer performance than that of common heat transfer fluids [3-18]. Similarly, based on advanced electronic devices, these devices became smaller and employed high speed and high power density such as computers, power electronics, car engines, and high-powered lasers or x-rays. Normally, these devices generate an unprecedented high load, whereas their surface area for heat removal is limited. Thus, proper cooling technologies for advanced electronic devices are necessarily required and it is a challenging task for a number of researchers. As mentioned above, it is the concept of microchannel heat sink (MCHS) for dissipating large amounts of heat from these devices in order to maintain the required performance and reliability.

Two decades ago, pioneer researchers Tuckerman and Pease [19] reported the heat transfer performance of microchannel heat sink (MCHS) for cooling the very-large-scale integrated (VLSI) circuit. However, a single-phase liquid is used as working fluid for cooling the microchannel heat sinks and shows a higher potential for heat removal than an air cooling system. In general, there are three approaches for increasing the cooling performance of advanced electronic devices with a high level of heat generation. The first is to find an optimum geometry of cooling devices in which the cooling performance is maximized. The second is to reduce the channel diameter for enhancing the heat transfer coefficient, which is reported by Tuckerman and Pease [19]. The last is to improve the heat transfer performance of coolants. Thus, the use of MCHS combined with nanofluids as a coolant is an innovative idea for cooling small electronic devices. So far, some existing published articles associated with this idea are described in the following sections.

Lee and Choi [20] investigated the thermal performance of MCHS with NF_2 and NF_3 nanofluids compared with pure water and liquid nitrogen, theoretically. Their results showed that thermal resistances of nanofluids were lower than that of a pure water and liquid nitrogen, respectively. On the contrary, the cooling rate and power density of nanofluids were much larger than those of pure water and liquid nitrogen.

Chein and Huang [21] proposed a mathematical model for predicting the heat transfer performance and pumping power of $MCHS_S$ using nanofluids as working fluids. Cu nanoparticles dispersed in water with various particle concentrations were used as testing fluids. Similarly, two specific geometries of MCHS were tested. Their results indicated that addition of nanoparticles in the base liquid remarkably enhanced the heat transfer performance of the base liquid and there was no penalty in pressure drop.

Koo and Kleinstreuer [22] presented a numerical study on the heat transfer and flow characteristics of MCHS with CuO nanoparticles dispersed in water and ethylene glycol, respectively. Their simulation data showed that heat transfer performance of ethylene glycol was higher than that of water. Moreover, they also suggested that nanoparticles with high thermal conductivity and MCHS with high aspect ratio of flow channel should be used.

Jang and Choi [23] presented the cooling performance of a MCHS by using Cu-water and diamond-water nanofluids as coolants, numerically. The results showed that the diamond–water nanofluids with a particle concentration of 1.0 vol.% gave a higher heat transfer performance than the base fluid by about 10%. Moreover, their results indicated that use of nanofluids can reduce both the thermal resistance and temperature difference between the heated surface of MCHS and the working fluid. They also demonstrated that nanofluids-cooled MCHS is the next generation cooling system for cooling the ultra-high heat flux devices.

Abbassi and Aghanajafi [24] investigated the heat transfer performance of MCHS using Cu-water nanofluids as a coolant, numerically. The thermal dispersion model was adopted for heat transfer analysis and a thermal dispersion coefficient was consid-

*Address correspondence to this author at the Fluid Mechanics, Thermal Engineering and Multiphase Flow Research Lab. (FUTURE), Department of Mechanical Engineering, King Mongkut's University of Technology Thonburi, Bangmod, Bangkok, Thailand; Tel: 024709115; Fax: 024709111;
E-mail: somchai.won@kmutt.ac.th

1875-6786/12 $58.00+.00

ered. Their data showed that nanofluids gave larger heat transfer enhancement than those of base fluid and this enhancement increased with increasing particle concentration as well as Reynolds number.

Chein and Chuang [25] presented the thermal performance of MCHS using CuO-water nanofluids as a coolant. Particle concentrations of 0.2 and 0.4 vol% were tested in their study. The results showed that the presence of nanoparticles results in a higher energy absorption than that of pure water at a low flow rate. In contrast, there is no contribution from heat absorption when the flow rate is high.

Tsai and Chein [26] analytically investigated the MCHS performance using nanofluids as a coolant. Cu-water and CNT-water nanofluids were used as the working fluids. The porous medium model was used to simulate the MCHS performance. Their simulation results demonstrated that the use of nanofluids can reduce the temperature difference between MCHS surface and fluid temperature compared with that of pure water. Moreover, at the porosity and aspect ratio less than the optimum porosity and aspect ratio, it was clearly seen that heat transfer performance of nanofluids-cooled MCHS was larger than that of base fluid. In contrast, for the case of the porosity and channel aspect ratio greater than optimum porosity and aspect ratio, the use of nanofluids did not create a significant change in thermal resistance of the MCHS.

Jung and colleagues [27] reported an experimental investigation on the heat transfer coefficient and friction factor of Al_2O_3-water nanofluids flowing through MCHS with a rectangular channel under laminar flow condition. Compared with pure water, the results indicated that the heat transfer coefficient of nanofluids was about 32% higher than that of water without penalty in pressure drop. This enhancement increased with increasing Reynolds number and particle concentration.

Ghazvini and Shokouhmand [28] determined the heat transfer performance of a MCHS using CuO-water nanofluids as a coolant, both analytically and numerically. The fin model and the porous media approach were used to analyze the thermal behavior of MCHS. The results showed that the overall heat transfer coefficient of nanofluids was larger than that of pure water and increased with an increasing Reynolds number. The porous media approach gave a higher heat transfer coefficient ratio than the fin model. Moreover, the dimensionless temperature increased with an increasing porosity of the MCHS.

Ho *et al*., [29] investigated the forced convective cooling performance of Al_2O_3-water nanofluids flowing through MCHS under laminar flow regime, experimentally. MCHS made from copper which consists of 25 parallel rectangular microchannels with a length of 50 mm was used as the test section. The results showed that the nanofluids have a much higher average heat transfer coefficient than those of pure water. Moreover, their results also indicated that nanofluids gave a lower thermal resistance and wall temperature than those of base fluid. Finally, use of nanofluids has little penalty in pressure drop.

Ebrahimi *et al*., [30] numerically investigated the cooling performance of a nanofluids-cooled MCHS. Carbon nanotubes (CNTs) dispersed in water were used as a coolant. The results showed that thermal conductivity of nanofluids increases with increasing nanolayer thickness, which leads to a decrease in temperature gradient in MCHS.

As aforementioned, the above literatures have focused on the heat transfer performance of nanofluids-cooled MCHS both experimentally and numerically. Their results showed that nanofluids-cooled MCHS gave a higher heat transfer potential than that of the common base liquid. Moreover, many researchers recommended that MCHS using nanofluids as a coolant is expected to be the next generation of the novel electronic cooling technology. Thus, the authors would like to address the heat transfer performance of MCHS with use of nanofluids as a coolant for dissipating large amounts of heat from a MCHS. Al_2O_3-water nanofluids with particle concentrations of 1 and 3 wt.% are used as working fluids and flow through MCHS with a rectangular flow channel.

2. SAMPLE PREPARATION

In the present study, nanofluids provided by a commercial source (DEGUSSA, Aerodisp. W630) were used as a working fluid. This mixture was composed of Al_2O_3 nanoparticles with an average diameter of 120 nm dispersed in water. The original particle concentration was 30 wt%. In order to produce other required particle volume fractions, dilution with water followed by a stirring action was effected. Moreover, an ultrasonic vibrator was used to sonicate the solution continuously for about two hours in order to break down agglomeration of the nanoparticles. The desired concentrations used in this study were 1.0%, 2.0%, and 3.0 wt%.

3. EXPERIMENTAL APPARATUS AND PROCEDURE

Fig. (**1**) shows schematic diagram of the experimental system used in the present study. It mainly consists of four main parts as follows: a test section (MCHS with rectangular channel configuration), a micro pump with an inverter, two storage tanks, and a receiver tank. A 50x50 mm MCHS with 20 rectangular flow channels is made from aluminum. Focused on the MCHS, the width and height of the channel are 1 mm and 1 mm, respectively. Similarly, hydraulic diameter (D_H) and heat transfer areas of MCHS are 1 mm and 0.003 m^2, respectively. A Schematic diagram of MCHS is shown in Fig. (**2**). Plastic tubes were placed at both ends of the MCHS for reducing the heat loss along the axial direction. Similarly, an acrylic plate was placed on the top of MCHS to prevent heat loss. Two 50 W heaters were used to supply heat load to the MCHS. The pressure drop and the bulk temperature of the nanofluids at inlet and exit of the test section were measured by using the differential pressure transmitter and T-type thermocouples, respectively. Similarly, three positions of wall temperatures measurement were carried out using T-type thermocouples. Two storage tanks with 20 L capacity were made from acrylic plate and used for adjusting the nanofluid temperature and reducing the nanofluid temperature leaving from the test section, respectively. The storage tank No.1 with a 9,000 Btu/hr cooling capacity, 2 kW heaters and a thermostat was used to keep the temperature of nanofluids constant. Similarly, storage tank No. 2 with a 9,000 Btu/hr cooling capacity and a thermostat was used to cool down the nanofluid temperature leaving from the test section to the setting temperature of tank No.1. The speed of the micro pump was controlled by using an inverter for adjusting the flow rate of nanofluids. The receiver tank was used to measure the nanofluid flow rate by the time taken for a given volume of nanofluids to be discharged.

The differential pressure transmitter was calibrated using an air operated dead weight tester. The uncertainty of the pressure measurement is ± 0.030 kPa. The nanofluid flow rates were determined by electronic balance. The uncertainty of the electronic balance was ± 0.001 kg. A standard thermometer was used to calibrate all of the T-type thermocouples with a maximum precision of 0.1 ^oC. Therefore, the uncertainty of the measured Nusselt number was around 5%.

During the test run, the pressure difference in the nanofluids, wall temperatures of the MCHS, mass flow rates of the nanofluids, and the inlet and exit temperatures of the nanofluids were recorded.

4. DATA REDUCTION

In the present study, Al_2O_3-water nanofluids with particle fractions of 1.0%, 2.0%, and 3.0 wt.% are used to evaluate the heat transfer performance of MCHS using nanofluids as a coolant. Thus, the heat transfer performance of nanofluids can be computed from the following equation.

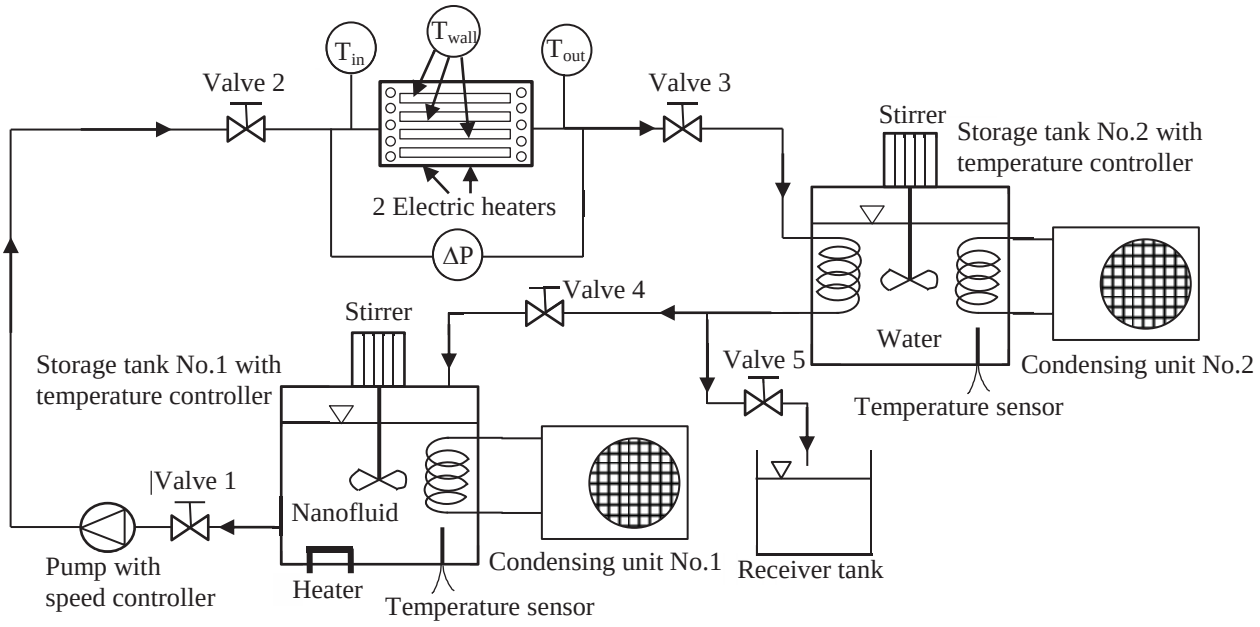

Fig. (1). Schematic diagram of the test apparatus used in the present study.

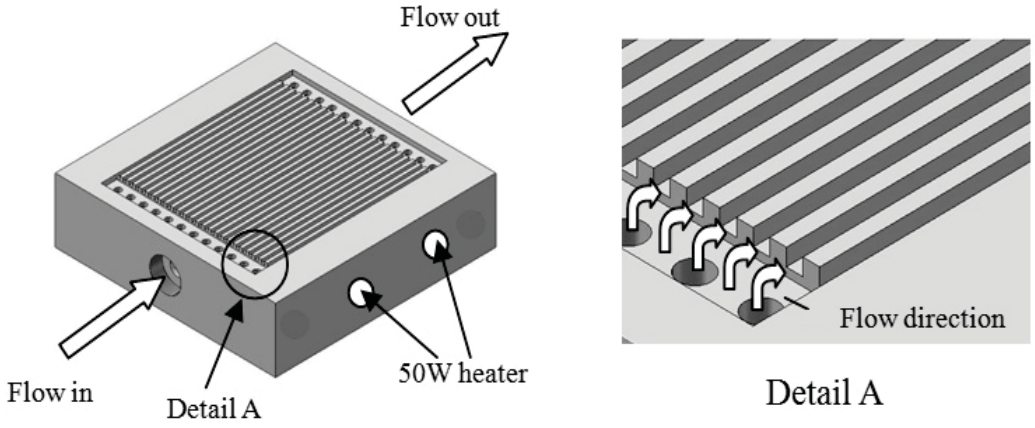

Fig. (2). MCHS used in the present study.

The heat transfer rate into the nanofluids is computed from:

$$Q_{nf} = \dot{m}_{nf} Cp_{nf} (T_{out} - T_{in})_{nf} \quad (1)$$

where Q_{nf} is the heat transfer rate of the nanofluids, $\dot{m}_{nf}$ is the mass flow rate of the nanofluids and T_{in} and T_{out} are the temperature of the nanofluids at inlet and exit of the test section.

The heat transfer coefficient and the Nusselt numbers of the nanofluids are evaluated from the following equations.

$$h_{nf} = \frac{Q_{nf}}{A_S (T_S - T_{nf})} \quad (2)$$

$$Nu_{nf} = \frac{h_{nf} D_H}{k_{nf}} \quad (3)$$

where h_{nf} is the heat transfer coefficient of the nanofluids, T_S is the average temperature of the heated surface of MCHS, T_{nf} is the bulk temperature of the nanofluids, which is the average fluid temperature across the test section, Nu_{nf} is the Nusselt number of the nanofluids, D_H is the Hydraulic diameter of the channel and k_{nf} is the thermal conductivity of the nanofluids.

Moreover, the Reynolds number can be calculated by using the following equation:

$$\mathrm{Re} = \frac{\rho_{nf} u_m D_H}{\mu_{nf}} \quad (4)$$

where ρ_{nf} is the density of the nanofluids, u_m is the mean velocity of the nanofluids and μ_{nf} is the viscosity of the nanofluids.

The density and specific heat of the nanofluids presented in the above equation are computed by use of the Pak and Cho [6] correlations, which are expressed as follows:

$$\rho_{nf} = \phi\rho_p + (1-\phi)\rho_w \tag{5}$$

and

$$Cp_{nf} = \phi Cp_p + (1-\phi)Cp_w \tag{6}$$

where Cp_{nf} is the specific heat of the nanofluids, Cp_p is the specific heat of the nanoparticles, Cp_w is the specific heat of the base fluid and ϕ is the particle volume fraction of the nanoparticles.

Similarly, the thermal conductivity and viscosity of nanofluids are calculated from Hamilton and Crosser model [31] and Einstein equation suggested by Drew and Passman [32] which are expressed as follows:

For thermal conductivity of the nanofluids;

$$k_{nf} = \left[\frac{k_p + (n-1)k_w - (n-1)\phi(k_w - k_p)}{k_p + (n-1)k_w + \phi(k_w - k_p)}\right]k_w \tag{7}$$

$$n = 3/\psi \tag{8}$$

where n is the empirical shape factor and ψ is the sphericity, defined as the ratio of the surface area of a sphere (with the same volume as the given particle) to the surface area of the particle. The sphericity is 1 and 0.5 for the spherical and cylindrical shapes, respectively. Moreover, k_p is the thermal conductivity of the nanoparticles and k_w is the thermal conductivity of the base fluid.

At a temperature of 15 ^{o}C, the thermal conductivity of water is 0.589 W/mK. Similarly, the thermal conductivity of the nanofluids with particle concentrations of 1.0, 2.0 and 3.0 wt.% are 0.594, 0.599 and 0.604 W/mK, respectively.

For viscosity of the nanofluids;

$$\mu_{nf} = (1 + 2.5\phi)\mu_w \tag{9}$$

where μ_w is the viscosity of the base fluid.

The thermophysical properties of the nanofluids shown in the above equations are calculated from water and nanoparticles at average bulk temperature.

For the case of pressure drop, the measured pressure drop of nanofluid-cooled MCHS is compared with the water-cooled MCHS.

5. RESULTS AND DISCUSSION

Fig. (**3**) shows the energy balance ratio, which is the ratio of the energy absorbed by fluid to the energy supplied to the fluid, plotted against Reynolds number for all three concentrations . The plot shows that at higher Reynolds number, both heat transfer rates are almost equal. However, in general, they are nearly 1. In our experiment, the heat loss was kept as small as possible.

In the present study, the experimental data are divided into two groups: 1) heat transfer performance and 2) pressure drop. The detailed results are shown as follows:

As shown in (Figs. (**4**) and (**5**)), the heat transfer coefficient and the Nusselt number of the nanofluids are higher than those of the base liquid, and increase with increasing Reynolds number as well as the particle concentrations. The enhancement range between 7 to 15% is obtained. This is because the nanoparticles presented in the base liquid increase the thermal conductivity. The chaotic movement of nanoparticles also increases the heat transfer rate which leads to an increase in the heat transfer performance. Moreover, increasing the Reynolds number leads to an increase in the heat transfer rate which results in an increase in the heat transfer coefficient.

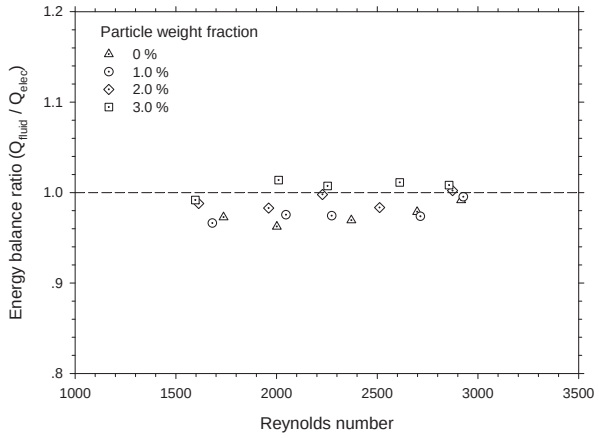

Fig. (3). Energy balance at various Reynolds number and concentrations.

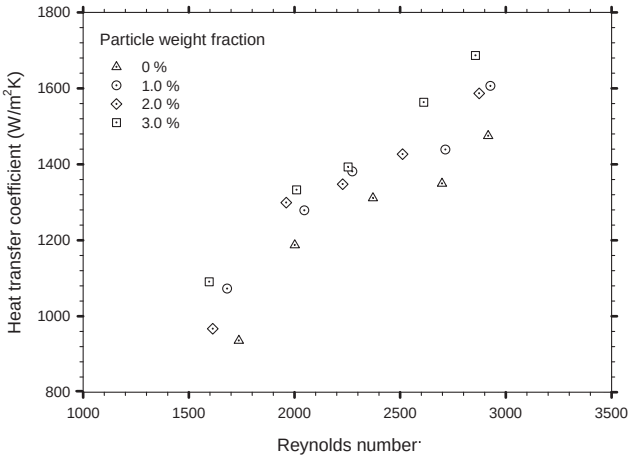

Fig. (4). Measured heat transfer coefficient for water and Al_2O_3-water nanofluids.

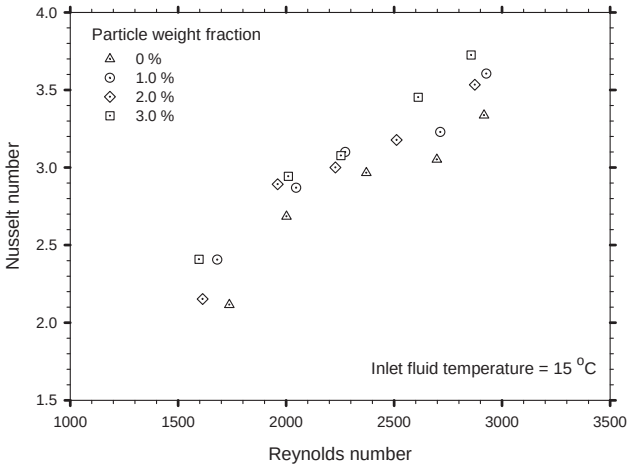

Fig. (5). Nusselt number versus Reynolds number for water-cooled MCHS and nanofluid-cooled MCHS.

Fig. (**6**) shows that the average wall temperature of MCHS decreases with increasing Reynolds number as well as particle concentrations, especially at lower Reynolds number. This is due to the fact that the addition of nanoparticles in the base fluid increases the energy exchange process, which leads to an increase in the heat transfer performance. At a lower Reynolds number, a higher wall temperature difference between water-cooled MCHS and nanofluid-cooled MCHS is obtained. This may be caused by the fact that the heat exchange period for a lower Reynolds number is longer than that for a higher Reynolds number.

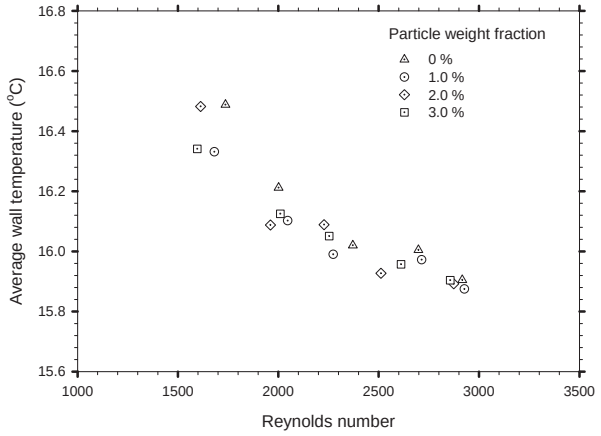

Fig. (6). Effect of particle weight fractions on the average wall temperature of MCHS.

As shown in Fig. (**7**), the results indicate that the pressure drop of the nanofluids increases with increasing Reynolds number and that there is a small increase with increasing particle concentrations. This means that the use of nanofluids will not cause a penalty in pressure drop. This is due to small particle size and very low particle concentrations. This is one of the benefits of using nanofluids as a heat transfer fluid in practical applications.

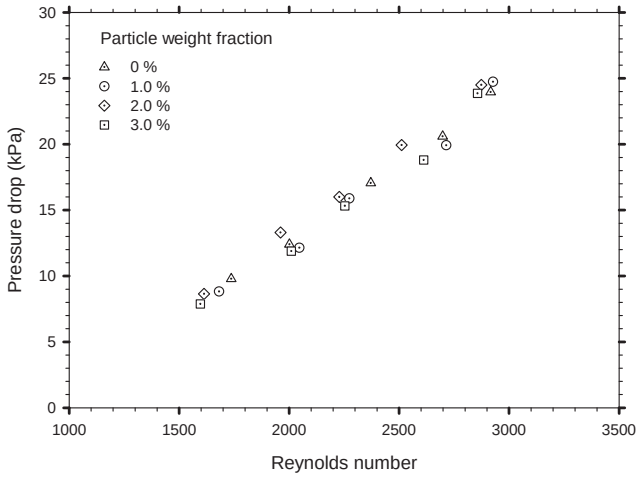

Fig. (7). Comparison of pressure drop between water-cooled MCHS and nanofluid-cooled MCHS.

CONCLUSIONS

The convective heat transfer performance and pressure drop characteristics of MCHS using Al_2O_3-water nanofluids as a coolant were experimentally investigated. The particle concentrations of 1 and 3 wt.% were tested. The effect of particle concentrations and the Reynolds number on the heat transfer performance and pressure drop of nanofluids-cooled MCHS were examined and then compared with the data for water-cooled MCHS. Important conclusions have been obtained and summarized as follows:

- The use of nanofluid-cooled MCHS gives significantly higher heat transfer coefficients than those of the water-cooled MCHS by about 7 - 15%.
- The wall temperature of MCHS decreases with increasing Reynolds number as well as particle concentrations. For the case of nanofluid-cooled MCHS, the average wall temperatures are lower than those of water-cooled MCHS, especially at a lower Reynolds number.
- The pressure drop of water-cooled and nanofluid-cooled MCHS increases with increasing Reynolds number and there is a small increase with increasing particle concentrations.

ACKNOWLEDGEMENTS

The authors would like to express their appreciation to the Office of Research, South-East Asia University, the Thailand Research Fund (TRF), the Office of the Higher Education Commission and the National Research University Project for providing financial support. The authors also wish to thank DEGUSSA AG, (Germany) for the valuable donation of the nanoparticles used in the present study.

CONFLICT OF INTEREST

None declared.

NOMENCLATURE

C_p	=	Specific heat, J/kgK
D_H	=	Hydraulic diameter, m
f	=	Friction factor
h	=	Heat transfer coefficient, W/m^2K
k	=	Thermal conductivity, W/mK
L	=	Length of the test tube, m
m	=	Mass flow rate, kg/s
Nu	=	Nusselt number
ΔP	=	Pressure drop, Pa
Q	=	Heat transfer rate, W
Re	=	Reynolds number
T	=	Temperature, ^oC
u	=	Velocity, m/s

Greek symbols

ϕ	=	Volume fraction
ρ	=	Density, kg/m^3
μ	=	Viscosity, kg/ms

Subscript

f	=	Fluid
in	=	Inlet
m	=	Mean
out	=	Outlet
p	=	Particles
nf	=	Nanofluid
s	=	Surface

REFERENCES

[1] Masuda, H.; Ebata, A.; Teramae, K.; Hishinuma, N. Alteration of thermal conductivity and viscosity of liquid by dispersing ultra-fine particles (Disper-

sion of Al_2O_3, SiO_2 and TiO_2 ultra-fine particles). *Netsu Bussei (Japan)*, **1993**, *7*(4), 227-233.

[2] Choi, S.U.S. Enhancing thermal conductivity of fluids with nanoparticle. *ASME FED.*, **1995**, *231*, 99-105.

[3] Trisaksri, V.; Wongwises, S. Critical review of heat transfer characteristics of the nanofluids. *Renew. Sust. Energ. Rev*., **2007**, *11*(3), 512-523.

[4] Duangthongsuk, W.; Wongwises, S. A critical review of convective heat transfer of nanofluids. *Renew. Sust. Energ. Rev*., **2007**, *11*, 797-817.

[5] Wang, X.Q.; Mujumdar, A.S. Heat transfer characteristics of nanofluids: a review. *Int. J. Therm. Sci.*, **2007**, *46*, 1-19.

[6] Pak, B.C.; Cho, Y.I. Hydrodynamic and heat transfer study of dispersed fluids with submicron metallic oxide particles. *Exp. Heat Transf.*, **1998**, *11*, 151-170.

[7] Li, Q.; Xuan, Y. Convective heat transfer and flow characteristics of Cu-water nanofluid. *Sci. China E*., **2002**, *45*, 408-416.

[8] Xuan, Y.; Li, Q. Investigation on convective heat transfer and flow features of nanofluids. *ASME J. Heat Transf.*, **2003**, *125*, 151-155.

[9] Tsai, C.Y.; Chien, H.T.; Ding, P.P.; Chan, B.; Luh, T.Y.; Chen, P.H. Effect of structural character of gold nanoparticles in nanofluid on heat pipe thermal performance. *Mater. Lett.*, **2004**, *58*, 1461-1465.

[10] Wen, D.; Ding, Y. Experimental investigation into convective heat transfer of nanofluids at the entrance region under laminar flow conditions. *Int. J. Heat Mass Transf.*, **2004**, *47*, 5181-5188.

[11] Yang, Y.; Zhang, Z.G.; Grulke, E.A.; Anderson, W.B.; Wu, G. Heat transfer properties of nanoparticle-in-fluid dispersions (nanofluids) in laminar flow. *Int. J. Heat Mass Transf.*, **2005**, *48*(6), 1107-1116.

[12] Ding, Y.; Alias, H.; Wen, D.; Williams, R.A. Heat transfer of aqueous suspensions of carbon nanotubes (CNT nanofluids). *Int. J. Heat Mass Transf.*, **2005**, *49*(1-2), 240-250.

[13] Heris, S.Z.; Etemad, S.G.; Esfahany, M.N. Experimental investigation of oxide nanofluids laminar flow convective heat transfer. *Int. Commun. Heat Mass Transf.*, **2006**, *33*, 529-535.

[14] Heris, S.Z.; Esfahany, M.N.; Etemad, S.G. Experimental investigation of convective heat transfer of Al_2O_3/water nanofluid in circular tube. *Int. J. Heat Fluids Fl.*, **2007**, *28*(2), 203-210.

[15] He, Y.; Jin, Y.; Chen, H.; Ding, Y.; Cang, D.; Lu, H. Heat transfer and flow behavior of aqueous suspensions of TiO_2 nanoparticles (nanofluids) flowing upward through a vertical pipe. *Int. J. Heat Mass Transf.*, **2007**, *50*, 2272-2281.

[16] Duangthongsuk, W.; Wongwises, S. Effect of thermophysical properties models on the prediction of the convective heat transfer coefficient for low concentration nanofluid. *Int. Commun. Heat Mass Transf.*, **2008**, *35*, 1320-1326.

[17] Duangthongsuk, W.; Wongwises, S. Heat transfer enhancement and pressure drop characteristics of TiO_2-water nanofluid in a double-tube counter flow heat exchanger. *Int. J. Heat Mass Transf.*, **2009**, *52*, 2059-2067.

[18] Duangthongsuk, W.; Wongwises, S. An experimental study on the heat transfer performance and pressure drop of TiO_2-water nanofluids flowing under a turbulent flow regime. *Int. J. Heat Mass Transf.*, **2010**, *53*, 334-344.

[19] Tuckeman, D.B.; Pease, R.F.W. High performance heat sinking for VLSI. *IEEE Electron. Device L.*, **1981**, *2(5)*, 126-129

[20] Lee, S.; Choi, S.U.S. *Application of metallic nanoparticle of metallic nanoparticles suspensions in advanced cooling systems*. Proceedings of the International Mechanical Engineering Conference Session on Application of Metallic Materials in Advanced Engineering System, Atlanta, GA, USA, November 17-23, **1996**.

[21] Chein, R.; Huang, G. Analysis of microchannel heat sink performance using nanofluids. *Appl. Therm. Eng.*, **2005**, *25*, 3104-3114.

[22] Koo, J.; Kleinstreuer, C. Laminar nanofluid flow in microheat-sinks. *Int. J. Heat Mass Transf.*, **2005**, *48*, 2652-2661.

[23] Jang, S.P.; Choi, S.U.S. Cooling performance of a microchannel heat sink with nanofluids. *Appl. Therm. Eng.*, **2006**, *26*, 2457-2463.

[24] Abbassi, H.; Aghanajafi, C. Evaluation of Heat Transfer Augmentation in a Nanofluid-Cooled Microchannel Heat Sink. *J. Fusion Energ.*, **2006**, *25*(3/4), 187-196.

[25] Chein, R.; Chuang, J. Experimental microchannel heat sink performance studies using nanofluids. *Int. J. Therm. Sci.*, **2007**, *46*, 57-66.

[26] Tsai, T.S.; Chein, R. Performance analysis of nanofluid-cooled microchannel heat sinks. *Int. J. Heat Fluids Fl.*, **2007**, *28*, 1013-1026.

[27] Jung, J.Y.; Oh, H.S.; Kwak, H.Y. Forced convective heat transfer of nanofluids in microchannels. *Int. J. Heat Mass Tran.*, **2009**, *52*, 466-472.

[28] Ghazvini, M.; Shokouhmand, H. Investigation of a nanofluid-cooled microchannel heat sink using Fin and porous media approaches. *Energ. Convers. Manage*., **2009**, *50*, 2373-2380.

[29] Ho, C.J.; Wei, L.C.; Li, Z.W. An experimental investigation of forced convective cooling performance of a microchannel heat sink with Al_2O_3/water nanofluid. *Appl. Therm. Eng.*, **2010**, *30*, 96-103.

[30] Ebrahimi, S.; Sabbaghzadeh, J.; Lajevardi, M.; Hadi, I. Cooling performance of a microchannel heat sink with nanofluids containing cylindrical nanoparticles (carbon nanotubes). *Heat Mass Transf.*, **2010**, *46*, 549-553.

[31] Hamilton, R.L.; Crosser, O.K. Thermal conductivity of heterogeneous two-component systems. *Ind. Eng. Chem. Fundam.*, **1962**, *1*(3), 187.

[32] Drew, D.A.; Passman, S.L. *Theory of multicomponent fluids*, Springer: Berlin, **1999**.

Received: December 19, 2011 Revised: January 20, 2012 Accepted: March 11, 2012

Journal of ASTM International, Vol. 9, No. 5
Paper ID JAI104409
Available online at www.astm.org

A. Suriyawong,[1] *A. S. Dalkilic,*[2] *and S. Wongwises*[3]

Nucleate Pool Boiling Heat Transfer Correlation for TiO_2-Water Nanofluids

ABSTRACT: This paper is a continuation of the authors' previous work on the nucleate pool boiling heat transfer of nanofluids [Suriyawong, A. and Wongwises, S., "Nucleate pool boiling heat transfer characteristics of TiO2-water nanofluids at very low concentrations," *Exp. Therm. Fluid Sci.*, Vol. 34, No. 8, 2010, pp. 992–999.] This study presents new correlation for predicting heat transfer coefficient for nucleate pool boiling of TiO_2-water nanofluids at several low concentrations. Unlike most previous studies, the proposed correlation consists of various relevant factors. Two horizontal circular plates made from copper and aluminum with different surface roughness values are used as heating surfaces. Because the calculation concerns with properties of nanofluids, this research uses various correlations from previous studies to find the properties of nanofluids and the best one is selected for the presentation. Compared with measured data of nucleate pool boiling of water and nanofluids from present and previous studies, it was found that the developed correlation could be used for prediction at a certain level.

KEYWORDS: nucleate boiling, nanofluids, nanoparticles, heat transfer, heat flux

Nomenclature

A = Area, m^2
bf = Base fluids
C_p = Specific heat, $kJ/kg \times K$
$cond$ = Conduction heated
$elec$ = Electric power
g = Gravitational acceleration, m/s^2
h_b = Boiling heat transfer coefficient, $W/m^2 \times K$
h_{fg} = Heat of vaporization, kJ/kg
I = Electric current, Amps
k = Thermal conductivity, $W/m \times K$
L_c = Characteristic length, m
l = Liquid phase
nf = Nanofluids
np = Nanoparticles
Pr = Prandtl number, Dimensionless
q'' = Heat flux, W/m^2
Ra = Average roughness, μmRz Mean peak-to-valley height roughness, μm
s = Heating surface
sat = Saturation
T = Temperature, K
V = Voltage, Volts
ν = Vapor phase
x = Position of temperature on test section, m

Manuscript received October 8, 2011; accepted for publication January 27, 2012; published online May 2012.
[1]Fluid Mechanics, Thermal Engineering and Multiphase Flow Research Laboratory (FUTURE), Dept. of Mechanical Engineering, King Mongkut's Univ. of Technology Thonburi, Bangmod, Bangkok 10140, Thailand.
[2]Heat and Thermodynamics Division, Dept. of Mechanical Engineering, Yildiz Technical Univ., Yildiz, Besiktas, Istanbul 34349, Turkey.
[3]Fluid Mechanics, Thermal Engineering and Multiphase Flow Research Lab. (FUTURE) Dept. of Mechanical Engineering, King Mongkut's Univ. of Technology Thonburi, Bangmod, Bangkok 10140, Thailand; and The Academy of Science, The Royal Institute of Thailand, Sanam Suea Pa, Dusit, Bangkok 10300, Thailand (Corresponding author), e-mail: somchai.won@kmutt.ac.th

ε = Roughness of the heating surface, m
μ = Dynamic viscosity, $\mathrm{kg/m} \times \mathrm{s}$
ρ = Density, $\mathrm{kg/m^3}$
σ = Surface tension of liquid–vapor interface, $\mathrm{N/m}$
ϕ = Volume fraction of the nanoparticles, Dimensionless

Introduction

As a result of the fact that thermal conductivity of nanofluids is higher than that of base fluid, the writers propose to use nanofluids as working fluids in heat exchanger. The study of pool boiling heat transfer characteristics is another important and necessary issue in the development of heat exchanger, in which the working fluid boils. Literature review reveals that, recently, many researchers have had an interest in and conducted experimental studies about pool boiling of nanofluids (as shown in Table 1).

To the best of our knowledge, there are only a few correlations available for predicting heat transfer coefficient for pool boiling of nanofluids. However, although some information is currently available, there still remains room for further research, especially relevant parameters or variables that are taken into account in the correlation. The outstanding feature of this research is the correlation to predict the boiling heat transfer coefficient. The proposed correlation consists of several parameters that contribute to heat transfer characteristics, i.e., nanofluids concentration; thermophysical properties of nanofluids (density, specific heat, viscosity, thermal conductivity); heating surface roughness; and heating surface material.

Preparation of Nanofluids

The preparation of nanofluids can be divided into three parts: *p*H control, addition of surfactants, and use of ultrasonic vibration. The preparation of nanofluids aims to make nanoparticles suspend in base fluids with stability, without sedimentation. The nanofluids used (VP Disp. W740) were supplied by Degussa Company. The fluids have TiO_2 nanoparticles with average diameters of 21 nm, suspended in a water base fluid that has a concentration of 40 wt. %. The nanofluids were diluted by adding water to achieve the desired concentration levels of 0.00005 vol. %, 0.0001 vol. %, 0.0005 vol. %, 0.005 vol. %, and 0.01 vol. %. After that, the fluids were treated with ultrasonic vibration for 2 h to distribute the nanoparticles evenly.

Sample photographs of nanofluids used in the experiment were taken from a transmission electron microscope (TEM) shown in Fig. 1(*a*). An initial analysis of the nanoparticles' sizes revealed an almost circular shape with average diameter of 21 nm (Fig. 1(*b*)), corresponding with data from the manufacturer.

Experimental Apparatus and Procedure

The experimental apparatus as shown in Fig. 2(*a*) consists of three main sections: test section, heating device, and pressure control in the pressure vessel. The test section was placed inside the twin-layered stainless steel pressure vessel. The inner layer of the pressure vessel contained the nanofluids used in the experiment. The outer layer contained water heated by a preheater (1.5 kW) to keep the temperature of the nanofluids inside the inner tank stable at saturation temperature. The temperature of the nanofluids was measured by a T-type sheath thermocouple with deviation of $\pm$ 0.1 °C.

Figure 2(*b*) shows the boiling test section, which consists of a heater (1.2 kW) placed inside a copper bar that will transfer heat from the heater to the test section installed at the upper end of the copper bar. The copper bar and the test section are covered with calcium silicate insulator which is 50 mm thick to prevent lateral heat loss. The test section was made from two materials: copper and aluminum. The heating surfaces have average roughnesses of 0.2 μm and 4 μm. The roughness can be measured by a Mahr Marsurf PS1 model roughness meter. The test section area contains four holes for installing sheath thermocouples. Thermocouples are placed at intervals of 10 mm. The distance between the uppermost sheath thermocouple and the heating surface is 20 mm. Temperatures at various locations in the test section would be used to calculate the temperature of the heating surface.

Pressure inside the inner tank was controlled by adjusting the water flow in the cooling coil to control the condensation rate of vapor at the outer surface of the cooling coil. During operation, the pressure inside both layers of the tank is kept at atmospheric condition.

TABLE 1—*The literature review for pool boiling nanofluids.*

Authors	Heating surface	Nanofluids	Concentration	Remarks
Li et al. [1]	Platinum wire	SiO_2-water	0.05–0.5 wt. %.	There was no subsidence of nanoparticles on Pt wire surface, as suffered on heated tube. The superheat of 0.05 wt. % nanofluids was lower than that of pure water.
Vassallo et al. [2]	Nichrome wire, D = 0.4 mm, L = 120 mm.	Si-water	0.5–9 vol. %.	The experimental data show a marked increase in CHF compared to pure water.
Kim et al. [3,4]	Nichrome wire, D = 0.2 mm. Titanium wire, D = 0.25 mm.	TiO_2-water Al_2O_3-water	0.00001–0.1 vol. %.	The nanofluids increased the CHF compared with pure water. The SEM photograph showed that the nanoparticles were deposited on the heating surface during pool boiling.
Golubovic et al. [5]	Nichrome wire, D = 0.64 mm, L = 50 mm.	BiO_2-water Al_2O_3-water	0.5714–6.4615 mg/l	The CHF increased with increase in the volume concentrations.
You et al. [6]	Square flat copper surfaces	Al_2O_3-water	0.001–0.05 g/l	The CHF increased dramatically (200 %) compared with pure water.
Bang and Chang [7]	Smooth flat copper surfaces	Al_2O_3-water	0.5–4.0 vol. %	The nanofluids have poor heat transfer performance compared to pure water. The HTC was decreased by increasing particle concentration.
Nishikawa et al. [8]	Copper flat plate	Water	-	The effect of surface orientation was remarkable in the low heat flux region, the HTC increased as the inclination angle was increased.
Kim et al. [9]	Stainless steel wire D = 0.381 mm. L = 120 mm.	Al-water ZrO-water Si- water	0.001–0.1 vol. %.	The nanofluids exhibited significant CHF enhancement compared with the base fluid. Some nanoparticles were coated on the heating surface during nucleate boiling to form a porous layer.
Liu and Liao [10]	Plain copper	CuO-water CuO-alcohol	0.5 wt. % and 1 wt. %	The boiling heat transfer characteristics of the nanofluids were slightly poor compared with water and alcohol.
Das et al. [11,12]	Stainless steel cylinders D = 4, 6.5, 20 mm	Al_2O_3-water	1–4 vol. %	The HTC deteriorated with the addition of nanoparticles.
Trisaksri and Wongwises [13]	Cylindrical copper tube	TiO_2-R141b	0.01–0.05 vol. %	The effect of pressure on the HTC was clear at higher heat flux.
Suriyawong and Wongwises [14]	Copper and aluminum flat surfaces.	TiO_2-water	0.00005–0.01 vol. %	For copper, at 0.0001 vol. %, higher nucleate pool boiling heat transfer coefficient was obtained compared with the base fluid. A 15 % increase was obtained for the roughness of 0.2 μm and a 4 % increase was obtained for roughness of 4 μm. For concentrations higher than 0.0001 vol. %, the higher the concentration, the lower the heat transfer coefficient. For aluminum, the corresponding heat transfer coefficients were larger than for the copper surface by around 30 % with a roughness of 0.2 μm and around 27 % with a roughness of 4 μm. The results indicated that the heat transfer coefficient obtained based on a roughness of 4 μm was higher than that for a roughness of 0.2 μm by around 12 % for aluminum and by around 13 % for copper.

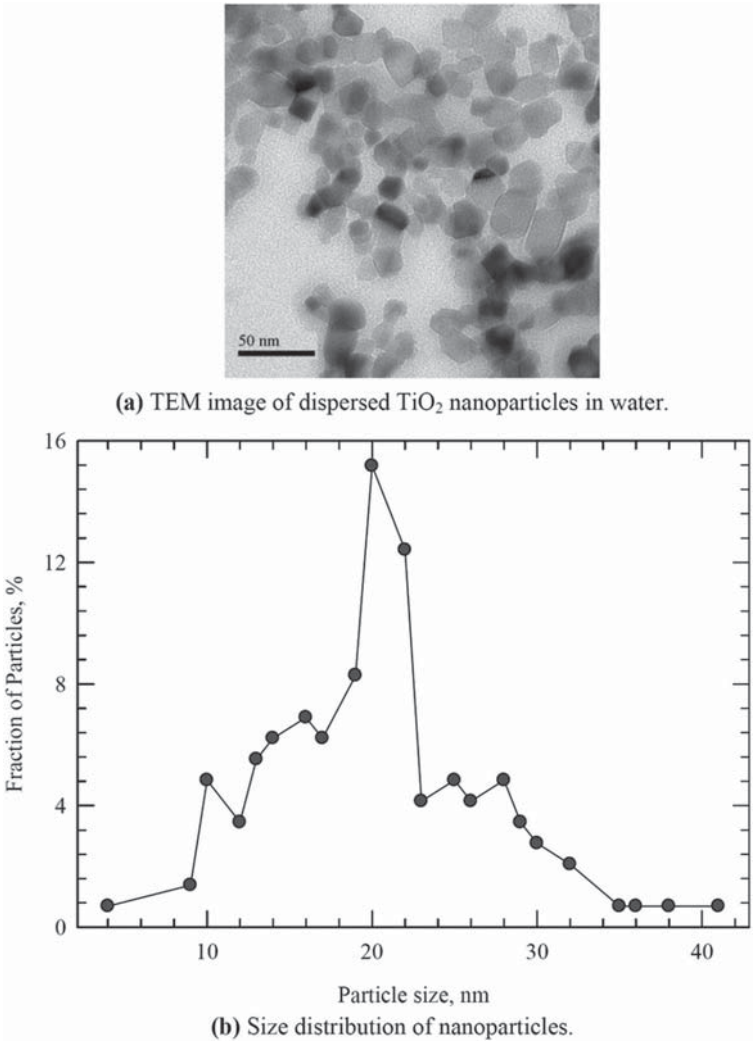

FIG. 1—*Nanofluids used in the present study (a) TEM image of dispersed TiO_2 nanoparticles in water; (b) size distribution of nanoparticles.*

In the experiment with high heat flux there was film boiling, which created film at the heating surface. When this happened, temperatures at various points of the test section increased rapidly. This condition can cause harm to the apparatus. Therefore, a wind blower was installed to eradicate film boiling on the heating surface; hence, the surface temperature decreased.

After experimenting under each condition, the experimental apparatus was dissected and cleaned to get rid of nanoparticles on various parts. The apparatus can be cleaned by using a high-pressure water injector to inject water on the heating surface. After that, the apparatus was dried with a blower before being assembled for use in experiments under other conditions. The experimental conditions for the present study are shown in Table 2.

Data Reduction

The heat fluxes, q (W/m^2), were calculated from the following equation:

$$q = \frac{IV}{A} \tag{1}$$

where:

I is the current (amps),
V is the voltage (volts), and
A is the heating surface area (m^2).

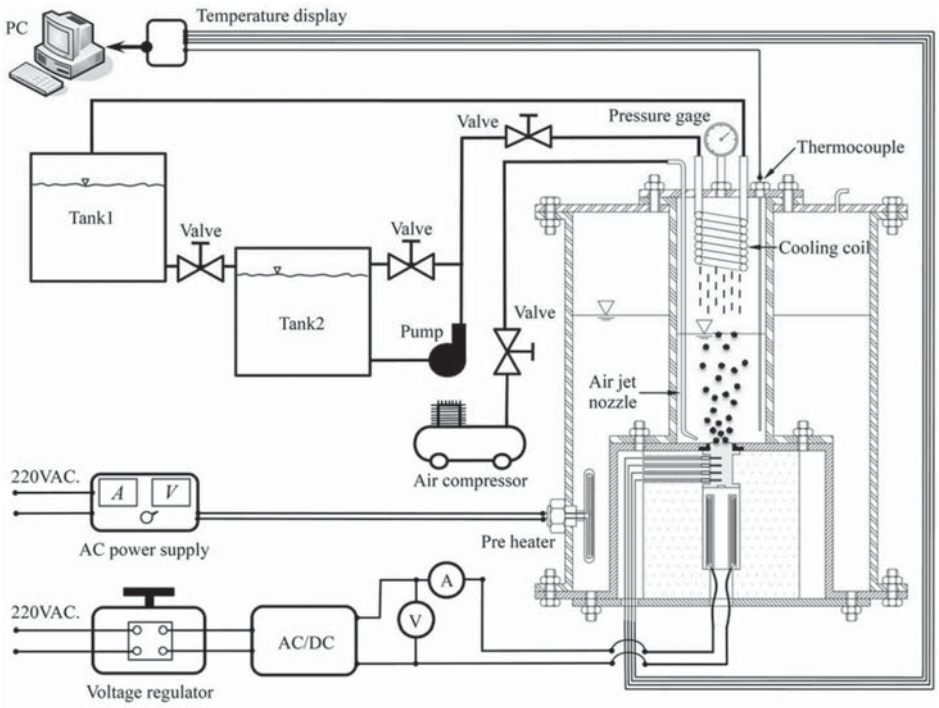

(a) Schematic diagram of the experimental apparatus.

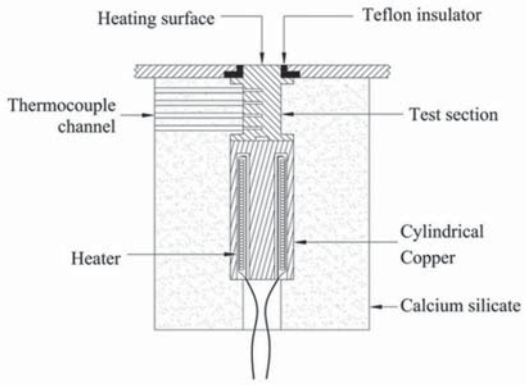

(b) Cross-sectional view of the boiling test section.

FIG. 2—*Experimental apparatus: (a) schematic diagram of experimental apparatus; (b) cross-sectional view of the boiling test section.*

The average boiling heat transfer coefficient, h_b (W/m^2 × K), is defined as

$$h_b = \frac{q}{T_s - T_{sat}} \tag{2}$$

where:

T_s is the average heater surface temperature (°C) calculated from Eq 3, and T_{sat} is the liquid saturation temperature (°C)

$$T_s = \frac{\sum_{i=1}^{4} T_i \sum_{i=1}^{4} x_i^2 - \sum_{i=1}^{4} x_i \sum_{i=1}^{4} x_i T_i}{4\sum_{i=1}^{4} x_i^2 - \left(\sum_{i=1}^{4} x_i\right)^2} \tag{3}$$

where T_i is the local temperature (°C) and x is the position of the temperature measurement (m) on the test section.

TABLE 2—*The present experimental conditions.*

Parameter	Value
Classification of boiling	Saturated pool boiling
Material of heating surface	Copper and Aluminum
Heating surface roughness	0.2–4.0 μm
Type of nanofluids	TiO_2-distilled water
Concentration of nanofluids	0.0001–0.01 vol.%
Heat flux	40–800 kW/m^2
Pressure	1 atm.

The uncertainties of the heat flux, heating surface temperature, and heat transfer coefficient are ±2.2 %, ±3.7 %, and ±11.6 %, respectively.

Results and Discussion

It is quite difficult to develop any general theoretical model for predicting the heat transfer coefficients in nucleate boiling [15]. In this section, the correlation for predicting the pool boiling heat transfer coefficient is developed. The correlation is modified from Rohsenow's correlation [16] for various liquid-surface combinations. The pool boiling heat transfer coefficient of nanofluids, $h_{b,nf}$, is assumed to be a function of the viscosity of nanofluids μ_{nf}, the heat flux q'', the thermal conductivity of nanofluids k_{nf}, the roughness of heating surface ε, the specific heat of nanofluids $C_{p,nf}$, the latent heat of vaporization h_{fg}, the volume fraction of nanoparticles ϕ, the surface tension σ, the gravitational acceleration g, the density of nanofluids ρ_{nf}, and the density of water vapor ρ_v.

The model is of the form

$$h_{b,nf} = f\left(\mu_{nf}, q'', k_{nf}, \varepsilon, C_{p,nf}, h_{fg}, (\phi + m), \frac{\sigma}{g(\rho_{nf} - \rho_v)}\right) \tag{4}$$

TABLE 3—*The thermophysical property models of nanofluids.*

Investigator	Correlation	Remarks
Density of nanofluids		
Pak and Cho [17]	$\rho_{nf} = \phi\rho_{np} + (1-\phi)\rho_{bf}$	For Al_2O_3- and TiO_2-water nanofluids.
Specific heat of nanofluids		
Pak and Cho [17]	$C_{p,nf} = \phi C_{p,np} + (1-\phi)C_{p,bf}$	For Al_2O_3- and TiO_2-water nanofluids.
Xuan and Roetzel [18]	$(\rho C_p)_{nf} = \phi(\rho C_p)_{np} + (1-\phi)(\rho C_p)_{bf}$	For the synthesized nanoparticle-liquid suspension.
Viscosity of nanofluids		
Wang et al. [19]	$\mu_{nf} = (1 + 7.3\phi + 123\phi^2)\mu_{bf}$	For Al_2O_3-water nanofluids, volume fractions less than 6 %.
Einstein's equation suggested by Drew and Passman [20]	$\mu_{nf} = (1 + 2.5\phi)\mu_{bf}$	For small rigid spherical particles in volume fractions less than 5 %.
Brinkman [21]	$\mu_{nf} = \mu_{bf}(1-\phi)^{-2.5}$	For oil-water nanofluids and Cu-water nanofluids.
Thermal conductivity of nanofluids		
Hamilton and Crosser [22]	$k_{nf} = \left(\frac{k_{np}+(n-1)k_{bf}-(n-1)\phi(k_{bf}-k_{np})}{k_{np}+(n-1)k_{bf}+\phi(k_{bf}-k_{np})}\right)k_{bf}$	Empirical shape factor (n = 3/ψ), where ψ is the sphericity, defined as the ratio of the surface area of a sphere per surface area of the particle.
Murshed et al. [23]	$k_{nf} = \frac{1}{4}[(3\phi-1)k_{np} + (2-3\phi)k_{bf}] + \frac{k_{bf}}{4}\sqrt{\Delta}$ $\Delta = \begin{pmatrix}(3\phi-1)^2(k_{np}/k_{bf})^2 + (2-3\phi)^2 \\ +2(2+9\phi-9\phi^2)(k_{np}/k_{bf})\end{pmatrix}$	For the TiO_2-water nanofluids, volume fractions less than 5 %.
Wasp [24]	$k_{nf} = \left(\frac{k_{np}+2k_{bf}-2\phi(k_{bf}-k_{np})}{k_{np}+2k_{bf}+\phi(k_{bf}-k_{np})}\right)k_{bf}$	For particle special case with the sphericity ψ = 1.0.
Yu and Choi [25]	$k_{nf} = \left(\frac{k_{np}+2k_{bf}+2(k_{np}-k_{bf})(1+\beta)^3\phi}{k_{np}+2k_{bf}-(k_{np}-k_{bf})(1+\beta)^3\phi}\right)k_{bf}$	The β is the ratio of the nanolayer thickness to the original particle radius, normally β = 1.

TABLE 4—*The groups of correlations used to determine the thermophysical properties.*

Nanofluids property correlations		
μ_{nf}	$C_{p,nf}$	k_{nf}
Wang et al. [19]	Pak and Cho [17]	Hamilton and Crosser [22]
Wang et al. [19]	Pak and Cho [17]	Yu and Choi [25]
Wang et al. [19]	Xuan and Roetzel [18]	Hamilton and Crosser [22]
Wang et al. [19]	Xuan and Roetzel [18]	Yu and Choi [25]
Einstein's equation [20]	Pak and Cho [17]	Hamilton and Crosser [22]
Einstein's equation [20]	Pak and Cho [17]	Yu and Choi [25]
Einstein's equation [20]	Xuan and Roetzel [18]	Hamilton and Crosser [22]
Einstein's equation [20]	Xuan and Roetzel [18]	Yu and Choi [25]

Using the Buckingham Pi theorem, a set of dimensionless terms was established as follows:

$$Nu_{nf} = a(\mathrm{Pr}_{nf})^b \left(\frac{q''\varepsilon}{\mu_{nf} h_{fg}}\right)^c \left(\frac{\varepsilon^2 g(\rho_{nf} - \rho_v)}{\sigma}\right)^d \left(\frac{L_c}{\varepsilon(\phi + m)^e}\right) \tag{5}$$

where

$$Nu_{nf} = \frac{h_{b,nf} L_c}{k_{nf}} \tag{6}$$

$$\mathrm{Pr}_{nf} = \frac{\mu_{nf} C_{p,nf}}{k_{nf}} \tag{7}$$

L_c is the characteristic length, and a, b, c, d, e, and m are the coefficients.

TABLE 5—*The coefficients for the correlation.*

Coefficient for copper surface						Coefficient for aluminum surface					
a	b	c	d	e	m	a	b	c	d	e	m
28.85	0.59	0.70	0.16	0.12	0.001	46.63	0.55	0.74	0.15	0.05	0.00001

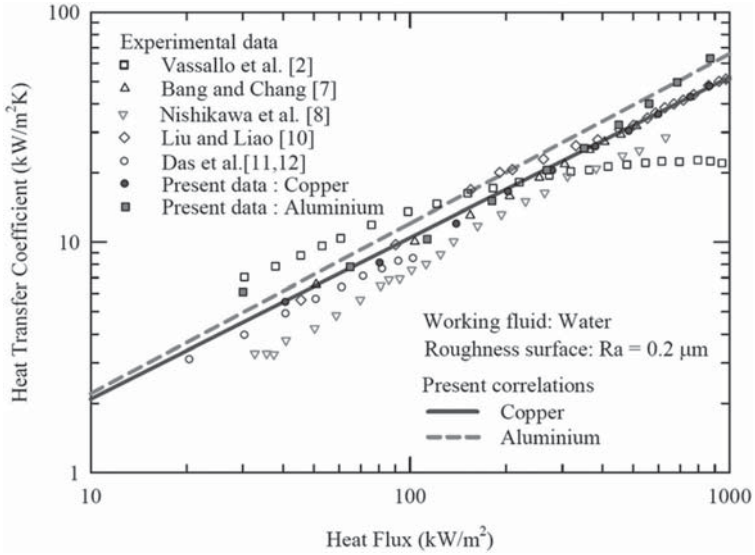

FIG. 3—*Comparison of the results obtained from the proposed correlations with the measured data obtained from several researchers.*

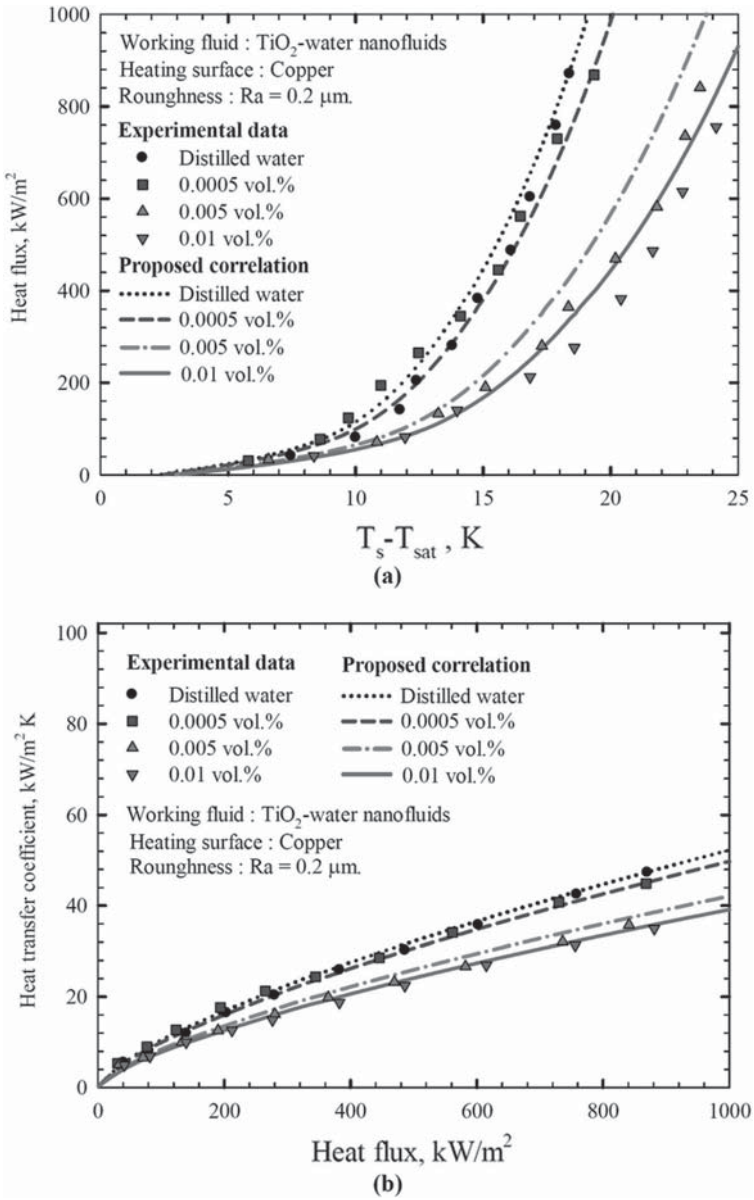

FIG. 4—*Comparison of the measured boiling curve and heat transfer coefficient with the proposed correlation (Copper heating surface, roughness Ra = 0.2 μm).*

The thermophysical properties such as density, viscosity, specific heat, and thermal conductivity of the nanofluid are calculated using different formulae as shown in Table 3. On the basis of the experimental result of Das et al. [11], the surface tension of water is used in the present study.

Because there are several equations for determining various thermophysical properties of nanofluids, the combinations of these equations, as shown in Table 4, are used to determine the coefficients in Eq 5.

The coefficients in Eq 5 are obtained by equation fitting for measured data obtained from the experiments with copper surface and aluminum surface. Comparisons between the heat transfer coefficients obtained from the proposed correlations and those obtained from the experiments show that there is no difference in heat transfer coefficient obtained from various properties. All existing correlations for specific heat, absolute viscosity, and thermal conductivity give very similar predicted results. As a result, in order to make it easy, the viscosity correlation of Wang et al. [19], specific heat correlation of Pak and Cho [17], and thermal conductivity correlation of Hamilton and Crosser [22] are used for the next calculations. The coefficients in Eq 5 for both surfaces are shown in Table 5.

Figure 3 shows comparisons between plots of heat transfer coefficients against heat flux, obtained from the present experiment and those obtained from the proposed correlations. The experimental data of

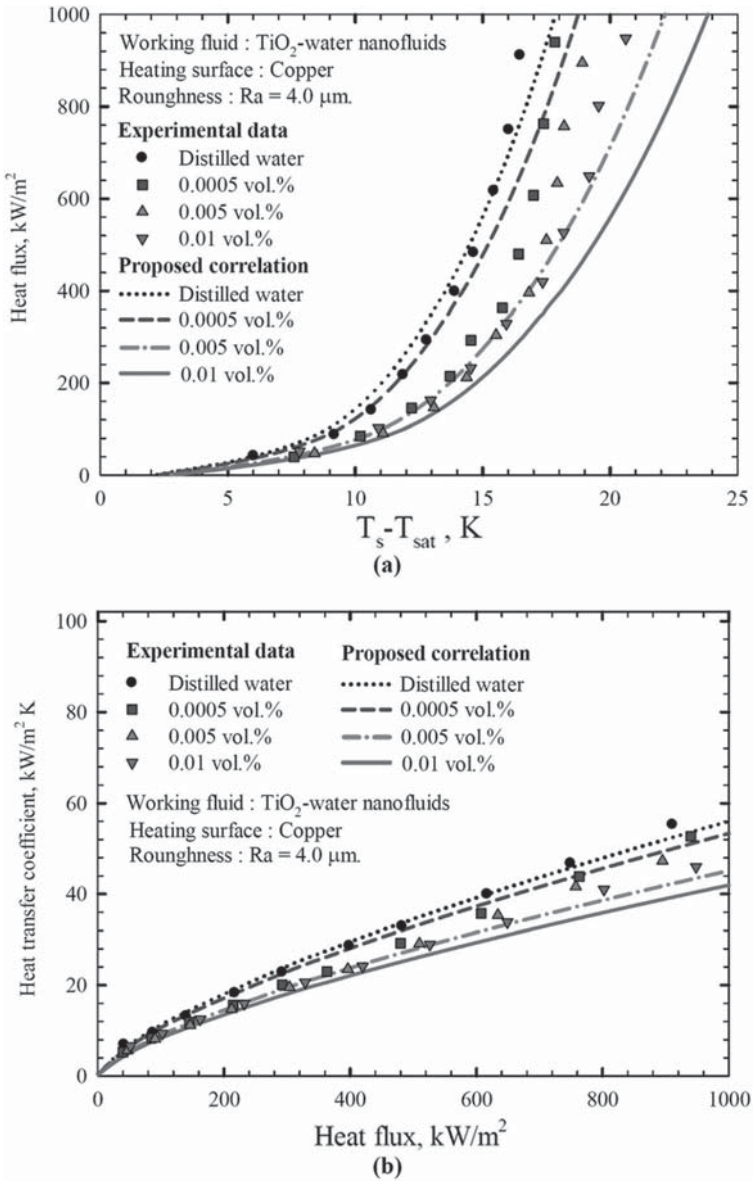

FIG. 5—*Comparison of the measured boiling curve and heat transfer coefficient with the proposed correlation (Copper heating surface, roughness Ra = 4 μm).*

Vassallo et al. [2], Bang and Chang [7], Nishikawa et al. [8], Liu and Liao [10], and Das et al. [11,12] obtained from various heating surface materials, surface roughnesses, nanofluids, and concentrations are also plotted in Fig. 3. From comparison between the measured heat transfer coefficients and the calculated ones for nucleate boiling of water on the horizontal circular plate, it is found that mean absolute error for copper surface and for aluminum surface are 5 % and 14 %, respectively.

Comparisons of the experimental boiling curves and experimental heat transfer coefficient with those calculated by the proposed correlations are shown in Figs. 4 and 5 for copper heating surface and Figs. 6 and 7 for aluminum heating surface.

All boiling curves shown in Figs. 4 through 7 present the experimental heat transfer data of nanofluids at various concentrations. Each data point was taken at steady state and each curve was obtained from the constant pressure experiment. The condition of steady state in pool boiling study is defined as a variation in the system saturation temperature of less than some accepted small temperature.

Considering each curve, we accept that the nanoparticle deposition, which is the transient process associated with boiling time, would occur and affect the nucleation site density. However we believe that

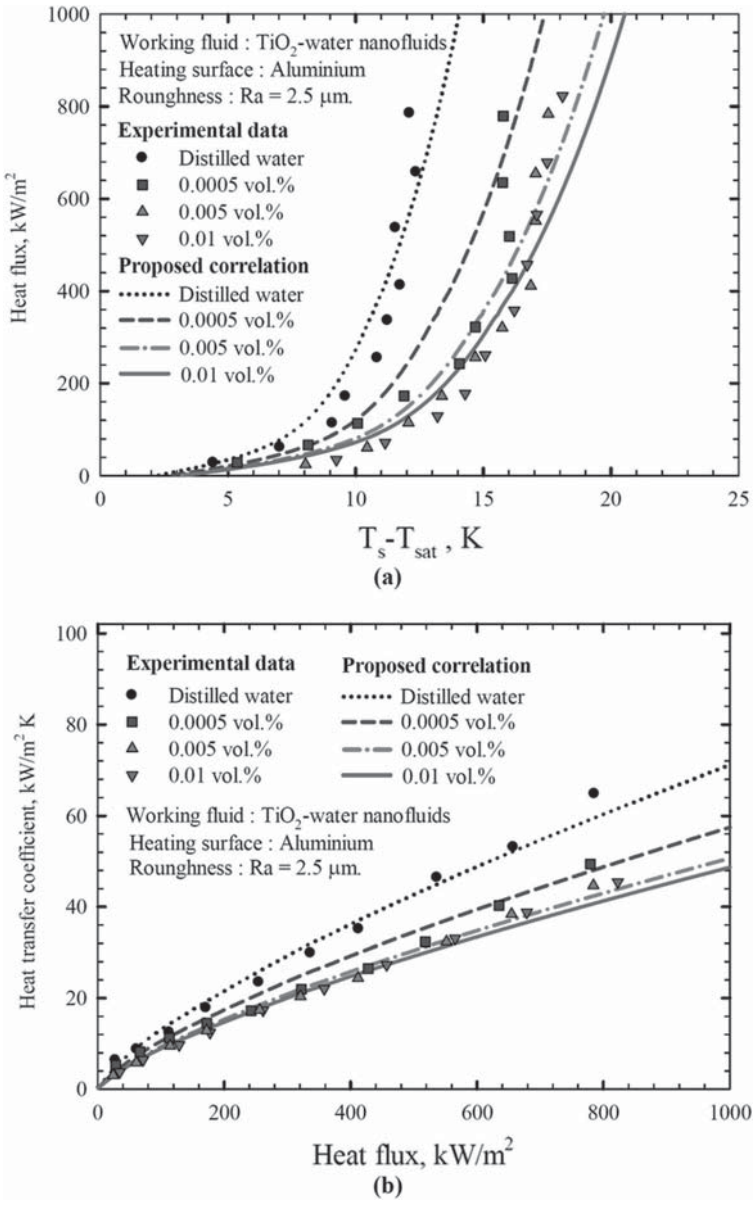

FIG. 6—*Comparison of the measured boiling curve and heat transfer coefficient with the proposed correlation (Aluminum heating surface, roughness Ra = 2.5 μm).*

the boiling curve in this style is still a good graphical presentation and is practical for pool boiling study. In other words, even though deposition occurs on the surface during the experiment and varies with boiling time, this type of curve is still useful and gives some physical information.

Because several parameters are included for the correlation fitting, it is quite hard to make this obtained correlation fit all data curves. However, the results obtained from the correlation tend to go in the same direction as the data, especially the heat transfer coefficient data of the copper surface. We do believe that this correlation will be useful to predict the heat transfer coefficients for nucleate pool boiling of TiO_2-water nanofluids under the same various conditions, and the results will be a guideline for the prediction of boiling heat transfer coefficients for any other nanofluids at various other conditions.

Conclusions

Correlations for nucleate pool boiling heat transfer coefficient for TiO_2-water nanofluids at low concentrations for heating surfaces made from copper and aluminum are proposed. Different from most previous